CHARACTERIZATION OF NONLINEAR HEAT RELEASE-ACOUSTIC INTERACTIONS IN GAS TURBINE COMBUSTORS

A Dissertation
Presented to
The Academic Faculty

By

Benjamin D. Bellows

In Partial Fulfillment
of the Requirements for the Degree
Doctor of Philosophy in
Aerospace Engineering

Georgia Institute of Technology
May 2006

CHARACTERIZATION OF NONLINEAR HEAT RELEASE-ACOUSTIC INTERACTIONS IN GAS TURBINE COMBUSTORS

Approved By:

Dr. Timothy Lieuwen, Advisor
Associate Professor
School of Aerospace Engineering
Georgia Institute of Technology

Dr. Ben T. Zinn,
Regents Professor, David S. Lewis Chair
School of Aerospace Engineering
Georgia Institute of Technology

Dr. Jerry Seitzman
Associate Professor
School of Aerospace Engineering
Georgia Institute of Technology

Dr. Jechiel Jagoda
Professor, Associate Chair for Research and Graduate Studies
School of Aerospace Engineering
Georgia Institute of Technology

Dr. Jeffrey Cohen
Aerodynamics Manager,
Combustor and Augmentor Technology
Pratt & Whitney

Date Approved: 2/28/2006

To my wife

"Now this is not the end. It is not even the beginning of the end. But it is, perhaps, the end of the beginning."

Sir Winston Spencer Churchill

1874 – 1965

ACKNOWLEDGMENTS

I would like to acknowledge the support and help of numerous people, without whom this thesis would not have been possible:

Many thanks to my thesis advisor, Dr. Tim C. Lieuwen, for his guidance and support of my research.

I also would like to thank Dr. Ben T. Zinn, Dr. Jerry Seitzman, Dr. Jeff Jagoda and Dr. Jeff Cohen for serving on my thesis committee and a great deal of advice and assistance.

Finally, I would like to acknowledge the graduate students, undergraduate students, and other research engineers for their help, friendship and support : Suraj Nair, Rajesh Rajaram, Antonio Cho, Venkat Narra, Aurelien Cottet, the Santoshes, Preetham, D.R. Noble, Qingguo Zhang, Sai Kumar, Muruganandam Thiruchengode, Mohan Bobba, Alex Hreiz, Joshua Gray, Andrew Meyers, David Scarborough, Dr. Yedidia Neumeier and Adam Coker.

The financial support of the United States Department of Energy through the High Efficiency Engines and Turbines (HEET) Research program is gratefully acknowledged.

TABLE OF CONTENTS

LIST OF TABLES

LIST OF FIGURES

NOMENCLATURE

p - pressure

Q – heat release

u – velocity

t – time

f – frequency

G_{ij} – transfer function gain between quantities i and j

Greek symbols

ϕ – equivalence ratio

γ_{ij} – coherence between quantities i and j

Δ - uncertainty estimate in measurements

θ_{ij} – phase angle between quantities i and j

ω – angular frequency = $2\pi f$

Subscripts and superscripts

( )’ – fluctuating amplitude

$( )_o$ – mean quantity

SUMMARY

This thesis describes an experimental investigation of the nonlinear flame response to large amplitude acoustic oscillations. The objective of this work was to characterize this nonlinear flame behavior, the parameters which affect it, and the responsible mechanisms. The effects of equivalence ratio, driving frequency, and Reynolds number on the nonlinear response of the flame chemiluminescence are investigated for two different combustors.

This thesis presents the first characterization of the nonlinear response to forced acoustic oscillations of turbulent, swirling flames. Nonlinearities in the flame chemiluminescence were observed for large velocity oscillation amplitudes for several operating conditions, but the transfer function remains linear for other conditions. The corresponding pressure amplitudes at the point of nonlinear response range between 1 – 2% of the mean pressure indicating that nonlinear combustion processes, as opposed to gas dynamic nonlinearities, dominate the response of the flame chemiluminescence.

Saturation of the chemiluminescence occurred at values of 20 – 100% of the mean values dependent on the operating condition. In addition, the shape and behavior of the transfer function between the velocity oscillation and chemiluminescence oscillation amplitudes changes significantly for different operating conditions, These results illustrate that a single combustor exhibits a variety of mechanisms controlling the nonlinear response of the flame at these large amplitude oscillations.

Three mechanisms have been identified in this thesis which control the nonlinear flame dynamics for different operating conditions – parametric instability, vortex roll-up, and unsteady flame liftoff. First, for lower mean velocity conditions, nonlinearity in the flame response is observed to occur when the subharmonic of the flame chemiluminescence oscillation reaches appreciable amplitudes. This subharmonic response is a manifestation of the parametric instability by the unsteady acceleration of the flame front by the velocity field. Secondly, for higher mean velocity conditions, vortex rollup and unsteady flame liftoff, are seen to control the nonlinear behavior. Both these mechanisms show that the central recirculation zone is an important controlling factor of the nonlinear flame dynamics. All of the mechanisms controlling the nonlinear flame response of the two combustors in this study are shown to depend on Strouhal number and the ratio of the oscillating velocity and laminar flame speed. In addition, the harmonic and subharmonic of the flame influence the flame's nonlinear behavior when acoustically forced.

Finally, the nonlinear combustion process is shown to significantly affect the frequency response of combustors in both stable and unstable operation when forced acoustically. Nonlinear oscillator theory provides qualitative explanations for the effects observed in these experiments.

CHAPTER 1

MOTIVATION AND BACKGROUND

1.1 Motivation

This thesis describes an experimental investigation on the nonlinear processes responsible for limit cycle behavior during combustion instability in dry, low NO_x (DLN) gas turbine systems. Increased demand for DLN turbines resulted from more stringent pollutant emission requirements, especially oxides of nitrogen (NO_x). Indeed, power generation from modern, land-based gas turbines has become the dominant technology in the United States and around the world. These turbines have extremely high operating efficiencies and produce fewer pollutant emissions than other combustion devices. In addition, the relatively low capital costs and ease of installation have made power turbine very enticing to investors.

Control and reduction of pollutant emissions is a major design factor of modern combustion systems. Traditionally, gas turbines have used diffusion-flame combustors because of their reliable performance and reasonable flame holding characteristics. The major side effect of such a system, however, is that they produce substantial amounts of NOx emissions. In order to reduce NO_x emissions in these systems, manufacturers typically inject water into the primary zone of the combustor. While NO_x emissions are

reduced, this comes at the expense of decreased efficiency and time between overhauls, as well as increased cost and complexity.

The Clean Air Act of 1990 imposed strict guidelines on the emission and control of nitrogen oxides (NOx) from stationary sources, such as industrial gas turbines. The increasingly strict regulation of pollutant emissions as well as increased demand for more efficiency and power has recently led engine manufacturers to develop low-emissions gas turbine engines to fulfill the regulatory requirements [1]. These regulations, as well as other pollutant requirements, have shaped the designs of modern, industrial gas turbines. Modern DLN gas turbines produce lower amounts of nitrogen oxides by operating fuel lean, and premixing the fuel and oxidizer. This mode of operation is illustrated by the schematic of a typical DLN combustor in Figure 1. Figure 1 shows the air from the compressor flowing into the inlet section from the left. Fuel is injected into this air stream by injectors at the upstream end of the mixing section. The fuel and air subsequently mix as they convect through the inlet and swirl vanes toward the flame. The lower temperatures in the combustion zone ($T_{comb} < 1800$ K) resulting from burning these leaner mixtures, decreases the thermal NOx formation, a predominant mechanism for NOx production in hydrocarbon flames [2]. The current engineering challenge is to reduce pollutant emissions while simultaneously improve or maintain power output, and increase the reliability and availability of the engines.

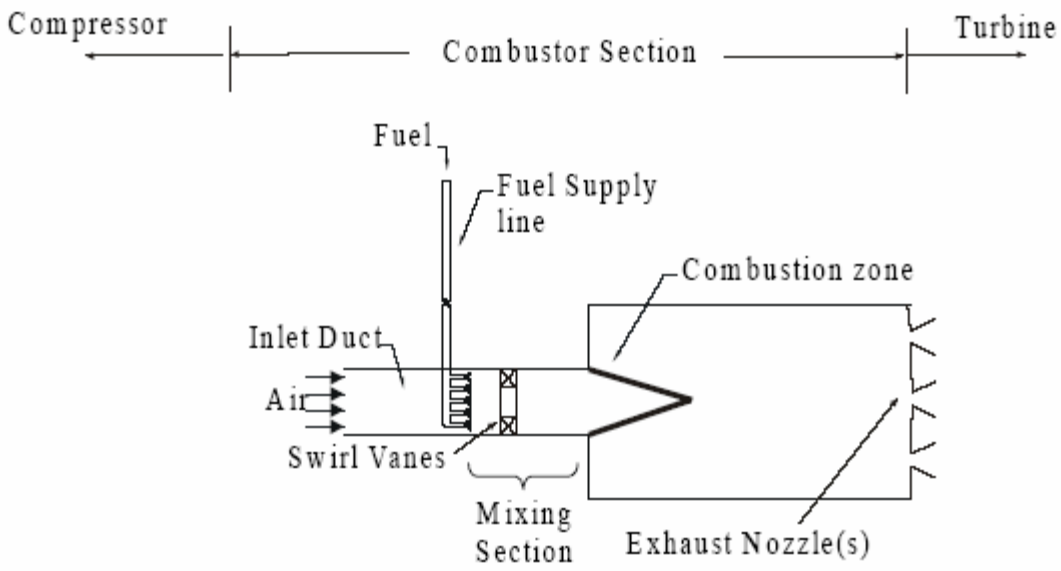

Figure 1. Schematic of a generic gas turbine combustor

One of the major side effects of operating at these low temperatures, however, is that combustion instabilities can become self-excited. Indeed, combustion dynamics continues to be one of the most serious issues hindering the development and operation of industrial gas turbines [3-6]. These instabilities generally occur when the unsteady combustion process couples with one or more of the natural acoustic modes of the combustion chamber, resulting in self-excited oscillations. The resultant flow and structural vibrations can substantially reduce hot section part life. As such, avoiding operating regimes where high dynamics occur often requires operating at lower power outputs and/or higher pollutant emissions than the turbine is otherwise capable.

1.2 Background

The following section on the coupling of the unsteady combustion process to a system's acoustic properties closely follows the discussion in Ref. [7]. Lord Rayleigh [8]

was the first to state the conditions under which a periodic heat addition process amplifies acoustic oscillations causing instability. Rayleigh's Criterion states that a periodic heat release process adds energy to the acoustic field when the time average product of the heat addition and pressure oscillations is greater than zero. Assuming harmonic oscillations, this condition is met when the magnitude of the phase between the pressure and heat release oscillations, θ_{pq}, is less than ninety degrees (i.e., $0<|\theta_{pq}|<90$). Conversely, when these oscillations are out of phase (i.e., $90<|\theta_{pq}|<180$), the heat addition oscillations damps the acoustic field. Specifically, this relationship can be stated as follows:

$$\int_V \int_T p'(x,t) q'(x,t)\, dt dV \geq \int_V \int_T \sum_i L_i dt dV \tag{1.1}$$

where $p'(x,t)$, $q'(x,t)$ and L_i are the combustor pressure oscillation amplitude, periodic heat addition process, and i-th acoustic energy loss process, respectively. Eq. (1.1) states that a combustor is unstable when the net rate of energy addition to the acoustic field (i.e., the left side of the inequality) exceeds the net rate of damping provided by inherent dissipative processes (i.e., the right side of the inequality).

This phasing condition described by Rayleigh describes the conditions under which energy is added to the acoustic field by the combustion process. This is a necessary, but not sufficient condition for instability. To drive instability in a combustor, the unsteady heat release process must supply energy to the acoustic field at a rate that is larger than the rate at which acoustic energy is dissipated within the combustor and/or transmitted through its boundaries. As long as this condition is satisfied, the energy of

the acoustic field increases with time. In such a case, the amplitude of oscillations will initially increase exponentially with time before saturating at some limit cycle amplitude. During limit cycle oscillations, the time average driving and damping of the mode are equal and no net energy is added to the oscillations.

As shown in Figure 2, combustion instabilities result from a feedback mechanism that can be generically described by the following sequence: (1) a perturbation in some flow or thermodynamic variable induces a fluctuation in the combustion process heat release rate, (2) the periodic heat release process excites acoustic oscillations that propagate away from the combustion region, and (3) the acoustic oscillations excite the flow or thermodynamic variable in (1), thus closing the feedback loop. Depending upon the relative balance between the energy added and removed from the oscillations, the amplitude of oscillations may decrease, stay the same, or grow during each cycle of this loop. Since the initial amplitudes of these instabilities are generally quite small, they are referred to as being "linear" because their characteristics are predicted by the solution of linear wave equations. The frequencies and mode shapes of these oscillations (as well as the conditions under which they spontaneously occur) are determined from the solutions of these equations. A linearly unstable system is one in which some state is unstable even with respect to infinitesimally small disturbances. Thus, since linearly unstable systems can't persist, they are never observed in nature. An example of a linearly unstable situation is a ball perfectly balanced at the crest of a peak where any small disturbance will cause it to roll away from this unstable equilibrium point.

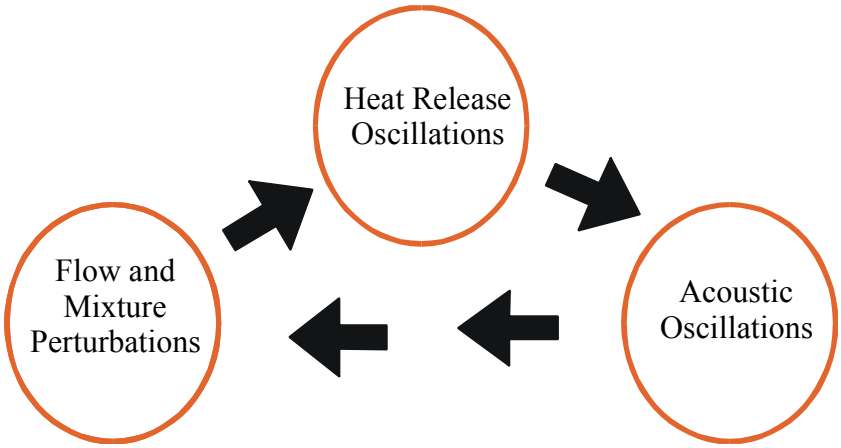

Figure 2. Illustration of the feedback processes responsible for combustion instability

Linear analyses cannot predict, however, the magnitude of the limit cycle amplitude attained by the instability because this magnitude is controlled by nonlinear processes [7]. Furthermore, nonlinear processes may allow a large amplitude disturbance whose amplitude exceeds a certain threshold value to "trigger" instabilities in a system that does not become unstable when subjected to small amplitude disturbances. Consequently, both the characteristics of the limit cycle oscillations and conditions under which finite amplitude disturbances can trigger instabilities can only be determined by solving a system of nonlinear wave equations.

The focus of this thesis is on the amplitude response of the heat release at some frequency, f, to a harmonic disturbance of amplitude, A, at that same frequency. The heat release response, H(A), generally exhibits a linear dependence upon the disturbance amplitude at small values of A. At high amplitudes, however, they are related nonlinearly. This is significant because the dynamics of an unstable combustor are controlled by both linear and nonlinear processes. This can be seen from Figure 3, which

plots the amplitude dependence of hypothetical driving, H(A), and damping, D(A), processes.

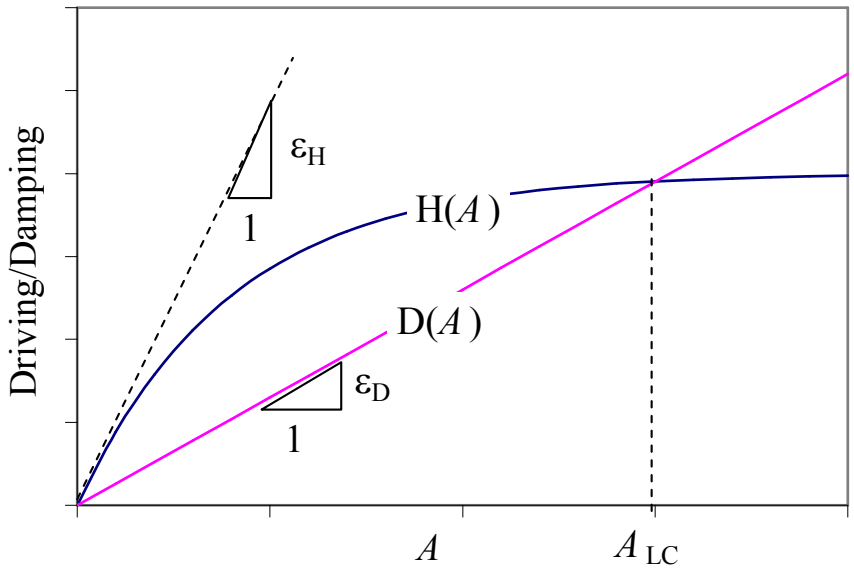

Figure 3. Qualitative description of the dependence of acoustic driving, H(A) and damping, D(A), processes upon amplitude, A.

To further illustrate the dependence of the stability and limit cycle of a system upon the amplitude of the oscillations, A, consider the hypothetical amplitude dependence of the driving, $H(A)=\varepsilon_H A + H_n(A)$, and damping, $D(A)=\varepsilon_D A + D_n(A)$, where the subscript "n" denotes the nonlinear part of the transfer function, in Figure 3. Since these curves intersect at the origin, a zero amplitude of oscillation is a potential equilibrium point. However, this equilibrium point is unstable, as any small disturbance that moves the system away from the origin produces a condition in which H(A) exceeds D(A), resulting in further growth of the disturbance. Because of the initial divergence of these two curves, their difference increases with amplitude, implying that the amplitude growth rate

increases with amplitude. When the amplitudes of the oscillations are small, both processes can be approximated by a linearized expressions; i.e., $H(A)=\varepsilon_H A$ and $D(A)=\varepsilon_D A$.

Thus, linear combustor processes (i.e., processes whose magnitude is directly proportional to amplitude, A) generally control the balance between driving and damping processes at low amplitudes of oscillation and, thus, determine the frequency and growth rate, $A \sim e^{\alpha t}$, of inherent combustor disturbances. This effect is shown in Figure 4, which plots a generic pressure time trace in a combustor transitioning to instability. The initial growth rate of the instability, α , is proportional to the difference between the driving and damping processes in the linear regime; i.e., $\alpha \sim \varepsilon_H - \varepsilon_D$ and therefore causes the dynamic pressure amplitude in the combustor to rise exponentially. For this reason, linear combustor stability models are routinely used to determine whether a given operating point is stable or unstable.

Nonlinear combustor processes control the dynamics of the oscillations as the driving and damping processes become amplitude dependent. Figure 3 describes a situation where $H(A)$ saturates and $D(A)$ increases linearly with the amplitude A, producing an intersection of the two curves at the limit cycle amplitude, A_{LC}. Note that this limit cycle amplitude is stable; i.e., a perturbation of the amplitude to the left (right) of this intersection point causes $H(A)$ to become larger (smaller) than $D(A)$, causing the amplitude to increase (decrease). The effect of the nonlinear combustion processes is also illustrated in Figure 4. When nonlinear combustor processes become dominant, the dynamic pressure in the combustor saturates into a limit cycle and the amplitude of oscillation becomes roughly constant.

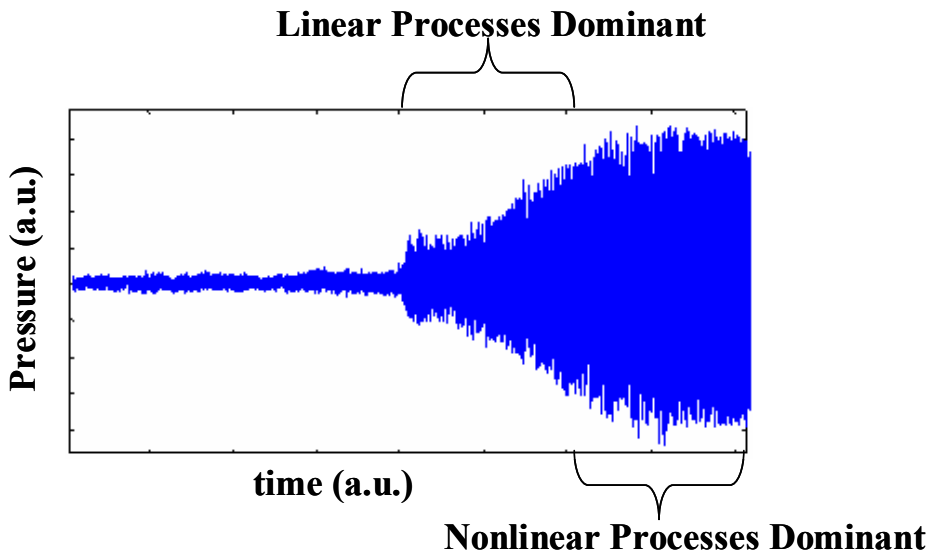

Figure 4. Generic pressure trace of a combustor illustrating growth rate and saturation to limit cycle of combustion instability

1.3 Overview of Present Work

The major thrust of this thesis is to determine the factors which affect the shape and behavior of the driving curve, H(*A*). There is a need to predict limit cycle amplitudes and the effects of operating conditions, geometry, etc. on the amplitude of finite amplitude oscillations. Specifically, the nonlinear flame response for two different experimental setups is experimentally determined over a range of driving frequencies, equivalence ratios, and flow rates. The parameters which influence the nonlinear characteristics of the curve, *H(A)*, are needed to improve the understanding of combustion instabilities and their associated limit cycle amplitudes. Consider a parameter, *B*, which changes the driving curve from *H(A)* to *G(A)* (i.e., *H(A)* ~ *G(A)f(B)*) as shown in Figure 5. For the same damping relationship as depicted in Figure 3, parameter *B* has decreased the linear gain of the curve and reduced the amplitude where

nonlinearity occurs. In the process, the point at which the driving curve intercepts the damping curve has changed as well. The limit cycle amplitude has reduced from A_{LC1} to A_{LC2}. A complete understanding of the factors and parameters such as the parameter B is needed to fully understand the characteristics of combustion instabilities.

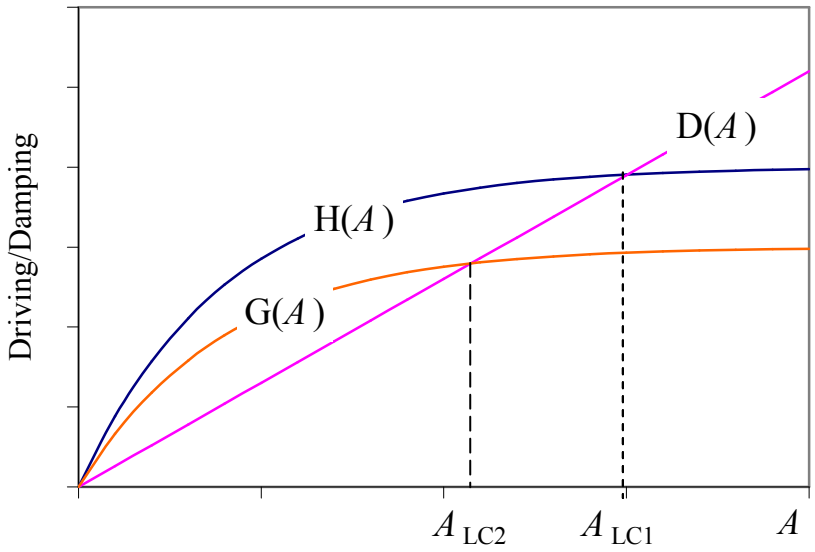

Figure 5. Dependence of qualitative driving curves, *H(A)* and *G(A)* on hypothetical parameter *B* detailing corresponding effect of nonlinear saturation amplitude on the limit cycle amplitude.

A number of important physical parameters are expected to influence the flame characteristics in a combustor under large amplitude forcing such as the frequency of oscillation, the distribution of the flame in the combustion chamber (which in turn is influenced by fuel/air ratio, geometry of the fuel nozzle, and flow velocity), and the characteristics of the unsteady flowfield. Therefore, an extensive investigation of the parameters that can significantly affect the nonlinear characteristics of the curve *H(A)* has

been performed. From these results, the mechanisms that control the nonlinear behavior of the flame response to large amplitude oscillations in two combustors have been determined through a variety of analysis techniques. In addition, the nonlinear interactions in the combustor between frequency regimes as well as the frequency response of a forced combustor are extensively investigated. In all, this thesis provides an extensive study of the nonlinear characteristics of premixed flames.

The remainder of this thesis is divided as follows. Chapter 2 provides an introduction to combustion instabilities and the types of nonlinear processes present in premixed combustion systems. In addition, a comprehensive literature review of previous work by other researchers in this field is presented, particularly focusing on the nonlinear flame response to large amplitude disturbances. The experimental facilities, instrumentation, and data analysis techniques are outlined and discussed in Chapter 3. Nonlinear flame response results and analysis, including a discussion of the mechanisms that control the nonlinear behavior of the flame to large amplitude oscillations, are described for two swirl-stabilized combustors in Chapters 4 and 5. Chapter 6 describes experiments detailing nonlinear interactions between driven oscillations and natural stable and unstable modes of both combustors. Finally, conclusions and recommendations for future works are described in Chapter 7.

CHAPTER 2

INTRODUCTION AND LITERATURE REVIEW

This chapter presents an introduction to combustion instabilities and describes the linear and nonlinear processes in premixed combustors. In addition, it presents a thorough review of the prior research performed on the nonlinear behavior of the flame's heat release to large amplitude acoustic forcing. The chapter is divided into four sections. Section 2.1 provides a brief introduction to combustion instabilities and a description of linear and nonlinear phenomena in unstable gas turbine combustors. Section 2.2 describes theoretical investigations of potential nonlinear mechanisms that control limit cycle amplitudes. Section 2.3 reviews corresponding experimental work on the nonlinear flame behavior. Finally, Section 2.4 discusses briefly how the added complexity of swirling, turbulent flows, characteristic of gas turbine combustors, makes the determination of potential nonlinear mechanisms even more difficult compared to laminar flame studies.

2.1 Introduction

Thermoacoustic oscillations or combustion instabilities have been observed in a variety of combustion applications, including rockets [9,10], ramjets [11], and land-based [3-5] and aero gas turbine engines [12,13]. These instabilities develop when the unsteady

combustion process couples with one or more of the acoustic modes in the combustor resulting in self-excited oscillations. In land based gas turbines, the focus for this thesis, the resultant flow and structural vibrations can substantially reduce hot section part life. Reduced part life leads to more frequent outages, downtime, and maintenance of the turbine itself. These additional costs are passed down to the consumer through increased prices of electricity. As such, avoiding operating regimes where high dynamics occur often requires operating at lower power outputs and/or higher pollutant emissions than the turbine is otherwise capable of producing.

The dynamics of an unstable combustor are controlled by a complex interplay of these linear and nonlinear processes. As mentioned in Chapter 1, linear combustor processes generally control the balance between driving and damping processes at low amplitudes of oscillation and, thus, determine the frequency and conditions under which inherent disturbances in the combustor grow or decay. Extensive work in this area has expanded the capabilities for modeling the acoustics of the combustor system; e.g., see Refs. [9,14]). Also, capabilities for modeling the interactions of flow and mixture disturbances with flames, needed to predict the conditions under which instabilities occur, are improving rapidly [15,16]. Much of this work is being transitioned to industry and being incorporated into dynamics predictions codes. In fact, most gas turbine manufacturers have reported model development efforts for predicting instability frequencies, mode shapes, and conditions of occurrence [17-20].

In order to describe the limit cycle dynamics of self-excited oscillations, extensive investigation of the important nonlinear processes controlling the saturation of the pressure fluctuations are necessary. Capabilities for predicting instability amplitude are

important because they would tell whether a given instability can be tolerated in the system or whether measures need to be taken to decrease the amplitude of oscillations to prevent damage. The need to predict instability amplitudes and observations of "triggered" instabilities in rockets that were linearly stable motivated past workers to consider these nonlinear effects; e.g., see Refs. [9,10,21]. Much of this work focuses on the role of nonlinear gas dynamics in combustors, however. This is due to the fact that the fluctuating pressure amplitudes achieve significant percentages of the mean pressure during instability. Therefore, second order terms in the pressure fluctuation amplitude (i.e., p'^2) are just as significant as the value of the pressure oscillation amplitude itself. Lean, premixed gas turbine combustors, on the other hand, experience instability amplitudes that are typically on the order of 1-5% of the mean pressure [4,22]. Therefore, such second-order terms in the pressure fluctuation amplitude can usually be neglected.

Recent studies suggest that acoustic processes essentially remain in the linear regime, even under limit cycle operation, and that it is the nonlinear relationship between flow and heat release oscillations that causes saturation of the instability amplitude [22-26]. As such, the flame's nonlinear response to harmonic disturbances may play a critical role in the overall dynamics of an unstable combustor. While there is general agreement on the significant role of combustion process nonlinearities, the dependence of nonlinear flame characteristics, such as saturation amplitude, on combustor geometry and disturbance parameters (e.g., frequency and flame shape) is poorly understood. Furthermore, the mechanism(s) responsible for these combustion process nonlinearities

are largely unknown. Studies which have focused on these nonlinearity mechanisms are discussed in the next two sections.

2.2 Theoretical Studies of Nonlinear Flame Response

Several theoretical studies have proposed nonlinear models based on local/global extinction of the flame [23, 25], nonlinear boundary conditions [27], pressure sensitivity of the mass burning rate [28], equivalence ratio perturbations [24, 26, 29], and flame front kinematics [30,31]. A review of these mechanisms is described below. For example, Dowling introduced a phenomenological model for the finite amplitude response of a flame to velocity perturbations [23]. The model is dynamic in nature, but the essential nonlinearity is introduced from a quasi-steady relation between flow velocity and heat release rate. Specifically, it assumes a linear relation between the heat release, Q, and velocity perturbation when the total velocity ($u(t)=u_o+u'(t)$) lies between 0 and 2. When $u(t)<0$, the heat release goes to zero and when it is greater than $2u_o$ it saturates at $2Q_o$. Thus, the essential mechanism of nonlinearity lies in the fact that the lowest amplitude of heat release oscillation cannot indefinitely decrease with perturbation amplitude because it cannot achieve negative values. The driving curve H(A) from Figure 3 is thus assumed to look like the adapted curve from Ref. [23].

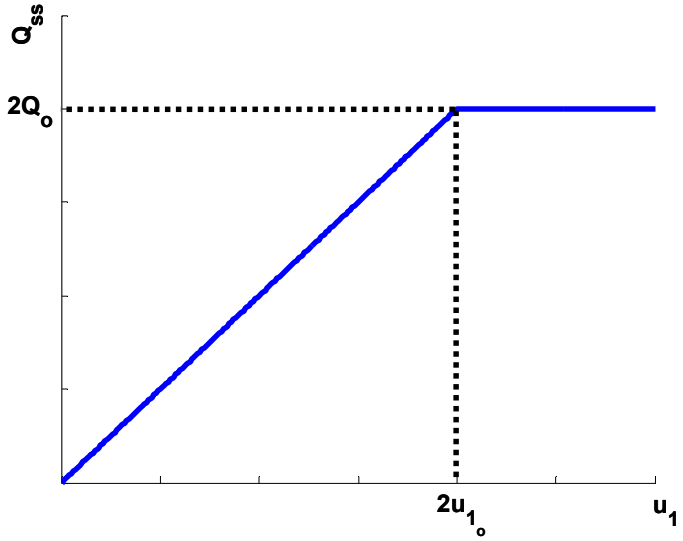

Figure 6: Schematic of driving curve H(A) for nonlinear global extinction flame response model adapted from Dowling [23].

Poinsot *et al*. in an earlier experimental study in a non-premixed combustor put forth a similar mechanism [25]. Specifically, the instability amplitude saturated into limit cycle when the heat release signal, measured by a photomultiplier tube (PMT), reached a zero minimum value. Thus the limit cycle amplitude was observed to be determined by the saturation of the combustion rate oscillations and not acoustic losses [25].

In another study, Dowling introduced a nonlinear boundary condition at the flame anchoring point [27]. She assumed that the instantaneous flame anchoring point was fixed when the total gas velocity exceeded the flame speed. When the gas velocity fell below the flame speed, the former condition was replaced by one that allowed the flame to propagate upstream.

Peracchio & Proscia developed a quasi-steady nonlinear model to describe the response of the flame to equivalence ratio perturbations [24]. They assumed the

following relationship for the response of the instantaneous mixture composition leaving the nozzle exit to velocity perturbations:

$$\phi(t) = \frac{\bar{\phi}}{1 + ku'(t)/\bar{u}} \tag{2.1}$$

where k is a constant with a value near unity. They also utilized a nonlinear relationship relating the heat release per unit mass of mixture to the instantaneous equivalence ratio. More recently, Stow and Dowling present a low order model to predict the amplitudes of limit cycle oscillations [26]. The main nonlinearity is in the combustion response to flow perturbations which are caused upstream by inlet fuel-air ratio variations. At large velocity fluctuation amplitudes, the heat release is reduced by the flow oscillations' effect on fuel-air ratio. Results were found to be heavily dependent on the operating conditions.

Belucci *et al.* utilize a thermoacoustic network approach to predict frequencies, mode shapes, and correlate limit cycle amplitudes [29]. In order to correlate the model to experimental rig data, they define a saturation term of the fuel flow rate to limit the oscillation amplitude. The value of this term was adjusted such that the measured and predicted instability amplitudes matched. Good agreement on the relative magnitudes of the combustor modes is shown, but this hindsight approach highlights that the lack of knowledge of the appropriate mechanisms causing nonlinear flame response precludes any *a priori* prediction of limit cycle amplitudes.

Baillot *et al.* and Lieuwen have studied the effect of acoustic perturbations on both conical and wedge-type laminar flames [30, 31]. The fundamental nonlinearity in their studies is that due to flame front kinematics. Specifically, an acoustic perturbation wrinkles the flame front as shown in Figure 7. A premixed flame, by definition, propagates normal to itself, and smoothes out the wrinkle. The effect of driving frequency, curvature effects and convective velocity fluctuations are studied in detail.

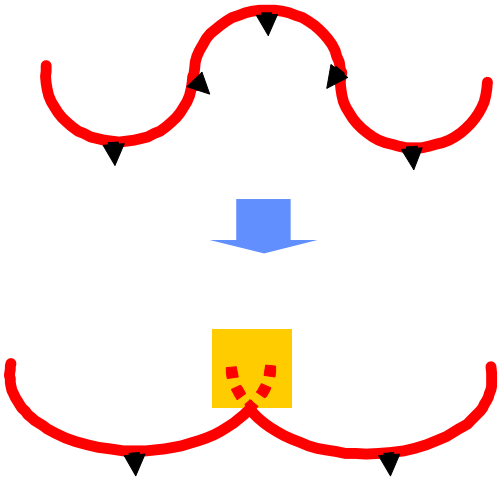

Figure 7. Schematic of a flame that is initially wrinkled (top), showing the destruction of flame area by kinematic restoration processes (bottom), taken from Ref. [31].

Finally, McIntosh investigated the pressure sensitivity of the mass burning rate [28]. Specifically, flame extinction or acceleration events due to sharp pressure changes can significantly affect the mass burning rate of the mixture and can cause local extinction of the flame, resulting in a nonlinear response of the heat release to the

pressure perturbation. In addition, the rate of the pressure change is seen to be just as important as the final pressure itself.

Several of the above analyses suggest that the ratio of fluctuating and mean velocity, u'/u_o, is an important non-dimensional parameter that controls the amplitude of the limit cycle oscillations through its effect upon the nonlinear relationship between flow disturbances and heat release oscillations. A similar conclusion was reached empirically in an experimental study by Lieuwen, who found that combustion instability amplitudes had a strong dependence upon a mean combustor velocity scale, u_o [22].

In addition, many of these theoretical studies have assumed the flame to be stabilized in a laminar flow, and thus the effects of turbulence on the flame speed are ignored. Only a few works have investigated the effect of harmonic forcing of turbulent premixed flames (e.g., see Ref. [32]). Furthermore, these theoretical studies, discussed above, assume that the combustor exhibits a particular mechanism for nonlinearity. Experimental studies (discussed in the next section) have been performed on both laminar and turbulent flames. The findings and the differences between the laminar and turbulent regimes are compared and contrasted.

2.3 Experimental Studies of Nonlinear Flame Response

Despite the large number of theoretical studies on nonlinear flame response, there are few experimental efforts which have characterized the nonlinear flame response to flow perturbations or determined the validity of these proposed nonlinear mechanisms. The potentially significant nonlinear transfer function relationship between acoustic perturbations and heat release perturbations suggested by the theoretical studies above,

are supported by recent measurements of Lieuwen & Neumeier [33], Lee & Santavicca [34] and Balachandran *et al*.[35] who characterized the pressure/velocity-chemiluminescence relationship as a function of oscillation amplitude. The former study found that the pressure-CH* chemiluminescence relationship was linear for pressure amplitudes below about 1% of the mean pressure. At higher forcing levels, they found that the chemiluminescence amplitude began to saturate. In contrast to the assumed model of Dowling [23] and the experimental work of Poinsot *et al.* [25], however, Lieuwen & Neumeier found saturation to occur at $CH^{*\prime}/CH^{*}_{o}$ values of ~25%, in contrast to the 100% value in these reported studies. Data were only obtained at one operating condition and two driving frequencies, however, so the manner in which these saturation characteristics depend upon operating conditions and frequency is unclear. Lee & Santavicca characterized this nonlinear relationship as well on a full-scale industrial fuel nozzle over a range of unstable combustion conditions [34]. They reported that the CO_2^* chemiluminescence saturates at $CO_2^{*\prime}/CO_2^{*}{}_o$ values of 25% as well.

Balachandran *et al.* investigated the nonlinear velocity-chemiluminescence relationship over a range of frequencies in a non-swirling, bluff-body stabilized flame [35]. Saturation is observed as well at $OH^{*\prime}/OH^{*}_o$ values of much less than 100%. The saturation values were seen to vary between $OH^{*\prime}/OH^{*}_o$ = 20-60% for the frequency ranges and equivalence ratios investigated. These results imply global extinction, as discussed by Dowling [23], was not an important nonlinear mechanism controlling the flame dynamics.

Külsheimer & Büchner measured the effect of driving frequency and driving amplitude on premixed swirled and unswirled flames [36]. They characterized the

conditions under which large-scale coherent ring-vortex structures were evident, a key mechanism for self-excited oscillations, as well as the resulting flame response on driving amplitude and frequency. They found that vortex formation occurred at lower driving amplitudes as the driving frequency was increased. Furthermore, the peak flame response in swirl flames shifted to higher frequencies for larger flow perturbations. No explicit characterization of the nonlinear interaction between the flame's heat release and the flow perturbations were reported, however. Hosseini & Lawn also investigated the effect of driving frequency on the flame response in a swirling, premixed burner [37]. Nearly linear behavior was observed for lower driving frequencies, while nonlinearity in the flame response to increased perturbations becomes more dominant at higher driving frequencies. They concluded that the nonlinear behavior of the flame response to increased acoustic perturbation amplitudes is due to the convection of large-scale ring vortices, similar to the above results of Külsheimer & Büchner [36].

The most extensive nonlinear flame response studies were performed by Baillot and co-workers on a laminar Bunsen flame [38,39]. While no measurements of the dependence of unsteady heat release or chemiluminescence emissions were reported, they reported a variety of flame behavior over the broad range of amplitudes for different driving frequencies. In particular, at low frequencies ($f < 200$ Hz) and velocity amplitudes ($u'/u_o < 0.3$), the flame front wrinkles symmetrically about the burner axis due to a convected wave traveling from the burner base to its tip. With increasing amplitude of low frequency velocity perturbations, they found that the flame exhibited a variety of transient flame holding behavior, such as flashback, asymmetric blowoff, and unsteady lifting and re-anchoring of the flame. However, at high frequencies and forcing

amplitudes, the flame remains firmly attached, but its overall shape dramatically changes. They found that the flame becomes "collapsed" with a rounded off tip region, and for sufficiently high forcing intensities ($u'/u_o > 1$), the flame's mean shape becomes hemispherical [39]. Baillot *et al*. also reported a theoretical study, where they solved the *G*-equation and showed good agreement between predicted and measured flame shapes, even at larger amplitudes of forcing where the flame front becomes strongly cusped [40] .

While these studies confirmed the basic saturating characteristics of the flame response to perturbations, the underlying mechanism for saturation was not fully explored, primarily due to the fact that they focused on global flame characteristics, such as chemiluminescence, making it difficult to determine what the flame is actually doing. While a number of higher fidelity optical observations of the flame dynamics in unstable combustors have been reported [34-36, 41-43], few have actually systematically measured the flame response as a function of amplitude. Baillot and co-workers [38, 39] qualitatively discuss the change in flame shape/structure to imposed velocity oscillations for the laminar Bunsen flame studies discussed above. Durox *et al.* obtained high speed images and transfer functions, $(Q'/Q_o)/(u'/u_o)$, of an acoustically forced inverted wedge flame [44]. The flame response was found to be significantly dependent on the incoming velocity perturbation amplitude, and the time delay between the flame response and the velocity fluctuations was dependent on the convective properties of vortices in the outer jet shear layer; e.g. see Figure 8. In addition, they showed that most of the key flame response characteristics could be quantitatively predicted by assuming that the flame's heat release was directly proportional to its instantaneous area.

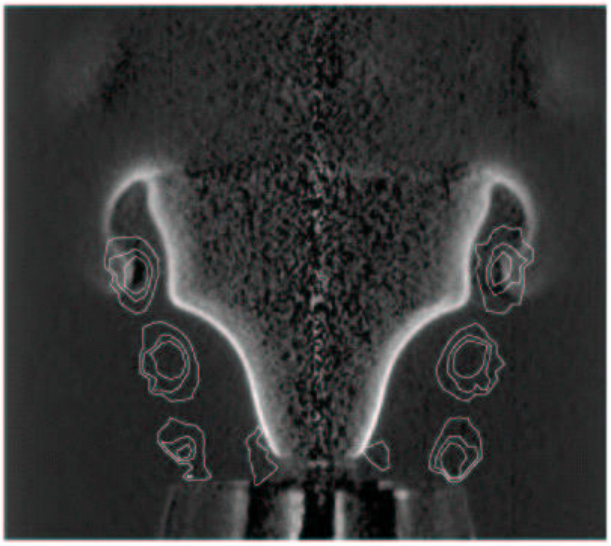

Figure 8. Vorticity field superposed with the flame front, taken from Ref. [44].

Balachandran *et al.*, as mentioned above, investigated the nonlinear transfer function and determined the flame response through simultaneous OH-CH_2O planar laser-induced fluorescence (PLIF) imaging in a non-swirling, turbulent, bluff-body burner [35]. They concluded that the rollup of the flame sheet by vortices forced by the acoustic disturbances, initiated kinematic destruction of the flame area and played an important role in the saturation of the transfer function.

2.4 Effect of Swirling Flows

As can be seen from the above review, much of the emphasis on nonlinear flame response to acoustic perturbations has focused on laminar, conical and inverted wedge flames. Previous studies that focused on turbulent flames have not fully quantified the governing mechanisms that dominate the nonlinear response of the flame to increased

oscillation amplitudes. The work of Balachandran *et al.* adds additional complexity by investigating non-swirling turbulent flames, their transfer functions and the mechanisms that appear to be governing the nonlinear dynamics [35].

While these experimental studies performed on laminar, Bunsen-type flame are useful, the flow regimes in typical lean, premixed gas turbine are inherently unsteady and turbulent. Specifically, in order to meet efficiency and performance requirements, large flow rates of fuel and oxidizer are needed. The corresponding velocity of the reactant stream is therefore much larger than the flame speed of typical hydrocarbons. Therefore, a local low velocity region is necessary to stabilize the flame. In most modern designs, the addition of swirl to the reactant stream is utilized to create this low velocity region. This adds additional complexity to the problem of instability.

In addition to the issues in predicting conditions of instability as well as limit cycle amplitude, there are many unresolved issues involving swirling flows, such as vortex breakdown and azimuthal instability. In most cases, combustion in a typical combustor occurs well past the critical vortex breakdown point in terms of swirl number. Flow phenomena such as one or more precessing vortex cores (PVCs) and radial-axial eddies are common features of the typical gas turbine combustor flowfields. Due to this inherent complexity, the effect of swirling flows on combustion instabilities, however, is largely unknown. This lack of understanding of flame/flow interactions is largely responsible for the lack of a solution to the instability problem [45].

A comprehensive understanding of these interactions, particularly in an environment typical of gas turbine combustor (highly turbulent, swirling flowfields) is necessary to establish design methodologies that account for and help lessen the effects

of instability. The understanding of vortex breakdown and swirl flows in the presence of exothermic chemical reactions is a fundamental problem that has limited previous researchers from developing a complete understanding of the combustion instability problem. This thesis expands on the work by previous researchers whose studies focused on laminar conical and wedge flames, as well as turbulent non-swirling bluff-body stabilized flames. The results presented herein are compared not only to the theoretical mechanisms that have been proposed in the literature, but are also compared to other experimental works on different flame and flow regimes.

CHAPTER 3

EXPERIMENTAL SETUP AND INSTRUMENTATION

This chapter describes the various experimental facilities, instrumentation, and data analysis techniques that were employed in this study. The first two sections explain the experimental setups and features of the two combustors employed in this investigation. The third section describes the measurement techniques and sensors used in this study. The fourth section briefly explains the flame imaging method utilized to view the flame under large amplitude forcing. Finally, the last section briefly describes the procedures for acquisition, processing and data analysis.

3.1 Low NO_x Gas Turbine Combustor Simulator

These investigations were performed in a DLN simulator facility that was developed at Georgia Tech. A schematic and a photograph of the facility are shown in Figure 9 and Figure 10, respectively. This facility consists of an air inlet section, a mixing section, a combustor section, and an exhaust section. The length of the inlet section can be varied between 104.1 and 163.8 cm by translating its upstream end with a ball screw driven by a stepper motor. High-pressure natural gas and air are supplied from building facilities, whose flow rates are measured with calibrated critical orifices.

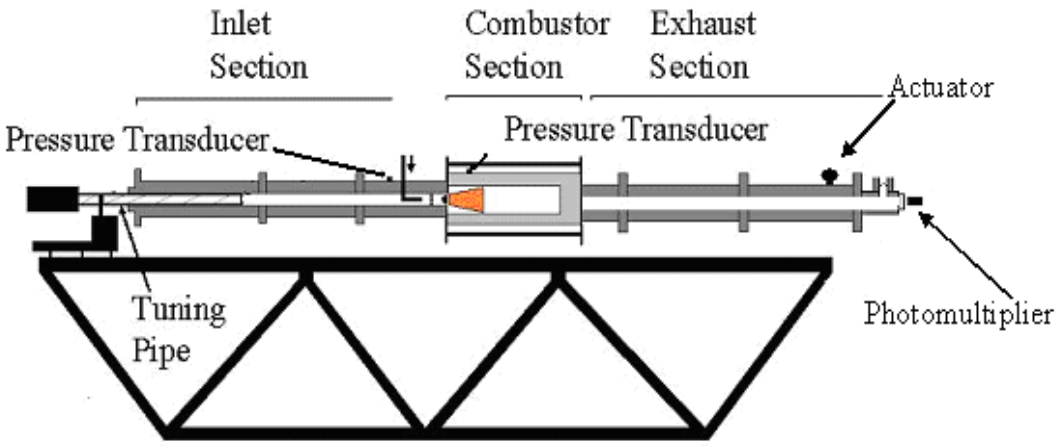

Figure 9. Schematic of lean, premixed combustor facility

The flame is stabilized by a conical bluff body at the interface of the mixing section with the combustor. The combustor is 47 cm long with side walls consisting of quartz and Pyrex glass windows that provide optical access for flow visualization and related measurements (e.g., flame chemiluminescence). On each side of the combustor the combustion process can be viewed through an arrangement consisting of a quartz window on the inside, a Pyrex window on the outside and high pressure, cold air flowing between the windows. This design allows the system of windows to withstand the high pressure and temperature environment within the combustor. The inner, 1.2 cm thick, quartz window is exposed to the high temperature and pressure flow on one side and to the cold, high pressure air on the other. Consequently, the quartz window is only exposed to a temperature gradient but no pressure gradient. In contrast, the 2.5 cm thick Pyrex glass window is exposed to high pressure, cold air on the inside and cold, low pressure air on the outside. Thus, the Pyrex window is exposed to a pressure gradient but no temperature gradient.

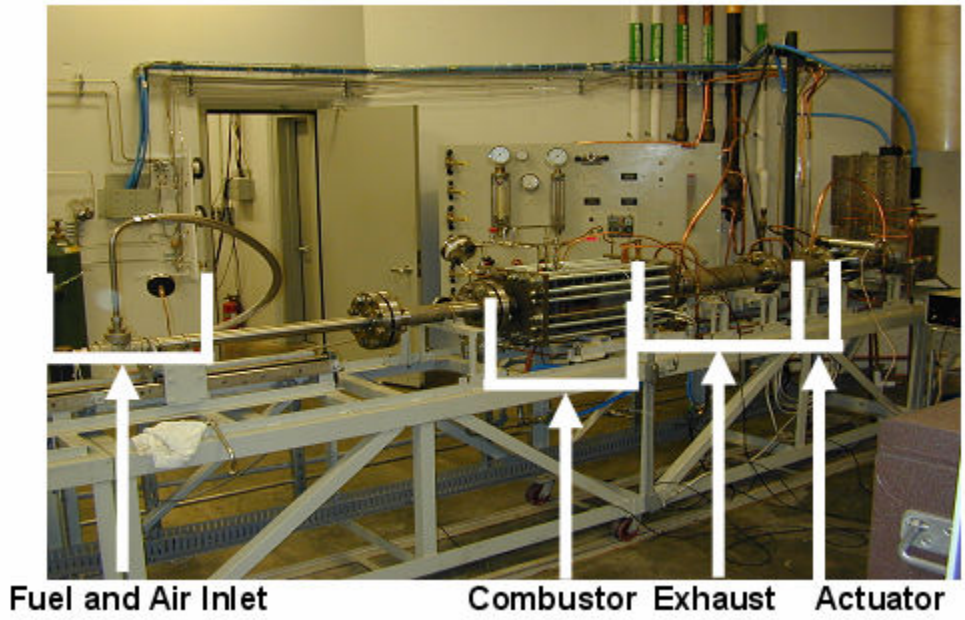

Figure 10: Photograph of lean premixed combustor facility

At the start of a test, an oxygen-methane pilot flame located downstream of the flame holder is used to ignite the combustible mixture. The combustion products are discharged from the combustor through an exhaust section terminated by a nozzle at its downstream end. A valve within the nozzle can vary the nozzle throat area. The combustor pressure and, therefore, the mean velocity can be controlled by this valve. The length of the exhaust section can also be varied between 192 and 350.5 cm by adding or removing pipe sections. The combustor and the exhaust section are water cooled to prevent damage due to overheating.

The natural acoustic frequencies of the combustor are approximately multiples of 100 Hz. These frequencies are clearly seen in the Fourier transform of the combustor pressure that was measured during unstable operation; see Figure 11 [7].

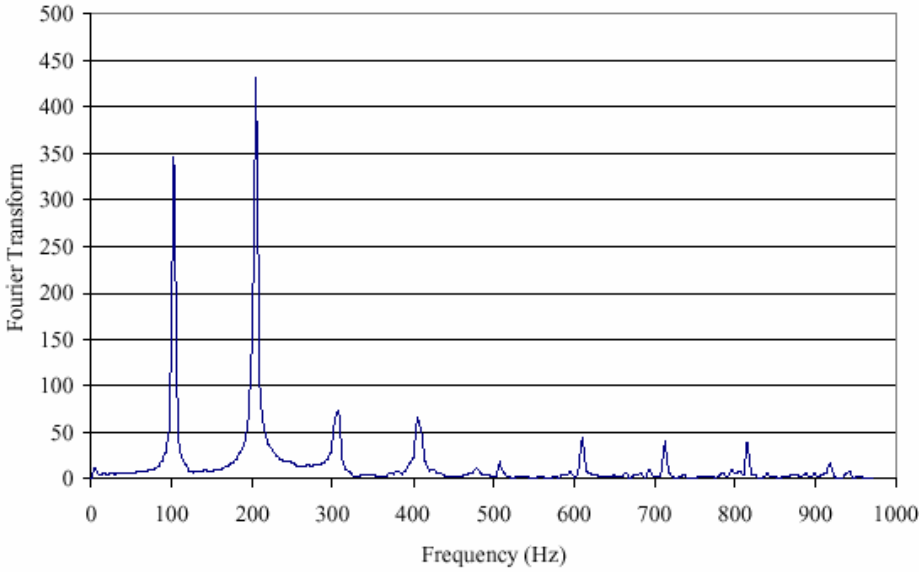

Figure 11. Fourier transform of gas turbine combustor simulator pressure data taken from Ref. [7].

3.2 Atmospheric Swirl-Stabilized Combustor

Experiments were also performed on an atmospheric, swirl-stabilized burner, schematically shown in Figure 12, which can be operated up to 100 KW. Natural gas and air are supplied from building facilities, whose flow rates are measured with rotameters. In order to ensure that acoustic oscillations do not affect fuel/air mixing processes, the air and fuel are again introduced upstream of a choke point – in this case, a gate valve which could be manually adjusted depending on the operating condition . Thus, the equivalence ratio of the reactive mixture entering the flame is essentially constant. This was done because of the sensitivity of the flame chemiluminescence levels to both heat release rate and equivalence ratio [34]. The loudspeakers are mounted just downstream of this choke point.

The inlet section is approximately 3m in length and roughly constant in area. The long, constant area allows for good system frequency response for the frequency range interest, as shown in Figure 13. Figure 13 plots the frequency response of the combustor in cold flow conditions for low amplitude driving. The plot illustrates that the combustor responds well for a large range of frequencies in the 150-500 Hz regime. The values of the oscillations are large enough such that nonlinear studies of the flame response can be performed.

After the inlet section, the mixture goes through the swirler section, consisting of a 40° swirler and an annular passage, see Figure 14. The premixer was designed such that the hydraulic diameter of the annular passage is essentially constant from the swirler location to the dump plane of the combustor. After the premixer, the flow then expands into a cylindrical 70mm i.d. and 190 mm long quartz tube combustion chamber.

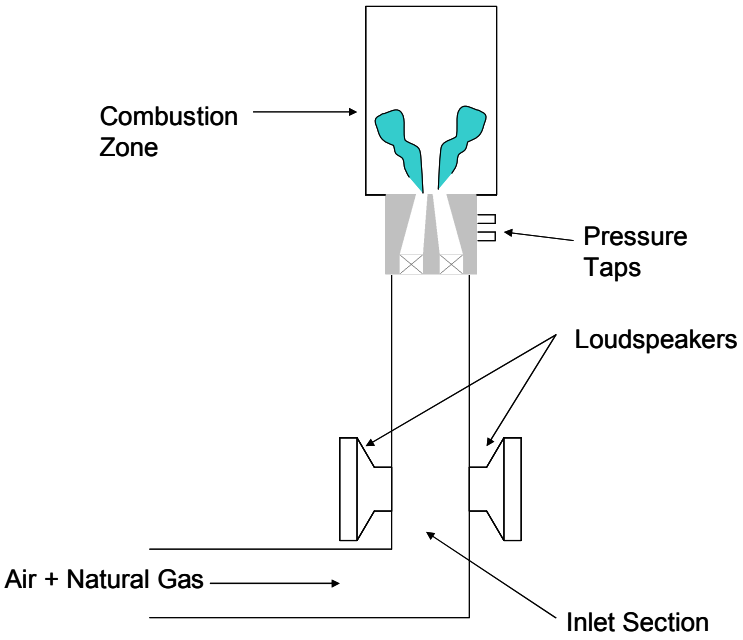

Figure 12. Schematic of swirl-stabilized combustor

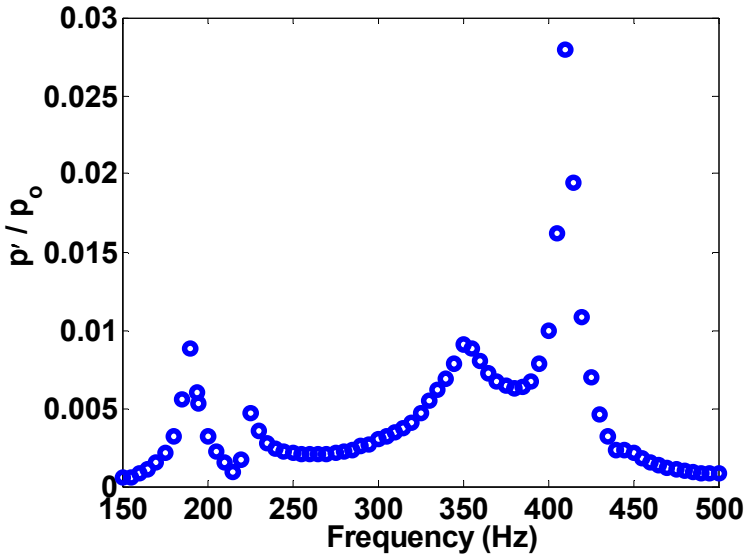

Figure 13. Dependence of pressure amplitude on driving frequency in swirl-stabilized burner

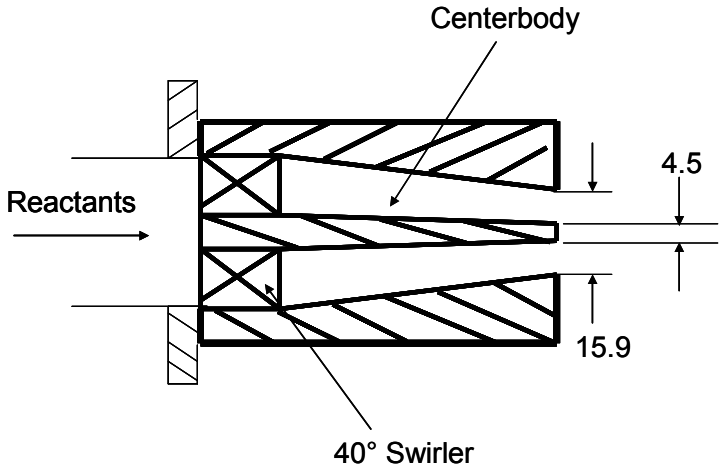

Figure 14. Schematic of swirler and premixer section. All dimensions in mm. Figure not to scale

3.3 Instrumentation

3.3.1 Dynamic Pressure Measurements

Pressure oscillations are measured with fast response Model 211B5 Kistler pressure transducers. These sensors employ quartz crystals and use the phenomenon of piezoelectricity — the tendency of some materials to produce a charge when strained — to convert sound vibrations into an electrical signal. These transducers' deviation from linearity and hysteresis are both less than 1%. They exhibit a flat frequency response to within 0.4 dB over the 100-700 Hz frequency range. For the gas turbine combustor simulator, these transducers are mounted in the inlet section and combustor. They are mounted 33.2 cm upstream and 5.1 cm downstream of the conical flame holder, respectively. The latter transducer was flush mounted and water-cooled. The approximate locations are shown qualitatively in Figure 9.

In the atmospheric swirl-stabilized burner, identical transducers are mounted 7 cm and 5.85 cm upstream of the combustion zone, but downstream of the swirlers. In addition to measuring the pressure oscillations at the flame stabilization point, these transducers are utilized for velocity measurements, as described in the next section.

3.3.2 Dynamic Velocity Measurements

As mentioned in Chapter 2, the velocity oscillations incident on the flamefront are deemed to be a controlling factor of combustion instabilities. In order to measure these velocity oscillations, a few different techniques have been utilized in this investigation, described below.

3.3.2.1 Gas Turbine Combustor Simulator

Velocity measurements were obtained in two different manners for the two test rigs employed in this research. The first apparatus, utilized in the gas turbine combustor simulator, was a TSI model 1201 hot-film constant temperature anemometer (CTA). The frequency response of these probes was about 80 kHz; however, the response curve begins to decrease sharply lower frequencies than 80 kHz. Since the frequencies of interest in this study are O(100s) of Hz, this was not a significant source of uncertainty or error. The limitation of using such a device was that it could not be used in high temperature and/or "dirty" environments due to its fragility. The maximum temperature for this probe was 60°C (333K). Therefore, it was located 23 cm upstream of the swirler location and oriented perpendicular to the inlet flow in the radial center of the inlet pipe, as shown in Figure 15.

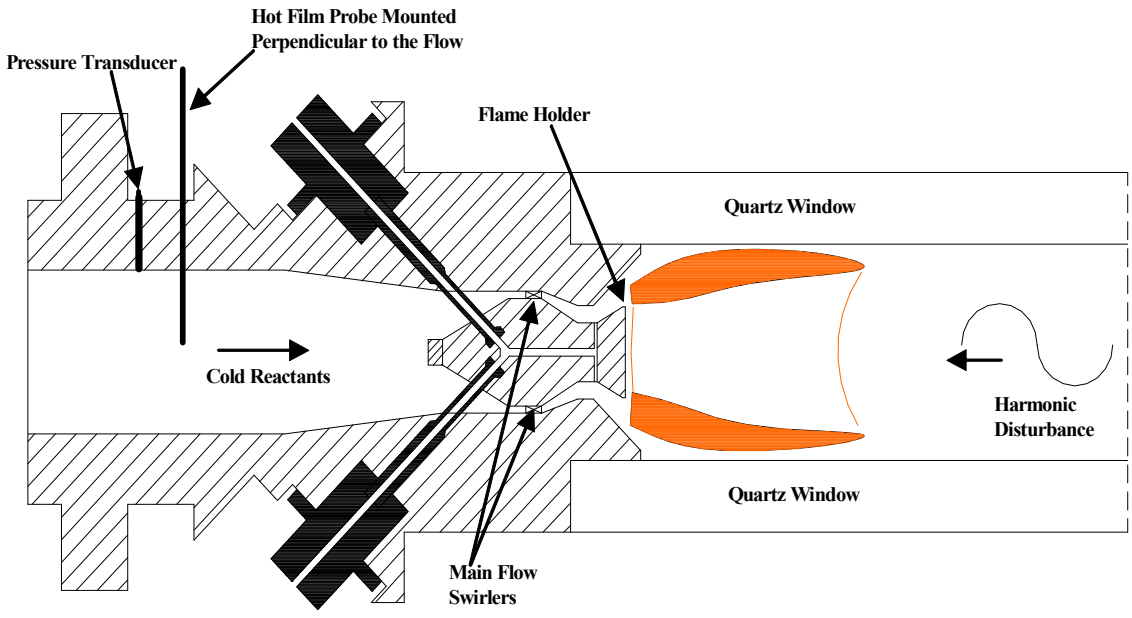

Figure 15: Detail of mixing and combustion section

The fluctuating velocity at the premixer exit was determined by measuring the transfer function between the velocity oscillations at the hot-wire location and the premixer exit in cold flow experiments. This transfer function was also calculated with a quasi-one dimensional analysis by discretizing the premixer domain into a series of regions characterized by their lengths and cross-sectional areas, and applying momentum and energy conservation at the interfaces (see Ref. [14] and Appendix B). The swirler was modeled as a resistance that was determined from the flow velocity and measured mean pressure drop. The model and measurements agreed very well over the 10-550 Hz frequency range, except in transfer function magnitude in the vicinity of 80 and 420 Hz. At these frequencies, the transfer function has large values (on the order of 5) and the model and measurements disagree by 100% in the peak magnitude; however, they agree quite well in predicting the frequencies at which these occur. At all other frequencies, the transfer function magnitude is essentially constant and equal to the cross sectional area ratio between the two points, as expected from quasi-steady considerations. Because of the sensitive frequency dependence of the velocity transfer function between the measurement location and premixer exit plane at 80 and 420 Hz, no nonlinear forced response studies were performed at these frequencies.

3.3.2.2 Atmospheric Burner

The use of hot film or hot wire probes was limited by temperatures and contaminants of the flow. In addition, the effect of turbulence can lead to substantial coherence issues at high flow rates. To eliminate the effect of turbulence on the signal-

to-noise ratio of the hot-film probe, the two-microphone method, outlined in Ref. [46, 47] and Appendix B, was utilized in all experiments. Specifically, the oscillation velocity can be determined by:

$$\frac{\partial u}{\partial t} = -\frac{1}{\rho}\frac{\partial p}{\partial x} \tag{3.1}$$

where u is the velocity, p is the pressure, and ρ is the density. Appropriate linearization of Eq. (3.1) allows one to calculate the velocity from two pressure signals. Additional details are provided in Appendix B.

3.3.3 Heat Release Measurements

In order to quantify the flame's dynamics, a non-intrusive device was needed to detect and "measure" the heat release oscillations from the flame. In many cases, chemiluminescence is used to provide such a measurement. Since the intensity of light emission from flame has been shown to be roughly proportional to the chemical production rate of the particular molecule, the chemiluminescence intensity can be related to chemical reaction rates [48]. For this reason, chemiluminescence has been used previously as a rough measure of reaction rate and heat release rate [49-53]. The primary chemiluminescent species of interest in a hydrocarbon flame are electronically excited OH (around 308nm), CH (around 430 nm) and C_2 (around 519 nm) radicals and the CO_2

molecule (broadband visible). In lean hydrocarbon flames, OH tends to be the strong emitter, followed by CH with little C_2 emission; see Figure 16 [54-56].

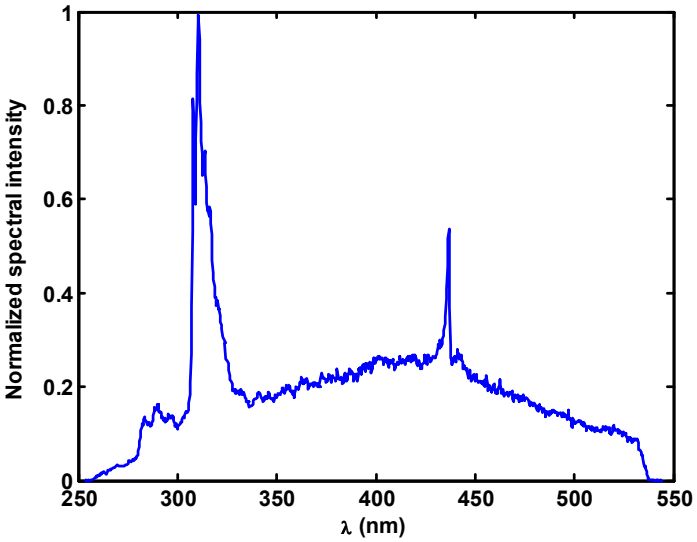

Figure 16. Typical spectral intensity of lean methane-air flame

Chemiluminescence measurements can be significantly affected by a variety of other factors, however. It is well-known that equivalence ratio fluctuations and increased turbulence levels may contaminate measurements in the turbulent, swirling flames which are investigated in this study [34]. Small fluctuations in these parameters may cause measurement discrepancies of upwards of 10-20%. If the equivalence ratio and heat release rate simultaneously vary, monitoring the flame chemiluminescence alone is not sufficient to infer information about heat release fluctuations. Note that the fuel/air mixing processes were not acoustically isolated in the study of Lieuwen & Neumeier [33]. Other parameters which may affect chemiluminescence measurements may include inlet temperature and significant pressure variations.

Therefore, as mentioned above, the fuel and oxidizer are premixed upstream of a choke point to eliminate forced equivalence ratio oscillations due to the external forcing of the combustor. In addition, while the effect of turbulence was not explicitly determined in this investigation, simultaneous measurements of visible (CH*) and ultraviolet (OH*) chemiluminescence were taken and compared to ensure consistent trends.

3.3.3.1 Gas Turbine Combustor Simulator

Global CH* and OH* chemiluminescence measurements were obtained for this setup with a photomultiplier tube (PMT) fitted with 10 nm bandwidth interference filters centered at 430 and 310 nm, respectively. No background correction for CO_2* chemiluminescence was performed. Thus the measurements in this study are the sum of OH* and CO_2* at 310 nm and CH* and CO_2* at 430 nm. As will be shown in Chapter 4, simultaneous measurements at 310 and 430 nm yield very similar results; thus, CO_2 * does not significantly affect the measurements.

The PMT is powered by a high-voltage source that was operated at 1.5kV. The PMT was installed downstream of a quartz window at the rear end of the setup, Figure 9. This arrangement permitted it to view the entire combustion zone. The linearity of the PMT output was verified over the entire range of instantaneous light intensity levels seen in these experiments.

3.3.3.2 Atmospheric Burner

The optical collection setup for these experiments employs a bundle of 365μm diameter fused silica optical fibers. The acceptance half angle of the bundle is approximately 20°. The bundle is connected to two miniature, metal package PMTs (Hamamatsu H5784-04). The bundle is split such that the collected radiation is evenly divided between the two PMTs. Global CH* and OH* chemiluminescence are detected by the two PMTs. These PMTs have a built-in amplifier (bandwidth of 20 kHz) to convert the current to voltage and operate from a 12VDC source.

3.3.4 Forced Oscillations in Combustors

3.3.4.1 Gas Turbine Combustor Simulator

Oscillations were driven in the gas turbine combustor simulator with an actuator developed at Georgia Tech for active combustion control applications [57]. The magnetostrictive actuator modulates a constant secondary supply of air, introduced 5m downstream of the flame zone near the exhaust of the experimental test rig, by periodically varying the degree of constriction of a valve. Maximum amplitude of driving occurs when the flow passage is completely blocked for a portion of the cycle and, thus, the actuator modulates 100% of the flow through the valve. The amplitude of forcing can be controlled via the supply pressure of air to the actuator.

The signal input to the actuator was supplied by a precision function generator which accurately produced sinusoidal harmonic signals from 1 Hz - 15 MHz. Since the frequency ranges of interest in these studies were O(100-500 Hz), the precision of the

input signals was approximately 10^{-5} Hz. The input signal was supplied across two high power resistors to an amplifier whose output was then supplied to the actuator.

3.3.4.2 Atmospheric burner

Oscillations in the atmospheric burner were excited with two (2) 100-Watt loudspeakers which were mounted directly opposite to each other in the inlet section at the location of a pressure maximum. This configuration along with the combustor setup allowed for oscillations to be driven at considerable amplitude for a wide range of frequencies, see Figure 13.

These loudspeakers produced linear outputs to sinusoidal inputs over the frequency range of interest (100-1000 Hz). The input signal was supplied by the same function generator as that mentioned in Section 3.3.4.1. The harmonic input was then supplied to two (2) Radio Shack P.A. amplifiers which amplified the initial signal and output it to the loudspeakers. The gains on the amplifiers were set such that the saturation limits for both were achieved when the amplitude of the input signal from the function generator reached 1.5 V.

3.4 Flame Imaging

Imaging of the flame under large amplitude forcing was performed using two methods: line-of-sight flame imaging and OH planar laser-induced fluorescence. The methods are described below.

3.4.1 High-Speed Line-of-Sight Images

High speed videos of the flame were obtained using a Phantom ICCD camera that can be operated up to 3000 frames per second (fps). The setup for these tests is shown below in Figure 17. The camera used 256x256 pixels for these tests, which corresponded to a physical viewing window of 70x70 mm. The camera is triggered by the driving input signal from the function generator. The acoustic cycle was divided into a maximum of 8 phases, so the actual frame rate utilized was dependent on the driving frequency. For driving frequencies above 350 Hz, the acoustic cycle was divided into 7 phases such that the frame rate of the camera is maximized, but less than 3000 fps.

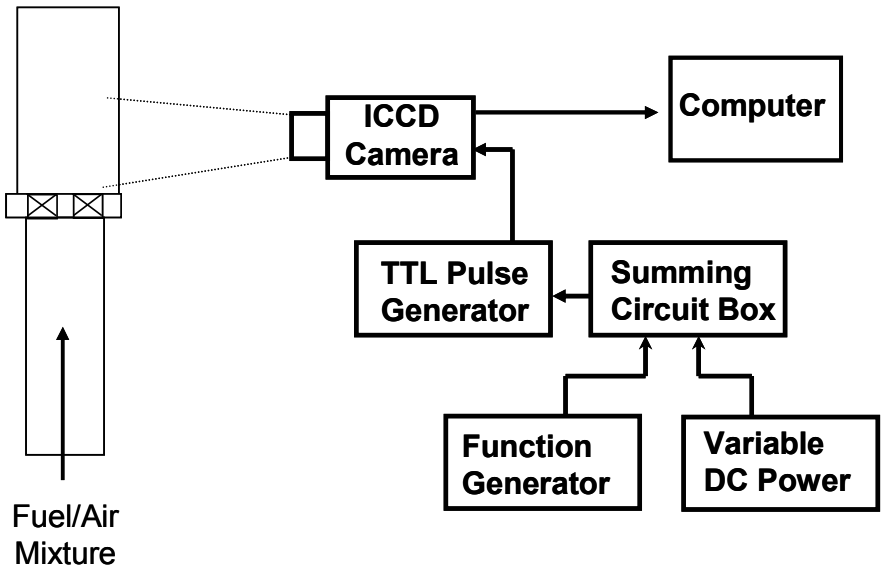

Figure 17. Schematic of line-of-sight flame imaging setup

In order to trigger the camera, the TTL pulse generator requires a positive voltage signal. Since the triggering signal from the function generator is AC voltage, a variable

DC power supply is included in the setup and a summing circuit box is utilized to give the signal a DC offset. A BG-38 Schott glass filter was placed in front of the ICCD camera to eliminate wavelengths of light above ~700nm.

3.4.2 OH Planar Laser Induced Fluorescence (PLIF)

High speed line-of-sight images, while helpful in some respects in understanding the effect of large amplitude forcing of the flame, do not provide the detailed insight of the flame dynamics during the acoustic cycle. In order to truly observe the flame, OH planar laser-induced fluorescence (PLIF) was utilized to obtain a two-dimensional image of the flame.

Figure 18 shows the layout of the laser diagnostics. The laser system consists of a Lambda Physik dye laser system pumped by the second harmonic of an Nd:YAG laser. The output of the dye laser system (around 570 nm) is frequency-doubled with a tunable second harmonic generator (Inrad Autotracker, BB crystal). The portion of light whose frequency is successfully doubled is separated from the rest of the light with two dichroic turning mirrors. The resulting ultraviolet (UV) laser beam is expanded into a sheet approximately 140 mm wide and 300 μm thick with two fused silica lenses. The UV sheet illuminates the entire width of the combustor and approximately 100 mm of the length measured from the dump plane where the flame is stabilized. For OH PLIF, the frequency-doubled output from the dye laser was tuned near 281.4 nm to pump the $R_1(9)$ transition of the $A^1\Sigma - X^2\Pi$ '(1, 0) band. The emitted fluorescence is detected at a right angle to the laser sheet using a 25mm intensified PI-MAX camera (256x1024 pixels) equipped with a UV-Nikkor lens system (105 mm, f#4). The detected fluorescence

signal is limited to 300-370 nm by WG-305 and UG-11 Schott glass filter placed in front of the camera lens. The camera's field of view includes the whole width of the combustor in all of the images, which results in a pixel resolution of ~300 μm.

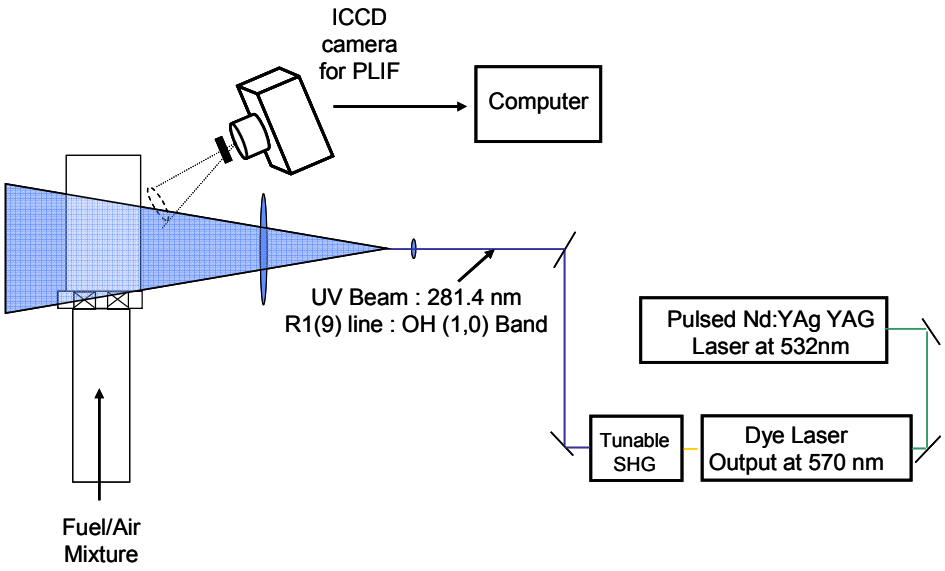

Figure 18. Schematic of laser setup for OH PLIF imaging

The laser imaging was phase locked with the driving signal input to the loudspeakers. The frequency of image acquisition is limited by the frequency of the Nd:YAG laser, which operates at 10 Hz. Therefore, since the frequencies of interest in this study are much greater than this value, successive phase-locked images were actually obtained several cycles apart from each other. Then, the flame response over a sequence of phase angles is reconstructed over different phases and different cycles. The acoustic cycle was divided into 8 phases, with 200 images taken at each phase angle.

A typical image is shown in Figure 19(a). OH is known to exist not just at the flame location, but well into the hot product zone [34]. Therefore, large intensities not

only signify flame location, but also hot products. Typically, researchers determine the flame location by thresholding the gradient of the OH signal; e.g., see Ref. [34]. In this study, the instantaneous images are only used to qualitatively determine the possible mechanisms for nonlinear flame behavior under large amplitude forcing. As such, the PLIF images were processed as follows. The OH PLIF intensity images were corrected for background noise and also for beam profile inhomogeneities (Figure 19(b)). A cutoff intensity was chosen based on the intensities of the reactant stream (~15% of maximum intensity). Any intensity that fell below this limit was set to zero. These images were then filtered with a 3 pixel width Gaussian filter and normalized by the maximum intensity of each image; see Figure 19(c).

To determine the "average" flame response, all 200 images at each phase were ensemble averaged; see Figure 20(a). A family of curves corresponding to constant average "progress variables" (defined as $c = I/I_{max}$ where I is the average intensity value and I_{max} is the maximum intensity) were then generated. From this point, an average flame front is qualitatively determined by visual inspection of the progress variable curve and the change in average intensities across that curve; see Figure 20(b). For the results shown in Chapter 5, $c = 0.3$ was chosen because higher values indicated that the average flame at low amplitudes of driving was lifted off the centerbody which was visually seen to be untrue at these amplitudes. For instance, from Figure 20(a), it clearly appears that the flame is stabilized off the centerbody near the dump plane of the combustor. Therefore, this value was used to denote the average flame location.

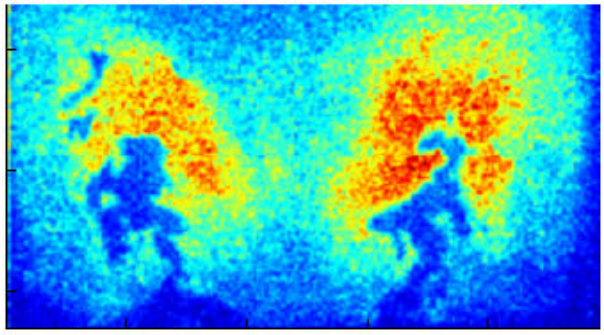

(a)

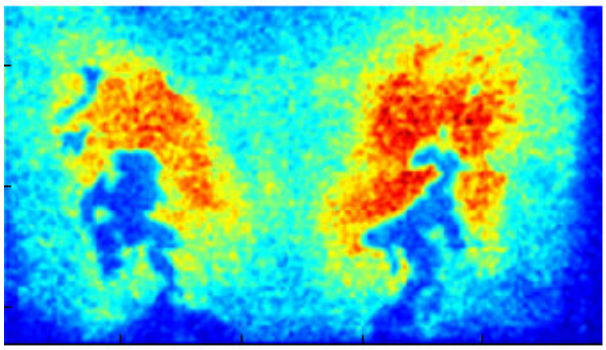

(b)

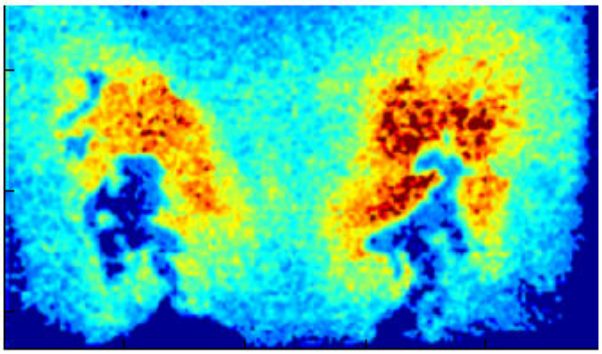

(c)

Figure 19. Instantaneous OH PLIF images: (a) original image, (b) corrected image for laser beam inhomogeneities, (c) corrected image after minimum intensity threshold applied

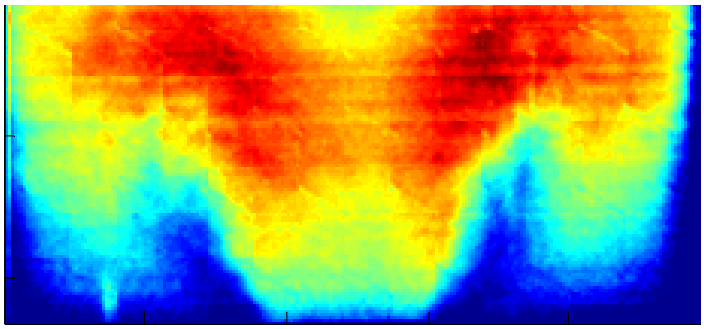

(a)

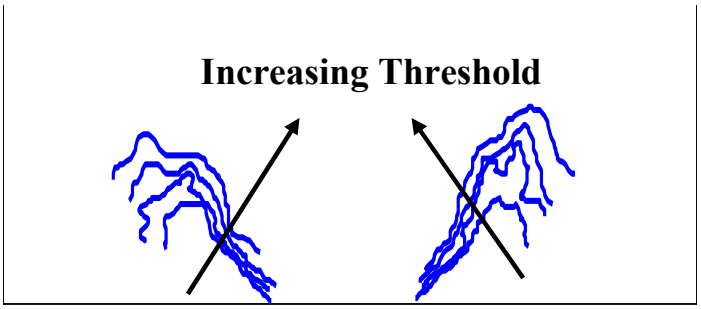

(b)

Figure 20. (a) Average OH PLIF image; (b) Family of flame edge curves for different threshold values of progress variable, c = 0.2 – 0.5. c = 0.3 is the threshold value used in Chapter 5.

3.5 Data Acquisition, Processing and Analysis Tools

3.5.1 Data Acquisition Requirements

Data were obtained with a National Instruments DAQ controlled by Labview software. The acquisition program allowed for user defined sampling rates and the total number of samples taken per test. The analog time-series signals were obtained for all tests utilizing a sampling rate of 10 kHz (Nyquist frequency = 5 kHz) with a total of 16,384 points (i.e., 2^{14}) taken for each test, unless otherwise specified. This sampling rate ensures accurate measurement of the fundamental frequencies of interest (f < 1000 Hz) as

well as the first few harmonics. All signals were sent through a low-pass Butterworth filter set at 2 kHz to eliminate any high-frequency electronic noise. To further ensure that the signals were accurately measured, the upper and lower voltage limits for all of the instrumentation used in these studies was varied to maximize the resolution of the A/D board and minimize digitization errors.

3.5.2 Experimental Procedure

In order to determine the nonlinear behavior of the flame response with increasing flow perturbation amplitude, it is easier (and often necessary) to perform open-loop forced response studies on the flame. This is due to the fact that an unstable combustor is, by definition, operating at the limit cycle amplitude. Therefore, the characteristics of the curve, H(A), in Figure 3, are unknown except at the point, A_{LC}. Therefore, in order to elucidate the effects of various parameters, open-loop forcing of the flame is typically used. Instead of a feedback mechanism, shown in Figure 2, the desired experimental technique is outlined schematically in Figure 21. In this manner, the amplitude of the acoustic oscillations is controlled by the driving signal input (typically to loudspeakers or actuators in the inlet or exhaust sections of the experimental setup). This control of the input fluctuation allows for detailed measurements of the flame response to increasing acoustic oscillations. Therefore, the nonlinear behavior of the flame at large amplitude of oscillations can be clearly ascertained and studied in further detail.

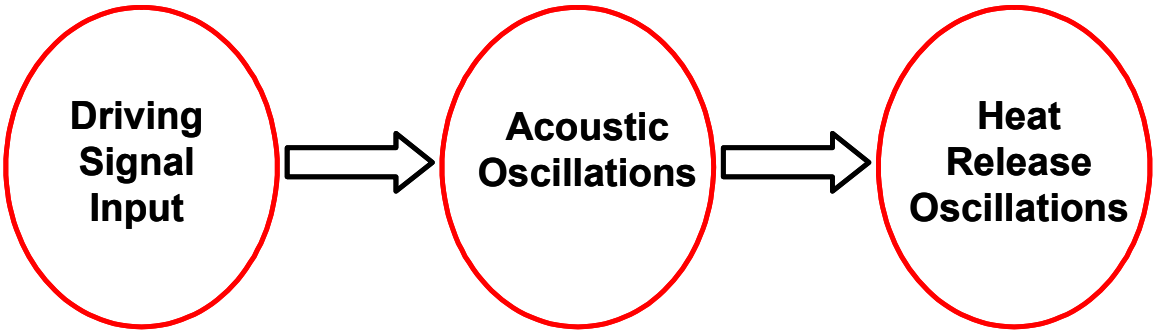

Figure 21: Schematic for open-loop forcing

One of the principal tools of the input-output representation is the transfer function. The idea of using the transfer functions to represent physical systems is a natural outgrowth of the use of Laplace transforms to solve linear differential equations. These operational methods have been so successful in simplifying and systematizing the problem of obtaining the time response of a system that it appears reasonable that they should also be valuable in system representation of flame dynamics.

In system dynamics, the transfer function is typically defined as a ratio of the Laplace transform of the output to the Laplace transform of the input, with zero initial conditions. Furthermore, a transfer function is an input-output description of the behavior of a system. Thus it does not include any information concerning the internal structure of a system and its behavior. Thus in the frequency domain, a transfer function relates the output of a system to its input. This can be written as:

$$\frac{Q'(s)}{u'(s)} = G(s) \tag{3.2}$$

where *Q'(s)* is the output from the system while *u'(s)* is the input to the plant, and *G(s)* is the transfer function. This can be expressed schematically as shown in Figure 22.

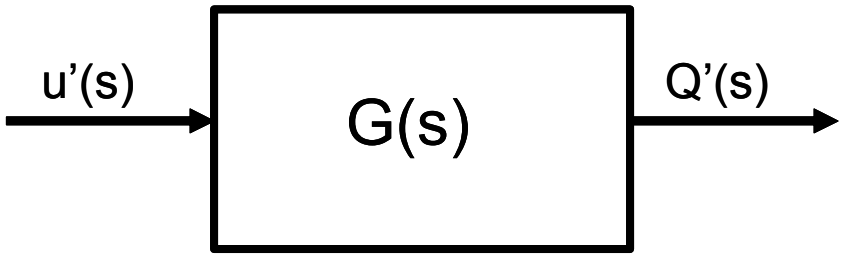

Figure 22: Block diagram representation of input-output relationship between parameters u and Q.

In terms of unstable combustors, the applicable transfer function is between the flame response (output) to imposed velocity oscillations (input). Instead of Laplace transforms, however, the magnitudes and phase of the two parameters are obtained by Fourier transforms. In equation form, this is typically depicted as:

$$\frac{Q'(\omega)/\bar{Q}}{u'(\omega)/\bar{u}} = G(\omega) \tag{3.3}$$

where Q is the heat release from the flame and u is the velocity at the flameholder location.

3.5.3 Data/Signal Processing

All of the measurements are stored as time-series signals for analysis. For the problem of interest, it is typically more instructive to transform it into the frequency domain using the Fourier transform. The Fourier transform of a time-series signal, x(t), is defined as:

$$X(\omega) = \int_{-\infty}^{\infty} x(t)\exp(-i\omega t)dt \tag{3.4}$$

where $X(\omega)$ represents the power spectral density at frequency, ω. $X(\omega)$ is by definition a complex number, i.e. $X(\omega) = Re(X(\omega)) + iIm(X(\omega))$. Therefore, it gives information of the gain or amplitude of the time signal at frequency, ω, as well as the phase of the signal. The amplitude and phase of the signal is simply:

$$\begin{aligned} \left|X(\omega)\right| &= \sqrt{\mathrm{Re}\left(X(\omega)\right)^2 + \mathrm{Im}\left(X(\omega)\right)^2} \\ \phi_{X(\omega)} &= \arctan\left(\frac{\mathrm{Im}\left(X(\omega)\right)}{\mathrm{Re}\left(X(\omega)\right)}\right) \end{aligned} \tag{3.5}$$

The use of the Fourier transform, however, has its limits. For instance, if the amplitude or $|X(\omega_o)|$ is an important quantity at a given frequency, ω_o, then use of the general Fourier transform may lead to substantial error in this value due to spectral

leakage. The calculated amplitude will be lower than what it really is and the phase angle can also be quite different as well. Since the measured signals in this work will be externally forced with a known fundamental frequency (and therefore known higher harmonic content), this problem can be avoided by simply calculating directly the Fourier transform at the frequency of interest instead of over the entire frequency range between 0 Hz and the Nyquist frequency. Thus for a signal, $x(t)=sin(\omega_o t)$:

$$\left|X\left(\omega_o\right)\right| = \frac{2}{\tau}\int_0^{\tau} x(t)\exp(-i\omega t)dt \tag{3.6}$$

Thus, accurate calculations of the amplitude and phase of the signals can be obtained. In addition, higher and subharmonic calculations can be performed very easily. These calculations can then be used to determine the flame transfer function and its dependence on various parameters. Uncertainties in all measurements are discussed in further detail in Appendix A.

CHAPTER 4

NONLINEAR FLAME RESPONSE TO FORCED ACOUSTIC OSCILLATIONS IN A GAS TURBINE COMBUSTOR SIMULATOR

This chapter describes an experimental investigation of the nonlinear flame response to large amplitude acoustic oscillations and its dependence on driving frequency and equivalence ratio. Sections 4.1, 4.2, and 4.3 describe the experimental operating conditions, the average flame dependence on external driving and the coherence characteristics between the measured signals, respectively. Baseline linear transfer function measurements are presented in Section 4.4. The dependence of the nonlinear flame response on driving frequency and equivalence ratio subject is described in Section 4.5. Section 4.6 details the corresponding higher and subharmonic characteristics associated with the heat release and flow perturbations as a function of frequency and oscillations amplitude. Finally, Section 4.7 discusses the mechanism by which nonlinearity in the flame response is governed as well as limitations in the measurements from making more concrete conclusions. The results are also compared to those mechanisms proposed theoretically in the literature.

4.1 Experimental Conditions

Tests were performed at a mean pressure of 1.7 atmospheres and mean equivalence ratios ranging from 0.83 to 1.0. All tests were performed at a total flow rate

of 5.5 g/s which corresponds to a premixer velocity of 11.5 m/s which corresponds to a Reynolds number of 22500 based on the premixer exit diameter. Inlet temperatures were kept constant at room temperature. The full list of operating conditions is listed below in Table 1.

Table 1. Operating conditions for linear/nonlinear flame response studies in gas turbine combustor simulator

Parameter	Linear Studies	Nonlinear Studies
Mean Premixer Velocity, u_o, m/s	**11.5**	**11.5**
Driving Frequency, f_{drive}, Hz	**100-500**	**250-340**
Equivalence Ratio, ϕ	**0.95**	**0.83, 0.87, 0.9, 0.95**

The basic experimental procedure consists of externally driving oscillations in the combustor with varying amplitude at a fixed frequency or fixed amplitude at varying frequencies while obtaining simultaneous measurements of pressure, velocity, and chemiluminescence. A typical result showing the time dependencies of these quantities are plotted in Figure 23. For all cases, the combustor was quite stable in the absence of driving ($p'/p_o < 0.03\%$, $u'/u_o < 0.8\%$). The flame length ranged from 5-15 cm between the equivalence ratios of 0.95-0.83, respectively.

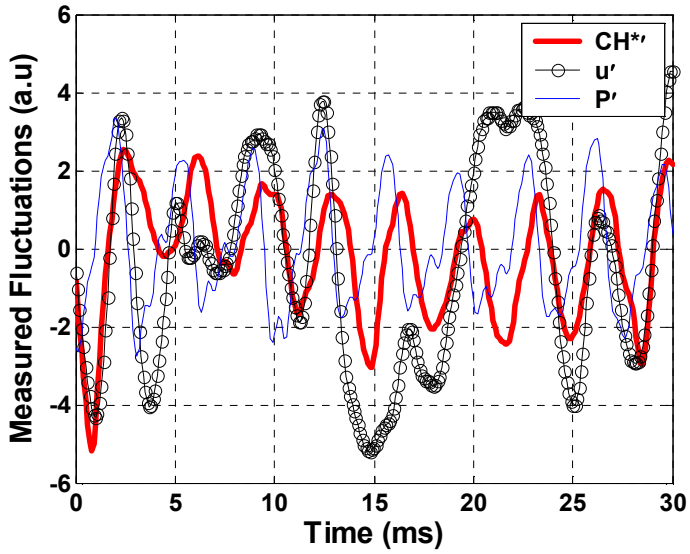

Figure 23: Time-series data of CH* chemiluminescence, pressure, and velocity at a driving frequency of 290 Hz (ϕ= 0.95)

4.2 Driving Effects on Average Flame Characteristics

The imposed driving altered the mean flame characteristics, similar to prior observations (e.g., see Ref. [58]). With increased driving levels, the flame's time-averaged visible length appears to increase in length up to an undetermined maximum. In addition, its local and global intensity generally decreased slightly, but not always in a monotonic manner. Typical results are shown in Figure 24. In general, OH* and CH* levels were found to exhibit similar dependence upon disturbance amplitude. This chemiluminescence-driving amplitude dependence could arise from at least two effects. First, the chemiluminescence levels depend not only upon heat release rate and equivalence ratio, but also strain rate (i.e., turbulence levels). Thus, this trend could reflect the strain sensitivity of the chemiluminescence emissions at a fixed rate of heat release. It is also possible that the mean heat release rate changes through incomplete combustion caused by local flame extinction events. In addition, the efficiency of

capturing flame length changes may be affected. Attempts were made to investigate this latter possibility through exhaust gas analysis measurements. The measurement location was unfortunately located very close to the actuator location in this facility. Therefore, the pulsing air from the actuator contaminated the measurement which resulted in very large uncertainties. Because of this uncertainty in interpretation of absolute chemiluminescence levels, all unsteady measurements are reported on a normalized basis.

4.3 Coherence Characteristics

In order to obtain accurate transfer function data, it is important to have high coherence levels between the pressure, velocity and chemiluminescence oscillations at the frequency of interest. The coherence ranges in value between zero and unity and is defined by the relation [59]:

$$\gamma_{ij}(f) = \frac{\left|F_{ij}(f)\right|}{\sqrt{F_{ii}(f)F_{jj}(f)}} \tag{4.1}$$

where F_{ij} , F_{ii}, and F_{jj} denote the cross-spectrum between quantities *i* and *j* and their power spectra, respectively. The subscripts p, u and E are used to denote the pressure, velocity and CH* chemiluminescence, respectively. Figure 25(a) plots the dependence of γ_{pE} upon frequency for a driving frequency of 280 Hz at a driving amplitude of u'/u_o = 0.3. The figure shows that the coherence has a value of roughly 0.99 at the driving frequency and 0.81 at its first harmonic, 560 Hz. Similarly, Figure 25(b) plots the

dependence of γ_{uE} upon frequency. Similar to the pressure-CH* case, the coherence is quite high (approximately 0.96) at the driving frequency.

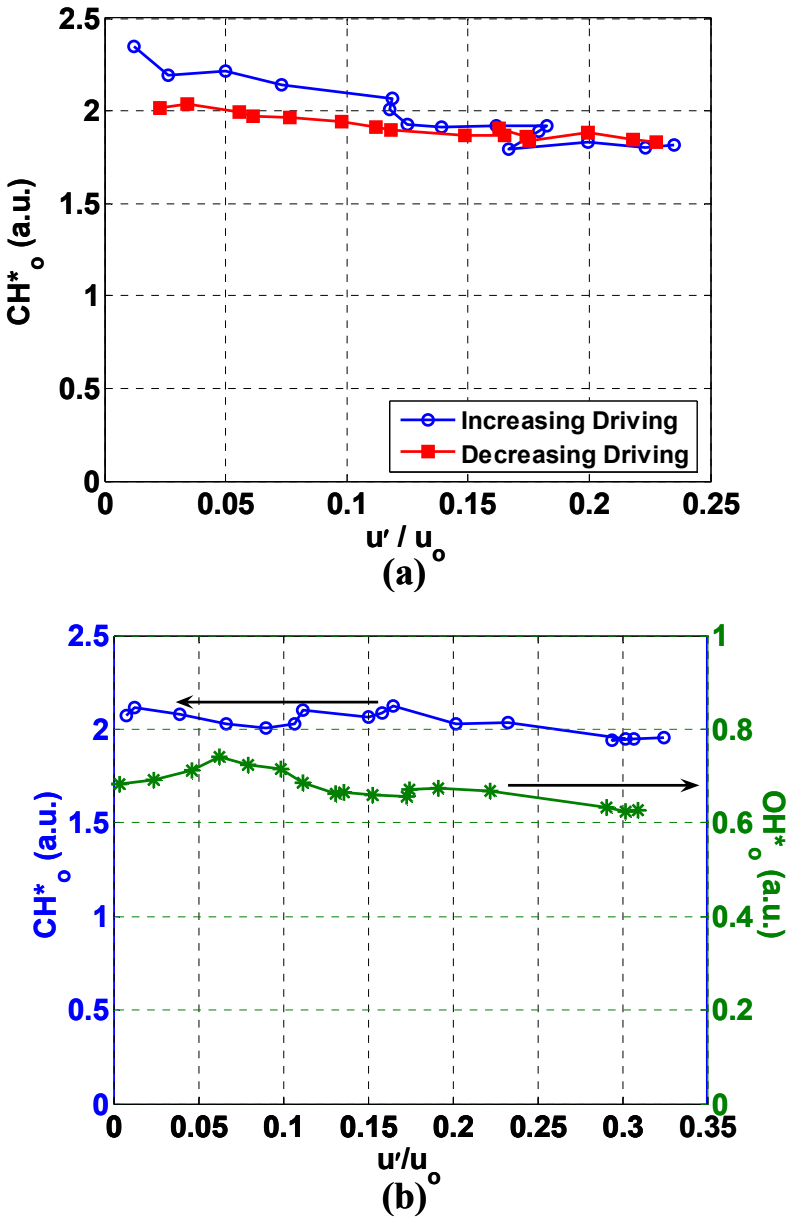

Figure 24. Dependence of mean CH* and OH* signals upon velocity oscillation amplitude (a) f_{drive} = 283 Hz, ϕ = 0.95; (b) f_{drive} = 280 Hz, ϕ = 0.95.

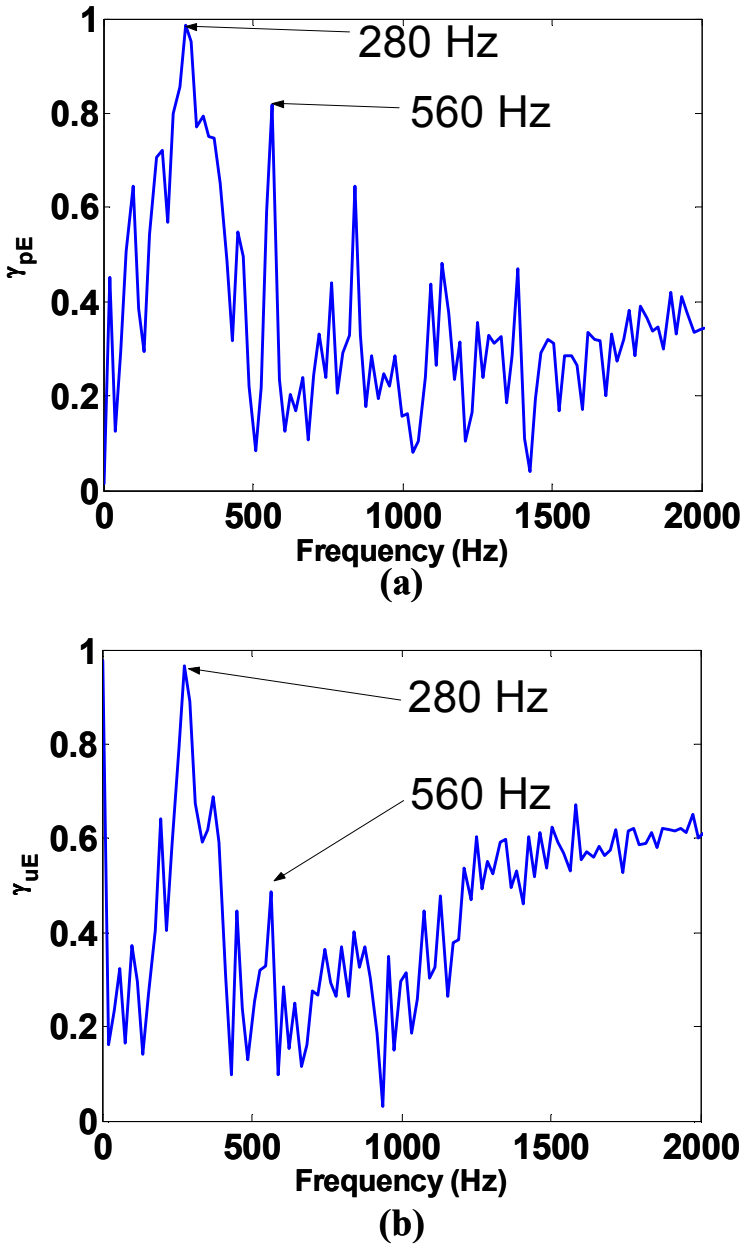

Figure 25: Dependence of (a) pressure-CH* and (b) velocity-CH* coherence upon frequency at f_{drive} = 280 Hz (ϕ = 0.95)

Figure 26 plots the dependence of the pressure-CH* and velocity-CH* coherence at the driving frequency (f_{drive} = 280 Hz) upon the amplitude of imposed oscillations. Its lowest value is ~ 0.3-0.4 at the lowest drive amplitudes, but quickly increases and for

most results has a value of ~0.97-0.99. The uncertainties in these coherence estimates, Δ, were obtained from the expression [59]:

$$\Delta\left(\gamma_{ij}\right) = \frac{\gamma_{ij}\sqrt{2\left(1-\gamma_{ij}^{\ 2}\right)}}{n} \tag{4.2}$$

where n=8 ensemble averages were used. These near unity coherence values at the driving frequency shows that the use of these data to determine the pressure-heat release and velocity-heat release transfer functions is appropriate. Note that the velocity-CH* coherence is consistently smaller than the pressure-CH* value. This is due to higher levels of background noise (turbulent velocity fluctuations) in the velocity.

4.4 Linear Flame Response

Consider next the amplitude and frequency dependence of the pressure/ velocity/ chemiluminescence transfer functions. The amplitudes of the oscillations and their respective phase angles were determined as shown in Chapter 3.

Baseline measurements of the linear flame response were obtained by driving oscillations at low amplitudes over the 10 – 550 Hz frequency range. The amplitude of the pressure-CH* and velocity-CH* transfer functions are plotted in Figure 27. The uncertainty in the gain and phase angle was determined from the following relation, using n=8 ensembles [59]:

$$\Delta\left(G_{ij},\theta_{ij}\right)=\frac{\sqrt{1-\gamma_{ij}^{\ 2}}}{\gamma_{ij}\sqrt{2n}} \tag{4.3}$$

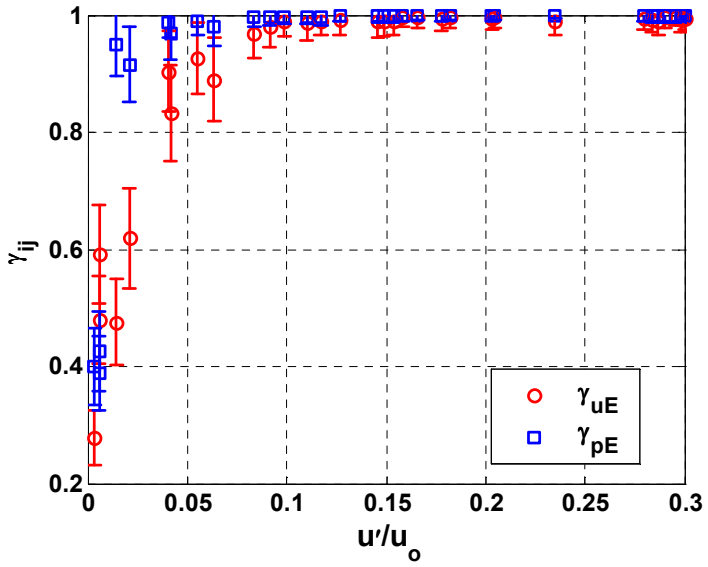

Figure 26: Dependence of coherence upon amplitude of velocity oscillations at f_{drive}= 280 Hz (ϕ = 0.95)

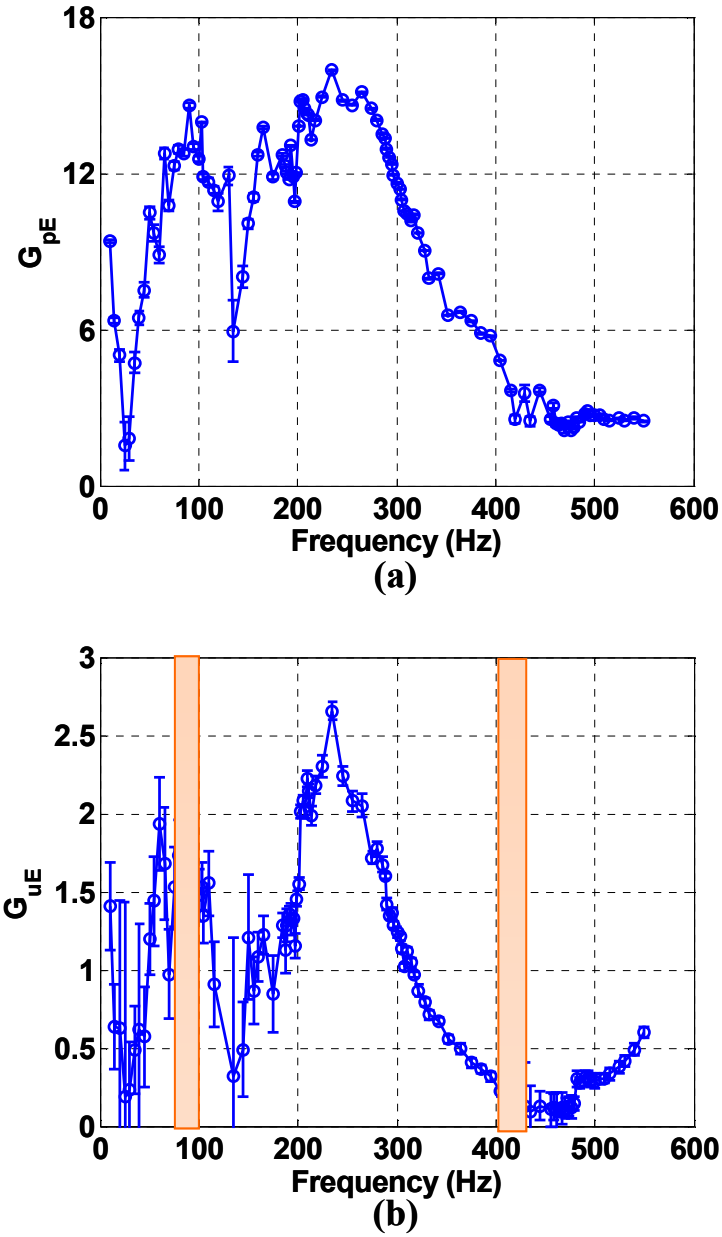

Figure 27: Dependence of linear (a) pressure-CH* and (b) velocity-CH* transfer function upon driving frequency (ϕ = 0.95). Frequency regions of high uncertainty in transfer function between velocity perturbations in premixer and flame base indicated by hatched region.

This transfer function has local maxima at 90 and 240 Hz and monotonically decays in the 250-400 Hz region. The transfer functions, G_{uE} and G_{pE} have values on the order of 2 and 15. The corresponding phases of these transfer functions are plotted in Figure 28. Both phase results exhibit a linear increase with frequency up to approximately 400 Hz. This phase dependence suggests a roughly constant time delay relationship between the pressure/velocity and chemiluminescence; i.e., $CH^*(t) \sim u'(t-\tau)$. These time delays can be estimated from the slope of this phase dependence to yield values of approximately 3.5 ms. For reference, the time required for a disturbance to convect the length of an 8 cm flame at the premixer exit velocity is $\tau_{flame} \sim$ 7 ms. The flame length, however, is based strictly on visual observations of the visible chemiluminescent flame brush. In reality, the reaction zone location is most likely much shorter than this length which results in the discrepancy between the time delay and convective time calculations. This linear phase dependence ceases at frequencies above 400 Hz as the phase dips then rises again. Recall, however, that the transfer function between the velocity oscillations at the measurement point and flame base changes rapidly in the vicinity of 80 and 420 Hz. Thus the results at these frequencies should be interpreted with caution.

There are similarities between these gain and phase results and the measured and predicted transfer functions reported by Schuller *et al.* [60]. The peaks in the gain and the dips in phase are reported in their study which modeled the effective of convective velocity oscillations on laminar, V-shaped flames. This is interesting because they obtained their results for a laminar flame while our data are obtained from a swirling, turbulent flame. Apparently, the average "V" shapes of the two flames are the primary

thing they have in common. This observation indicates that the theoretical result used to describe laminar flame dynamics can be fit to our data very satisfactorily. Similar peaks at intermediate frequencies were reported experimentally by Külsheimer and Büchner [36].

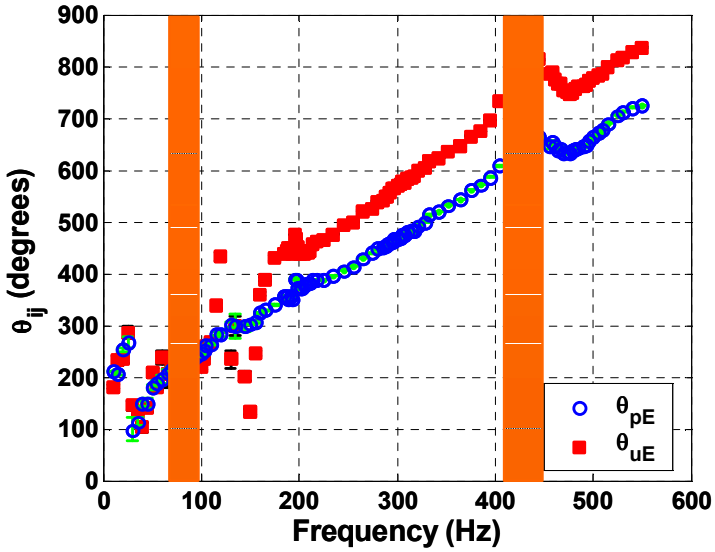

Figure 28: Dependence of linear pressure-CH* and velocity-CH* phase angle upon driving frequency (ϕ= 0.95). Frequency regions of high uncertainty in transfer function between velocity perturbations in premixer and flame base indicated by hatched region.

4.5 Nonlinear Flame Response

Next, consider the amplitude dependence of this transfer function. For brevity, only velocity results are presented since the pressure-velocity relationship is linear over the entire driving amplitude range, e.g., see Figure 29. Therefore, the p'-CH* transfer function has an identical form (although the results are "cleaner" due to the larger p'-CH*

coherence values). Figure 30(a) presents typical results showing the dependence of the normalized CH* and OH* chemiluminescence amplitudes upon the normalized velocity amplitudes over a range of driving amplitudes. The departure of this transfer function from linearity is illustrated by comparing the data with the straight line in the figure. Note also that the normalized amplitudes of the pressure and heat release oscillations at the point where nonlinear effects become obvious are roughly 2 – 3% and 25 – 30% while the normalized chemiluminescence oscillation is 35%. These relatively low pressure fluctuations and significant chemiluminescence oscillations lend credibility to speculations that heat release nonlinearities, as opposed to gas dynamic ones, control the nonlinear dynamics of similar lean, premixed combustion systems. It should be pointed out that these pressure amplitudes where nonlinearities in the p'-CH* relationship are observed ($p'/p_o \sim$ 2-3%) are of similar magnitude as typical natural instability amplitudes ($p'/p_o \sim$ 0.5-2%) that were measured in other tests on this combustor [61]. Also, the maximum amplitude of the normalized CH* oscillations are on the order of 30-40% of the mean, consistent with previous experiments [33].

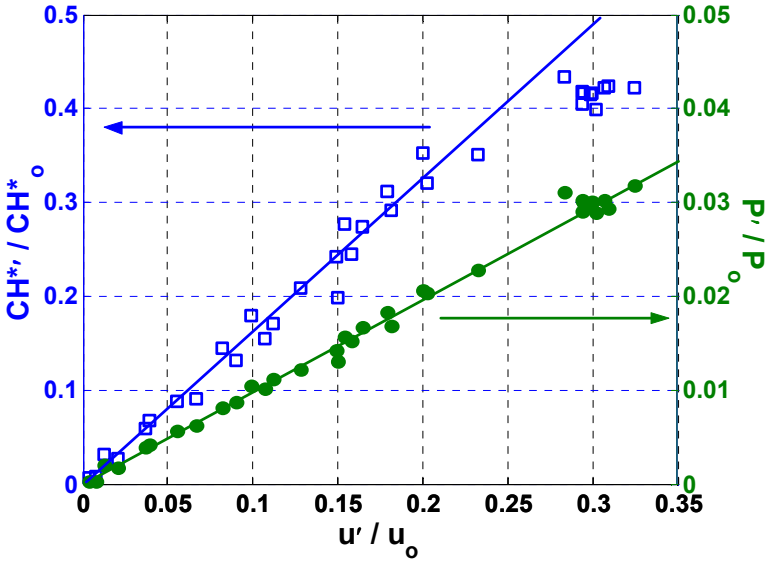

Figure 29: Dependence of CH* chemiluminescence and pressure oscillation amplitude on velocity fluctuation amplitude (f_{drive} = 280 Hz, ϕ = 0.95)

Figure 30(b) presents the phase relationship between the velocity oscillations and the normalized chemiluminescence. The figures indicate that the phase angle has a complex dependence on the amplitude of oscillations. It increases monotonically by about 40 degrees from $0.05 < u'/u_o < 0.15$. At larger disturbance amplitude, the phase decreases somewhat, then levels off. Note that the phase exhibits amplitude dependence at disturbance levels significantly lower than the gain. It is likely that the monotonic phase increase in the $0.05 < u'/u_o < 0.15$ region is due to the lengthening of the flame with increased disturbance amplitudes. Due to the strong similarity in both the CH* and OH* results indicating that the CO_2* contribution is not particularly significant in these measurements, only CH* results are presented in the remainder of the chapter.

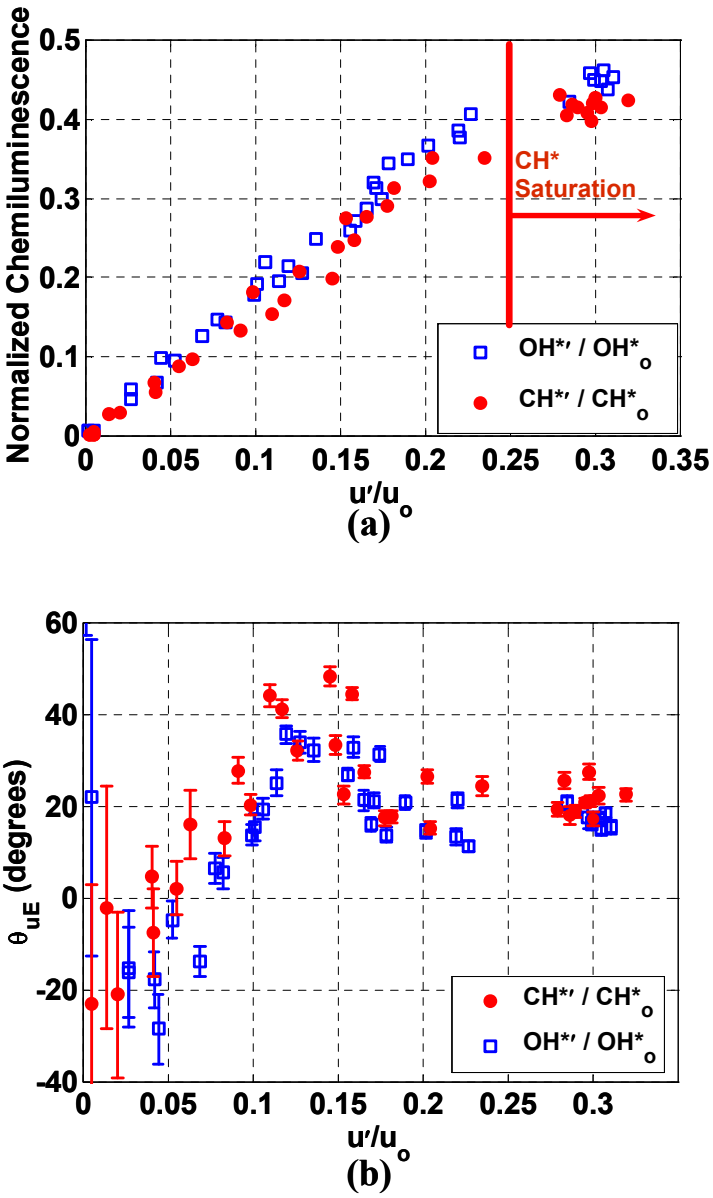

Figure 30: Dependence of CH* and OH* chemiluminescence (a) amplitude and (b) phase angle (right) on velocity oscillation amplitude (f_{drive} = 280 Hz, ϕ = 0.95)

4.5.1 Nonlinear Flame Response - Equivalence Ratio Dependence

Figure 31 presents the dependence of *CH*'* upon *u'* for equivalence ratios ranging from 0.83 to 0.95. It is important to note that the maximum driving amplitude point is not due to actuator limitations, but flame blowoff. It is clearly seen that the slope in the linear regime as well as the CH* saturation amplitude decreases as the equivalence ratio is decreased. The sudden transition from the linear regime to nonlinear implies that saturation is perhaps a change in state of the flame. The results also show that the blowoff velocity oscillation amplitude for the majority of tests is approximately constant except for the leanest case investigated, $\phi = 0.83$. This result clearly shows that the saturation amplitude is a function of the equivalence ratio. Furthermore, recall from Figure 5 that for smaller saturation amplitudes of the curve, H(A), the corresponding limit cycle amplitude would be smaller as well. These results indicate that that as the equivalence ratio is decreased in this combustor, the instability amplitude would be expected to decrease. Instability studies using this combustor indicate that this result holds true. These same data are replotted in Figure 31(b), where each curve is normalized by its linear gain, the slope of the transfer function in the linear regime. For equivalence ratios between 0.87 and 0.9, the velocity-CH* relationship is highly nonlinear while the richest case investigated shows little nonlinearity, presumably because blowoff occurs before saturation. Figure 32 presents the corresponding phase relationship between *u'* and *CH*'*. In all cases, the phase angle initially increases to a maximum and then decreases or stays roughly constant with increase in velocity oscillation amplitude. The initial increase in phase angle appears to be due to lengthening of the flame for initial increases in driving. For increased flame length, a

velocity disturbance would take a longer time to convect along the flame's length, resulting in an increased delay between the velocity and chemiluminescence oscillations.

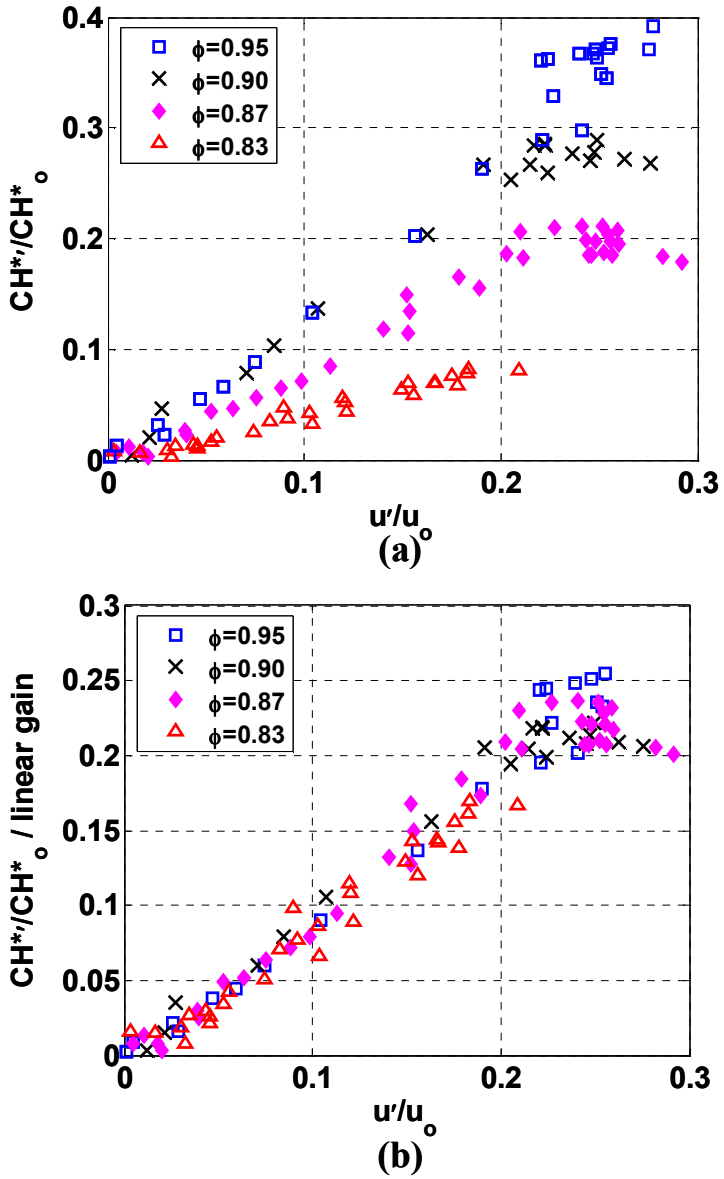

Figure 31: Dependence of (a) normalized and (b) normalized/linear gain CH* chemiluminescence amplitude upon amplitude of velocity oscillations at several equivalence ratios (f_{drive} = 300 Hz)

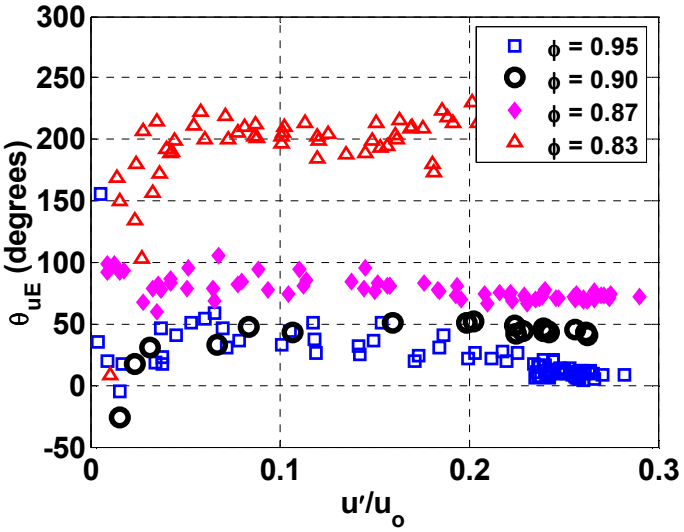

Figure 32: Dependence of velocity-CH* chemiluminescence phase angle on amplitude of velocity oscillations at several equivalence ratios. Uncertainty in phase angle for $u'/u_o < 0.05$, $\Delta\theta \sim 30°$; for $u'/u_o > 0.05$, $\Delta\theta \sim 2°$ ($f_{drive} = 300$ Hz).

4.5.2 Nonlinear Flame Response - Driving Frequency Effects

In addition to varying the equivalence ratio, the effect of driving frequency between 260 and 320 Hz was extensively analyzed. This range was chosen because of the high quality data that could be obtained at these frequencies due to the large flame response, see Figure 27, and its proximity to a 310 Hz combustor resonance (discussed further below). Figure 33(a) presents the dependence of the CH* amplitude and phase upon u'/u_o over the 260 to 320 Hz frequency range at $\phi = 0.95$. Note that the slopes of these curves in the linear region are equal to the transfer function values plotted in Figure 27. Nonlinearities in the *CH*' -u'* relationship are prominent in the 280 and 290 Hz driving cases, while the transfer function is substantially more linear at the remaining frequencies. The near linearity of the transfer function in some cases all the way to flame

blowoff strongly suggest that nonlinearity is not due to flame holding; if flame holding were a key nonlinear mechanism, one would expect the transfer function at all frequencies and equivalence ratios to become nonlinear near the blowoff point. The normalized CH* fluctuations at the point where nonlinearity is evident have similar values for 280 and 290 Hz, but the corresponding velocity amplitudes appear to vary slightly with driving frequency. These results suggest that nonlinearity becomes important when the normalized CH* fluctuations attain a certain value (in this case $CH^{*\prime}/CH^{*}_{o} \sim 0.4$ for $\phi=0.95$), while the resultant value of the unsteady velocity is governed by the linear velocity-CH* transfer function; e.g., see Figure 27. This is in contrast to saturation occurring at a certain u'/u_o value, such as might be the case if nonlinearity were due to flameholding as discussed in Ref. [27]. Figure 33(b) shows that the phase exhibits similar amplitude dependence as in the other results. Again, note that nonlinearity is evident in the phase behavior at very low amplitudes, e.g., $u'/u_o \sim 0.05$, where the gain is still very linear. In addition, the phase angle saturates in value where the gain remains linear as well.

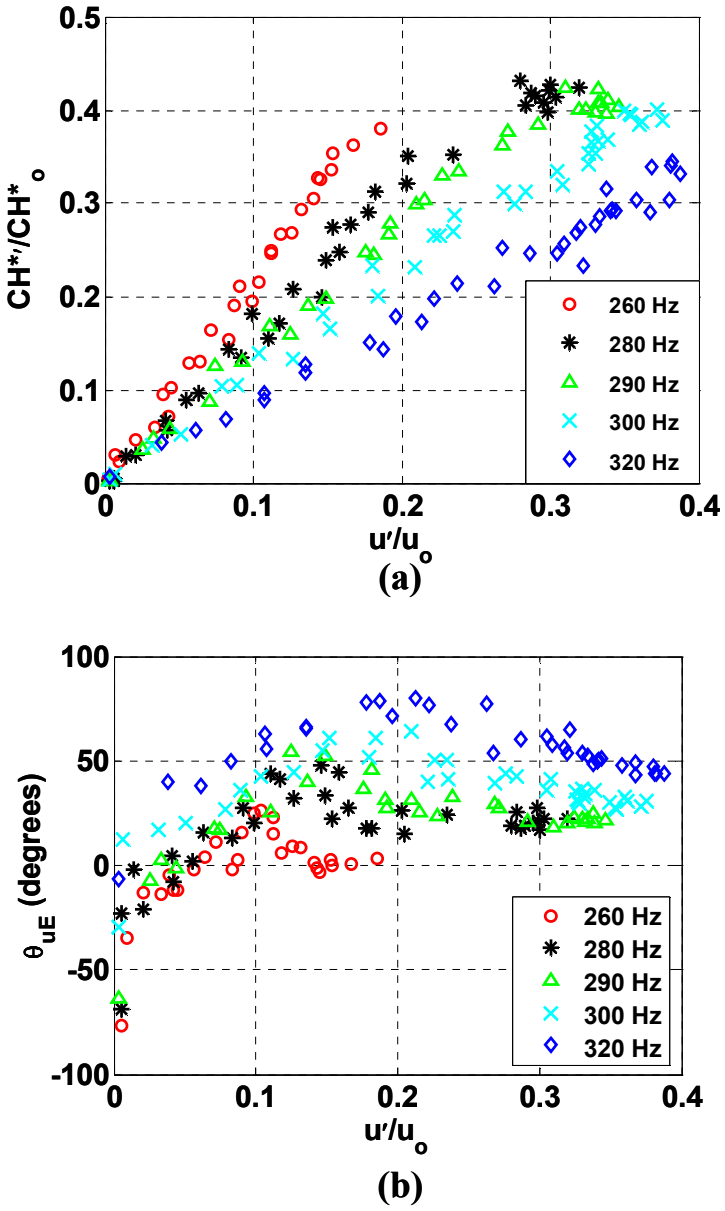

Figure 33: Dependence of CH* chemiluminescence (a) amplitude and (b) phase upon velocity amplitude at several driving frequencies. Uncertainty in phase angle for $u'/u_o < 0.05$, $\Delta\theta \sim 30°$; for $u'/u_o > 0.05$, $\Delta\theta \sim 2°$ ($\phi = 0.95$).

Figure 31 and Figure 33 suggests that the saturation amplitude and the transfer function gain in the linear regime are related; i.e., lower saturation amplitudes are associated with lower gains and vice versa. This relationship is plotted in Figure 34. This figure plots the cases where the *u'-CH** transfer function became noticeably nonlinear (i.e., 280 and 290 Hz, as well as $\phi = 0.90$, 0.87, and 0.83) and shows that this relationship is nearly monotonic. Note that while this behavior seems quite intuitive, there is no *a priori* reason why it must occur. For example, it is possible to think of examples where the opposite behavior occurs; i.e., larger saturation amplitudes occur at lower linear gains. One example is the flame kinematic nonlinearities discussed by Lieuwen [31]. In this case, it is known that the linear gain increases with flame speed. However, the flame exhibits a linear response for higher disturbance values (i.e., higher saturation amplitude) when the flame is longer; i.e., when the flame speed is lower.

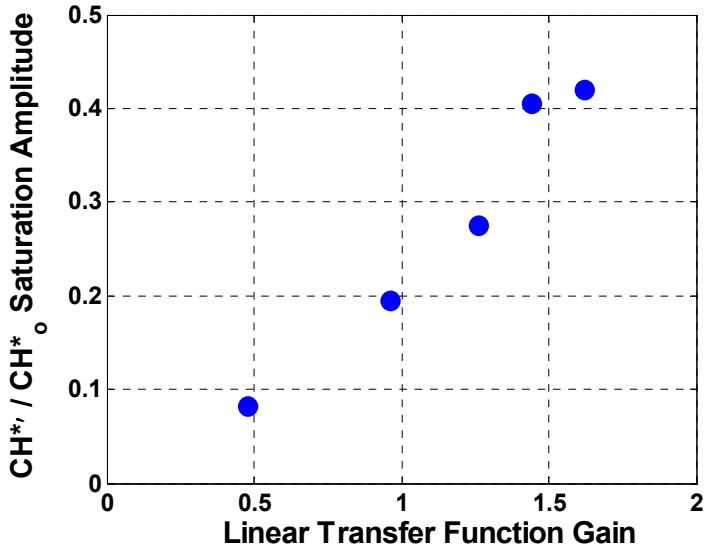

Figure 34: Dependence of CH* saturation amplitude on transfer function gain in linear regime (f_{drive} = 280, 290 Hz, ϕ = 0.9, 0.87, 0.83).

4.6 Harmonic and Subharmonic Characteristics

4.6.1 Harmonic Characterization

In addition to characterizing the dependence of the flame transfer function on the fundamental driving frequency, extensive analysis of the higher harmonics of the dynamic signals was performed. Prior studies suggest that such data are needed to obtain a comprehensive understanding of the nonlinear combustion process. For example, it is well established from forced response studies in various mixing layers, jets, and wakes that such understanding is key to the system's nonlinear dynamics (e.g., see Ref. [62]). In addition, harmonics of the unstable combustor mode are observed routinely; e.g., see Figure 11.

Higher harmonic phenomena can be understood by considering a nonlinear system's response to harmonic forcing. For instance, the gas dynamic nonlinearity that is generated by the isentropic relationship between pressure and density values is:

$$\frac{p(t)}{\bar{p}} = \left(\frac{\rho(t)}{\bar{\rho}} \right)^{\gamma} \tag{4.4}$$

Now, assume the density oscillates harmonically such that:

$$\frac{\rho'(t)}{\bar{\rho}} = A \sin(\omega t) \tag{4.5}$$

where A is the amplitude of oscillation and ω is the angular frequency. Substituting Eq. (4.5) into Eq. (4.4) and expanding this expression in a Taylor series about the point A = 0 yields the following expression for the pressure oscillations:

$$\frac{p'(t)}{\gamma \overline{p}} = \frac{(\gamma-1)}{4} A^2 + \left(A + \frac{(\gamma-1)(\gamma-2)}{8} A^3 \right) \sin(\omega t) - \frac{(\gamma-1)}{4} A^2 \cos(2\omega t) - \frac{(\gamma-1)(\gamma-2)}{24} A^3 \sin(3\omega t) + \ldots \tag{4.6}$$

This expansion consists of a linear term (second term on the right), as well as many nonlinear terms that are proportional to higher powers of the amplitude A. The time-independent term (first term on right hand side) represents the change in *mean* pressure that can occur by an oscillatory density field (more important in rocket engines than in land-based gas turbines since A<<1 in gas turbines under limit cycle conditions). The harmonics (i.e., third and fourth terms on right hand side) are proportional to A^2 and A^3, oscillating at two and three times the angular frequency, ω. Therefore, the higher harmonics will be compared to these proportionalities (i.e., first harmonic amplitude compared to square of fundamental amplitude).

In general, these harmonic amplitudes are substantially smaller than those of the fundamental, however, which results in lower coherence between the fundamental and first harmonic, $\gamma_{i=f,j=2f.}$ compared to coherence values between the two fundamentals. As such, only a single subharmonic and harmonic of the chemiluminescence signal

($CH^{*\prime}_{f=fdrive/2}$ and $CH^{*\prime}_{f=2fdrive}$) could be accurately quantified. The first subharmonic and first to third harmonics of the pressure signal could be quantified due to much higher coherence values.

An important question to answer beforehand, however, is whether the presence of higher harmonics in the data is due to actuator or combustion process nonlinearities. Analysis of the data indicates that the dominant source of harmonic generation can be attributed to the nonlinear combustion process. Figure 35 shows two possible pathways by which higher harmonics can be generated. In Pathway A, the actuator generates the harmonics (i.e., for a disturbance input at $f = f_{drive}$, the actuator also excites oscillations at $2f_{drive}$, $3f_{drive}$, etc.), which then drive oscillations in chemiluminescence, velocity and pressure. Conversely, combustion process nonlinearities may generate harmonics, as illustrated by Pathway B. The origin of these harmonics was analyzed by comparing the relative ratios of the harmonics of the chemiluminescence and velocity to the linear transfer function results shown in Figure 27(b). Specifically, the amplitudes of the chemiluminescence and velocity first harmonics are calculated in the data set included in Figure 31 and Figure 33. The value of this first harmonic transfer function is defined as:

$$G_{u_{2f}E_{2f}} = \frac{CH^{*\prime}_{f=2*f_{drive}} / CH^{*}_{o}}{u'_{f=2*f_{drive}} / u_{o}} \tag{4.7}$$

$G_{u_{2f}E_{2f}}$ is then directly compared to the measured linear transfer function in Figure 27(b). If actuator nonlinearities are the origin of the higher harmonics, then the value of

the transfer function at the first harmonic should equal these linear transfer function results. Figure 36 illustrates this comparison for the frequency range 500-550 Hz which corresponds to a fundamental forcing frequency of 250-270 Hz. While the large difference (~2) between these two curves does not eliminate the role of actuator nonlinearities, it does suggest that they are not as dominant a source of the harmonics as the flame.

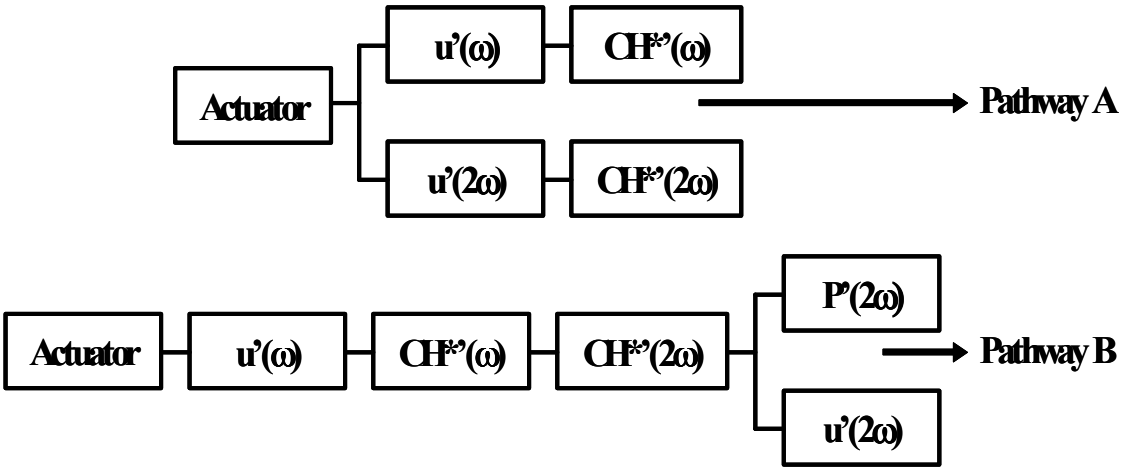

Figure 35: Schematic illustrating mechanisms for generation of higher harmonics by actuator and heat release nonlinearities.

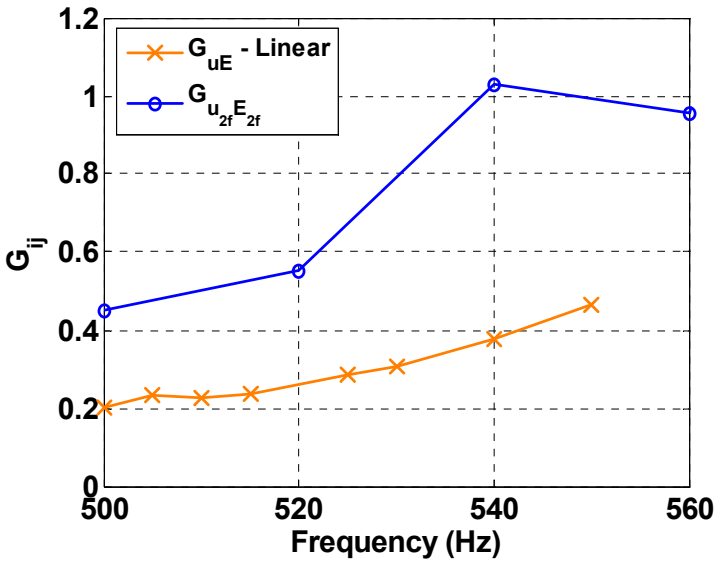

Figure 36: Comparison of velocity-CH* linear transfer function and 1st harmonic transfer function with variation driving frequency (u'/u_o = 0.15, ϕ= 0.95)

The first harmonic characteristics are illustrated in Figure 37, which plots the dependence of the first harmonic of the CH* and velocity oscillations upon the fundamental at several driving frequencies. For clarity, results are shown for only a few representative cases. At low amplitudes, a general quadratic behavior between the chemiluminescence fundamental and the first harmonic is shown. The relative independence of the ratio, $(CH^{*\prime}_{2*fdrive}/CH^{*}_{o})\,/(CH^{*\prime}_{fdrive}/CH^{*}_{o})^2$, on frequency indicates that the flame response has the following form:

$$\frac{CH^{*\prime}(2f_{drive})}{CH^{*}_{o}} = a\left(\frac{CH^{*\prime}(f_{drive})}{CH^{*}_{o}}\right)^2 \tag{4.8}$$

where *a* is a constant. Similar behavior is seen in the velocity measurements (the quadratic dependence between the fundamental and first harmonic is more clearly evident with less scatter in the pressure data, which has a much higher signal to noise ratio), except that the relationship is frequency dependent, i.e.:

$$\frac{u'(2f_{drive})}{u_o} = \left(\frac{u'(f_{drive})}{u_o}\right)^2 F(f_{drive}) \tag{4.9}$$

For both the chemiluminescence and velocity first harmonics, this quadratic dependence on the fundamental is not followed over the entire range of disturbance amplitudes, however. In some cases, the harmonic's characteristics change at disturbance amplitudes where saturation occurs. For example, at 280 Hz and possible 290 Hz, there is a falloff in the relative magnitude of the first harmonic amplitude after the saturation point ($CH^{*\prime}/CH^*_o > 0.4$). In contrast, the 260 Hz result exhibits an essentially constant quadratic character over the entire disturbance amplitude range.

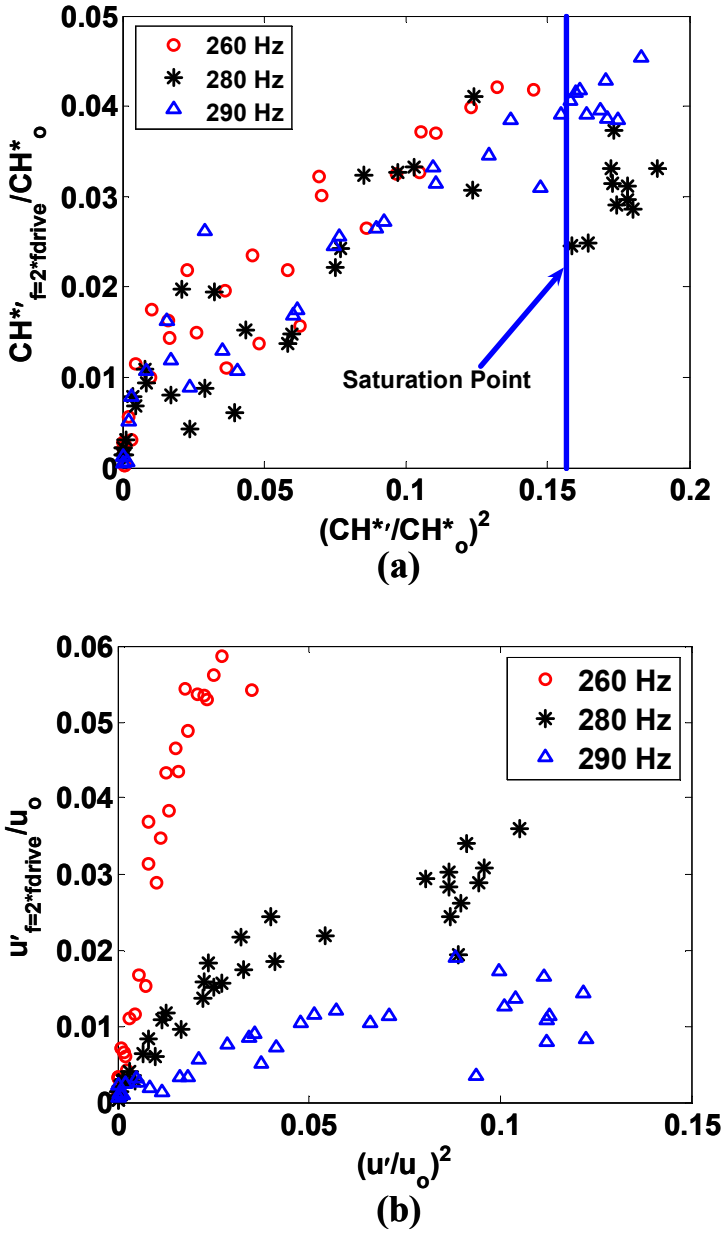

Figure 37: Dependence of (a) CH* and (b) velocity 1st harmonic amplitude upon the square of the fundamental amplitude at several driving frequencies ($\phi = 0.95$)

Further first harmonic characteristics of the CH* oscillations are presented in Figure 38 for two equivalence ratios, $\phi = 0.95$ and $\phi = 0.90$ at a driving frequency of 300 Hz. These two cases provide examples where the flame transfer function remained linear throughout the range of disturbance amplitudes as well as where the flame transfer function saturated at large amplitudes of velocity oscillations. Figure 38 again illustrates that the first harmonic behavior can change markedly between linear and nonlinear cases. For the linear case, $\phi = 0.95$, the first harmonic of the chemiluminescence exhibits a quadratic behavior on the fundamental throughout the measured range. This result is indicative of the other cases where the transfer function remains linear, e.g. 260 Hz in Figure 37(a). For nonlinear cases, however, the functional relationship between the first harmonic and the fundamental changes. At low disturbance amplitudes, the general quadratic behavior is followed for $\phi = 0.90$. At forcing amplitudes above the saturation point of the fundamental, however, the first harmonic has been found to exhibit a variety of behaviors. For $\phi = 0.90$, the first harmonic deviates from the quadratic dependence saturating at the saturation point of the fundamental ($CH^{*\prime}/CH^{*}_{0} = 0.25 \Rightarrow (CH^{*\prime}/CH^{*}_{0})^2 = 0.05$) and then increases increasing much more rapidly. The quadratic dependence between the fundamental and first harmonic is more clearly evident in the pressure data which has a much higher signal to noise ratio, see Figure 39. In addition, the amplitude of the second harmonic of the pressure (due to its higher coherence values) is essentially proportional to the third power of the fundamental, as might be expected, see Figure 39.

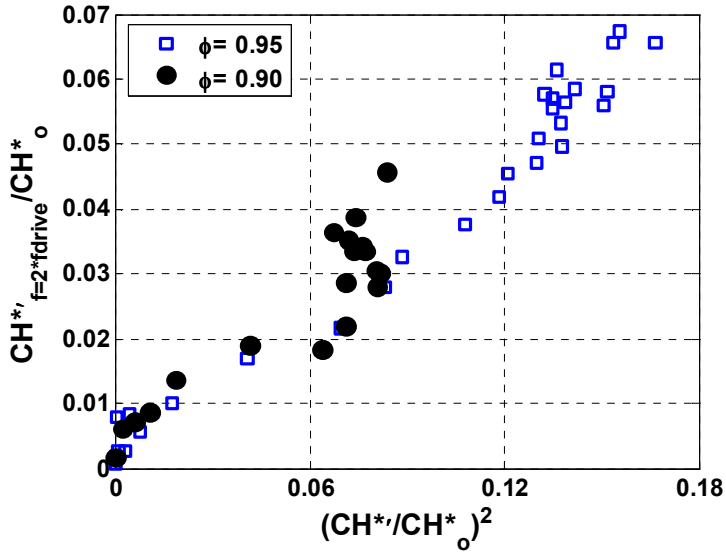

Figure 38. Dependence of CH* 1st harmonic on the square of CH* fundamental at two equivalence ratios (f_{drive} = 300 Hz)

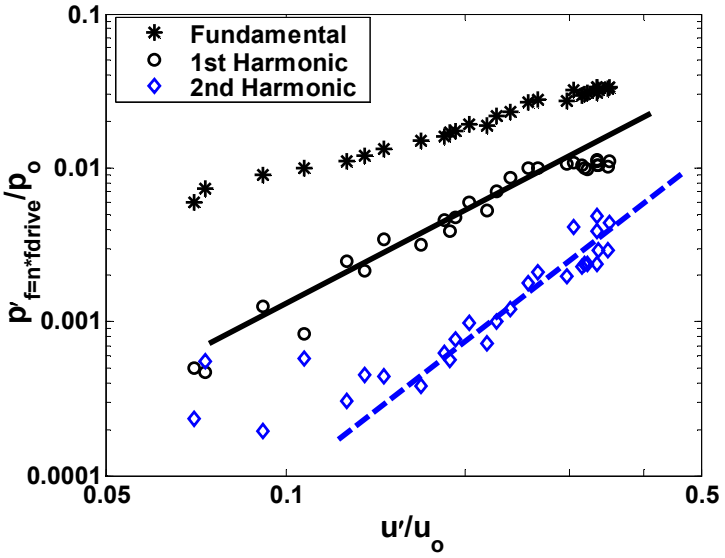

Figure 39. Dependence of pressure harmonic amplitude on velocity oscillation amplitude (f_{drive} = 290 Hz, ϕ = 0.95). Quadratic trend indicated by the solid line, cubic trend indicated by dashed line.

Figure 40 presents the phase angle between the CH* chemiluminescence fundamental and first harmonic. While the overall phase dependence upon disturbance amplitude is approximately linear at each driving frequency, the amplitude dependence of the phase angle slope switches signs between 290 and 300 Hz (not shown). Furthermore, there is substantial amplitude dependence of this phase angle, as it changes by over 800 degrees.

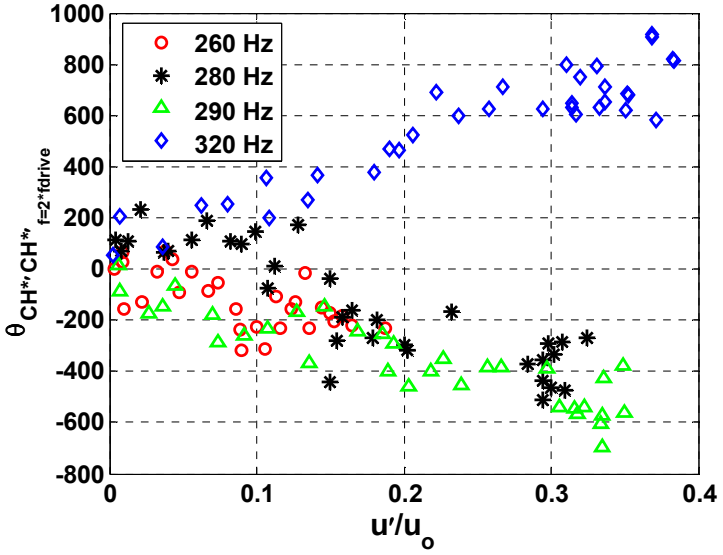

Figure 40. Dependence of CH* chemiluminescence fundamental-1st harmonic phase angle on velocity oscillation amplitude at several driving frequencies ($\phi = 0.95$). Uncertainty in phase angle for $u'/u_o < 0.05$, $\Delta\theta \sim 30°$; for $u'/u_o > 0.05$, $\Delta\theta \sim 3°$.

4.6.2 Subharmonic Characterization

Consider next the CH* subharmonic characteristics; i.e. $CH^*_{f=fdrive/2}$. Its amplitude is strongly affected by saturation of the fundamental, as shown in Figure 41(a).

This is in contrast to the first harmonic's characteristics, where no general trends could be determined. Also, the subharmonic amplitudes do not exhibit a power law dependence upon the fundamental. Consider first the 260 Hz result, where the transfer function remains linear throughout the entire amplitude range, see Figure 33(a). Figure 41(a) shows that the $CH^{*\prime}_{f=fdrive/2}/CH^{*\prime}$ ratio remains nearly zero for this driving frequency. In contrast, for the 280 and 320 Hz cases, the magnitude of the subharmonic also has negligible amplitudes at most points, except for a sharp increase at certain velocity amplitudes. At these points, the coherence between the subharmonic and fundamental has values of ~ 0.99; over the rest of the velocity oscillation amplitude range, it is substantially lower. At the same point in the 280 Hz case, there is no such peak in the subharmonic of the pressure signal, see Figure 41(b). The velocity subharmonics are not shown because of their low coherence in this frequency range (~ 130-160 Hz), as can be anticipated from Figure 27(b). The 290 Hz case (not shown) exhibits similar behavior compared to the 280 Hz case.

Similar results are found when analyzing the effect of equivalence ratio in Figure 42. As above, the chemiluminescence subharmonic increases in amplitude at the saturation point. The three cases where saturation was found (i.e., $\phi < 0.95$) have distinct peaks in the same velocity amplitude range where saturation is observed. Note also that the peak subharmonic amplitude increases with decreasing equivalence ratio.

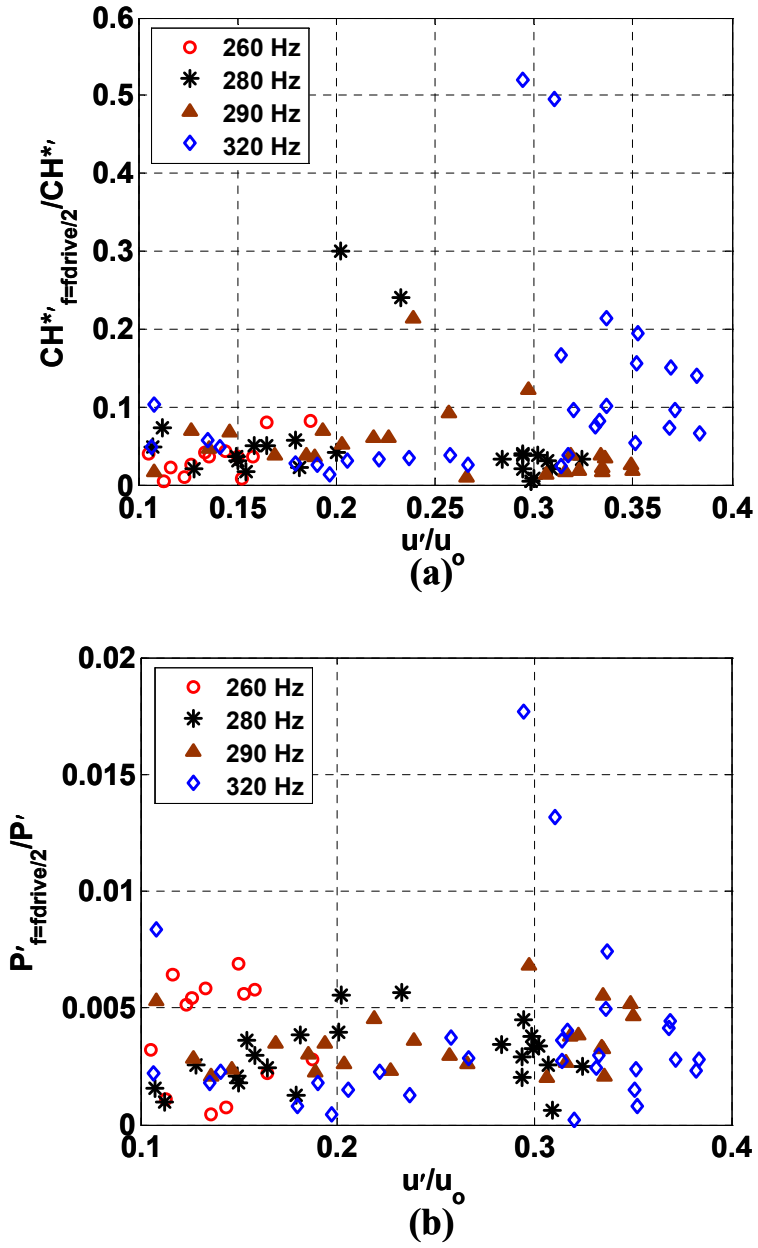

Figure 41: Dependence of (a) CH* and (b) pressure subharmonic amplitude on velocity oscillation amplitude at several driving frequencies (ϕ = 0.95)

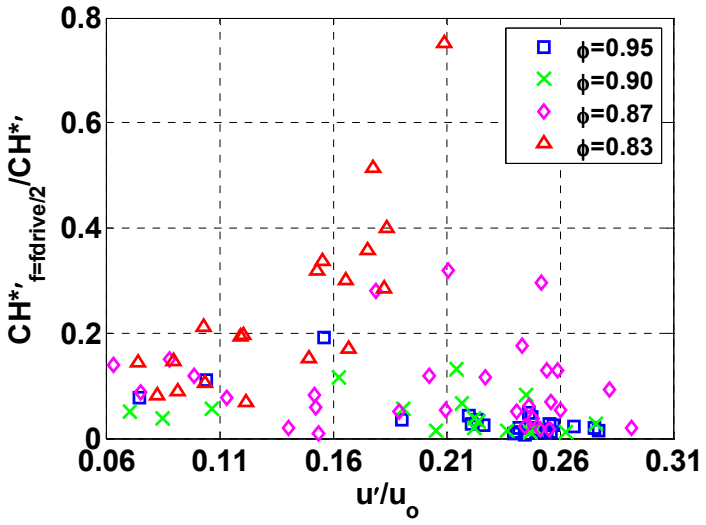

Figure 42: Dependence of CH* chemiluminescence subharmonic on fundamental versus velocity oscillation amplitude at several equivalence ratios (f_{drive} = 300 Hz)

4.7 Discussion

Returning to the subharmonic data, the presence of these peaks appears to be a necessary, but not sufficient condition, for saturation of the transfer function at the fundamental. Therefore, the subharmonic response influences this behavior. This conjecture is supported by the fact that saturation never occurs when this peak is not present in the chemiluminescence subharmonic. This peak does not always signify saturation, however, as seen in the 320 Hz case. In this case, however, the peak in the chemiluminescence subharmonic at 320 Hz in Figure 41(a) is matched by a similar peak in the pressure subharmonic in Figure 41(b). Further analysis of this subharmonic behavior indicates that the peak occurs near the point where the gain of the transfer function begins to decrease. This is clearly shown in Figure 43 which plots the dependence of both the *CH** subharmonic and the change in gain of the transfer function, G_{uE}, on the velocity oscillation amplitude. The velocity amplitude at which the

subharmonic peaks roughly coincides with the velocity amplitude where the transfer function gain begins to decrease for both f_{drive} = 280 and 290 Hz.

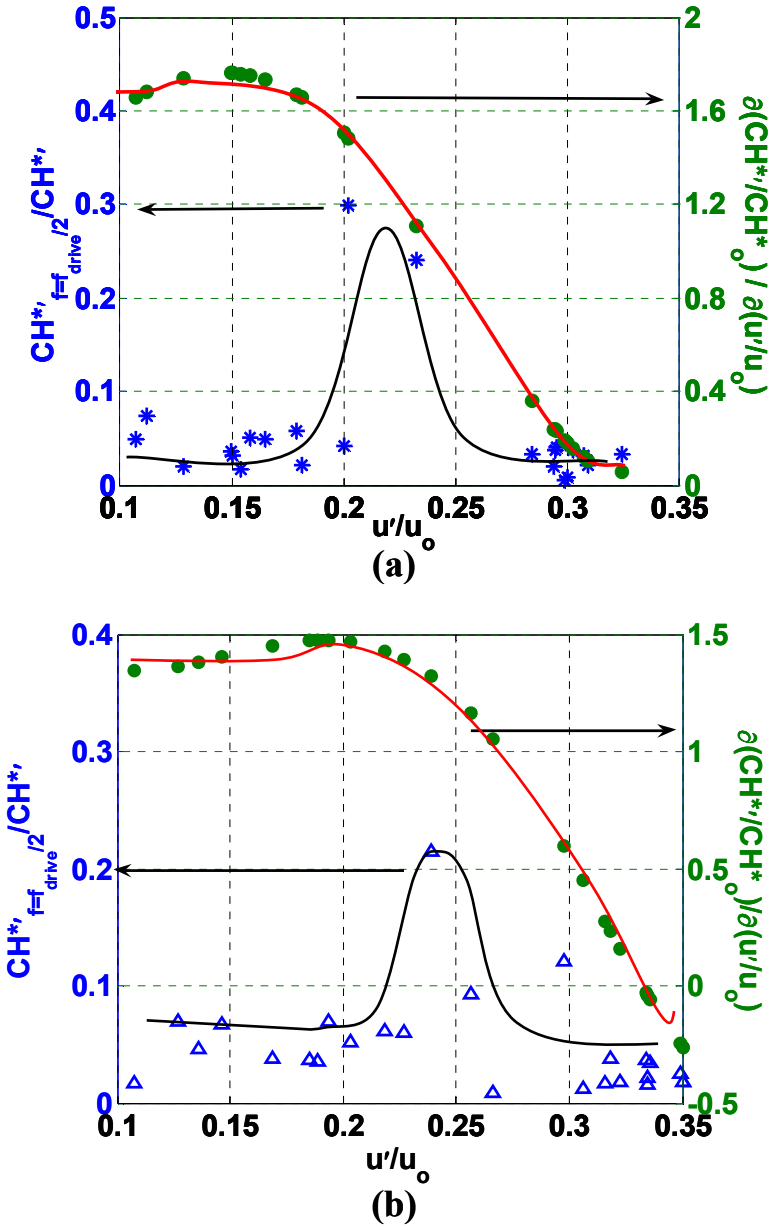

Figure 43. Dependence of CH* subharmonic and transfer function change in gain on velocity oscillation amplitude for (a) f_{drive} = 280 Hz and (b) f_{drive} = 290 Hz (ϕ = 0.95)

The subharmonic's dependence upon amplitude is similar to the measurements by Baillot and co-workers in a laminar, Bunsen flame [38,63,64]. At intermediate forcing amplitudes, Bourehla & Baillot, in some cases, observed a subharmonic flame response [38]. Analysis of this response showed that the subharmonic amplitude increased and the fundamental amplitude decreased as one went downstream from the burner lip. That is, the flame base responded more at the fundamental frequency and the flame tip responded more at the subharmonic frequency. In all cases, the subharmonic response disappeared at the highest forcing amplitudes, and the flame exhibited hemispherical behavior as mentioned in the literature review in Chapter 2. The amplitude of oscillation where this subharmonic response is observed is quantified in more detail by Baillot *et al.* [63] and Durox *et al.* [64]. Specifically, depending on burner configuration, cellular structures appeared on the flame when forcing amplitudes reached u'/S_L values between 5.6 and 7.05. For smaller diameter burners, the presence of these subharmonic cellular structures was transient in nature and did not persist at higher driving amplitudes [63]. For larger burners, the subharmonic behavior persisted after the critical value of driving was achieved [64]. At the equivalence ratios utilized in this study (ϕ = 0.83 – 0.95), the laminar flame speed for natural gas-air flames ranges between approximately 30 – 40 cm/s. At the point of saturation, the velocity values (u'/u_o) range between 0.2 and 0.3. Since the mean velocity in all of these tests is held constant at roughly 11 m/s, the corresponding u'/S_L values are approximately 7.3 – 8.1 at the point where the subharmonic response occurs, consistent with the values observed in the laminar, Bunsen flame studies outlined above. In addition, the lack of subharmonic response at the highest disturbance amplitudes is also consistent with these previous studies [63].

This phenomenon appears to be manifestation of the so-called "parametric instability", where pulsating cellular structures appear on the flame, which oscillate at half the instability frequency [65-68]. Analogous to Bourehla and Baillot's result, these studies in nominally flat flames found the subharmonic response only at intermediate amplitudes; at very high amplitudes the flame response was highly chaotic and disordered. This instability is produced by the unsteady acceleration of the flame front by the velocity field, which separates two regions of differing densities, coupling with the three-dimensional flame dynamics. With increased amplitudes, the structures lose their well-defined nature and break up into disordered, turbulent wrinkles. This period doubling was recognized by Markstein as indicative of a parametrically pumped oscillator that can be described by an equation of the form [69]:

$$A\frac{d^2y(k,t)}{dt^2}+B\frac{dy(k,t)}{dt}+\left[C_o-C_1\cos(\omega t)\right]y(k,t)=0 \qquad (4.10)$$

where A, B, C are coefficients defined by Markstein, k is the wave number of the perturbation, and ω is the frequency of the imposed oscillations. The damping coefficient, B, is always positive, but the coefficient C_o is negative if the nominal planar flame front is unstable. Such an equation has the well known property that sub-harmonic oscillations (i.e., $\omega/2$) are excited for large enough parametric disturbance amplitudes, C_1.

This is the first observation, to the author's knowledge, of the possible presence of the parametric instability in a swirl-stabilized turbulent flame. Vaezi and Aldredge [67,68] have performed the only experimental work analyzing the parametric instability

during turbulent flame propagation. They found substantial enhancement of axial and circumferential velocity fluctuations as a result of the parametric instability for all levels of pre-ignition turbulence. Also, the magnitude of amplification decreased with increasing Reynolds number. In our experiments, the Reynolds number defined by the premixer exit diameter was substantially larger than those investigated by Vaezi & Aldredge [67,68]. Analogous to their results, no sudden visible changes in the flame position, length, or shape were noted before saturation of the transfer function occurred which indicate that turbulent flame speed enhancement was minimal.

Therefore, one of the key conclusions of this study is that nonlinear interaction between the flow forcing and the chemiluminescence subharmonic (possibly through a manifestation of the parametric instability) is responsible for saturation of the flame response. The presence of the parametric instability is defined by the jump in amplitude of oscillations at half the driving frequency at certain disturbance amplitude values. This jump in subharmonic amplitude occurs at essentially the same value as that at which saturation occurs. Furthermore, subharmonic oscillations are always present in cases where saturation of the fundamental occurs. To the author's knowledge, this observation of the parametric instability is the first in a turbulent, swirl-stabilized flame.

In addition, however, there are other potential mechanisms which may also be present. These include local extinction of the flame and flame sheet kinematics. For example, increased amplitudes of oscillation lead to increased flame strain that could cause local flame extinction events. Increased extinction could, in turn, result in decreased heat release response. This mechanism could be responsible for the decreasing mean chemiluminescence levels upon perturbation amplitude seen in some test cases.

Additionally, flame sheet kinematics also may be important. While their significance was alluded to above in the context of the parametric flame instability (i.e., fluctuating flame position effects), they may play additional roles through nonlinear dependencies of flame area destruction with disturbance amplitude. For example, large amplitude corrugations of the flame may be consumed by flame propagation faster than small amplitude perturbations, as emphasized by Lieuwen [31] based on theoretical considerations and very recently, by Balachandran *et al.* [35], based on experimental imaging studies.

While it is not possible to conclusively determine the relative roles of all potential mechanisms of nonlinearity, some mechanisms, which have been suggested as potentially significant, can be eliminated:

"Global" Extinction – This is the mechanism proposed by Dowling [23] and Poinsot *et al.* [25] which follows from the simple observation that the instantaneous heat release cannot go negative, thus limiting the chemiluminescence fluctuations to 100% of the mean value. These data indicate saturation at substantially lower amplitudes, however, implying that this mechanism is not significant in this combustor.

Chemical Kinetics – Reaction rates depend upon pressure and temperature in a nonlinear manner; e.g. see Ref. [28]. These nonlinearities will apparently become significant when the fluctuating pressure achieves amplitudes on the order of its mean value. This mechanism does not appear likely here, however, as nonlinearity occurs at p'/p_o values of ~ 2%.

Equivalence ratio oscillations – The nonlinear dependence of the equivalence ratio amplitude and heat release response discussed by Peracchio & Proscia [24] and

Lieuwen [7] is not important here, as the fuel/air mixture had a constant composition. As such, though it is not possible to comment on the magnitude of these types of nonlinearities in situations where they are present, the data presented here indicate that other flame processes also cause nonlinearities in flame response. However, mixing between the reactants and products due to the enhanced recirculation associated with the swirling flow could impact these measurements. This is difficult to speculate further on because no imaging of the flame was performed in this part of the thesis.

Flame holding – The many data indicating a linear CH* response all the way to blowoff indicate that nonlinearities due to marginal flame holding, proposed by Dowling [27] are probably not important.

From these data, several conclusions can be drawn regarding the nonlinear response of the unsteady heat release to flow perturbations. The role of heat release nonlinearities due to the nonlinear combustion process has been illustrated experimentally. However, the amplitude relationship between the pressure/velocity and heat release saturates at sufficiently high forcing levels at certain frequencies and equivalence ratios, but remains linear at others due to flame blowout. This result indicates the need for an improved flame-holder design in future experiments to probe higher velocity disturbance amplitude ranges. Also, substantial amplitude dependence of the CH* phase was found at all driving frequencies and equivalence ratios. These results suggest that heat release-acoustic nonlinearities in both gain and phase may play comparable roles in swirling, premixed combustors.

The higher harmonics generally exhibited a power law dependence upon disturbance amplitude. However, these characteristics stayed the same in some cases and

changed substantially in others, at amplitudes above and below the point where saturation occurs. No general conclusions were drawn for the cases where either behavior occurred. The chemiluminescence subharmonic is negligible at disturbance amplitudes well above and below the saturation amplitude of the fundamental. Over the same velocity amplitude range over which the transfer function changes from linear to saturating, the subharmonic generally has appreciable amplitudes. The excitation of the chemiluminescence subharmonic, possibly through a manifestation of the parametric instability, is seen to be a controlling factor in the saturation of the flame transfer function in this combustor.

CHAPTER 5

NONLINEAR FLAME RESPONSE TO FORCED ACOUSTIC OSCILLATIONS IN ATMOSPHERIC SWIRL-STABILIZED BURNER

This chapter describes further parametric studies on the nonlinear flame response to forced acoustic perturbations. Specifically, the effects of driving frequency and Reynolds number are studied at fixed equivalence ratio. The frequency range investigated is greatly expanded from the results presented in Chapter 4. Sections 5.1 and 5.2 describe the experimental conditions investigated and the coherence characteristics of the measured quantities. Section 5.3 describes the parametric study which investigated the nonlinear flame response to large amplitude oscillations over a broad frequency range and three different flow rates. The higher harmonic dependence of the flow and heat release measurements is detailed in Section 5.4. Detailed response of the flame over the entire range of disturbance amplitudes was investigated and described in Section 5.5 at two operating conditions using OH PLIF. Section 5.6 then describes the governing mechanisms controlling the nonlinear flame response to large amplitude acoustic disturbances for these two operating conditions.

5.1 Experimental Conditions

Results were obtained by externally driving oscillations in the combustor with varying amplitude at a fixed frequency. Simultaneous measurements of pressure,

velocity, and chemiluminescence were taken. For all cases, the combustor was quite stable in the absence of driving ($p'/p_o < 0.06\%$, $u'/u_o < 0.6\%$). All tests in this chapter were performed at a fixed equivalence ratio of 0.8. The flow rate regime investigated ranged from Reynolds numbers of Re_D= 21,000 – 43,000 (based on premixer exit diameter) corresponding to average premixer exit plane velocities of 22 – 43 m/s. A detailed list of the operating conditions is given below in Table 2. Simultaneous OH* and CH* measurements were taken and the gain and phase of each measurement were quite similar.

Table 2. Operating conditions for linear/nonlinear flame response studies in atmospheric, swirl-stabilized burner

Parameter	Nonlinear Studies
Mean Premixer Velocity, u_o, m/s	22, 30, 43
Driving Frequency, f_{drive}, Hz	100-420
Equivalence Ratio, ϕ	0.8

5.2 Coherence Characteristics

The results presented in Chapter 4 were obtained for varying driving frequencies and equivalence ratios, but at constant flowrate because of reduced coherence characteristics between the velocity oscillations measured with the hot-film probe and the chemiluminescence fluctuations. Therefore, as mentioned in Chapter 3, the two microphone technique was utilized in this set of experiments for two reasons: 1)

increased coherence values between the velocity and chemiluminescence measurements for increasing Reynolds number and 2) the ability to determine the velocity oscillation amplitude and phase very close to the burner exit, instead of upstream of the swirler location as was the case in Chapter 4, from which a separate velocity transfer function between the inlet section and the burner lip needed to be calculated and validated experimentally in offline experiments.

Figure 44 illustrates the advantages of using the two microphone technique for increasing coherence values. The coherence values for increasing Reynolds number is presented in Figure 44 at a driving frequency of 410 Hz and $\phi = 0.80$. For the entire disturbance amplitude range, the coherence values between the velocity and chemiluminescence oscillations are greater than 0.9. The uncertainties in these coherence values were calculated using Eq. (4.2) with $n = 8$ ensembles. Since the coherence values are all quite large, the dependence of the heat release oscillations on the velocity fluctuations can be more accurately calculated. These increased values of the coherence over the Reynolds number range investigated are due to the fact that the pressure measurements used to calculate the velocity oscillations are not as affected by turbulence fluctuations and background noise compared to a hot-film or hot-wire probe. Still, it is seen that the lowest coherence values are obtained for the highest flow rate due to increased turbulence levels. In addition, Figure 44 plots the coherence values at f_{drive} = 410 Hz, which generates large amplitude oscillations as noted in Figure 13.

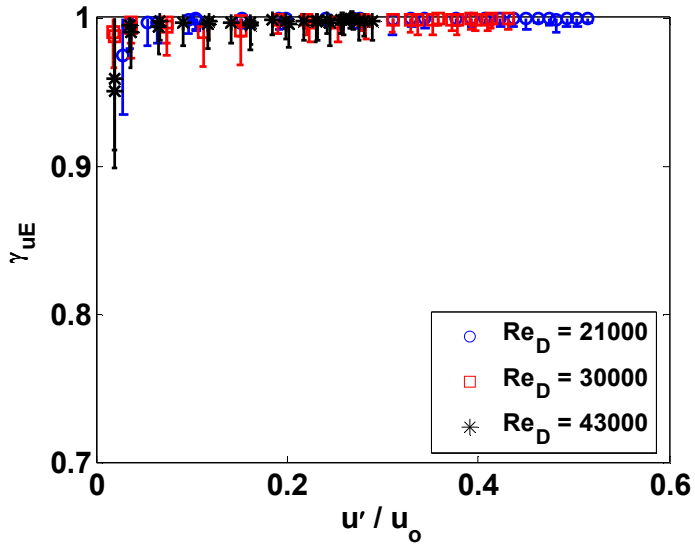

Figure 44. Dependence of coherence between velocity and CH* chemiluminescence fluctuations on amplitude of velocity oscillations for three different Reynolds numbers (f_{drive} = 410 Hz, ϕ = 0.80).

5.3 Nonlinear Flame Response

5.3.1 Nonlinear Flame Response – Driving Frequency

A typical transfer function between simultaneously measured CH* chemiluminescence and velocity oscillations is shown in Figure 45(a) at a Reynolds number of 21000 and equivalence ratio of 0.8. For low forcing amplitudes, Figure 45 shows that the CH* chemiluminescence increases with perturbation amplitude in a linear manner. At large velocity amplitudes, the CH* chemiluminescence rapidly saturates at values of CH*'/CH*$_o$ of ~0.45. These velocity and CH* values where saturation occurs are roughly similar with the results presented in Chapter 4. In addition, the rapid transition from linear to nonlinear behavior is consistent with the results in Chapter 4 as well. Furthermore, this result confirms that global extinction, where oscillating heat release amplitudes reach 100% of the mean, proposed theoretically by Dowling [23], is

not an important mechanism at this condition. Figure 45(b) presents the corresponding u'-CH*' phase relationship. The phase relationship exhibits a complex amplitude dependence on the amplitude of velocity oscillations. The phase angle changes by nearly 50 degrees while the transfer function remains linear. The sharp decrease in phase angle at u'/u_o ~0.45 occurs well after the $CH^{*\prime}/CH^*_o$ value saturates. Note that this decrease in phase angle occurs at similar u'/u_o values as the slight decrease in the chemiluminescence values after saturation occurs.

Figure 46(a) presents transfer function results for driving frequencies between 130-150 Hz at a Reynolds number of 21000. Figure 46 illustrates that the transfer function at 130 Hz and 140 Hz remains linear up to $CH^{*\prime}/CH^*_o$ values near 0.95 before saturating. Additional measurements presented later in this chapter indicate that this technique is valid for such large values of $CH^{*\prime}/CH^*_o$ values. Thus, the saturation amplitude here is substantially higher than that in Figure 45, illustrating the substantial dependence of saturation amplitude upon flow conditions and disturbance frequency. Note that the saturation amplitude here is quite close to 100%, suggesting a global extinction type mechanism as proposed by Dowling [23].

Figure 46(b) presents the corresponding u'-CH*' phase. In contrast to the comparison between the saturation amplitudes between the cases at 210 and 130 Hz, the phase angle shapes for these two frequencies are roughly similar. The phase angle at these frequencies exhibits significant amplitude dependence at velocity oscillation amplitudes where the gain of the transfer function remains in the linear regime, again consistent with the results that were presented in Chapter 4. The phase angle is seen to almost saturate as well and remain relatively constant around 85-90 degrees over nearly

50% of the velocity amplitude range. In addition, due to the increased coherence values over the entire velocity amplitude range, the uncertainty in the phase angle is quite small ($\Delta\theta_{uE} < 5°$).

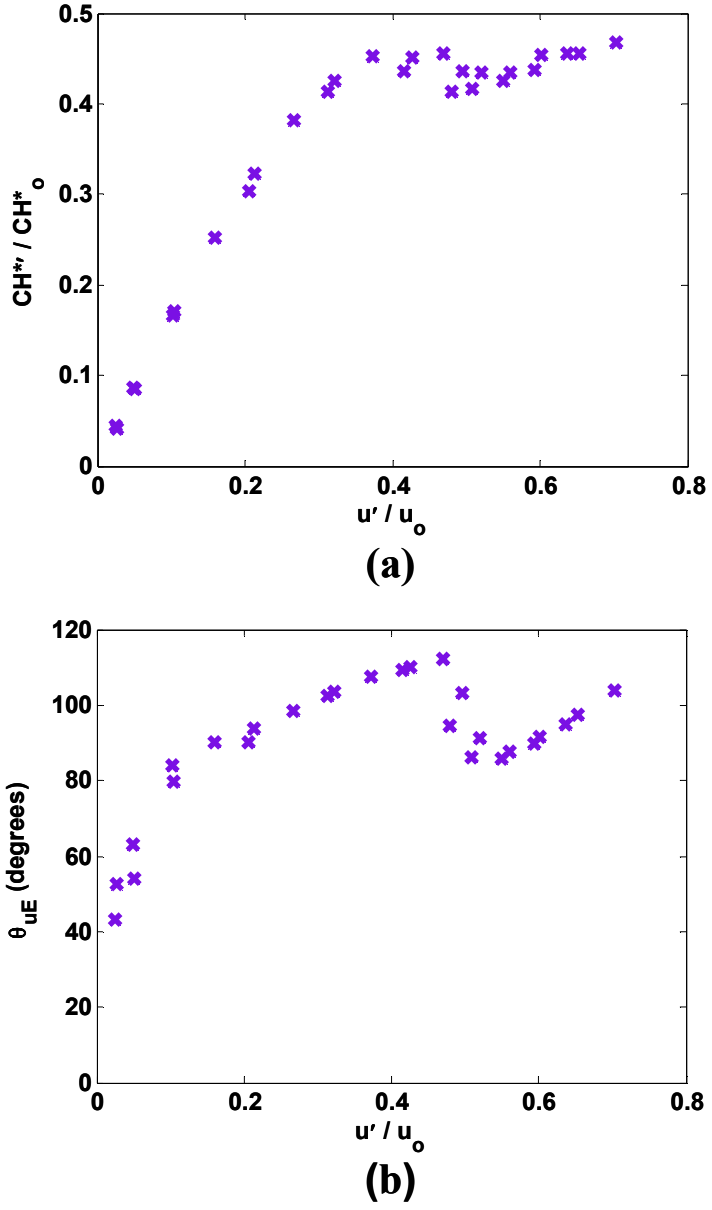

Figure 45. Dependence of (a) CH* oscillation amplitude and (b) u'-CH*' phase angle upon velocity oscillation amplitude (f_{drive} = 210 Hz, ϕ = 0.80, Re_D = 21000). CH* saturation amplitude = 0.45. Uncertainty in phase angle < 5°.

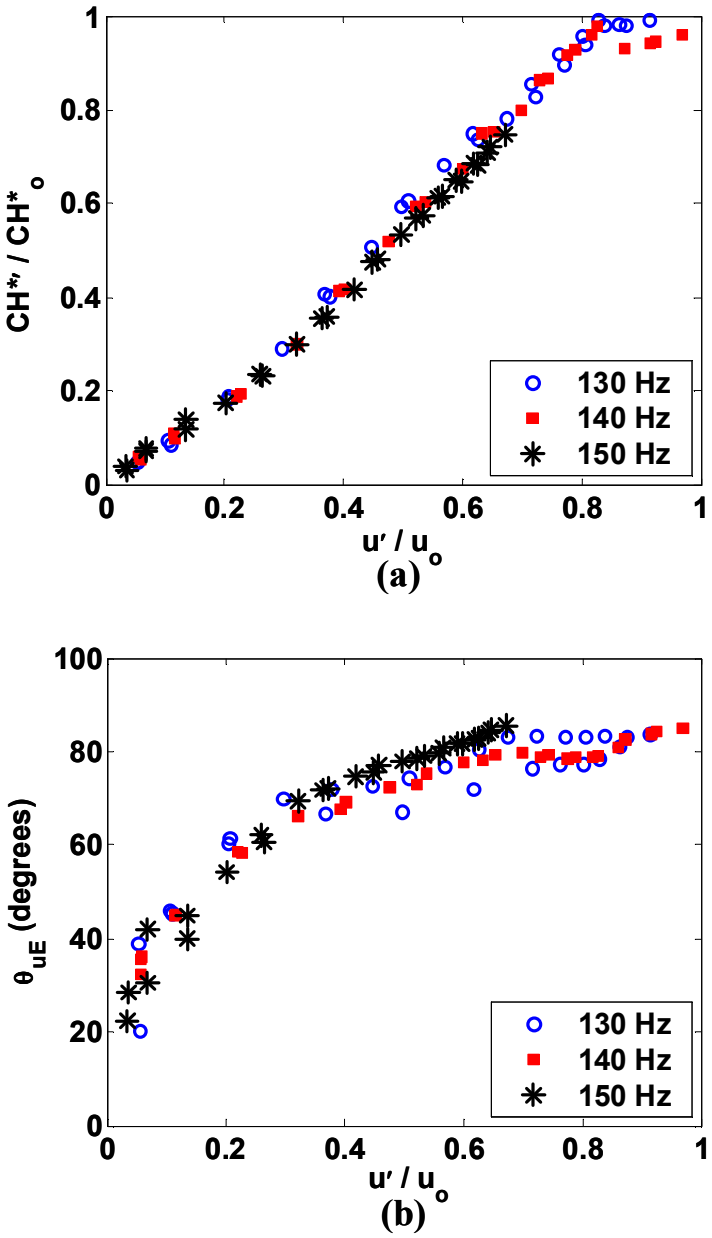

Figure 46: Dependence of (a) CH* oscillation amplitude and (b) u'-CH*' phase angle upon velocity oscillation amplitude, $\phi = 0.80$, $Re_D = 21000$. CH* saturation amplitude ~ 0.98. Uncertainty in phase angle < 5°.

Both Figure 45 and Figure 46 illustrate typical shapes of transfer functions that have been observed experimentally and proposed theoretically. For low velocity amplitudes, the corresponding heat release oscillations increase linearly. At the largest velocity amplitudes, the heat release fluctuations saturate. However, more complex amplitude dependencies were observed at other conditions. Figure 47 shows two such cases, obtained at 340 and 410 Hz. Both curves show that the CH* chemiluminescence increases linearly with increasing velocity oscillation amplitudes at low values of driving. At 340 Hz, the CH* oscillation amplitude begins to saturate at values around 0.65-0.7 of the mean value. However, instead of remaining nearly constant, with further increases in excitation amplitude, the response increases again. In a similar manner, for 410 Hz, Figure 47 shows that the transfer function begins to saturate at a $CH^{*\prime}/CH^{*}_{o}$ value of 0.35. Similar to the 340 Hz case, the flame response begins to increase again before saturating again at $CH^{*\prime}/CH^{*}_{o}$ value of nearly 0.6. This trend is similar to the experimental results of Balachandran *et al.* for a bluff-body stabilized flame without swirl [35].

The corresponding u-CH* phase angles for f_{drive} = 340 and 410 Hz are presented in Figure 47(b). Both phase angles are change in value by 30° - 40° over the velocity disturbance amplitude range and both are slightly affected when saturation occurs. The phase angle for f_{drive} = 340 Hz increases in value for low velocity oscillation amplitudes before peaking at u'/u_o = 0.35 and decreases from that point. The point of the peak phase angle roughly coincides with the initial saturation point of the transfer function. The phase angle for f_{drive} = 410 Hz, on the other hand, shows a slight change in amplitude dependence near the first saturation point as well. The phase angle does not decrease

after this point, however, but increases instead. Further discussion on these differences can be found later in this chapter.

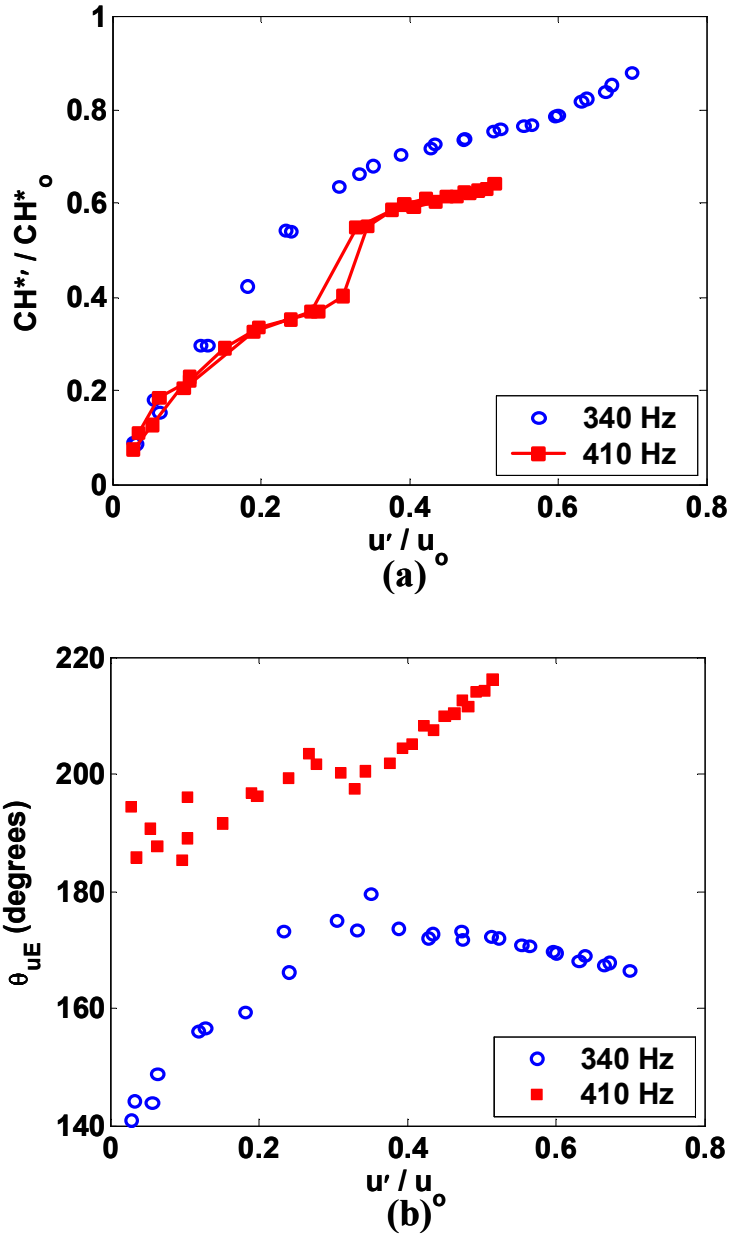

Figure 47. Dependence of (a) CH* oscillation amplitude and (b) u-CH* phase angle upon amplitude of velocity oscillations for f_{drive} = 340 Hz and 410 Hz (Re_D = 21000, ϕ = 0.80). Uncertainty in phase angle < 5°.

5.3.2 Nonlinear Flame Response – Reynolds number effects

The transfer functions shown and described in Figure 45 - Figure 47 illustrate the typical behavior of the flame response at the lowest Reynolds number investigated, Re_D= 21000; see Appendix C for transfer functions and phase angles for the entire frequency range investigated at this flow rate. At the two higher flowrates, more complex behavior was observed. For instance, Figure 48 presents the u'-CH*' transfer function for 160-180 Hz at a Reynolds number of 30000 and equivalence ratio = 0.8. For these three cases, after an initial linear increase in heat release oscillations, there is a sharp decrease in these values, followed by an increase. This sharp decrease in the gain of the transfer function is also manifested in the corresponding phase between the velocity and chemiluminescence oscillations. Figure 48(b) shows the phase angle at f_{drive}= 170 Hz drops considerably (over 100 degrees) between normalized velocity oscillation amplitudes of 0.1 and 0.2. After this drop, the phase angle remains constant around 80 degrees, at similar values as the 130-150 Hz cases shown in Figure 46. Furthermore, as the frequency is increased the decrease in the phase angle becomes more pronounced. For f_{drive} = 180 Hz, the velocity amplitude dependence of the phase angle between the velocity and chemiluminescence oscillations nearly becomes discontinuous.

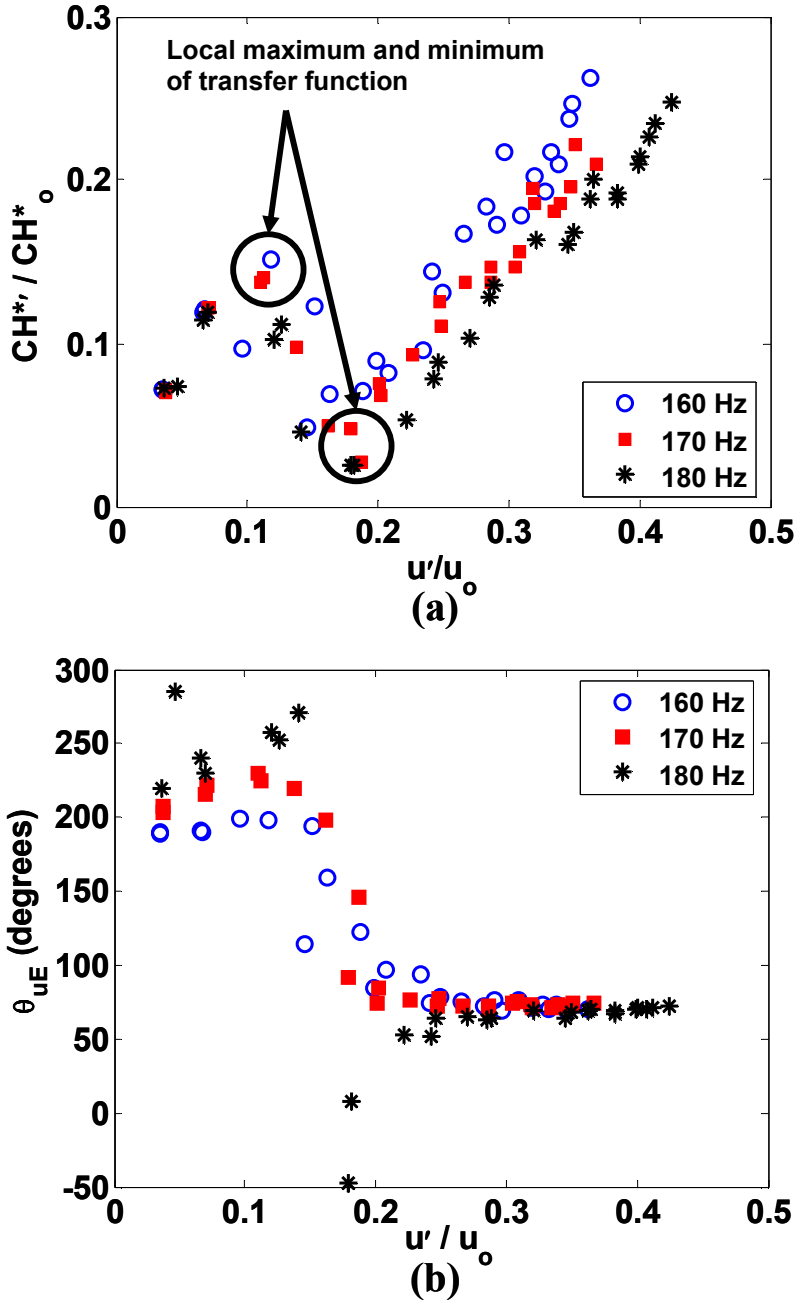

Figure 48. Dependence of (a) CH* oscillation amplitude and (b) *u'-CH*'* phase angle upon amplitude of velocity oscillations for f_{drive} = 160-180 Hz (Re_D = 30000, ϕ = 0.80). Uncertainty in phase angle < 5°.

This shift in transfer function behavior, i.e. the change in shape of the transfer function itself appears to be a function of frequency and Reynolds number. As shown in the sequence of graphs in Figure 49, the dependence of the flame response changes significantly. Figure 49 shows the dependence of the CH* chemiluminescence on the velocity oscillation amplitude for f_{drive} = 160-180 Hz for Re_D = 43000. The behavior of the transfer functions at these frequencies mirror those depicted in Figure 45 and Figure 46, that of simple saturation. As driving frequency is increased, however, the transfer function exhibits a local maximum near u'/u_o values of 0.1-0.15 followed by a decrease in value, similar to that shown in Figure 48. The degree of decrease depends on the driving frequency. The local minima in these figures occur at roughly u'/u_o values of 0.2. This type of behavior is seen for a driving frequency range of f_{drive} = 190 Hz – 320 Hz; see Figure 49(b-f). From this point the classical (simple saturation) transfer function shape is restored; see Figure 49(g).

Similar behavior is seen for the middle flow rate investigated, Re_D = 30000. These results are shown in Appendix C. For Re_D = 30000, however, this transitional behavior is observed between f_{drive} = 110 – 240 Hz. As mentioned above, this behavior does not appear to occur for the lowest flow rate investigated which indicates that this behavior is dependent on the mean velocity at the flameholder.. However, it appears from the two highest flow rates that as Reynolds number increases, the frequency range, where this behavior occurs, increases. If one takes the cases where the most discontinuous behavior occurs (f_{drive} = 180 for Re_D = 30000 (Appendix C) and 270 Hz for Re_D = 43000, respectively), the calculated Strouhal numbers ($St = \frac{2\pi f_{drive} D_{eff}}{u_o}$) are approximately the same (0.57 and 0.6, respectively).

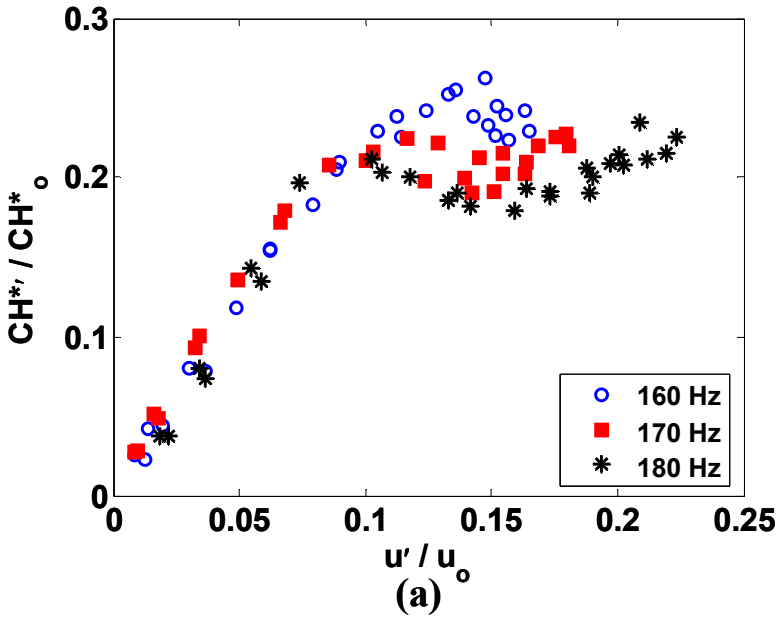

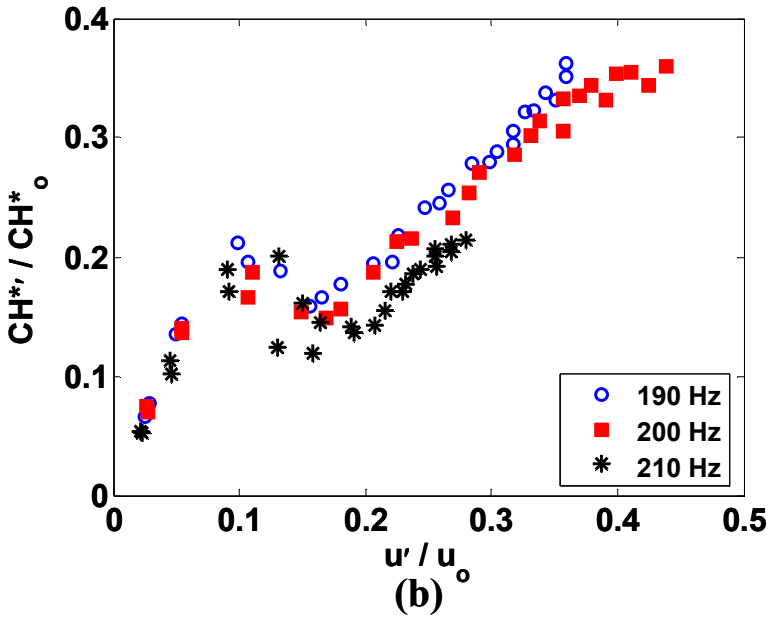

Figure 49(a)-(g) Dependence of CH* chemiluminescence on velocity oscillation amplitude for varying driving frequencies (Re_D = 43000, ϕ = 0.80)

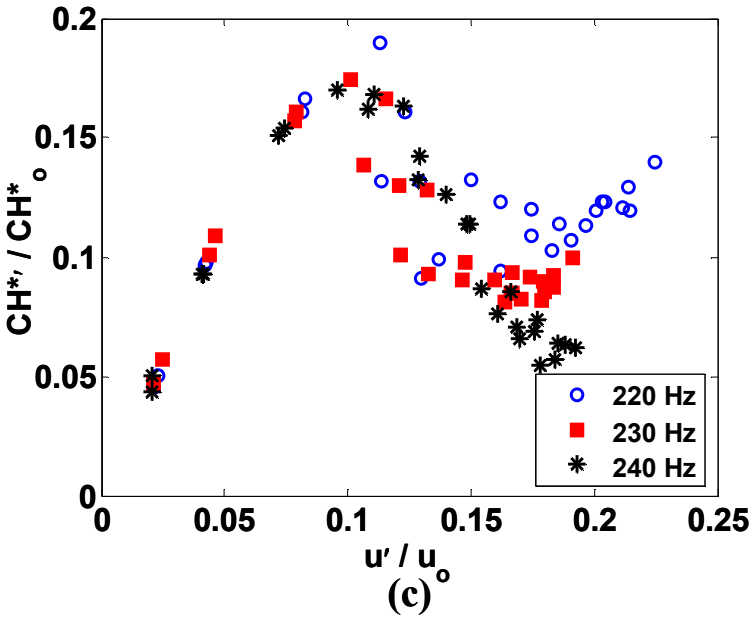

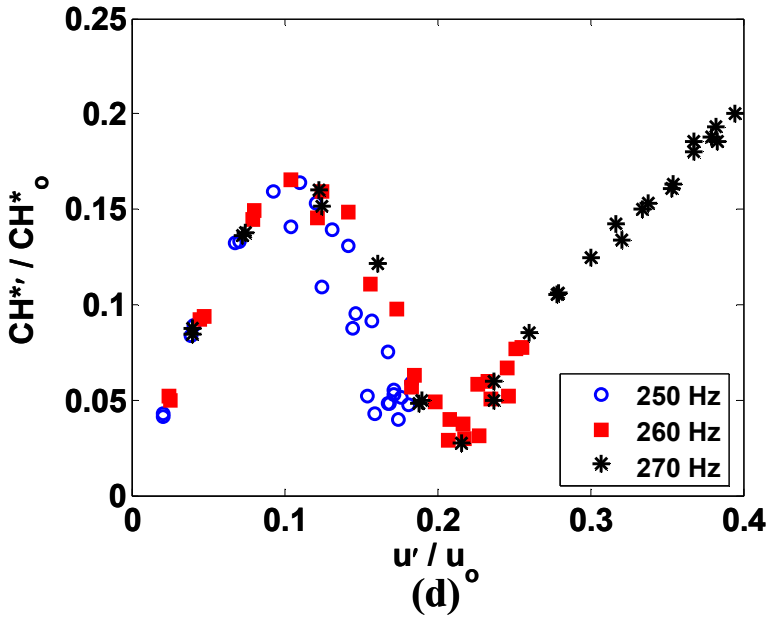

Figure 49 continued

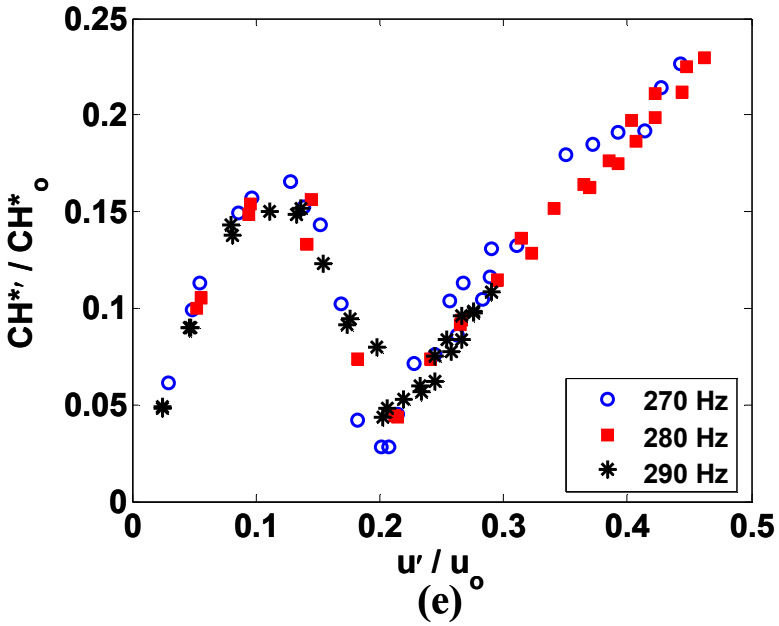
0.25
0.2
0.15
0.1
0.05
0
0
0.1
0.2
0.3
0.4
0.5
CH*′ / CH*o
u′ / uo
270 Hz
280 Hz
290 Hz

(e)

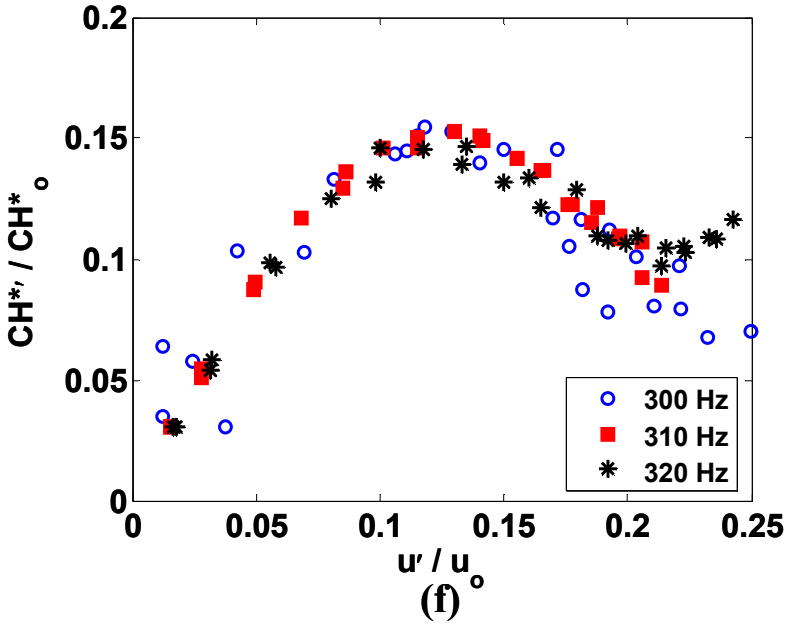
0.2
0.15
0.1
0.05
0
0
0.05
0.1
0.15
0.2
0.25
CH*′ / CH*o
u′ / uo
300 Hz
310 Hz
320 Hz

(f)

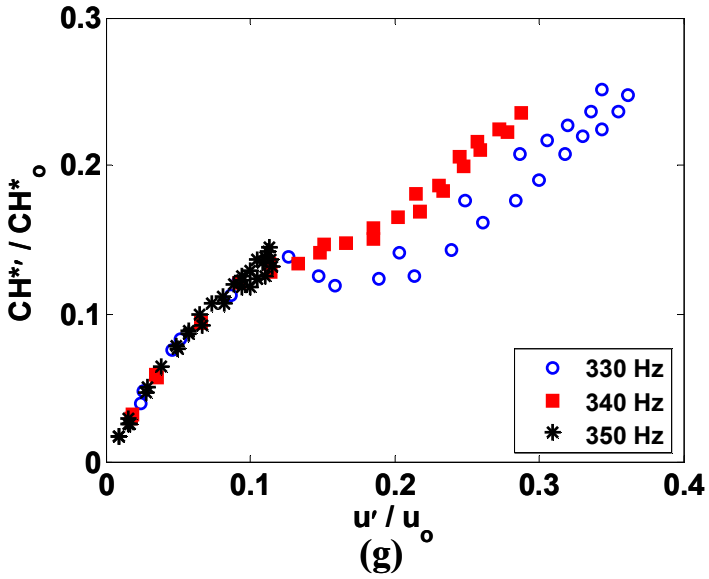

Figure 49 continued

This transition in the transfer function behavior indicates that the transfer function itself may be a superposition of two types of behaviors. Consider two transfer functions, representative of simple saturation and saw-tooth type, denoted as $H_1(A)$ and $H_2(A)$, as shown in Figure 50. A weighted superposition of these two functions gives a variety of shapes as shown in Figure 50. This superposition of the transfer function can be described qualitatively as:

$$H(A) = S_s H_1(A) + S_W H_2(A) \tag{5.1}$$

where the $S_s + S_w = 1$, and $H_1(A)$ and $H_2(A)$ represent the simple saturation and saw-tooth type transfer functions. For different values of S_s and S_w, the resulting driving curve, $H(A)$ becomes qualitatively different. Increases in S_w / S_s transform the curve,

$H(A)$, from simple saturation ($H_1(A)$) to more saw-tooth behavior ($H_2(A)$). Thus, instead of three independent transfer function behaviors as seen in Figure 45 – Figure 48, the transfer function is a weighted superposition of two behaviors that depends on the ratio of S_w/S_s. At the lowest Reynolds number, however, this behavior is found to be basically suppressed. 90% of the nonlinear cases at $Re_D = 21000$ are due to simple saturation of the transfer functions (see Appendix C).

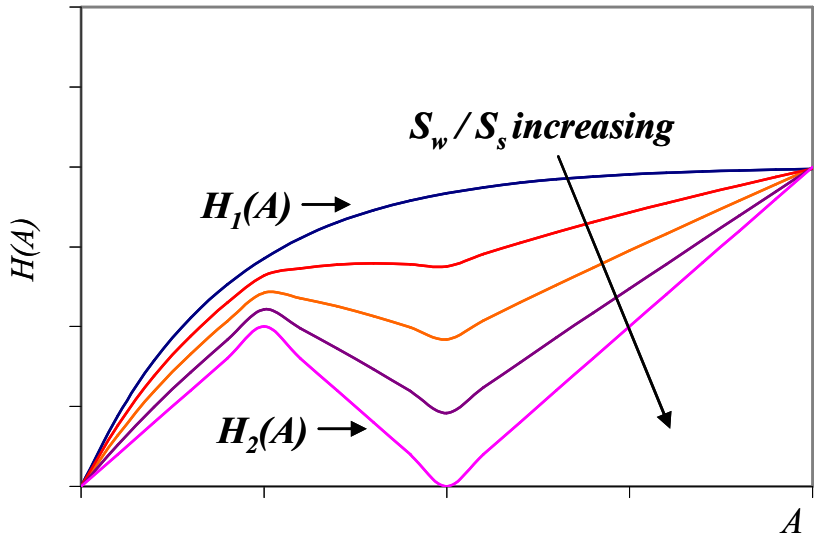

Figure 50. Family of curves, $H(A)$, illustrating transition between simple saturation and saw-tooth behavior for increasing S_w/S_s ratio.

For higher Reynolds numbers, there are frequency regimes where S_W becomes significant in value compared to S_s. These regimes were shown earlier to correlate reasonable well with Strouhal number. The corresponding u'/S_L values, where S_W is significant, are found to range from 15 – 21. These St (u'/S_L) values are smaller (larger)

than the minimum (maximum) values investigated in the experiments described in Chapter 4. This may explain why this phenomenon was not observed in those cases. A map of St and u'/S_L values where nonlinearity becomes evident in the measured transfer function is shown in Figure 51 for all cases in this thesis. This amplitude was defined as the point where the transfer function deviates from its linear value by more than 10-20%. The lower limit is set for cases such as those in Figure 46, where saturation occurs at nearly 100% of the mean chemiluminescence value. The upper limit is set for saturation/nonlinear behaviors that occur at values much less than 100% of the mean, e.g., Figure 47 and Figure 48. Figure 51 shows many points for Re_D = 30000 and 43000 are grouped near one another in St and u'/S_L space (see denoted region). In this region, S_w appears to be significant in amplitude compared to S_s. For the remainder of the points, either St or u'/S_L is larger in value. At these points, simple saturation ($S_W << S_s$) of the transfer function appears to occur, except for the circled points where this general trend does not hold (Re_D = 21000 and f_{drive} = 200, 340, and 410 Hz). Note that Chapter 4 results have low u'/S_L values, but much higher St values. Therefore, the simple saturation observed for those cases is generally consistent with the trend seen in this combustor. A comparison of the possible mechanisms governing this behavior is discussed further below.

Therefore, one of the key conclusions drawn from this parametric study was that the flame response characteristics are more varied and complex than a simple linear response regime followed by a saturation regime. However, one of the goals for the study was to parameterize the dependence of saturation amplitude upon operating conditions, frequencies, etc. In order to compile all the results into one graph, the

chemiluminescence amplitude at which nonlinearity in flame response becomes evident was determined, see Figure 52. At the lowest flow rate, Figure 52 indicates that the saturation amplitude varies with frequency by a factor of almost five. This frequency sensitivity is diminished at the higher flow rates. At the highest Reynolds number, the saturation amplitude is nearly constant over the frequency range investigated. Saturation at 100% chemiluminescence is only seen for the lowest flow rate. The results presented indicate that a variety of behaviors can exist in a single combustor.

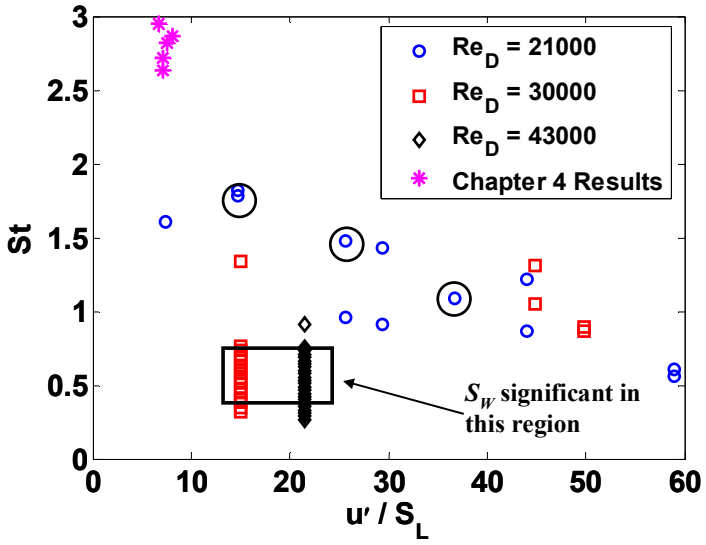

Figure 51. Map of u'/S_L vs. St at point of nonlinearity in measured transfer functions for all nonlinear flame response cases in this thesis. S_W has significant value compared to S_s in denoted region. Circled points (for $Re_D = 21000$) indicate the remainder of cases where S_w is significant in amplitude compared to S_s.

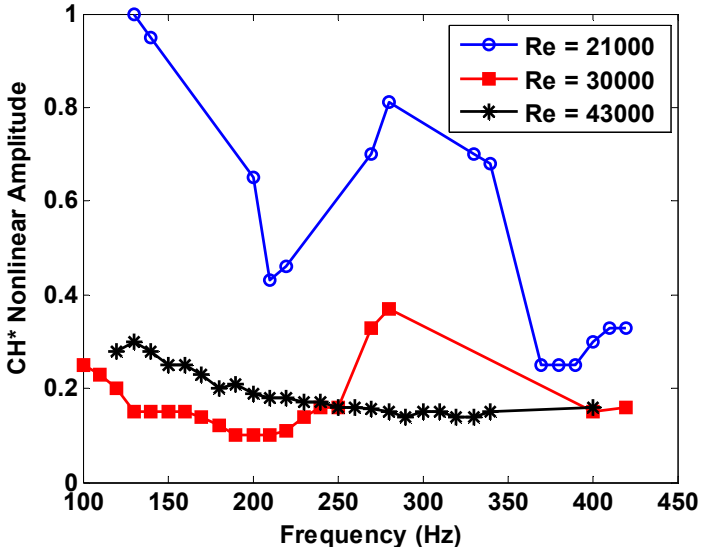

Figure 52. Dependence of CH* nonlinear amplitude on driving frequency as a function of Reynolds number (ϕ = 0.80).

5.4 Higher and Subharmonic Characteristics

This section discusses the higher harmonic and subharmonic characteristics of the flame dynamics under large amplitude forcing. The characteristics of the velocity/pressure harmonics are not discussed here due to the fact that turbulent fluctuations due to the presence of the swirler contaminate the higher frequency content of the pressure/velocity spectra.

Complex first harmonic behaviors were observed as shown in Figure 53. Figure 53 illustrates the 1st harmonic dependence on the fundamental for cases outlined in Figure 46 and Figure 47. It is clear that the dependence of the 1st harmonic is markedly different for these frequencies and that correlating the first harmonic behavior to the saturation behavior of the transfer function is difficult, as was concluded in Chapter 4. For these cases, the 1st harmonic amplitude reached approximately 20-25% of the fundamental

amplitude. After saturation occurs for these cases, the 1st harmonic either increases or decreases in amplitude depending on the driving frequency. By comparison, substantially different 1st harmonic characteristics were observed in the cases where the transfer function exhibited behavior such as in Figure 49(c-e). The 1st harmonic is seen to reach appreciable amplitudes compared to the fundamental. Analysis of the various spectra indicates that the point of decrease in flame response at the driving frequency corresponds to a shift in frequency of flame response to the first harmonic. This effect is discussed below.

Figure 54 presents the Fourier transform of the chemiluminescence and one pressure transducer for two cases: at the local maximum in the transfer function and the local minimum in the transfer function (circled in Figure 48) for f_{drive} = 180 Hz. Comparing the two chemiluminescence spectra, it is clear that the flame response shifts from the fundamental frequency to the 1st harmonic with an increase in driving from 10% velocity oscillation to 20% velocity oscillation. The pressure FFT, on the other hand (and thus the acoustic velocity) always responds at the fundamental, however, and increases with increased driving. Similar behavior has also been reported in bluff-body ethylene-air flames by Balachandran *et al*. [35]. For the conditions where this behavior was observed, the OH* chemiluminescence time series was observed to have increased harmonic content while the corresponding velocity only responded at the fundamental frequency. In addition, this response occurred at $u'/u_o \sim 0.55$ at $\phi = 0.67 - 0.70$. The corresponding u'/S_L values for Balachandran *et al.* were approximately 16 (based on ethylene-air laminar flame speed data [70]). Recall that for the results presented above for Re_D = 43000 and for the results above as well as in Appendix C for Re_D = 30000,

u'/S_L ranges between about 15 – 21. However, *St* values for Balachandran *et al.*'s results are much larger than those shown in Figure 51 for the sawtooth type behavior. Based on the hydraulic diameter of their burner, *St* was approximately 2.5 for their results where the modal shift occurred compared to values less than 1 in this combustor. The cause of these discrepancies is not clear, except that for lower flow rates (as seen for a few cases in this combustor for $Re_D = 21000$), it appears that these St-u'/S_L trends are less universal. A better characteristic length, such as flame length, may correlate these results better. Flame lengths were not obtained, however, in this study at these conditions. Another parameter may also scale these results closer together as well.

The amplitude of the 1st harmonic compared to the fundamental when this superposition occurs depends on how much the fundamental amplitude decreases (i.e., how dominant is S_W at that frequency). Figure 54 illustrated that the interactions between the first harmonic and fundamental can apparently occur and drastically influence the transfer function. At the point of lowest fundamental flame response, the first harmonic flame response dominates the spectral content of the chemiluminescence signal while the corresponding pressure/velocity spectra exhibit a dominant response at the fundamental frequency instead. Analysis of this behavior, over the entire velocity disturbance amplitudes and the range of frequencies/flow rates where seen, indicates that the 1st harmonic dominates the fundamental more and more as the transfer function exhibits more discontinuous behavior. Thus, the heat release oscillations are transferred more and more to the first harmonic.

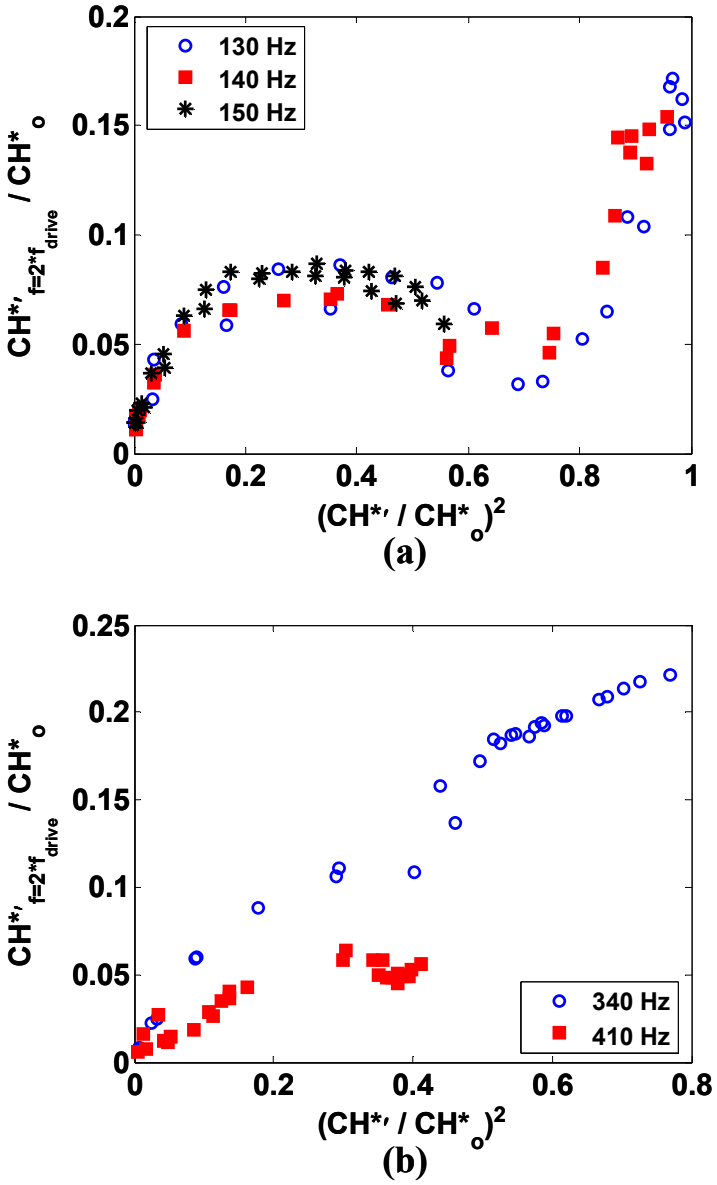

Figure 53. Dependence of CH* chemiluminescence 1st harmonic amplitude on CH* fundamental amplitude for varying driving frequencies (f_{drive} = 130-150, 340, 410 Hz, ϕ= 0.80).

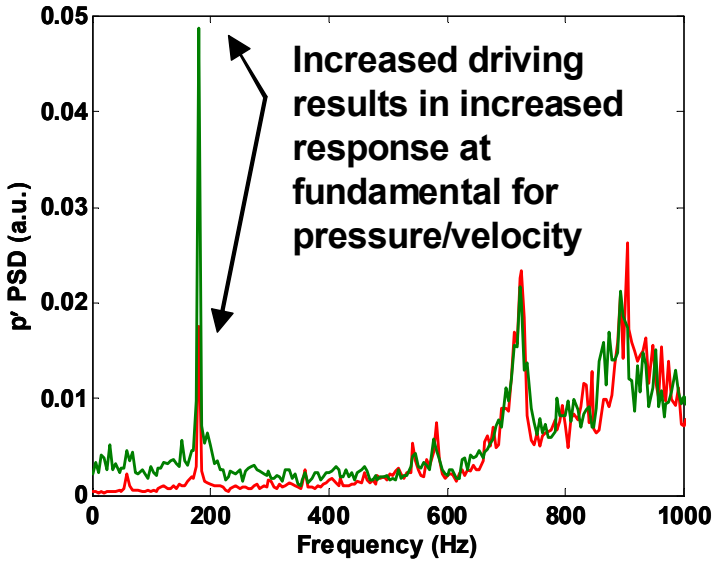

(a)

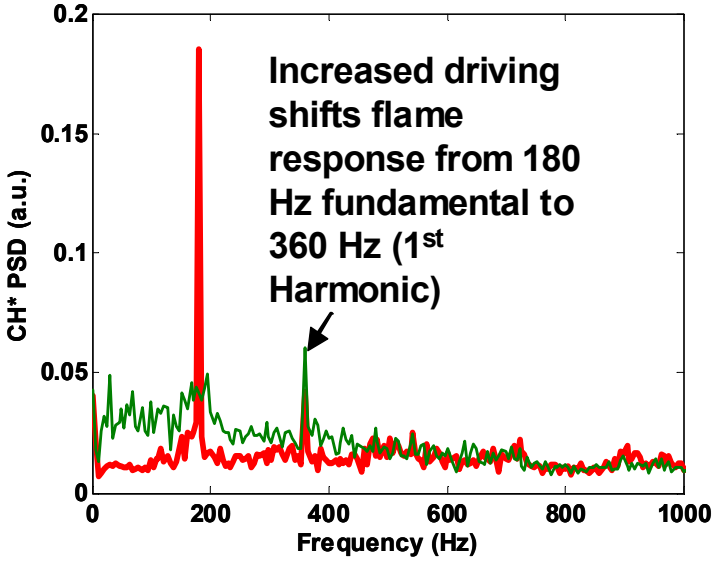

(b)

Figure 54. Fourier transforms of (a) pressure and (b) CH* chemiluminescence signals at local maximum of transfer function (red) and local minimum of transfer function (green) for f_{drive} = 180 Hz (Re_D = 30000, ϕ = 0.80).

A typical example of this behavior is shown in Figure 55, which plots the ratio of the chemiluminescence 1st harmonic to the fundamental versus the velocity oscillation amplitude for f_{drive} = 220-270 Hz. Recall from Figure 49(d) that for f_{drive}= 250 – 270 Hz, the transfer function is more discontinuous and the flame response at the fundamental nearly reaches zero. In contrast, for f_{drive} = 220 – 240 Hz, the behavior is less discontinuous in nature; see Figure 49(c). Figure 55 illustrates that the first harmonic amplitude relative to the fundamental for f_{drive} = 250 – 260 Hz reaches much larger values than for f_{drive} = 220 – 240 Hz. In addition, for both cases, the 1st harmonic values are much greater (relative to both CH^*_o and $CH^{*\prime}$) than for cases where the transfer function exhibits nonlinear characteristics similar to those shown in Figure 45 – Figure 47.

These results indicate that the interactions of the higher and subharmonics with the fundamental can be very important in a given system. For the gas turbine combustor simulator in Chapter 4, the chemiluminescence subharmonic contributed to the nonlinear behavior observed and measured in the experiments. In contrast, the transfer of energy from the chemiluminescence fundamental to the first harmonic for the swirl-stabilized combustor affects the shape of the transfer function and appears to be a function of flowrate and frequency, indicating a Strouhal number, *St*, dependence. The major difference between the subharmonic and first harmonic response is due to the increase in the mean velocity of the respective tests.

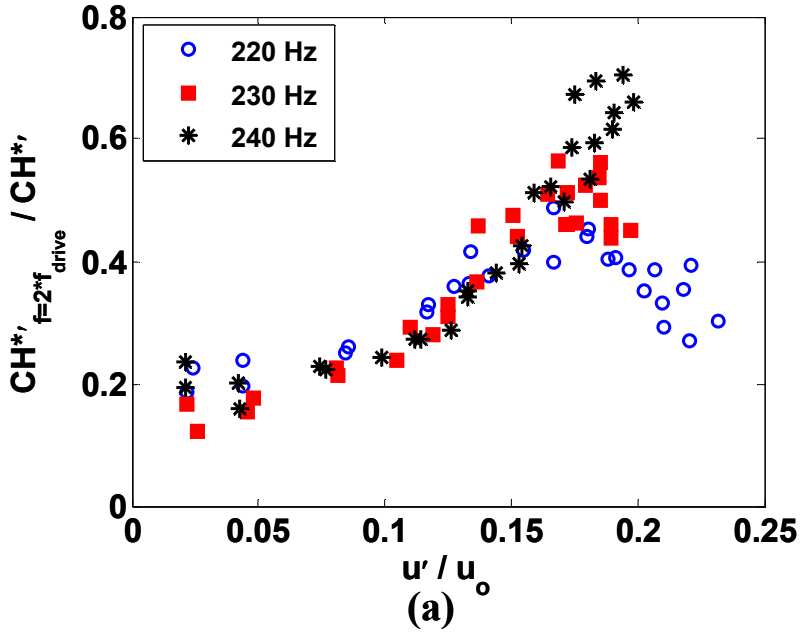

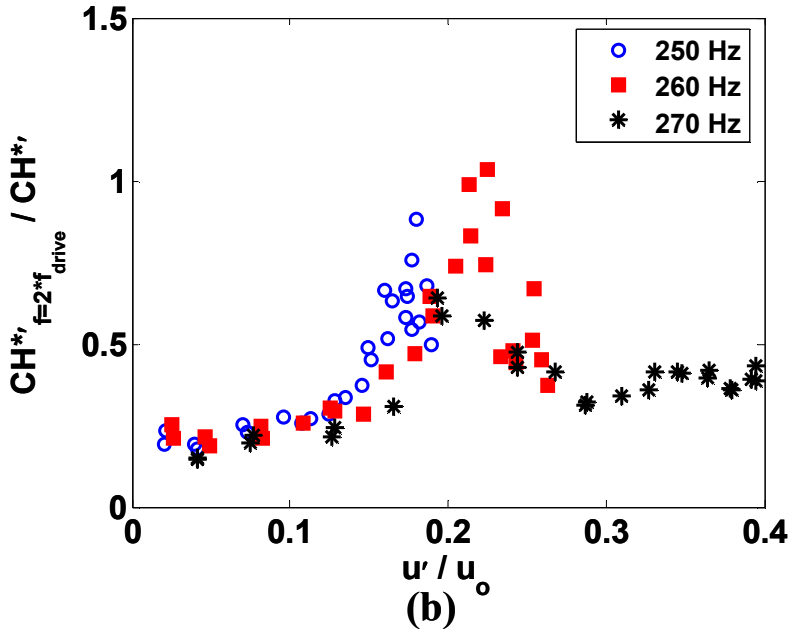

Figure 55. Dependence of CH* chemiluminescence 1st harmonic amplitude on CH* fundamental amplitude for varying driving frequencies (f_{drive} = 220-270 Hz, ϕ= 0.80).

Unlike the gas turbine simulator experiments outlined in Chapter 4, however, the subharmonic of the CH* chemiluminescence was found to be insignificant for all of the frequencies and flowrates investigated on the swirl-stabilized burner. Recall from Chapter 4 that the u'/S_L values where chemiluminescence subharmonic was observed was approximately 7 – 8. For the operating conditions investigated in this chapter, these u'/S_L values correspond to $u'/u_o < 0.1$. At these low velocity values, the signal to noise ratio is quite low in the chemiluminescence. The coherence values between the *CH** chemiluminescence fundamental and subharmonic varied between 0.05 and 0.3. Therefore, any subharmonic response that may be present will be drowned out by the background noise in the measured signal. In addition to the signal to noise ratio effect, it should also be noted that *St* range investigated for these operating conditions is much lower than for the gas turbine combustor simulator in Chapter 4. Again, based on the hydraulic diameter of the gas turbine combustor simulator in Chapter 4, *St* ranges from 2.3 – 3.1. Therefore, the parameters u'/S_L and *St* appear to be two important parameters which affect the type of nonlinear flame behavior observed at large amplitude forcing.

5.5 Imaging of Flame under Large Amplitude Forcing

During this parametric study it was observed that the flame visibly changed in structure at the point where the transfer function saturates when significant saturation occurred (e.g., f_{drive} = 210 Hz and 410 Hz); however, this was not necessarily the case in all situations (e.g., f_{drive} = 130 Hz). High speed, line of sight images of the flame confirmed this observation as shown in Figure 56, which presents images of the flame at two different driving amplitudes at a driving frequency of 410 Hz. These sequences of

images were obtained by phase locking an ICCD high speed camera to the input driving signal. A BG-38 Schott glass filter was placed in front of the ICCD camera to filter out wavelengths of light above ~700nm.

Figure 56(a) shows the line-of-sight view of the flame at low velocity amplitude where the transfer function (f_{drive} = 410 Hz) remains linear in Figure 47. The phase angles shown are with respect to the calculated velocity oscillations. At this low amplitude of oscillation, the flame is easily observed to have a well-defined shape and stabilization point throughout the cycle. The flame responds to forcing by increasing and decreasing in length. No significant visible change in the shape is seen over the cycle. In contrast, Figure 56(b) shows the line-of-sight view of the flame at a velocity amplitude where the flame transfer function has saturated. From these images, it appears that the flame is not stabilized by the centerbody as shown in Figure 56(a). Instead the flame appears to have "lost" its structure. This behavior begins to occur exactly at the point of saturation (e.g., $u'/u_o \sim 0.35$ in Figure 47). Note, however, that the coherence between the velocity and chemiluminescence oscillations is still very high when this change in flame structure occurs; see Figure 44

Since similar flame behavior seen in Figure 56 for 410 Hz was not observed for 130 Hz, these two operating conditions will be the focus for the remainder of this chapter. In an effort to further investigate some of the potential mechanisms controlling the nonlinear flame dynamics, extensive OH-PLIF studies were performed at these two driving frequencies. Two key limitations of these images should be emphasized. First, the flow is highly three-dimensional, so that flame structures come in and out of the images. Thus, one cannot estimate the instantaneous flame area, of interest because of its

relationship to heat release. Second, "consecutive" images are not truly consecutive, as they were taken several cycles apart – thus, one should only attempt to infer global flow features, and not try to track the evolution of a particular flow feature from image to image.

Figure 57(a) presents instantaneous OH PLIF images for the 130 Hz case at a low velocity oscillation amplitude. Here the heat release is in the linear response regime. The images obtained are phase-locked to the driving signal, but the phase angles presented in these figures are with respect to the velocity oscillations calculated from the two microphone method. These figures indicate that the flame is anchored on the centerbody throughout the cycle. The oscillating velocity is evident, as the flame moves back and forth throughout the cycle. Figure 57(b) shows the corresponding flame response for high velocity oscillations; at this level of driving, the flow velocity oscillates between 2-42 m/s through out the cycle. Thus the flow oscillates between nearly reversing itself to a very high speed jet. At the velocity minimum the turbulent flame speed is on the same order as the local velocity value and the flame is propagating towards the premixer. The flame, however, never flashes back into the premixer, but remains just at the premixer exit. Thus there is a lower limit to the flame response. At the point of highest flow velocity and maximum flame length, the clear rollup of the flame into the central recirculation zone is evident, see 45 and 90 degrees.

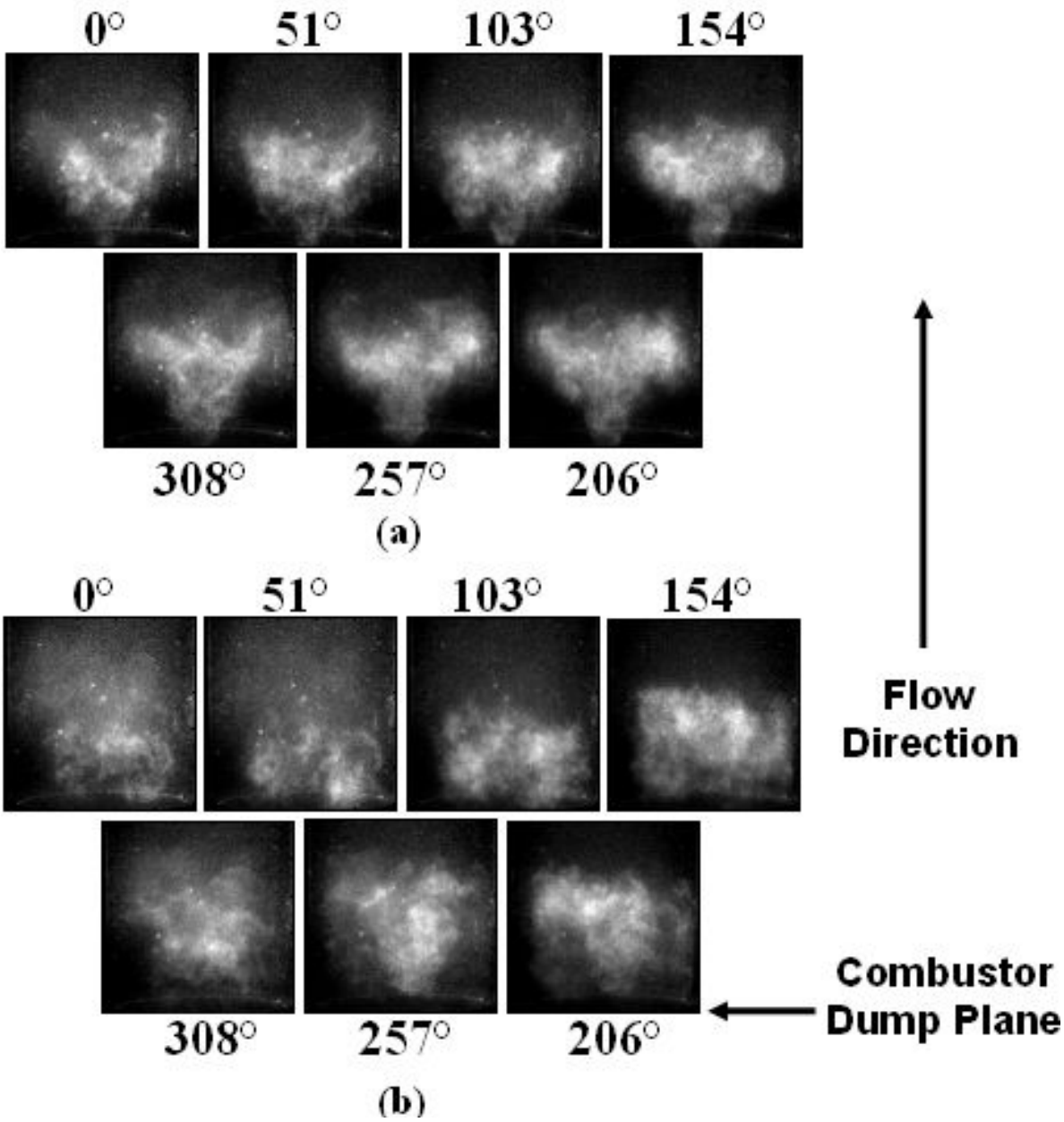

Figure 56: Phase-locked instantaneous line-of-sight images of flame over 1 cycle of acoustic forcing for (a) low (linear – u'/u_o = 0.2) and (b) high (nonlinear – u'/u_o = 0.6) amplitude of oscillation (f_{drive} = 410 Hz, Re_D = 21000, ϕ = 0.80).

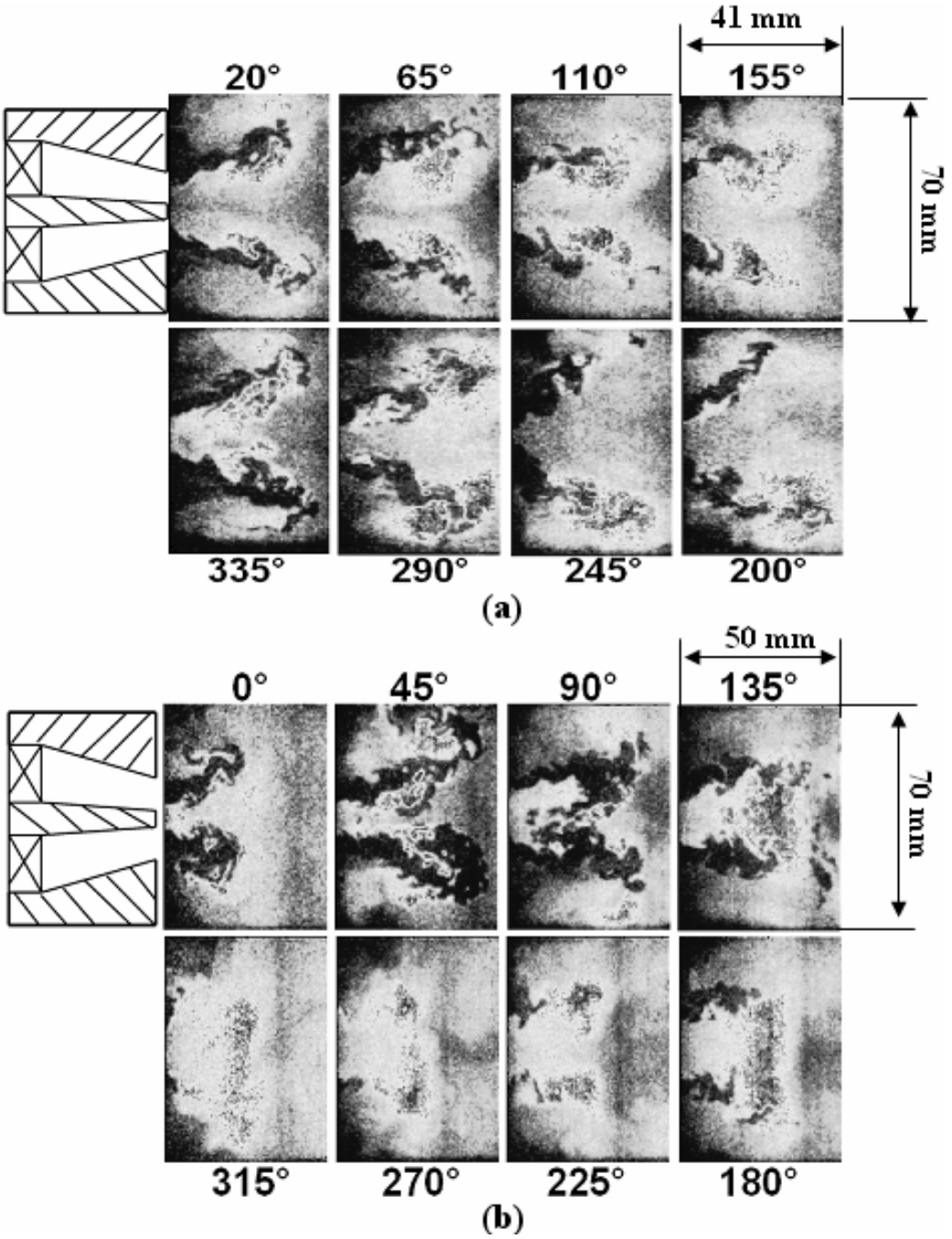

Figure 57. Instantaneous OH PLIF images showing evolution of flame response over 1 cycle of acoustic forcing for (a) low – u'/u_o = 0.3 (linear) and (b) high – u'/u_o = 0.9 (nonlinear) velocity oscillation amplitudes (f_{drive} = 130 Hz, Re_D = 21000, ϕ = 0.80)

This rollup of the flame into the central recirculation zone causes occasional merging of the two flamefronts. The rapid reduction in flame area associated with this rollup, and the subsequent flame propagation and rapid reduction in flame area, is believed to be the mechanism causing saturation of the flame response since this behavior is observed in most of the 200 images obtained at these phases. This assertion is also supported by the fact that rollup is first observed roughly at the point where the *CH** chemiluminescence saturates at $u'/u_o \sim 0.8$ in Figure 46. This is the same observation of Balachandran *et al.* in a non-swirling flame [35]. At this point, the flame area is very rapidly reduced, due to flame propagation normal to itself. Also, note that the flame remains attached throughout the cycle, even at the highest amplitudes, in contrast to the 410 Hz result shown next

Due to the inherent complexity of analyzing instantaneous images of swirling, three dimensional flames as well as determining whether the effects seen in the instantaneous images are truly occurring, the OH PLIF images at each phase were ensemble averaged; see Figure 58 and Appendix D. The average flame edge shown in these images were obtained by averaging the PLIF images, and extracting the flame edge using the method described in Chapter 3. In Figure 58(a), for low amplitude forcing at f_{drive} = 130 Hz, the flame is stabilized off of the bluff body at the exit of the premixer and confirms many of the observations made from the instantaneous images in Figure 57. On average, the flame lengthens and shortens throughout the cycle of acoustic forcing. In contrast, Figure 58(b) shows the phase averaged flame fronts for high amplitude forcing at f_{drive}= 130 Hz, after the point where the *u'-CH*'* transfer function has saturated. In this figure, it is clear that the average behavior of the flame has changed significantly. Figure

58(b) shows the reactants on average are consistently rolled up towards the centerline of the burner at the point of peak response in the cycle, see 90 degrees.

This can be further seen in Figure 59, which illustrates the manner in which the peak flame in the cycle (defined as the phase angle where the reactant jet appears largest in the cycle) varies with disturbance amplitude. The dashed lines indicate the average flame front location (at this particular phase) at excitation amplitudes where the transfer function remains linear, u'/u_o= 0.3 and 0.6. These curves show that the downstream flame displacement increases with perturbation amplitude, but with a similar shape. In contrast, the solid lines show average flame front locations at excitation amplitudes near and beyond the point where saturation in flame response occurs, u'/u_o= 0.83 and 0.9. Here the downstream displacement of the flame position clearly stops growing with perturbation amplitude. Instead of lengthening, the flame is rolled into the central recirculation zone and interacts with the associated vortex. This vortex interaction will stretch and strain the flame, similar to a material line of fluid that is stretched while interacting with a vortex. The interaction of the flame with the vortex will stretch it, increasing the surface to volume ratio compared to the flame just lengthening downstream as it did when the response was linear. Thus, as the flame is rolled up into the recirculation zone, its surface area increases which therefore increases the burning rate of the reactants and then reduces the flame area. This roll-up of the flame causes a very rapid reduction in its area and, therefore, heat release rate. As such, the flame heat release response does not increase proportionately with the perturbation, and saturation occurs. Thus, these results highlight the well-known significance of flame-vortex interactions driving combustion instability; e.g., see Ref. [71, 72].

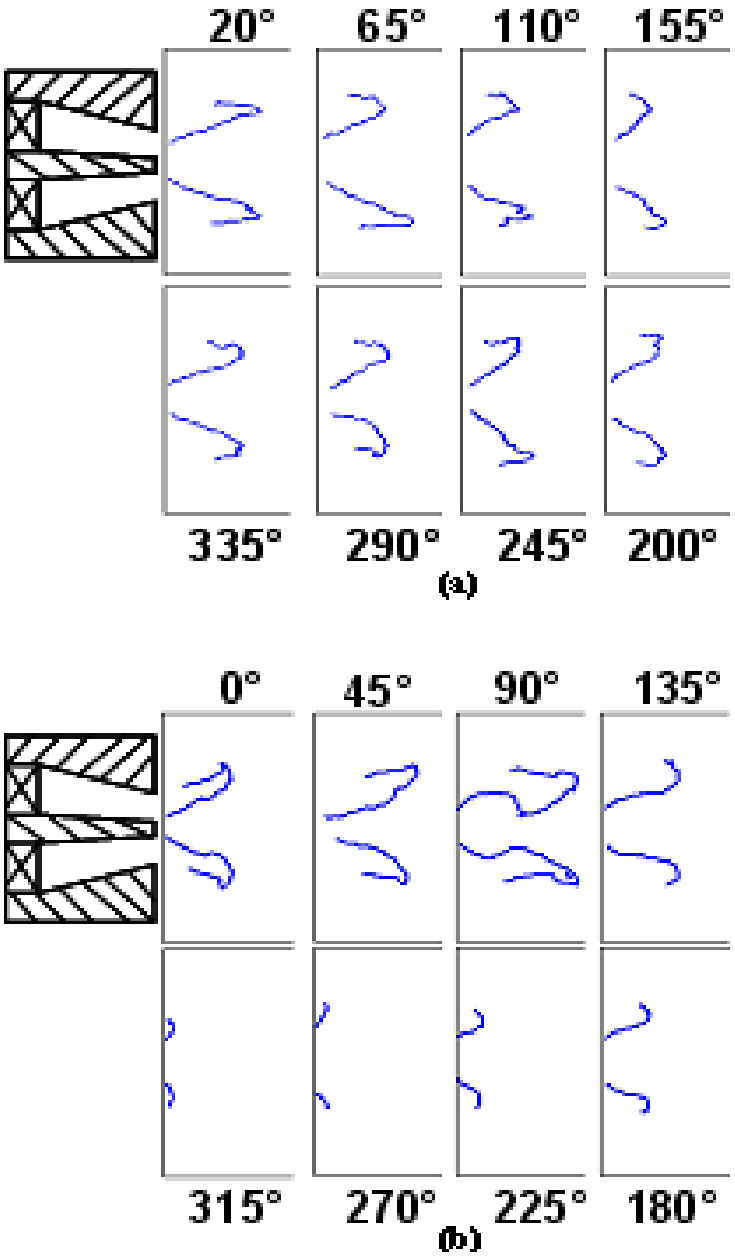

Figure 58. Phase-averaged flame edges showing evolution of flame response over 1 cycle of acoustic forcing for (a) low (linear, u'/u_o = 0.3) and (b) high (nonlinear, u'/u_o = 0.9) velocity oscillation amplitudes (f_{drive} = 130 Hz)

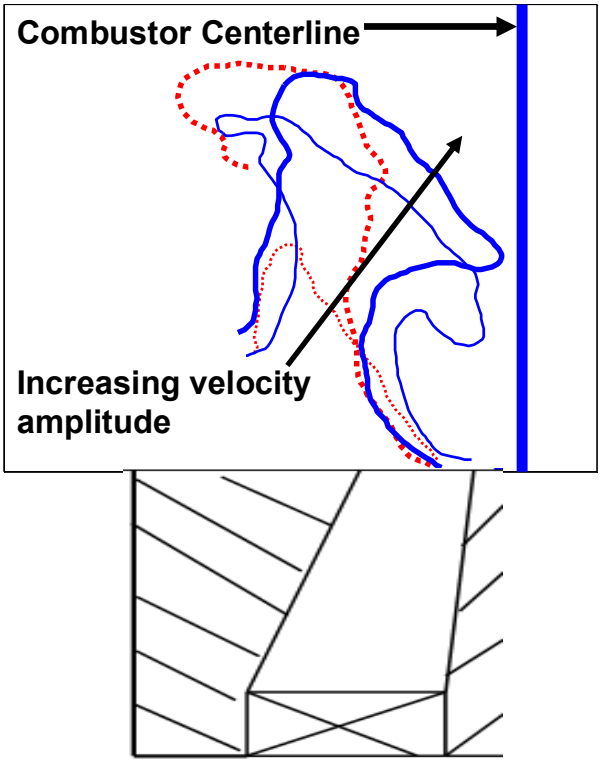

Figure 59. Averaged flame edges at 65-110 degrees phase angle at four velocity oscillation amplitudes (f_{drive} = 130 Hz, u'/u_o = 0.3, 0.6, 0.83, 0.90). Dashed (- - -)/ solid (—) lines indicate peak flame response when transfer function is linear/saturated, respectively.

Consider next the 410 Hz results. Recall from Figure 47, that saturation occurred well below 100% CH* chemiluminescence amplitude. Figure 60(a) shows the flame response at a low velocity amplitude for 410 Hz. Similar to the 130 Hz in Figure 57(a) and inferred from Figure 56, the average flame is stabilized at the centerbody of the premixer. The flame increases in length and shows increased wrinkling at the peak of the cycle. Figure 60(b) illustrates the flame response at a high velocity oscillation amplitude, where the flame exhibits a very different behavior from the 130 Hz results. First, at all 8 phases, the flame is clearly lifted off the centerbody and appears to be stabilized near the stagnation point in a low velocity region associated with the central recirculation zone, as

also shown in the direct flame images in Figure 56. Only at for one portion of the cycle, 45-90 degrees, can the flame be seen attempting to stabilize itself on the centerbody. Since the flame is lifted off, the "two" flamefronts that are present in the linear regime are merged together into one flame- it can be seen that the flame area is lower than it would be if the flame were attached. This unsteady liftoff, and consequent reduction in flame area, is believed to be the mechanism of nonlinearity as it is first observed in the images at u'/u_o amplitudes around 0.35; i.e., where the transfer function begins to saturate.

As with the previous case, the ensemble averaged flame edges provide insight into the possible mechanism for the nonlinear flame response. Figure 61 shows ensemble averaged flame edges for the two driving amplitudes illustrated instantaneously in Figure 60 (also, see Appendix D). Figure 61(a) illustrates that, at low forcing, the flame is indeed anchored throughout the cycle and responds by lengthening and shortening throughout the cycle. For large velocity oscillation amplitudes at and beyond the saturation point, the flame is lifted off throughout the cycle at large amplitude driving as shown in Figure 61(b). The peak response (180-225 degrees) shows that the flame is detached from the centerbody. It appears that the flame liftoff reduces its area (compare 180, 225 degrees in Figure 61(a) and (b)), causing the flame response to saturate at these velocity oscillation amplitudes.

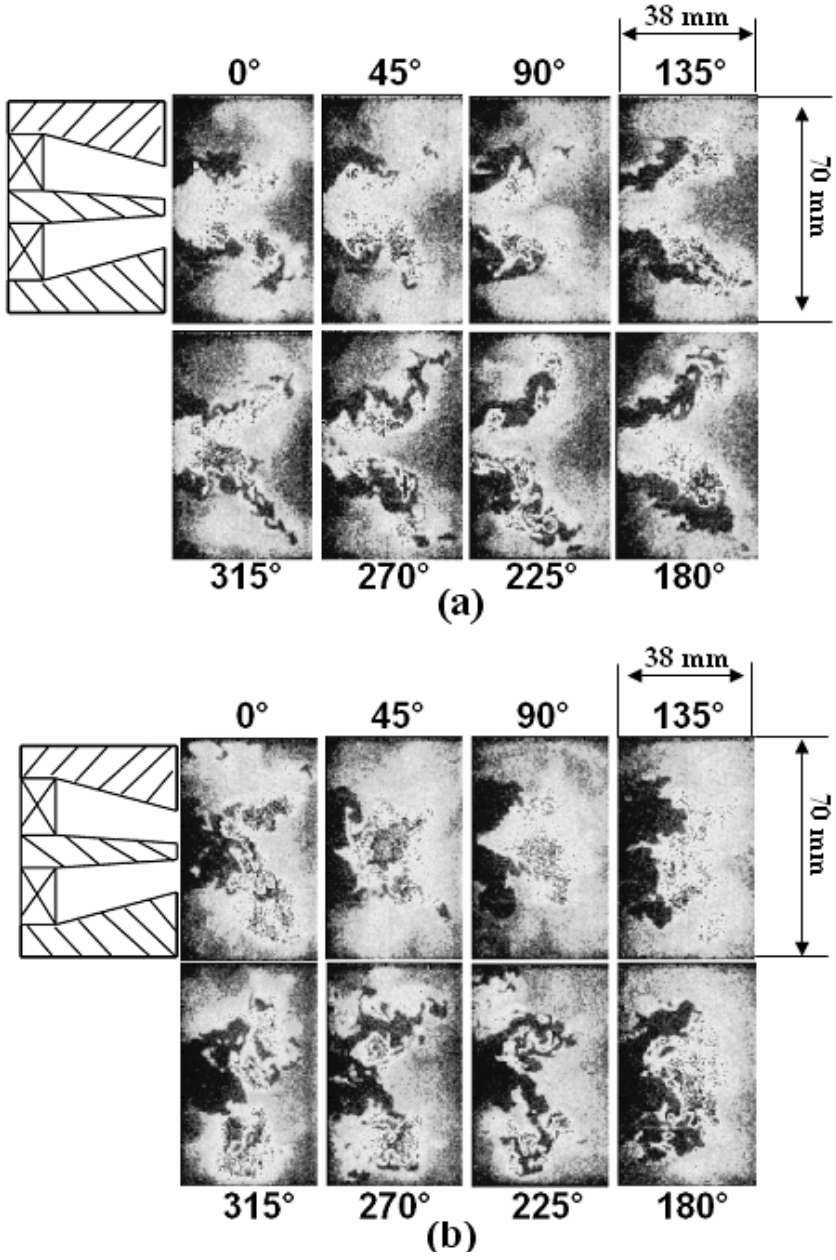

Figure 60. Instantaneous OH PLIF images showing evolution of flame response over 1 cycle of acoustic forcing for (a) low – u'/u_o = 0.2 (linear) and (b) high – u'/u_o = 0.6 (nonlinear) velocity oscillation amplitudes (f_{drive} = 130 Hz, Re_D = 21000, ϕ = 0.80)

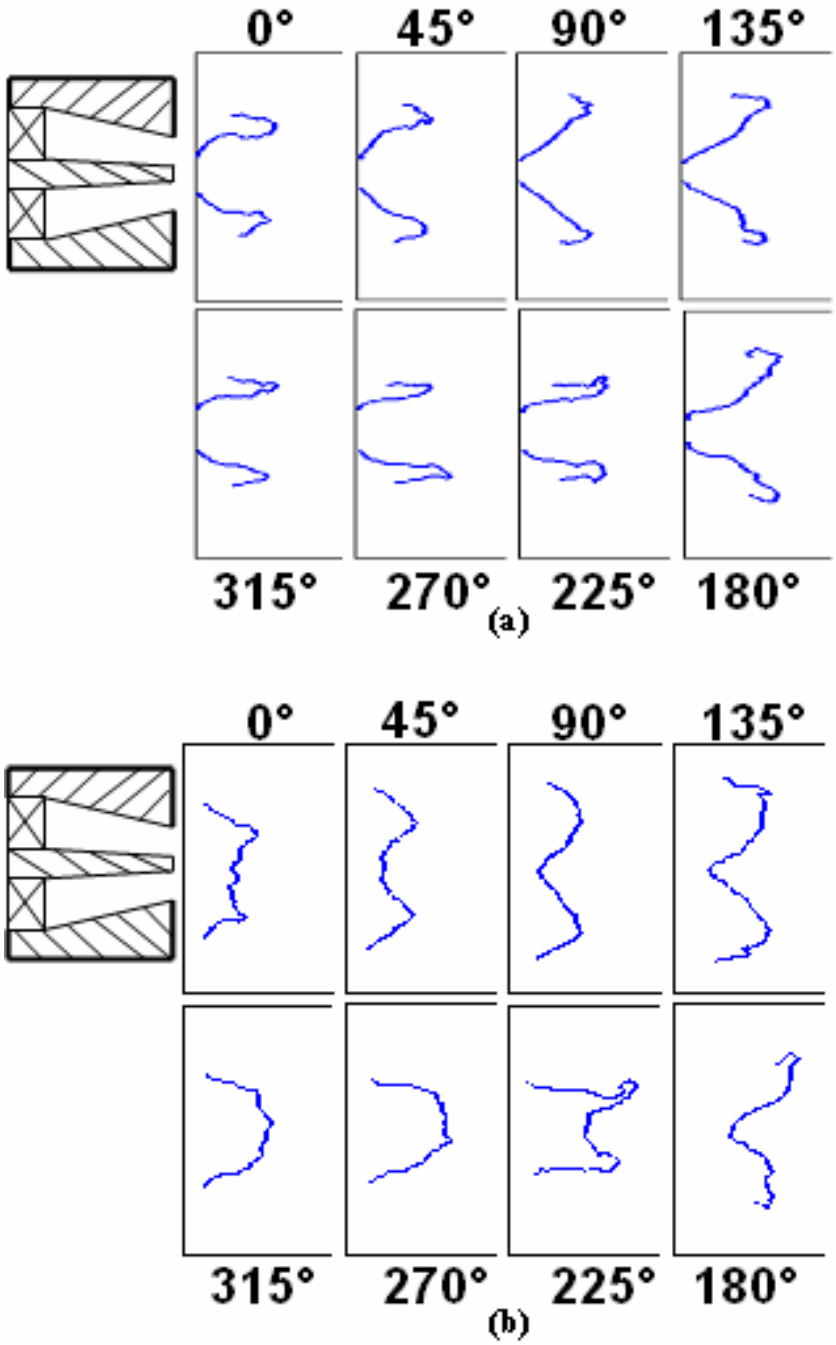

Figure 61. Phase-averaged flame edges showing evolution of flame response over 1 cycle of acoustic forcing for (a) low (linear, u'/u_o = 0.2) and (b) high (nonlinear, u'/u_o = 0.6) velocity oscillation amplitudes (f_{drive} = 410 Hz).

This liftoff behavior and change in flame structure is more clearly seen in Figure 62, which shows phase-averaged peak response flame edges at different velocity oscillation amplitudes. Similar to Figure 59, dashed lines indicates peak flamefronts where the transfer function is linear (u'/u_o = 0.2, 0.3) and the solid lines indicates peak response flame edges near and beyond the saturation point of the transfer function (u'/u_o = 0.53, 0.6). The plot clearly shows the transition of the stabilization point of the flame from the centerbody to a point downstream. This liftoff and subsequent merging of the two flame fronts reduce the flame area substantially, and causes the subsequent saturation of the transfer function.

5.6 Discussion

The governing mechanisms outlined in this combustor for the two driving frequencies have been briefly compared to past experiments on either laminar flames or turbulent, non-swirling flames. These results are the first to be outlined and examined in a turbulent, swirling flame. The vortex rollup mechanism, seen for f_{drive} = 130 Hz, and outlined by Balachandran *et al.* [35], wraps the flame around the reactant jet into the central recirculation zone (or outer shear layer in non-swirling), at which point flame propagation normal to itself reduces its area at the peak of the cycle, due to stretching and straining induced by the central recirculation zone. The corresponding *St* and u'/S_L values are 0.56 and 59. Note that for all of the cases studied in this chapter, u'/S_L for this case is nearly 20% larger than any other.

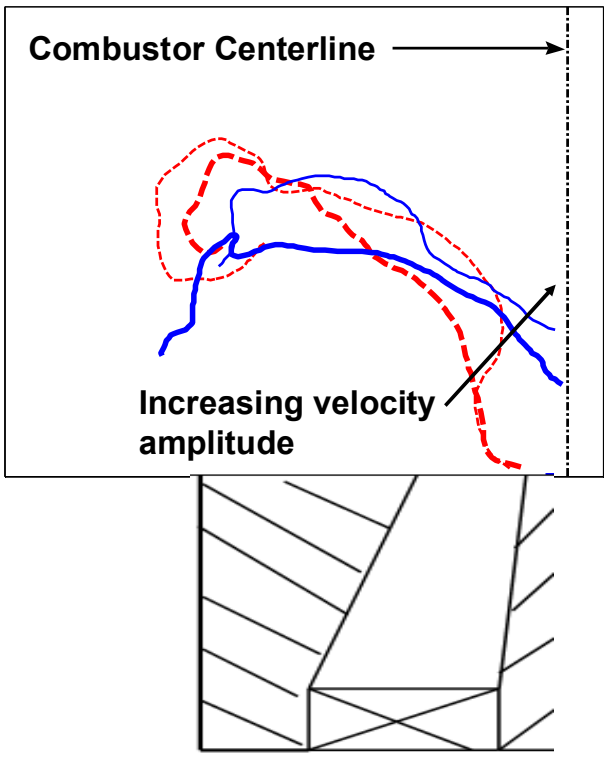

Figure 62. Average flame edges at 180-225 degree phase angle at four velocity oscillation amplitudes (f_{drive} = 410 Hz, u'/u_o = 0.2, 0.3, 0.53, 0.6). Dashed (- - -)/ solid (—) lines indicate peak flame response when transfer function is linear/saturated, respectively.

In contrast, the unsteady flame liftoff mechanism has not been reported previously in the literature. At high driving amplitudes, the flame flattens out by lifting off of the centerbody and becomes hemispherical after the peak of the cycle. The heat release is moved outwards towards the walls of the combustor and away from the central recirculation zone. The corresponding reduction in instantaneous flame area reduces the flame response from its linear value. Flattened and hemispherical flame shapes have been seen previously in laminar, conical flames at high frequencies and driving amplitudes by Durox *et al.* [39]. However, this behavior was accompanied by the parametric instability which was discussed in the results in Chapter 4. No evidence of a

subharmonic response was observed during the transition to this unsteady liftoff mechanism in this chapter. This is further discussed below. In this case, the *St* and u'/S_L values are 1.8and 26. .

In conclusion, substantial nonlinearities in the flame response to forced velocity oscillations have been shown. The nonlinear behavior of the flame to these oscillations is much more pronounced in this combustor compared to the gas turbine simulator experiments discussed in Chapter 4. This result is mainly due to the fact that forcing of the flame does not lead to blowoff as was the case for many operating conditions in Chapter 4. The phase between the flow oscillation and heat release is also seen to have substantial amplitude dependence.

The significant variation in the nonlinear chemiluminescence amplitudes over the range of driving frequencies and Reynolds numbers investigated implies that various mechanisms appear to be important in different frequency and flowrate regimes. For instance, at low flow rates, the saturation amplitude of CH* can vary greatly with driving frequency and range from 25-100% of the mean value. In contrast, for higher flow rates, it is observed that the nonlinear amplitude of CH* is roughly independent of driving frequency. In addition, the shape of the transfer function can change markedly for different driving frequencies and flow rates. Therefore, there are a variety of behaviors which are present in a single combustor. Thus, one single theory is not adequate to describe the nonlinear dynamics of a forced or unstable combustor.

The results presented in this chapter provide important details on the processes that can affect the nonlinear flame response to large acoustic oscillations in gas turbine combustors. OH PLIF imaging of the flame was performed at two frequencies where two

mechanisms potentially controlled the saturation amplitude of the global heat release from the flame. Two phenomena, vortex rollup and flame liftoff, are proposed to be the likely mechanisms that govern saturation of the flame transfer function from these images. The latter mechanism visibly changes the flame structure when comparing these results with line-of-sight images. Both mechanisms act to reduce the flame area, but occur at very different St and u'/S_L values. Furthermore, both mechanisms appear to be related to the size and strength of the central recirculation zone. These results indicate that further understanding of the flame stabilization processes in swirling flows is quite necessary. Since these results were obtained at one equivalence ratio, the effect of the central recirculation zone (size, strength, etc) on the nonlinear flame behavior is unknown at this point.

No sub-harmonic flame response was observed in any of these studies as opposed to the studies outline in Chapter 4. Despite the fact that parametric flame instabilities occur at high forcing amplitudes, resulting in this subharmonic response, most of the studies that have investigated this phenomenon were performed at relatively low Reynolds numbers. The results presented in Chapter 4, where the subharmonic response was found to occur, were performed at Reynolds numbers higher than those presented in the literature on nominally flat propagating flames and conical, Bunsen flames. However, the experiments performed in the swirl-stabilized combustor in Chapter 5 investigated even higher velocities (even the lowest Reynolds number investigated) than those associated with the Chapter 4 experiments which resulted in lower Strouhal numbers, St. Therefore the u'/S_L values, where one might expect a subharmonic response of the flame (i.e., $u'/S_L \sim 5 - 8$), in these studies corresponded to velocity values of u'/u_o

< 0.1. At these low velocity values, the signal to noise ratio is quite low and could possible "drown" out any subharmonic response that may be present. Therefore, the nominal, mean velocity at the flame location is an important parameter that affects the nonlinear flame response to large acoustic oscillations by altering the shape of the transfer function, as well as influences the mechanisms which cause transfer function saturation. In addition, it is clear that the nonlinear flame behavior in both combustors is affected by at least two other parameters, the Strouhal number, *St*, and the ratio of the oscillating velocity amplitude to the laminar flame speed, u'/S_L. Both mechanisms in this chapter were important at much different *St* and u'/S_L values. The parametric instability mechanism in Chapter 4 was also found to occur at much different *St* and u'/S_L values as well. The correct characteristic length scale defined in *St* needs to be further investigated, however, to better correlate results between combustors operating with different fuels and flame stabilization mechanisms.

Despite the lack of subharmonic response of the flame, many results indicate significant interactions between the chemiluminescence fundamental frequency and the first harmonic. The importance of these interactions varies with Reynolds number and frequency, and correlate well with *St*. Thus based on the results presented in Chapter 4 and Chapter 5, it is clear that the frequency interactions between natural modes (stable and unstable) and other frequency regimes (harmonics or otherwise) are very important to understand in order to develop a more complete knowledge-base of combustion instabilities.

CHAPTER 6

FREQUENCY INTERACTION CHARACTERISTICS IN COMBUSTORS

This chapter describes experiments that investigate the interaction of the acoustics of the system with natural (both stable and unstable) modes of the combustor. These results are compared qualitatively to nonlinear second order oscillator theory. Section 6.1 discusses experiments that investigate how the nonlinear combustion process changes the frequency response curve of a combustor around a stable natural mode. Section 6.2 describes experiments that investigate the effect and characteristics of non-resonant forcing on a natural mode in an unstable combustor. Section 6.3 provides additional discussion about these results as well as the limitations in describing these nonlinear interactions with simple, forced oscillator theory.

These characteristics between natural unstable acoustic modes and driven oscillations were determined in the two combustors utilized in Chapter 4 and Chapter 5. Specifically, the effects of the spacing between these driven and natural, stable and unstable oscillations are investigated to elucidate these characteristics. In addition, these studies investigate the effectiveness of open-loop non-resonant control of the unstable combustion process.

Chapter 4 and Chapter 5 have investigated the nonlinear behavior of the flame to incident acoustic oscillations. In term of a general feedback diagram for combustion instabilities, such as shown previously in Figure 2 and below in Figure 63, this

investigation has focused on the determination of the nonlinear heat release response to forced acoustic fluctuations. This subject of this chapter is the effects of the forced heat release response on the acoustics of the system. Specifically, how does the forced flame alter the frequency response characteristics of the system itself. The key difference between Section 6.1 and Section 6.2 is that the effect of the nonlinear heat release on the acoustics of the system is investigated for a damped oscillator in Section 6.1 and for a self-excited oscillator in Section 6.2.

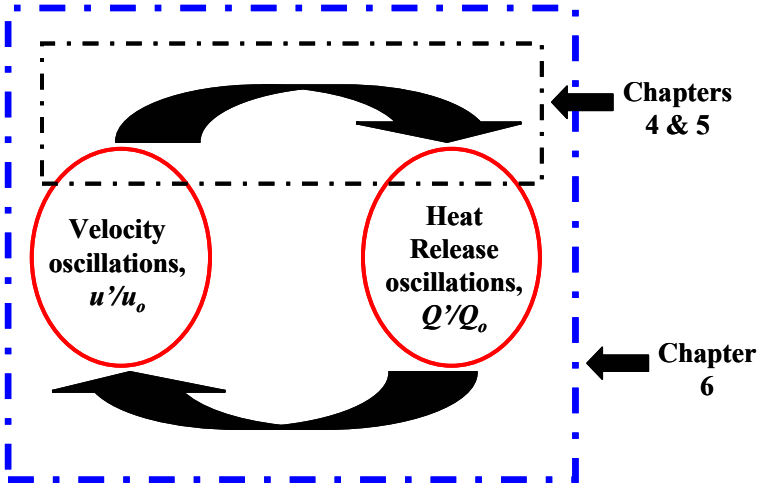

Figure 63. Schematic of combustion instability feedback mechanism and the pathways investigated in this thesis

6.1 Nonlinear Heat Release-Linear Acoustics Interaction: Damped Oscillator

This section describes further analysis of experiments performed on the gas turbine combustor simulator described in Chapter 4. The frequency response of the system near a stable, natural mode is analyzed. It has been argued previously that the dynamics of an unstable combustor are dominated by heat release nonlinearities which interact with linear acoustic processes. Because the combustor is a reverberant acoustic

environment, it possesses a number of acoustic modes. Culick [73] and Zinn & Powell [10] have shown that the dynamics of each mode may be described by an oscillator equation of the form:

$$\ddot{x}_i + 2\xi\omega_o\dot{x}_i + \omega_o{}^2 x_i = F\left(x_i, \dot{x}_i\right) + E\left(t\right) \tag{6.1}$$

where ω_o is the linear natural frequency, ζ is the damping coefficient, $F\left(x, \dot{x}\right)$ refers to the system nonlinearities, and *E(t)* is the external excitation.

Before presenting further data, several classical results are summarized below for a nonlinear system that is externally forced at a frequency near resonance, i.e. $E(t) = A\cos\Omega t$, where $\Omega \approx \omega_o$. Consider first nonlinearities in "stiffness", i.e. $F = F(x_i)$. It is well known that such a system exhibits “bending” in the frequency response curve, such as shown in Figure 64(a). As such, the frequency of the maximum oscillator response shifts with frequency; e.g., increases/decreases in the effective stiffness with increasing disturbance amplitude cause the curve to bend toward higher/lower frequencies. As the frequency of the large amplitude excitation is swept, the response of the nonlinear system follows one branch of the curves to a bifurcation point where the system jumps discontinuously to the other branch. This manifests itself in hysteresis in frequency and amplitude where this jump occurs. Consider next nonlinearities in damping, i.e., $F=F(\dot{x})$. The peak amplitude of this type of nonlinear system will not increase proportionally to the disturbance amplitude. If damping grows nonlinearly, amplitude saturation causes a flattening of the response curve around the resonant frequency

Therefore, the maximum response is distributed over a broader range of frequencies than a linear damped oscillator, see Figure 64(b); see Ref. [74].

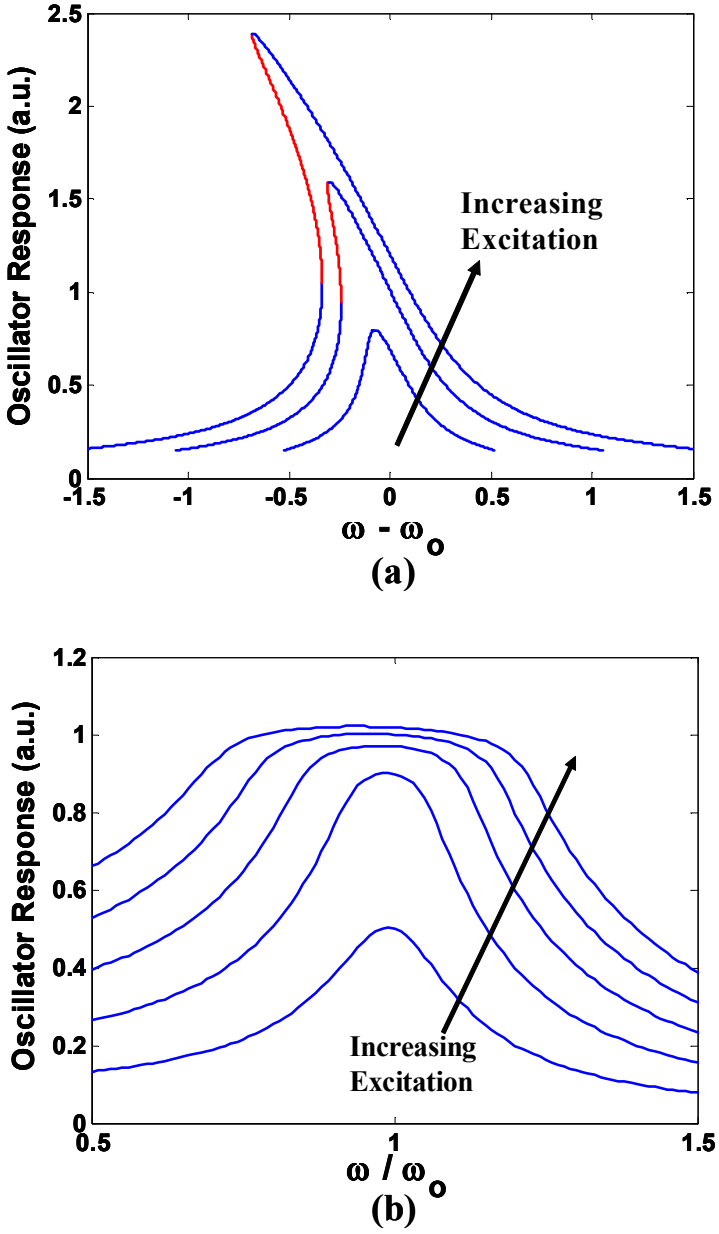

Figure 64: Frequency–response curves at several excitation amplitudes for a second order oscillator with nonlinearities in (a) stiffness, $F(\dot{x},x) \sim x^3$ and (b) damping, $F(\dot{x},x) \sim \dot{x}^{20}$.

Both types of behavior illustrated in Figure 64 were observed in the current data. A representative result is shown in Figure 65(a), which plots the frequency dependence of the pressure amplitude at a large disturbance amplitude. The pressure amplitude response bends over to the left indicative of a "softening" spring. Second, the pressure amplitude jumps in the 285-290 Hz range, with hysteresis in the frequency value where this jump occurs. Third, the peak response of the pressure remains relatively constant over a range of driving frequencies, indicating nonlinearity in damping. This behavior can be seen more clearly in Figure 65(b), which plots similar results at several driving amplitudes. The plot clearly shows the progressive trend away from a classical forced-resonant linear system at low disturbance amplitudes to a response that bends over toward lower frequencies and "flattens" in response.

If the forcing frequency is held constant, while the excitation amplitude is varied, a similar bifurcation occurs. A simulated result is shown in Figure 66 for the same model described by Eq. (6.1). Figure 67 shows that the pressure oscillation data have a similar dependence on frequency. As noted above, the linear natural frequency is approximately 310 Hz. At 280 Hz there is a noticeable jump in the pressure response. At frequencies below and above 310 Hz, the pressure response exhibits a "quadratic" and "square root" dependence upon excitation amplitude.

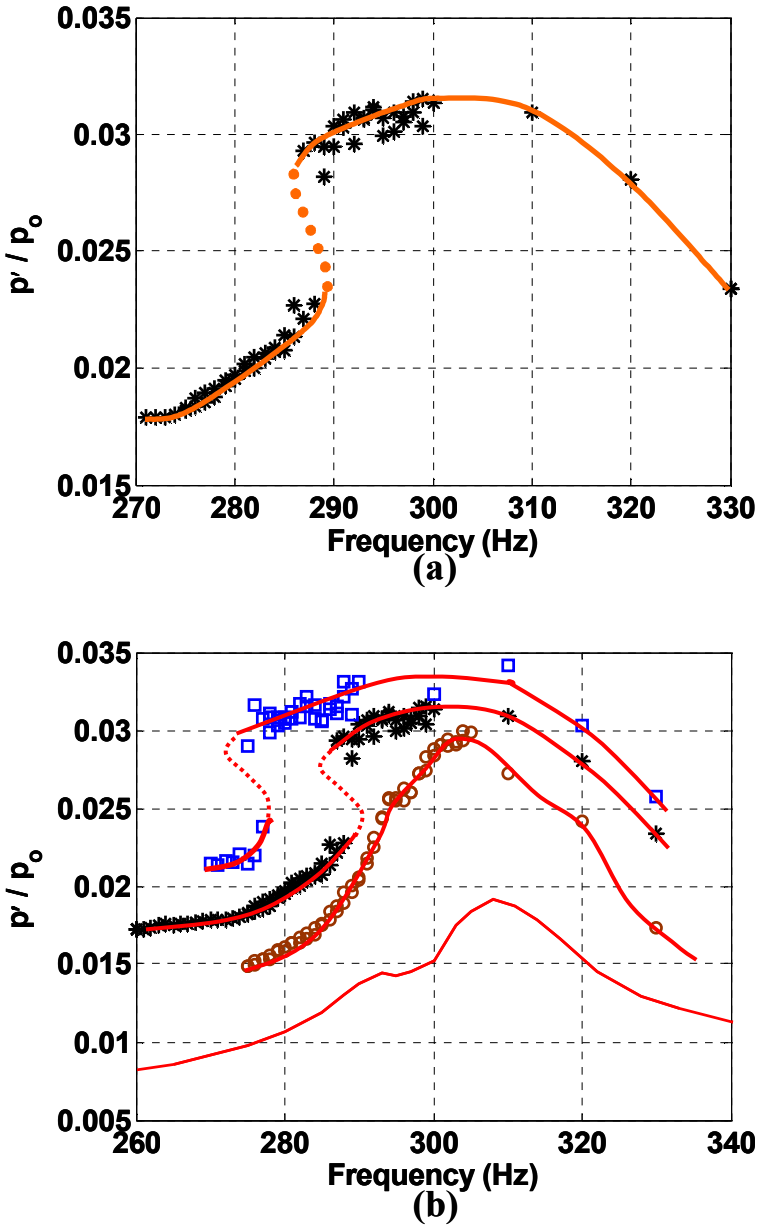

Figure 65: Dependence of pressure amplitude upon frequency at (a) a single disturbance amplitude, 2.8 Amperes and (b) several disturbance amplitudes, 1.8-3.0 Amperes (ϕ = 0.95).

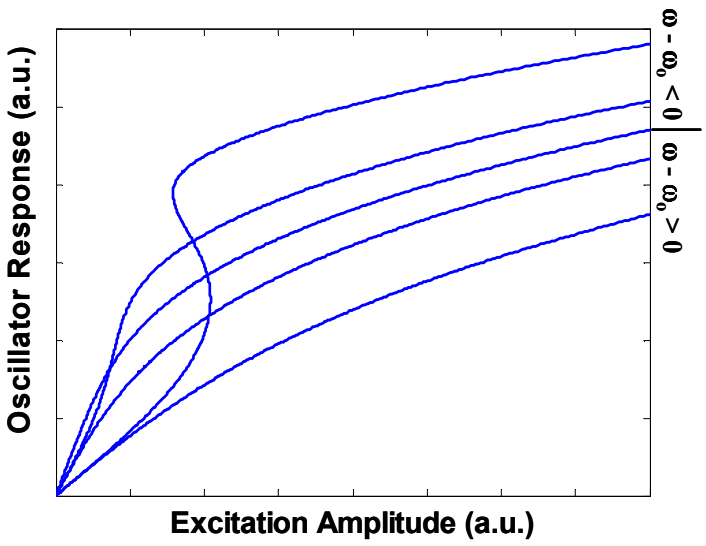

Figure 66: Excitation–response curves for softening spring oscillator at several excitation amplitudes, $F(x,\dot{x}) \sim x^3$

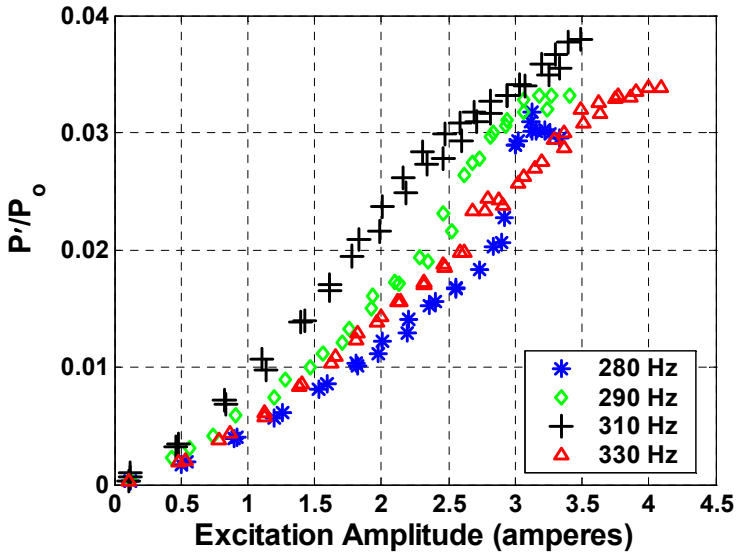

Figure 67: Dependence of pressure oscillation amplitude on excitation amplitude for varying driving frequencies ($\phi = 0.95$)

Referring back to Figure 33(a), note the clear saturation of the CH*-velocity transfer function at 280 Hz. Referring to the specific data points, note that a clear "jump" in the velocity amplitude is observed at a point coinciding with that where saturation is observed. It should be noted that the driving levels were increased in a regular, stepwise fashion over the whole range of amplitudes. This jump in the velocity coincides with the jump in pressure amplitude illustrated in Figure 67; i.e. the jump in pressure and velocity coincides with the point where the heat release response exhibits nonlinearity.

A detailed study of this bifurcation and the associated hysteresis was performed in the 280-290 Hz frequency range. Figure 68 summarizes the amplitude-frequency parameter regions where single and multi-valued behaviors occur. Hysteresis occurs at driving amplitudes larger than about 2.6 Amperes (A) and extends all the way to 3.1A, where blowout occurred. The corresponding frequencies range from 292 to 276 Hz at the low and high amplitude driving ranges.

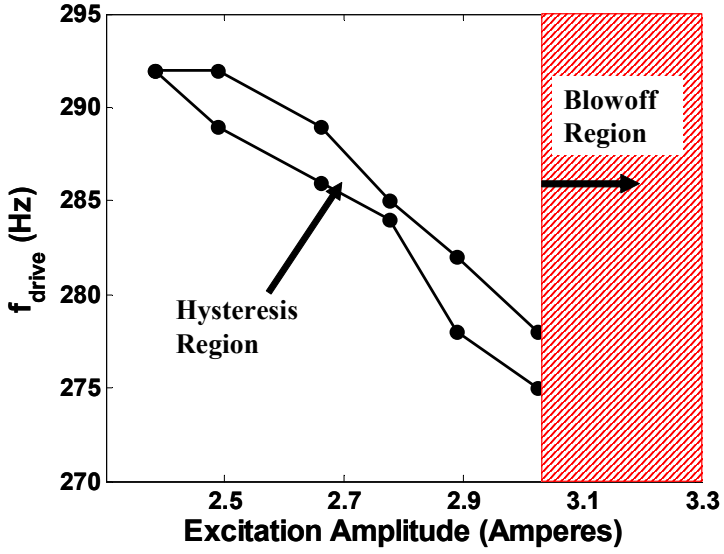

Figure 68: Amplitude-frequency ranges over which the chemiluminescence-pressure-velocity relationship exhibited single and multi-valued behavior

Figure 69 provides a further visualization of this bifurcation by quantifying the CH* - pressure transfer function as a function of frequency at fixed driving amplitudes (the CH*-pressure relationship is illustrated here due to the fact that the uncertainty values are smaller than those for the velocity measurements; the trends, however, are identical). The figure plots these dependencies at both a low and high driving amplitude of 2.4 and 3.0 Amperes. For low driving amplitudes, the transfer function exhibits a smooth, monotonically decreasing dependence upon frequency, as would be anticipated by the results shown in Figure 27. However, when the driving amplitude is increased beyond the cutoff point of 2.6 Amperes, the transfer function changes significantly. This result is illustrated in Figure 69(b), where a clear jump in the transfer function values occurs (~14% for the CH*-pressure transfer function value) for the 3.0 Amperes driving case. Note that the frequency dependence of the transfer function is much "flatter" in the high driving case. The frequency where the jump occurs depends upon the direction of frequency change (increasing/decreasing) with a total hysteresis of about 3 Hz. Note that the transfer function itself does not likely exhibit a discontinuous dependence upon amplitude; rather the pressure amplitude exhibits a discontinuity in the region where the transfer function changes. This transfer function change is responsible for the bifurcation in pressure amplitude. As such, it is not possible to measure a monotonic change in the transfer function at these frequencies because of the discontinuous jumps that occur in acoustic amplitude.

Figure 70 plots the corresponding phase relationships between the pressure oscillations and CH* fluctuations. As in the gain transfer function results, the phase exhibits a smooth, monotonic increase dependence on driving frequency below the

bifurcation amplitude. Above the bifurcation amplitude, the phase angle jumps; i.e., approximately 8 degrees in value in Figure 70(b).

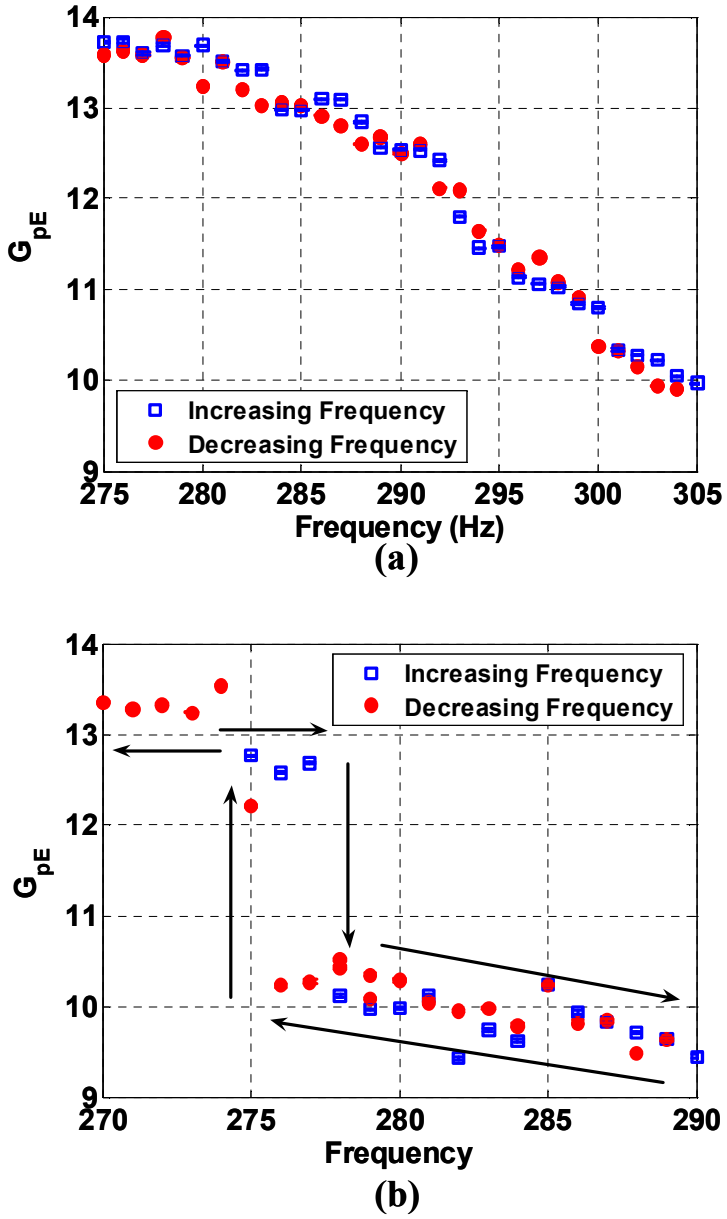

Figure 69: Dependence of pressure-CH* transfer function on driving frequency (excitation amplitude = 2.4 amperes (a), excitation amplitude = 3.0 amperes (b), ϕ = 0.95)

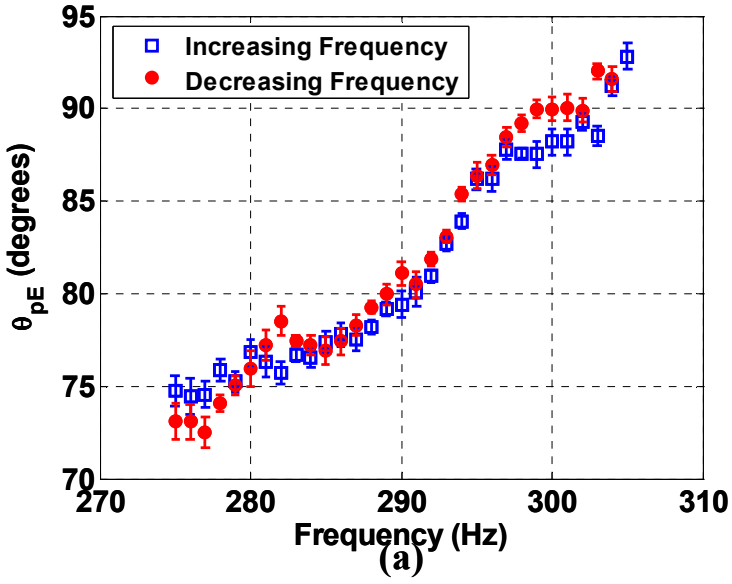

(a)

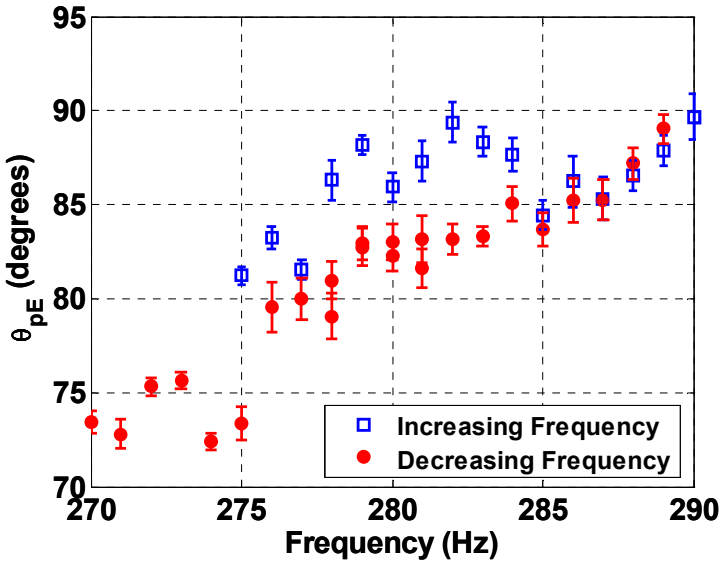

(b)

Figure 70: Dependence of pressure-CH* phase relationship on driving frequency (excitation amplitude = 2.4 Amperes (a), excitation amplitude = 3.0 amperes (b), ϕ = 0.95)

6.2 Nonlinear Heat Release – Linear Acoustics Interaction: Self-Excited Oscillator

This section describes experiments performed on the atmospheric, swirl-stabilized combustor utilized in Chapter 5. In contrast to the previous section, the interaction between the nonlinear heat release oscillations and the linear acoustics is investigated when the combustor is self-excited. Previous studies have performed small investigations on the effect of open-loop forcing on unstable combustors [33] and attributed the observed behavior to frequency locking or quenching of the instability. This nonlinear phenomenon is manifested as a decrease of the self-excited or natural mode oscillations as the amplitude of the driven oscillations increases.

Lieuwen & Neumeier [33] performed a limited investigation of the effect of forcing frequency upon this frequency locking phenomenon by considering two forcing frequencies. Their data did not indicate a significant change in the entrainment amplitude at the two driving frequencies. This was contrary to expectation, however, as the entrainment amplitude was anticipated to be proportional to the frequency spacing between the forced and self-excited frequency. These considerations motivated this study, which more systematically investigates these frequency spacing effects on entrainment amplitude.

The basic phenomenon of frequency locking can be illustrated from the model problem considered in Section 6.1, where the system is self-excited (i.e., $\zeta < 0$). Explicit solutions have been worked out below for a nonlinearity in damping of the form, $F\left(x,\dot{x}\right)=\frac{1}{3}\dot{x}^3$. Therefore, Eq. (6.1) becomes:

$$\ddot{x} + 2\xi\omega_o\left(\dot{x} - \frac{\dot{x}^3}{3}\right) + \omega_o^2 x = E(t) \tag{6.2}$$

where $E(t) = K\cos(\Omega t)$ is the external forcing. For this analysis, $2\zeta\omega_o$ is small and the forcing frequency, Ω, does not equal $\omega_o/3$ or $3\omega_o$, i.e. a superharmonic or subharmonic resonance. The leading order solution of Eq. (1) is a superposition of the limit cycle and forced oscillations and takes the form:

$$x = A_s\cos\left(\omega_o t + \beta(t)\right) + A_F\cos(\Omega t) + O(\varepsilon) \tag{6.3}$$

where $A_F = \dfrac{K}{\omega_o^2 - \Omega^2}$. Following Nayfeh & Mook [74], the amplitude of the response, A_s, can be determined analytically.

$$A_s^2 = \frac{4\eta}{\omega_o^2 + \left(\dfrac{4\eta}{a_o^2} - \omega_o^2\right)\exp(-\varepsilon\eta t)} \tag{6.4}$$

where a_o is the initial amplitude of oscillation and $\eta = 1 - \dfrac{1}{2}\Omega^2 K^2\left(\omega_o^2 - \Omega^2\right)$. For $K = 0$ (i.e., η=1), the amplitude $A_s(t)$ tends toward the limit cycle amplitude of $A_s(t)=2/\omega_o$. For $K > 0$, this solution for the limit cycle amplitude is dependent on both the external driving amplitude and the frequency spacing between the driven and natural mode. However, if

the response is parameterized in terms of the amplitude of the system response at the forcing frequency, A_F, and not the actual input driving signal, this solution becomes independent of frequency spacing since:

$$\eta = 1 - \frac{1}{2}\Omega^2 {A_F}^2 \tag{6.5}$$

Figure 71 plots the steady state solution ($t \to \infty$) of the self-excited amplitude for increasing forcing amplitude. It shows the monotonic reduction in instability amplitude, $A_s(t)$, (until its amplitude reaches zero, the quenching amplitude), as the forcing amplitude, $E(t)$ is increased. The quenching amplitude, $A_{F,q}$, is therefore the value of A_F when $A_s(t)$. Similar behavior is observed experimentally, as shown in Figure 71 and described in the remainder of this section.

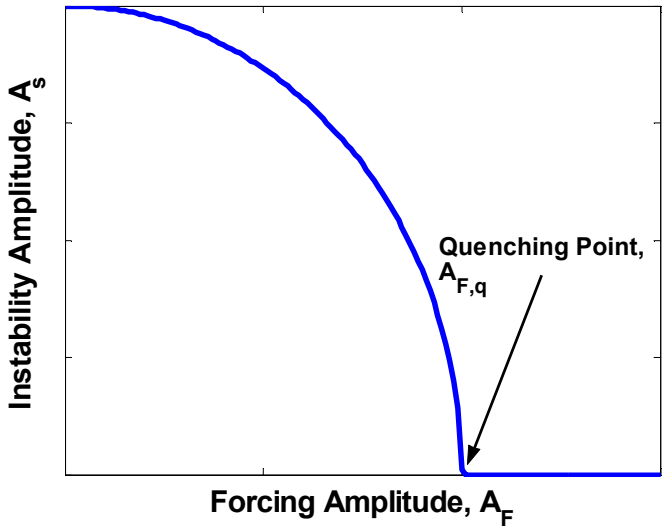

Figure 71. Theoretical response curve of nonlinear self-excited oscillator to forced oscillations

Experiments were performed with the atmospheric, swirl-stabilized burner, schematically shown in Figure 12. Two flow rates were investigated, Re_D=23,000 and 34,000 (based on premixer exit diameter) corresponding to average premixer exit plane velocities of 23 and 33 m/s, respectively. Reactant inlet temperatures were kept constant at room temperature. Three operating conditions were investigated in this study. These conditions examined the effect of instability frequency and amplitude on the quenching/entrainment characteristics of the system. The complete operating conditions are outlined in Table 3 below.

Table 3. Operating conditions for nonlinear frequency interactions investigation in atmospheric, swirl-stabilized burner.

	Condition 1	**Condition 2**	**Condition 3**
Equivalence ratio, ϕ	**0.83**	**0.83**	**0.87**
Natural frequency (Hz) $\pm$ 5 Hz	**461 Hz**	**350 Hz**	**510 Hz**
Flow velocity (m/s)	**23 m/s**	**23 m/s**	**33 m/s**
Pressure instability amplitude (p'/p_o)	**0.013-0.015**	**0.02-0.024**	**0.01-0.013**

Condition 1 tests were performed at a nominally unstable condition, with an instability frequency of 461 Hz. The forcing frequencies investigated ranged from 150 to 430 Hz and for all cases, the overall acoustic power was substantially reduced by the presence of acoustic forcing. Some results were obtained at forcing frequencies higher than the instability amplitude, but are not reported here, as the speaker lacked the

authority to substantively influence the instability. A typical result is shown in Figure 72. The nominal amplitude of the 461 Hz instability is about 1.5% of the mean pressure in the combustor. In this particular case, forced oscillations are excited at 200 Hz over a range of amplitudes. As shown in Figure 72(a), increased forcing levels cause the 461 Hz mode amplitude to decrease, and to nearly disappear at high driving amplitudes. In addition, the harmonic associated with the instability at 922 Hz also disappears. Due to this reduction in the instability mode and its harmonic the acoustic power in the 0-1000 Hz range is significantly reduced. The maximum reduction in acoustic power in the spectra between 0 and 1000 Hz is 90% for this case.

The typical dependence of the natural instability amplitude on the driving amplitude is shown in Figure 72(b). At the highest driving amplitudes, the instability has essentially disappeared at the cost of the increase in amplitude of the driven pressure. There are several basic features of the instability amplitude dependence upon driving amplitude that can be discerned from Figure 72(b). First, the instability amplitude is independent of the forcing amplitude for some amplitude range before decreasing; the driving amplitude at which this decrease begins is referred to as A_L. Second, the instability amplitude decreases with some slope, δ_p, for further driving amplitude increases. Third, the instability amplitude essentially goes to zero, or to near zero values above some driving amplitude, referred to here as the entrainment amplitude, A_e. For example, in Figure 72(b) the entrainment amplitude is ~25% of the mean velocity at the premixer exit. Also shown in the figure is the overall RMS pressure amplitude of the driven oscillation and natural mode, which has a minimum near the entrainment amplitude and then begins to rise with increased forcing levels, due to the growing

amplitude of the imposed oscillations. Finally, the dependence of the unstable mode amplitude upon the driving amplitude exhibits some hysteresis, with typical levels on the order of $u'/u_o = 0.03$.

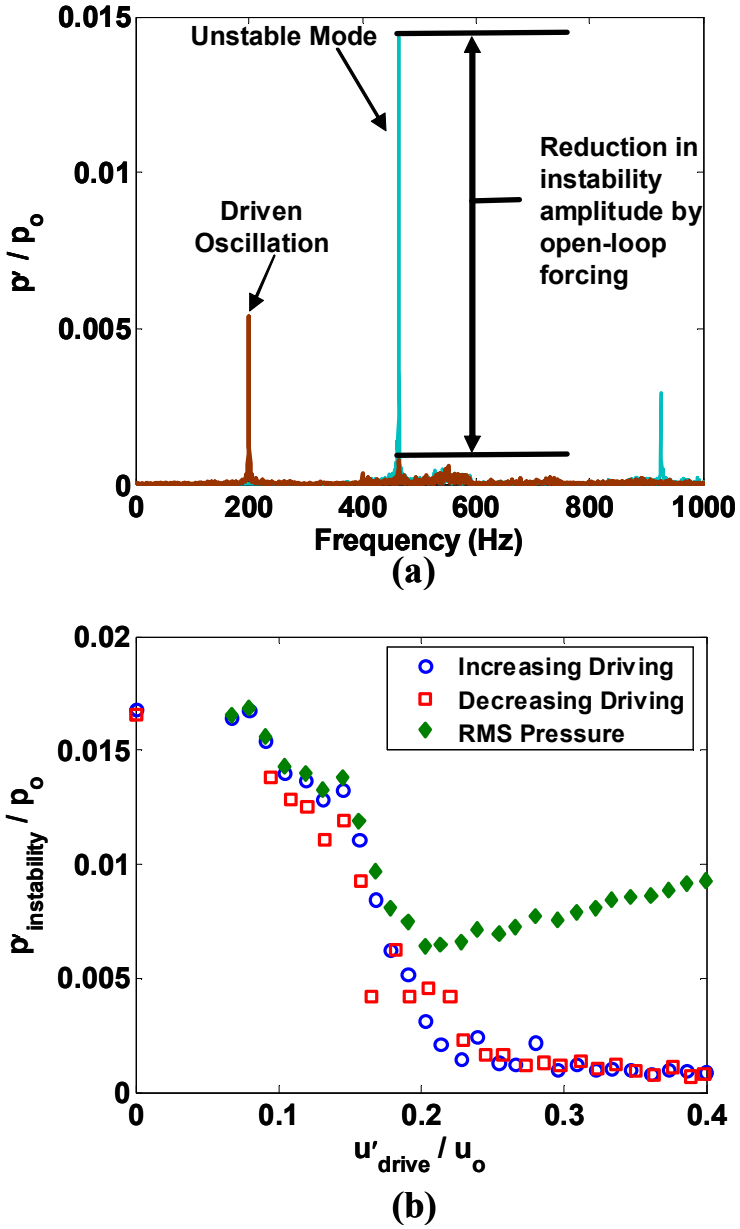

Figure 72. (a) Spectrum of combustor pressure at two driving amplitudes showing decrease in combustor instability mode as driving amplitude is increased (f_{ins} = 461 Hz, f_{drive} = 200 Hz). (b) Dependence of instability amplitude on driving velocity amplitude at 200 Hz driving frequency

These characteristics depend significantly upon driving frequency. Consider first the entrainment amplitude dependence upon driving frequency, which is plotted in Figure 73. The entrainment amplitude, A_e, grows as the forcing frequency is moved away from the instability frequency of 461 Hz, except very close to the instability (f_{drive} = 400-430 Hz). The trend in Figure 73 seems intuitively reasonable, although there is not any specific theory upon which this intuition is based. It should be pointed out, however, that A_e is actually independent of forcing frequency for the model problem considered earlier.

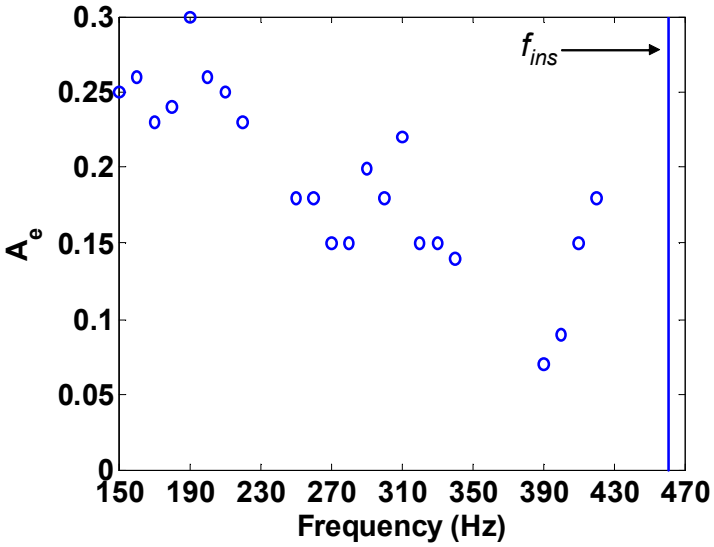

Figure 73. Dependence of velocity entrainment amplitude, A_E upon driving frequency (f_{ins} = 461 Hz).

The entrainment amplitude based upon perturbation pressure, rather than velocity, exhibits a different trend. It increases monotonically with decreasing frequency down to about 230 Hz and then decreases for lower frequencies. This is due to the frequency dependence of the pressure-velocity relation. This result explains the confusion over

this issue raised in the study of Lieuwen & Neumeier, which used the perturbation pressure as a measure of disturbance amplitude [33].

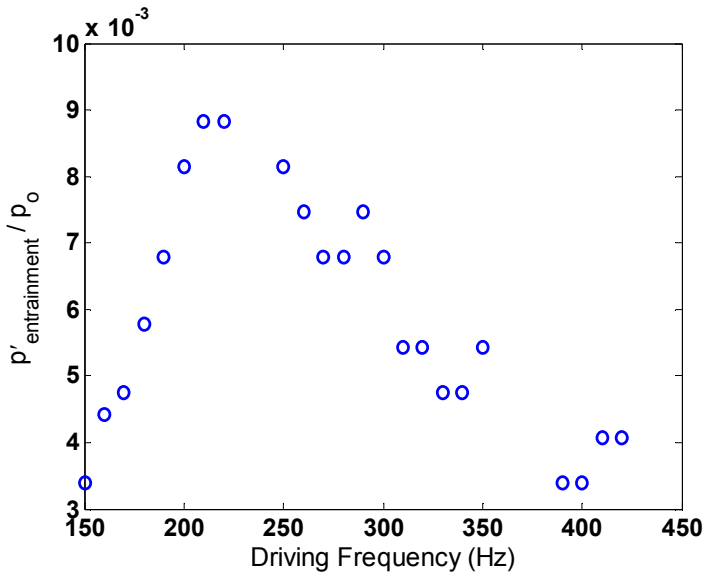

Figure 74. Dependence of pressure entrainment amplitude, A_E upon driving frequency (f_{ins} = 461 Hz).

Next, consider the slope of the instability amplitude rolloff, δ_p, shown in Figure 75. The instability rolloff has a complex dependence on frequency. The highest slopes, and therefore the most rapid rolloff of the instability amplitude, occur at 250 and 400 Hz. Local minima are seen at 160 Hz and 310 Hz. Similarly, the parameter A_L*'s* frequency dependence is shown in Figure 76. In general, A_L is found to be largest at frequencies which are far away from the instability and smallest at frequencies closer to the instability. The values of A_L range from u'/u_o= 0.02-0.10. At 240 Hz, this value decreases linearly from its maximum value, near where the instability rolloff hits its maximum, and flattens out after 310 Hz, where the instability rolloff hits a minimum. In

general, the parameter A_L is seen to change values near local minima and maxima in the instability rolloff value.

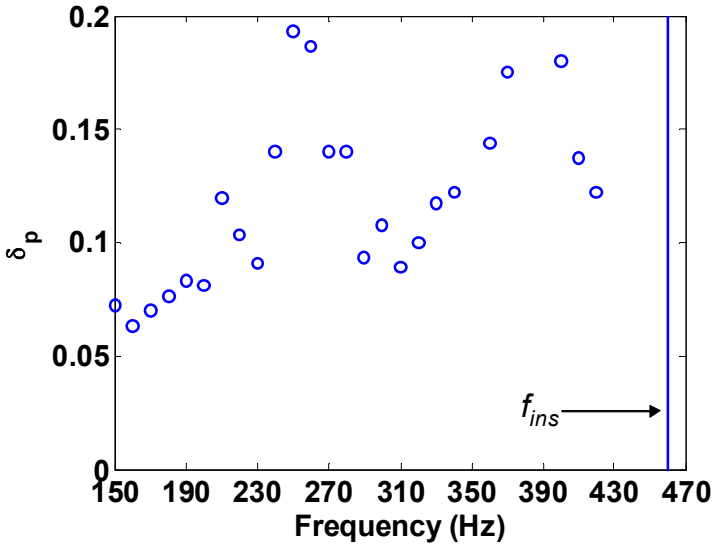

Figure 75. Dependence of instability rolloff, δp, on driving frequency (f_{ins}= 461 Hz).

As these results have direct implication on open loop forcing as an active control methodology, it is of interest to analyze the total acoustic power reduction in the 0-1000 Hz range where power is defined as:

$$Power = \int |p'|^2 df \tag{6.6}$$

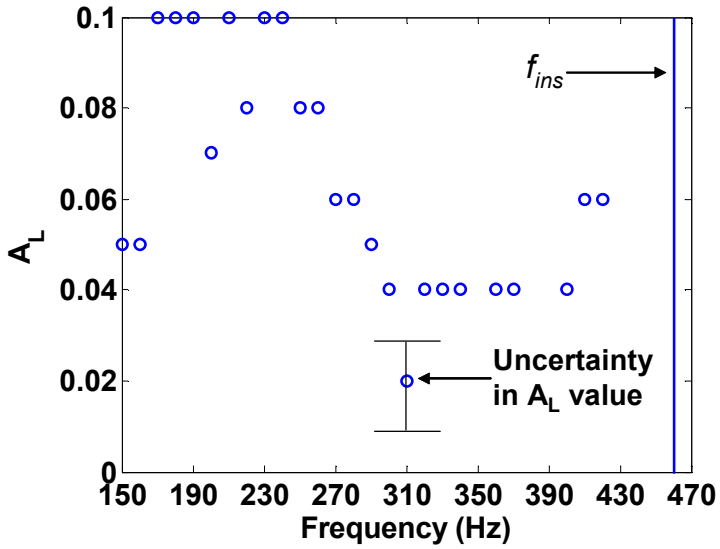

Figure 76. Dependence of A_L parameter (velocity oscillation amplitude range which is independent of forcing) on driving frequency (f_{ins} = 461 Hz)

Figure 77 plots the frequency dependence of the maximum reduction in acoustic power due to open-loop forcing at each forcing frequency. This reduction in acoustic power is quantified by:

$$Power_{red} = \frac{Power_o - Power_{\min}}{Power_o} \tag{6.7}$$

where $Power_o$ and $Power_{min}$ represent the acoustic power in the absence of driving and the minimum acoustic power achieved over the velocity amplitude range. This maximum reduction in acoustic pressure power usually occurs at a forcing amplitude close to A_e. The figure shows that in all cases, the acoustic power is reduced by at least 70%. The best results occur at frequencies where the entrainment pressure amplitude is smallest and

the worst results are where the entrainment pressure amplitude is highest, as may be expected. For larger entrainment amplitudes, more acoustic power is being added into the system at the point of entrainment. Therefore, the reduction in instability amplitude comes at the cost of larger driven amplitudes.

The second condition, delineated Condition 2, was set at an operating condition which corresponded to a lower instability frequency of 350 Hz (obtained with a longer tube). The nominal air and fuel flow rates were identical to those in Condition 1. The effect of increasing the tube length besides lowering the instability frequency was that the instability amplitude is about 50% higher than Condition 1, about 2.2% of the mean pressure. This condition allowed for forcing the unstable mode at frequencies above and below the instability frequency.

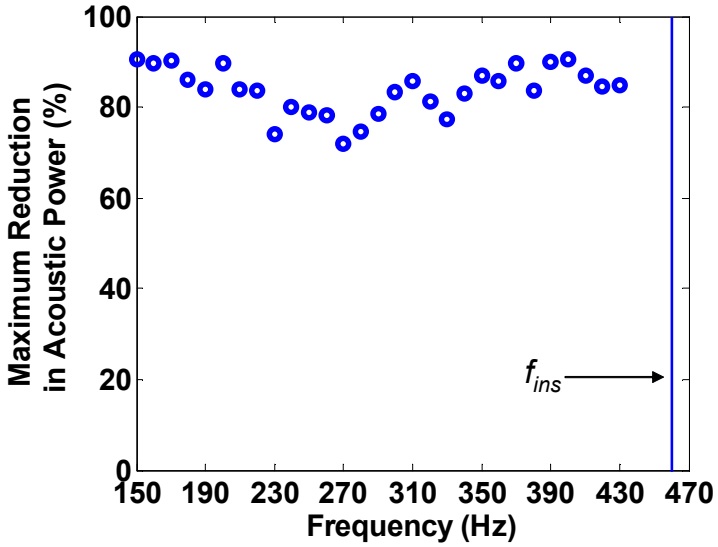

Figure 77. Dependence of maximum acoustic pressure power reduction on driving frequency (f_{ins}= 461 Hz).

Figure 78 plots the maximum percentage reduction in acoustic power in the 0-1000 Hz range that can be achieved. Note that at this operating condition, the effect of driving does not reduce the instability amplitude to near the extent it did for Condition 1. Although the reasons for these differences in the effects of open loop forcing are not fully understood, two factors seem significant: 1) larger levels of acoustic forcing required to overcome the initially higher amplitude oscillations and 2) these higher driving amplitudes, besides acting to quench the instability, introduce other nonlinear phenomenon, such as frequency shifts and spectral broadening..

This latter point is clearly shown in Figure 79, which indicates that the instability shifts from the nominal instability frequency to higher values near 390 Hz. This figure plots two pressure spectra for a driving frequency of 260 Hz, one corresponding to the nominal unstable condition and the other at a driving velocity amplitude of u'_{drive} / u_o = 0.25, where entrainment was seen to occur in Figure 73 at many of the frequencies investigated in Condition 1. For the no driving case, the pressure spectrum shows the oscillations at the fundamental, 350 Hz, and slightly at the first harmonic around 700 Hz. As acoustic forcing is added, the instability amplitude at 350 Hz decreases somewhat, and shifts to a higher frequency, 390 Hz. At this driving frequency (260 Hz), the peak seen near 380-390 Hz does not readily correspond to any harmonics of the fundamental frequency of the driving signal, nor of the natural mode in the combustor.

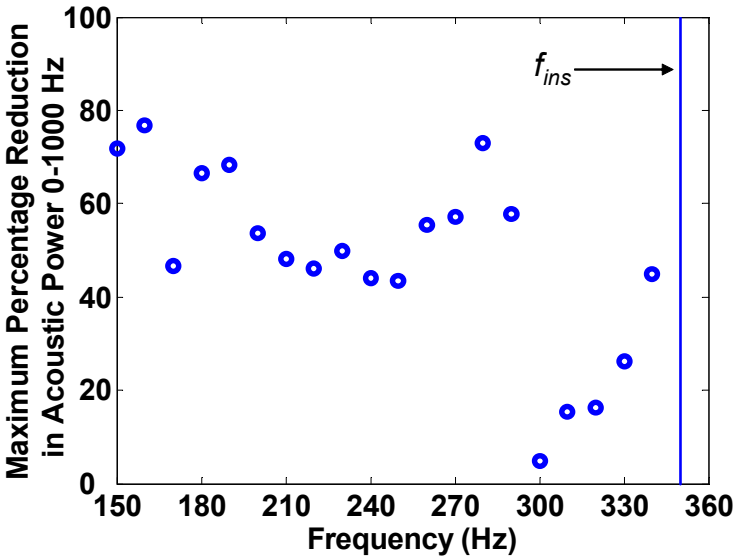

Figure 78. Dependence of maximum acoustic power reduction on driving frequency (f_{ins} = 350 Hz)

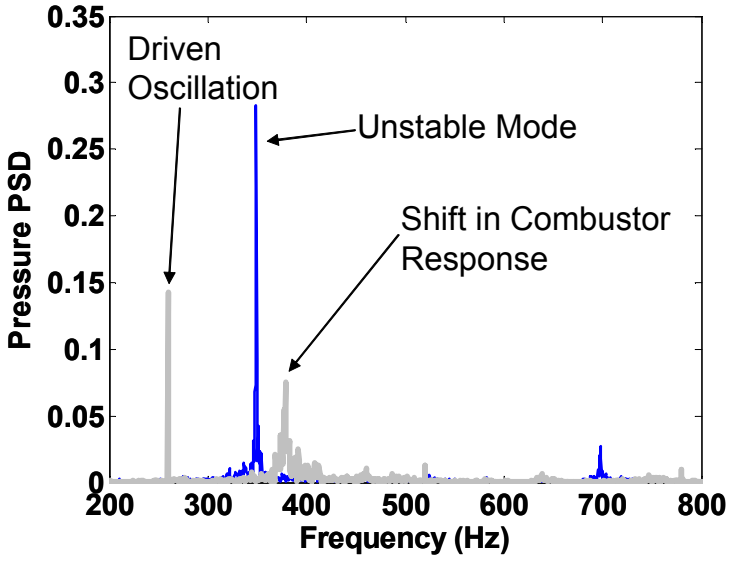

Figure 79. Spectra of combustor pressure at two driving amplitudes showing decrease and frequency shift of combustor instability mode as driving amplitude is increased (f_{ins}= 350 Hz, f_{drive} = 260 Hz)

This behavior is illustrated further in Figure 80. Figure 80(a) plots the pressure spectra in the frequency range of 340-400 Hz for a driving frequency of 260 Hz. For increasing driving amplitudes, the pressure spectra clearly shows the transition of the instability to higher frequencies, away from the nominal value of 350 Hz. In addition, the frequency shifted band is also clearly broadened in frequency space. In contrast, Figure 80(b) plots similar spectra for Condition 1 between 450 and 500 Hz for increasing driving velocity amplitudes for a driving frequency of 200 Hz. In this case, it is clear that the instability is quenched and no such shift in the frequency is present. This difference, while not understood, appears to be the distinguishing feature between cases where open loop forcing was and was not effective.

Furthermore, the instability amplitude, even when shifted, never is reduced to zero with increasing driving amplitude – the pressure spectra in Figure 80(a) indicates that there are still some remnants of the instability at the highest driving, compared to essentially none in Figure 80(b). Therefore, the driving does not truly quench the instability for this condition compared to the previous case. The "final" frequency to which the instability settled at highest driving levels ranged between 380 and 400 Hz, with no apparent relationship to the fundamental driving frequency or instability mode (except for driving frequencies whose harmonics are in this regime – e.g. f_{drive} = 190 Hz).

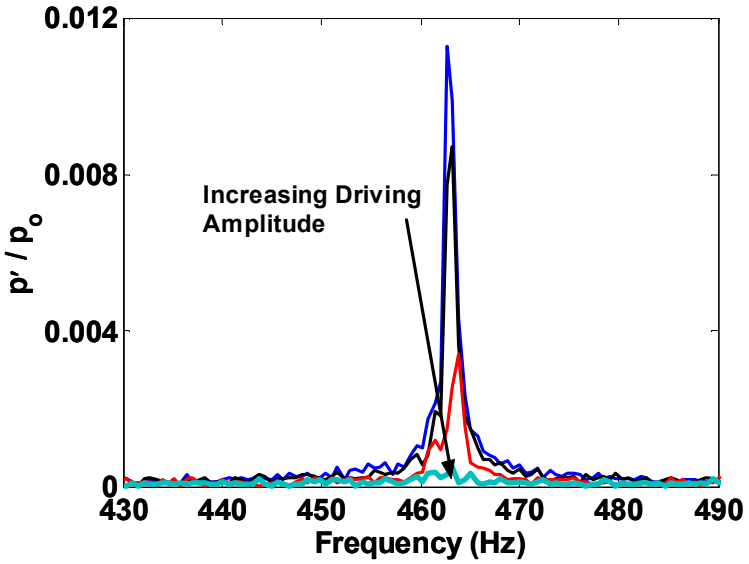

(a)

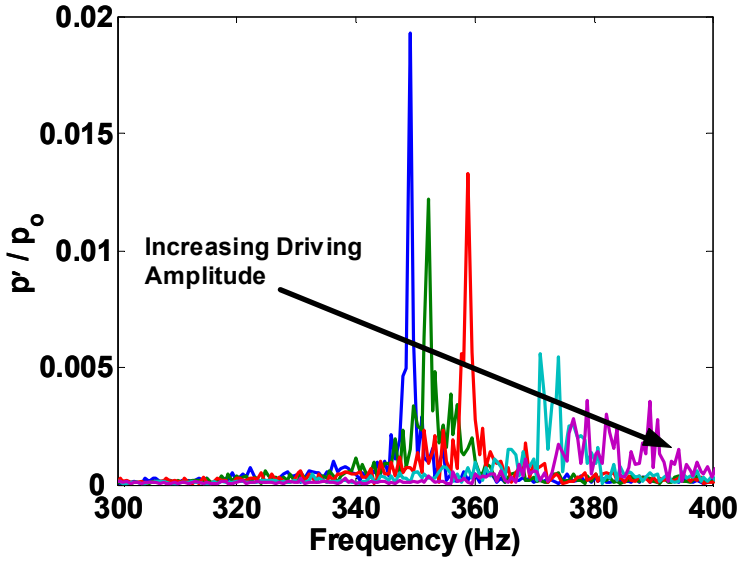

(b)

Figure 80. Dependence of pressure spectra in vicinity of nominal instability frequency for (a) Condition 1 (f_{ins} = 461 Hz, f_{drive}= 200 Hz) and (b) Condition 2 (f_{ins} = 350 Hz, f_{drive} = 260 Hz)

For both Condition 1 and Condition 2, forcing of the combustor at driving frequencies greater than the instability frequency was largely unsuccessful. For instance, Figure 73 (instability frequency = 461 Hz) shows that forcing at f_{drive} = 390 Hz results in an extremely low quenching amplitude of u'/u_o = 0.05. For the corresponding case for Condition 2 (instability frequency = 350 Hz), the effect of forcing at 390 Hz is almost negligible. Figure 81 shows that the instability neither changes significantly in amplitude (as manifested by the area under the curve) nor shifts to 390 Hz. The small shift in frequency around 350 Hz is not monotonically dependent on driving amplitude. This effect is not understood at this point. The effect of these larger driving frequencies was investigated up to 500 Hz. Only one frequency was found to cause the significant frequency shift with slight amplitude reduction (~20%), f_{drive} = 420 Hz. All other driving frequencies either did not have an effect on the instability or were beginning to cause the frequency to shift, but were limited due to loudspeaker limitations.

Similar behavior was observed for Condition 3, which used the same tube length as Condition 1. Figure 82 illustrates the shift in instability frequency for increasing driving amplitude at a driving frequency of 160 Hz. Figure 82 shows that for initial increases, the instability frequency varies very little, but then changes significantly between u'/u_o = 0.1 – 0.15. For this condition, the instability frequency shifts from its nominal value around 510 Hz to approximately 550 Hz at high driving amplitudes. In addition, the effect of non-resonant driving is, at best, as effective in reducing the acoustic power in the system as the results shown for Condition 2, and in many cases is less effective. Figure 82 indicates that the maximum reduction in acoustic power is approximately 50% for this case.

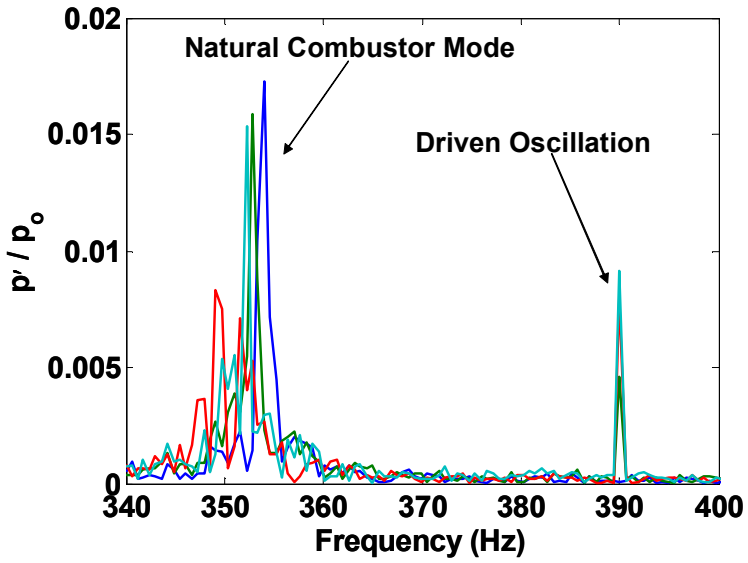

Figure 81. Combustor pressure spectra for increasing driving amplitude for f_{drive} greater than f_{ins} (f_{drive} = 390 Hz)

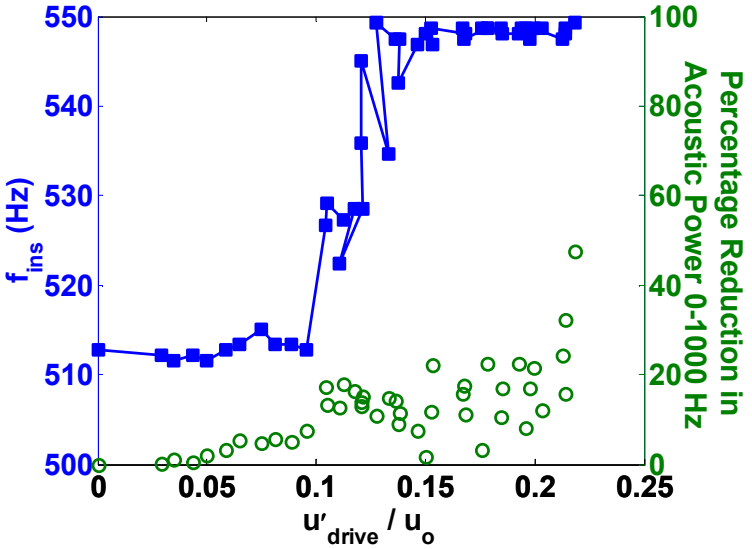

Figure 82. Dependence of instability frequency and acoustic power on driving amplitude, f_{drive} = 160 Hz)

6.3 Discussion

The nonlinear interactions between driven and natural combustor modes, both stable and unstable, are analyzed in this chapter. The results presented are qualitatively similar to nonlinear oscillator theory, but there are substantial differences which raise new questions.

In Section 6.1, it is found that the nonlinear combustion processes introduces a saddle-node bifurcation in pressure amplitude occurs around the natural frequency. Noting this, it seems important that active control methodologies must be appropriately cognizant of these dynamics (e.g., see Ref. [75]). The effects that the nonlinear combustion process introduces can be qualitatively compared to nonlinear oscillator theory, but the use of the transfer function as the source of the external driving, *E(t)* in Eq. (6.1), cannot account for these effects.

In Section 6.2, the effect of external is seen to have several effects on the self-excited oscillations by altering their amplitude, spectral bandwidth and/or frequency. The effectiveness of open-loop control of the combustor significantly depends on the operating condition. For cases where the instability mode is reduced slightly and shifts in frequency, quenching does not occur, although some amplitude reductions may be observed. In addition, for both conditions investigated, the ability to significantly affect the self-excited mode is quite difficult at driven frequencies above the instability frequency. Only at a few select cases has open-loop forcing been able to achieve this quenched state. The instability rolloff, δ_p, and parameter, A_L, are seen to both have complex dependencies on the driving frequency and are substantially dependent on the frequency spacing. The shift in frequency observed in some cases when forcing is

increased implies that the dominant nonlinearity in the system may not be in the damping term as outlined in Eq. (6.2), but actually nonlinearity in stiffness. The reason why the combustor shifts exhibits one type of nonlinearity over another is unclear, however.

CHAPTER 7

CONCLUSIONS AND FUTURE WORK RECOMMENDATIONS

This chapter discusses the main findings and conclusions for this thesis and provides recommendations for future work.

The first two chapters provided an introduction to nonlinear processes in unstable combustors as well as a thorough literature review of the previous theoretical and experimental research which has been performed. These chapters emphasized two specific needs: 1) a thorough understanding of how operating conditions (driving frequency, equivalence ratio, etc) can affect nonlinear combustion processes and thus the limit cycle behavior in unstable combustors and 2) a need to determine which mechanisms proposed theoretically in the literature are important in unstable combustors. Furthermore, it was stressed that the nonlinear flame dynamics of a turbulent, swirl-stabilized combustor may be substantially different from the dynamics of laminar, Bunsen-type flames.

The results presented in this thesis demonstrated nonlinearities in the flame chemiluminescence for large velocity oscillation amplitudes at several operating conditions. The corresponding pressure amplitudes at the point of nonlinear response range between 1 – 2% of the mean pressure indicating that nonlinear combustion

processes, as opposed to gas dynamic nonlinearities, dominate the response of the flame chemiluminescence.

Saturation of the chemiluminescence occurred at values of 20 – 100% of the mean values dependent on the operating condition. In addition, the shape and behavior of the transfer function between the velocity oscillation and chemiluminescence oscillation amplitudes changes significantly for different operating conditions. These results stress that a single combustor exhibits a variety of mechanisms controlling the nonlinear response of the flame at these large amplitude oscillations.

Three mechanisms have been identified in this thesis that control the nonlinear flame dynamics for different operating conditions – parametric instability, vortex roll-up, and unsteady flame liftoff. First, for lower mean velocity conditions, nonlinearity in the flame response is observed to occur when the subharmonic of the flame chemiluminescence oscillation reaches appreciable amplitudes. This subharmonic response appears to be a manifestation of the parametric instability by the unsteady acceleration of the flame front by the velocity field. Secondly, for higher mean velocity conditions, vortex rollup and unsteady flame liftoff are seen to control the nonlinear behavior. Both these mechanisms show that the central recirculation zone is an important controlling factor of the nonlinear flame dynamics. All of the mechanisms controlling the nonlinear flame response of the two combustors in this study are shown to be affected significantly by Strouhal number and the ratio of the oscillating velocity and laminar flame speed, stressing the importance of the mean and oscillating velocity on the nonlinear flame response. In addition, the harmonic and subharmonic of the flame influence the flame's nonlinear behavior when acoustically forced.

Finally, the nonlinear combustion process is shown to significantly affect the frequency response of combustors in both stable and unstable operation when forced acoustically. Nonlinear oscillator theory provides qualitative explanations for the effects observed in these experiments.

This thesis also identified many areas for future research. First, this thesis has emphasized the lack of understanding of nonlinear processes in unstable gas turbine combustors. Specifically, while this thesis has outlined important mechanisms that influence the nonlinear flame behavior, additional work is necessary to incorporate these effects into a complete model that captures all of the dynamics. In addition, further experimental work is needed that investigates factors such as swirl number, higher Reynolds number flows, and fuel type.

Secondly, further results pointed out that the central recirculation zone and more generally swirling flows may play a large role in the nonlinear flame behavior to large amplitude forcing. A detailed study of the velocity field that focuses on recirculation zone size, strength, and general characteristics under large amplitude forcing is necessary to couple with the results from the OH PLIF images presented. Furthermore, further work on vortex-flame interactions is necessary to improve current modeling approaches in this area.

Finally, the interactions between different frequency regimes under large amplitude forcing have been shown in this thesis to be important. No analysis of the flame response under the influence of self-excited and driven oscillations has been performed up to this point. The dynamics of the flame could play a very large role in the quenching/entrainment behavior of the system response. The nonlinear behavior of the

flame response to forced oscillations and its influence on the frequency response curves in a gas turbine combustor was shown in the previous chapter. Detailed imaging of the flame along with corresponding chemiluminescence could perhaps give better information on the fundamental differences between the two operating conditions presented herein. Further work in modeling these interactions is also important for improving nonlinear combustion process models.

APPENDICES

APPENDIX A

FLOW MEASUREMENTS AND UNCERTAINTY ANALYSIS

A.1 Flow Metering and Equivalence Ratio Measurements

A.1.1 Gas Turbine Combustor Simulator

The air flow rate through the combustor was metered by fixing the supply pressure upstream of a calibrated, sonic orifice with a regulator on the control panel. The following empirical equation describes the dependence of the air mass flow rate through this orifice upon the supply pressure:

$$\dot{m}_{air} = 0.0484\left(P_{air,gauge}\right) \tag{A.1}$$

where the pressure is given in psi (English rather than SI units are used because the gauge used for calibration measured pressure in psi). Equation (A.1) is a linear, least square fit through the data and differs by no more than 5 percent from the measured flow rates in the range between 5-26 g/s. The pressure gauge that was used to determine the air flow

rate was inscribed with 2 psi subdivisions and was accurate within 0.25 percent over the full scale (0-600 psi). Assuming that these different uncertainties are independent and can be added in a mean squares sense [76] yields a maximum overall uncertainty in air flow rate of $\sqrt{(0.05)^2 + (0.0025)^2 + (0.005)^2}$ = 5 percent, where it was assumed that the pressure could be read off the gauge with an accuracy of ±1 psi over a range of 200-600 psi.

Fuel was metered in the same way, where the following empirical equation describes the dependence of the fuel mass flow rate upon the supply pressure:

$$\dot{m}_{gas} = 0.0022\left(P_{gas,gauge}\right) \tag{A.2}$$

The flow rates predicted by Eq. (A.2) differ from the measured rates by no more than 3 percent over the fuel flow rates of 0.3-1.0 g/s. The pressure gauge that was used to determine the fuel flow rate was identical to the air pressure gauge discussed above. The different uncertainties in the flow rate and pressure can be added in a mean squares sense to yield an overall uncertainty in fuel flow rate of 3 percent.

The corresponding uncertainty in the equivalence ratio, ϕ, is determined using the following formulation [76]. The dependence of an uncertainty, U, in the value of some function f(x,y,..) where x and y are independent variable is given by:

$$U = \sqrt{\left(\frac{\partial f}{\partial x} U_x\right)^2 + \left(\frac{\partial f}{\partial y} U_y\right)^2 + \ldots} \tag{A.3}$$

Using the uncertainties obtained above for the fuel and air flow rates, the uncertainty in the equivalence ratio, ϕ, is given by:

$$\begin{aligned} \frac{U_\phi}{\phi} &= \sqrt{\left(\frac{U_{air}}{\dot{m}_{air}}\right)^2 + \left(\frac{U_{fuel}}{\dot{m}_{fuel}}\right)^2} = \sqrt{(0.05)^2 + (0.03)^2} \\ &= 0.06 \end{aligned} \tag{A.4}$$

Therefore, the uncertainty in the equivalence ratio measurements is 6 percent.

A.1.2 Atmospheric Swirl-Stabilized Burner

The air and gas flow rates through the combustor were measured with rotameters. The air and fuel rotameters were inscribed with 0.5 SCFM and 2 SCFH markings, respectively. The uncertainty in the flowrate readings therefore, were 0.25 SCFM and 1 SCFH for the air and fuel. The maximum uncertainty in the flow rates would occur at the lowest Reynolds number investigated. These values were calculated to be 5% for both the fuel and air. As the Reynolds number increased, the uncertainty values diminished to approximately 2.2%.

The resulting uncertainty in the equivalence ratio using Eq. (A.4) is ranges between:

$$\frac{U_\phi}{\phi} = \sqrt{(0.05)^2 + (0.05)^2} \rightarrow \sqrt{(0.022)^2 + (0.022)^2} \\ = 0.07 \rightarrow 0.03 \tag{A.5}$$

Showing that the uncertainty in ϕ ranges from 7 percent at the lowest flowrate to 3 percent at the highest flowrate investigated.

A.2 Frequency Resolution

The uncertainty in the spectral characteristics of the combustors utilized in this study can be determined by noting that the data was sampled at 10000Hz and 16384 data points were taken, implying a resolution of 10000/16384 = 0.61 Hz/data point. The maximum uncertainty in the instability frequency is half of this resolution, implying an uncertainty in the instability frequency of 0.3 Hz.

APPENDIX B

VELOCITY MEASUREMENTS

B.1 Determination of Velocity at Flameholder in Gas Turbine Combustor Simulator

This section describes the acoustic analysis to obtain the velocity oscillation amplitude at the flameholder from the hot film measurement location in the inlet of the combustor described in Chapter 3; see Figure 15. The geometry is idealized from that in Figure 15 to the following schematic shown below in Figure 83 .

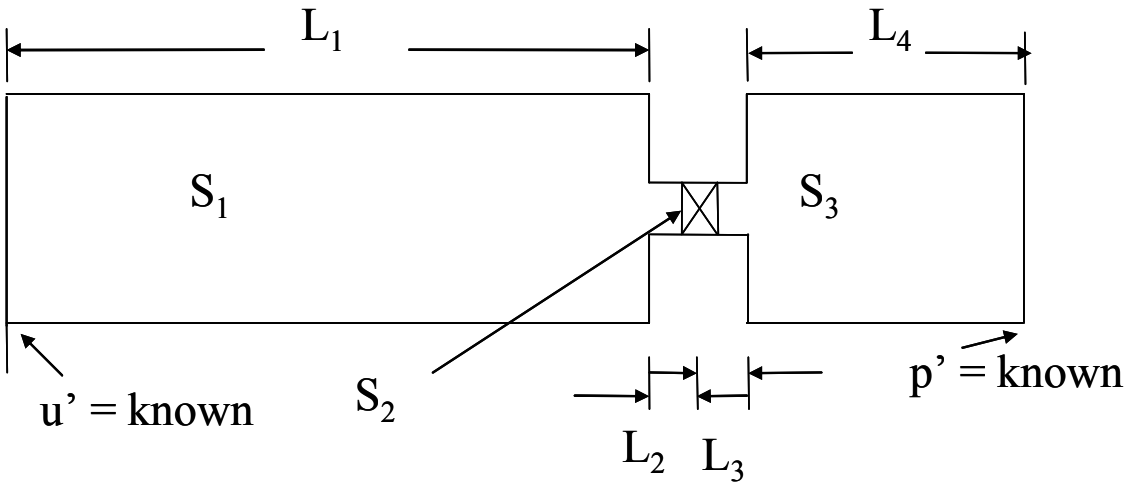

Figure 83. Schematic of combustor geometry for acoustic model

The model assumes (1) an inviscid, perfect gas, (2) low Mach number mean flow, (3) the regions of interest are uniform and isentropic (i.e., $Ds/Dt = 0$), (4) the acoustic

fields are one-dimensional, and (5) the swirler has a purely resistive impedance. Assumption (4) is appropriate because the model predicts the longitudinal velocity oscillation amplitude at the flameholder (although higher dimensional wave motions are excited by, e.g., scattering by turbulence and inhomogeneities, these disturbances are evanescent, or non-propagating, acoustic disturbances that are rapidly damped [77]). Assumption 2 implies that all terms that are O(M^2) can be neglected as well. Therefore, the acoustic field can be described with the equations of mass, momentum and energy:

Mass: $$\frac{\partial \rho}{\partial t} + \nabla \bullet \rho \vec{u} = 0 \tag{B.1}$$

Momentum: $$\rho \frac{\partial \vec{u}}{\partial t} + \rho \vec{u} \bullet \nabla \vec{u} = -\nabla p \tag{B.2}$$

Energy: $$\rho \frac{\partial e}{\partial t} + \rho \vec{u} \nabla \bullet h = 0 \tag{B.3}$$

Using assumptions (2) – (4), the appropriate linearized conservation equations are:

Mass: $$\frac{\partial \rho'}{\partial t} + \bar{\rho} \frac{\partial u'}{\partial x} + \bar{u} \frac{\partial \rho'}{\partial x} = 0 \tag{B.4}$$

Momentum: $$\bar{\rho} \frac{\partial u'}{\partial t} + \bar{\rho}\bar{u} \frac{\partial u'}{\partial x} = -\frac{\partial p}{\partial x} \tag{B.5}$$

Energy: $$\frac{\partial s'}{\partial t}+\overline{u}\bullet\nabla s'=0\Rightarrow\frac{1}{\overline{\rho}}\left(\frac{\partial\rho'}{\partial t}+\overline{u}\frac{\partial\rho'}{\partial x}\right)=\frac{1}{\gamma\overline{p}}\left(\frac{\partial p'}{\partial t}+\overline{u}\frac{\partial p'}{\partial x}\right) \tag{B.6}$$

Eq. (B.4)-(B.6) can be combined into the acoustic wave equation given by [77]:

$$\left(\frac{\partial}{\partial t}+\overline{u}\frac{\partial}{\partial x}\right)^2 p'-c^2\frac{\partial^2 p'}{\partial x^2}=0 \tag{B.7}$$

Since this study was performed using harmonic oscillations, the solutions for the acoustic pressure and velocity can be determined [77]:

$$p'=\left(Ae^{\frac{ikx}{1+M}}+Be^{\frac{-ikx}{1-M}}\right)e^{-i\omega t} \tag{B.8}$$

$$u'=\frac{1}{\overline{\rho c}}\left(Ae^{\frac{ikx}{1+M}}-Be^{\frac{-ikx}{1-M}}\right)e^{-i\omega t} \tag{B.9}$$

where the coefficients, A and B, represent the magnitudes of the acoustic waves propagating in the positive and negative directions, respectively. Eq. (B.8) and (B.9) can be applied to each region of interest. In order to solve for the amplitudes and phase of the acoustic waves, appropriate boundary conditions and matching conditions must be applied, however.

The boundary conditions for the model are simply the measured velocity oscillation in the inlet section measured with the hot film probe and the measured pressure oscillation in the combustor. Matching conditions are used at all area changes in the form of pressure and mass continuity, i.e.:

$$\begin{aligned} p'_i &= p'_j \\ A_i \vec{u}_i' &= A_j \vec{u}_j' \end{aligned} \tag{B.10}$$

where *i* and *j* signify different regions. The swirler, as mentioned above in assumption (5), is treated as a resistance defined by:

$$\Delta p = k \rho u^2 \tag{B.11}$$

Linearizing Eq. (B.11) yields:

$$\Delta p' = 2k \bar{\rho} \bar{u} u' \tag{B.12}$$

The solutions for the pressure and velocity in Eq. (B.8) and (B.9) can be used for each region (denoted by L_1, L_2, L_3, and L_4) in the schematic in Figure 83. Thus the problem becomes a set of 8 linear, algebraic equations from which the velocity of the flameholder can be determined for the (given) frequency of interest. The result from this

model is given in Figure 84 which plots the ratio of the inlet velocity oscillation amplitude to the calculated burner-mouth velocity oscillation amplitude. The solid line in Figure 84 marks the area ratio between the two "measurement" locations. Figure 84 shows that the model predicts the velocity ratio to be equal approximately to the area ratio for the frequency range of 150 – 350 Hz. Above and below this point, significant deviation of the curve from the area ratio line is observed. As mentioned in Chapters 3 and 4, due to these large deviations near 100 and 420 Hz, observed trends in these frequency regimes must be treated with care. In addition, no nonlinear flame response studies were performed near these frequencies.

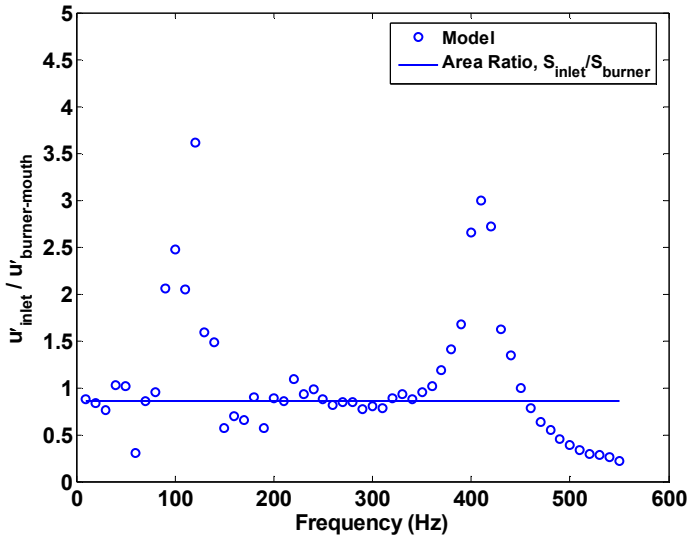

Figure 84. Calculated velocity ratio between inlet and burner-mouth locations in gas turbine combustor simulator

B.2 Determination of Velocity at Flameholder in Atmospheric Swirl Burner

A number of velocity measurement techniques and instrumentation have been implemented for the past many years, to perform the standard task of flow field characterization and instantaneous velocity measurement. In addition, many of these instrumentation techniques cannot handle the potentially high temperatures very close to the flameholder location. This was the case for the experiments in Chapter 4. Since the flame transfer function is defined by the oscillating heat release divided by the oscillating velocity amplitude at the flameholder location, this effect can introduce error unless accounted for. Therefore, the two microphone method was utilized in all experiments on the atmospheric, swirl-stabilized combustor.

The discussion for the remainder of this section follows that from Waser and Crocker [47]. The two microphone method is derived from Euler's equation which states:

$$-\nabla P_o = \rho\left[\frac{\partial u}{\partial t} + \left(u \bullet \nabla\right)u\right] \tag{B.13}$$

where P_o is the hydrostatic pressure, ρ is the density of the medium, u is the velocity and t is time. Linearizing Eq. (B.1) and neglecting mean flow effects yields:

$$\frac{\partial u}{\partial t} = -\frac{1}{\rho}\nabla p \tag{B.14}$$

In this study, the axial velocity oscillations are dominant in the frequency range of interest (f_{drive} < 500 Hz). Therefore, Eq. (B.2) can be further simplified to account for the velocity in one direction:

$$\frac{\partial u_x}{\partial t} = -\frac{1}{\rho}\frac{\partial p}{\partial x} \tag{B.15}$$

Expressing the pressure gradient by a finite difference approximation where ∂p is replaced by $\Delta p = p_2\text{-}p1$, the difference in pressure between the two pressure transducers, and ∂x is replaced by Δx, the separation difference, Eq. (B.3) becomes:

$$\frac{\partial u_x}{\partial t} = -\frac{1}{\rho}\left[\frac{p_2 - p_1}{\Delta x}\right] \tag{B.16}$$

By applying the Fourier Transform, defined in Eq. (3.4), Eq. (B.4) becomes:

$$\int_{-\infty}^{\infty} \frac{\partial u_x}{\partial t}\exp(-i\omega t)dt = -\frac{1}{\rho\Delta x}\left[P_2 - P_1\right] \tag{B.17}$$

where P_1 and P_2 are the Fourier Transforms of the pressure signals p_1 and p_2, respectively. Integrating the left hand side of Eq. (B.5) by parts yields:

$$e^{-i\omega t}u\Big|_{-\infty}^{\infty} + i\omega\int_{-\infty}^{\infty} ue^{-i\omega t}dt = -\frac{1}{\rho\Delta x}\left[P_2 - P_1\right] \tag{B.18}$$

The second term on the left hand side is simply the Fourier transform of the velocity multiplied by $i\omega$. The first term on the left hand side is undefined. Waser and Crocker [47] show that by forcing the velocity in this first term to be zero at plus and minus infinity, the consequence is that the ordinary Fourier transform becomes a finite Fourier transform. However, since a finite Fourier transform is utilized in most practical signal processing techniques, this approach is valid within the limits of digital signal processing. Therefore, Eq. (B.6) is rearranged to give:

$$U \simeq \frac{i}{\omega\rho\Delta x}\left[P_2 - P_1\right] \tag{B.19}$$

The two pressure transducers (Kistler model 211B5) were calibrated at a nominal driving frequency of 200 Hz using a Model 4228 Brüel & Kjäer calibrator. The calibrated sensitivities were within 1 percent of their factory calibrations. The spacing of the transducers was set to 0.014 m which allowed for accurate velocity measurements of frequencies down to approximately 100 Hz [47]. For the frequency range of interest in

these studies (100 – 420 Hz), the ratio of the acoustic wavelength to the transducer spacing ranged from 58 – 245. Therefore finite difference errors of the pressure gradient are insignificant. In addition, since the sources (loudspeakers) are nearly 3m from the measurement location, near field effects on this measurement technique are insignificant as well [47].

APPENDIX C

ADDITIONAL TRANSFER FUNCTIONS AND PHASE ANGLES

This appendix presents flame transfer functions which were not shown in the main body of this thesis in Chapter 4 and Chapter 5. In addition, the corresponding *u'-CH** phase angles are also presented.

C.1 Flame Transfer Function Measurements – Gas Turbine Combustor Simulator

This section presents transfer function measurements for the gas turbine combustor simulator described in Chapter 4. Four frequencies were not presented in the discussion in Chapter 4. These transfer functions and corresponding phases are presented below in Figure 85. In all four cases, the transfer function remained linear throughout the entire velocity amplitude range. In addition, the phase angle amplitude dependence follows the trends which were shown in Figure 33.

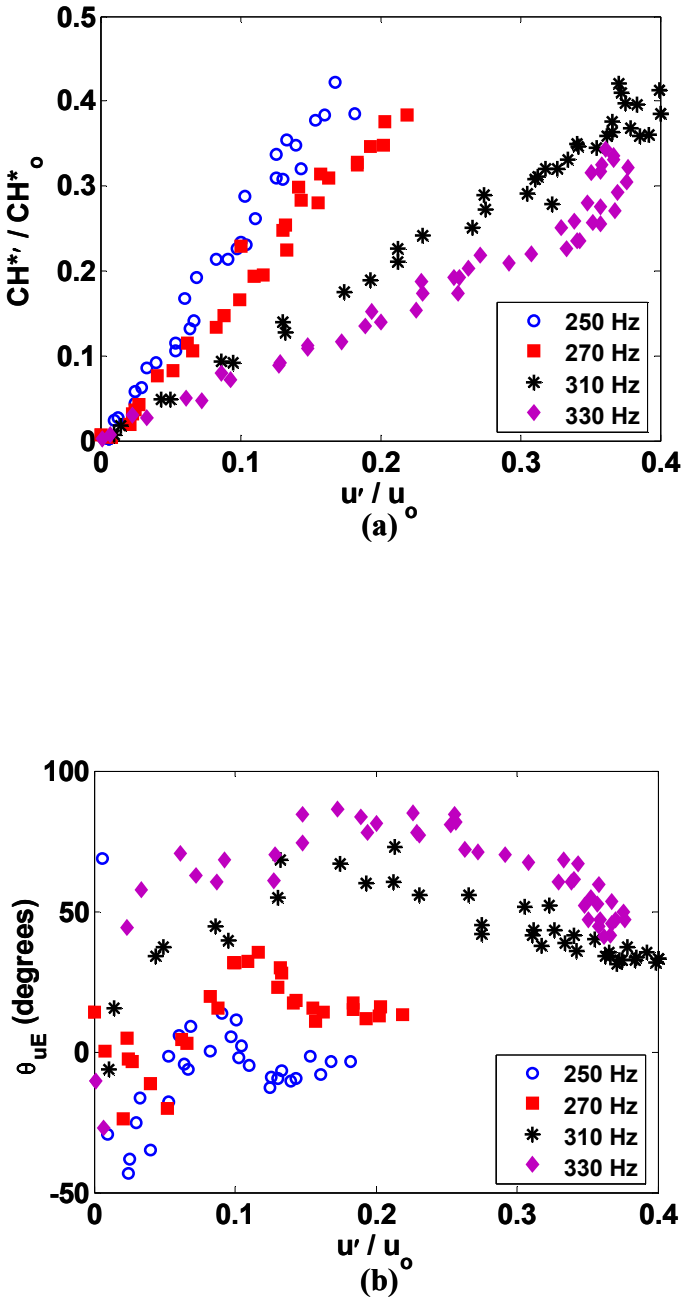

Figure 85. Dependence of (a) *CH chemiluminescence and (b) *u'-CH*'* phase angle on velocity oscillation amplitude for varying driving frequencies. Uncertainty in phase angle for $u'/u_o < 0.05$, $\Delta\theta \sim 30°$; for $u'/u_o > 0.05$, $\Delta\theta \sim 2°$ ($\phi = 0.95$).**

C.2 Flame Transfer Function Measurements – Atmospheric Swirl Combustor

C.2.1 Re_D = 21000

This section illustrates the remainder of the flame transfer functions which were obtained for the lowest Reynolds number investigated in Chapter 5, Re_D = 21000; see Figure 86. Transfer functions for 130 – 150 Hz are not shown. The frequency range for these tests, as outlined in Chapter 5, was f_{drive} = 100 – 420 Hz. In addition the corresponding phase angles are also presented; see Figure 87.

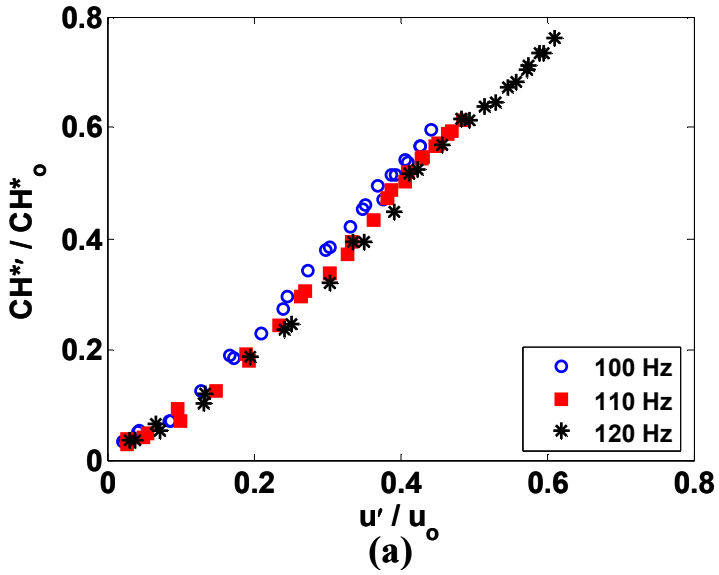

Figure 86(a-j) Dependence of CH* chemiluminescence oscillation amplitude on amplitude of velocity fluctuations for varying driving frequency (f_{drive} = 100 – 420 Hz, Re_D = 21000, ϕ = 0.80).

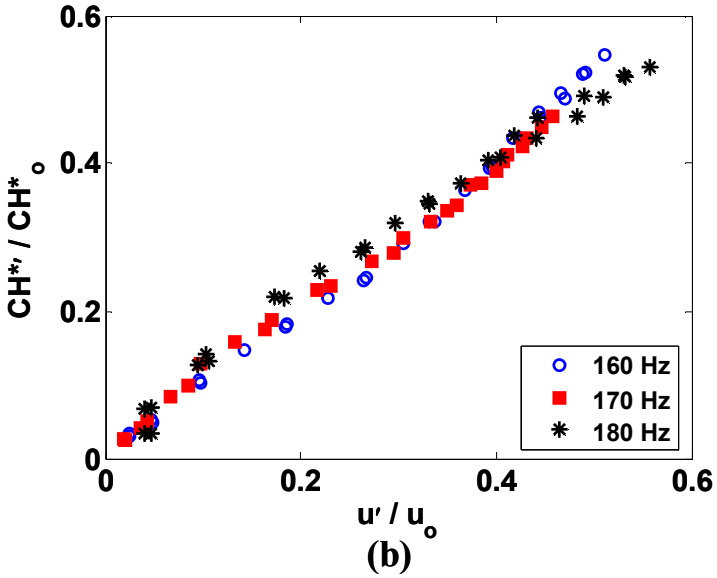

(b)

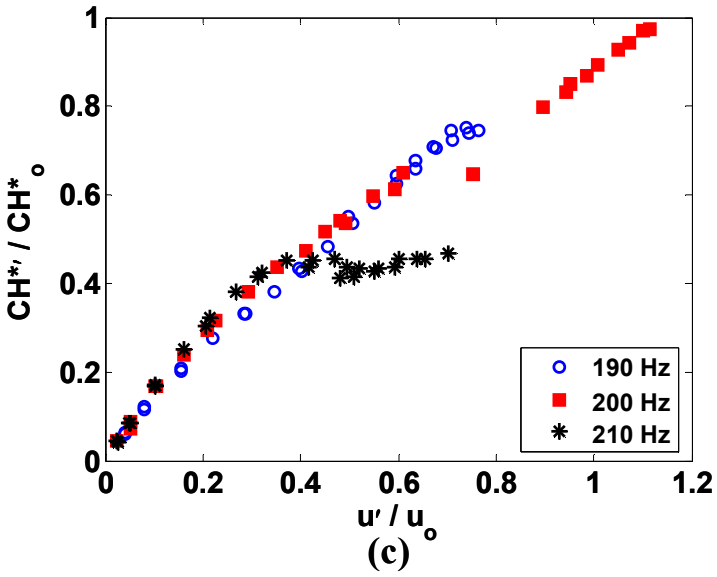

(c)

Figure 86 continued

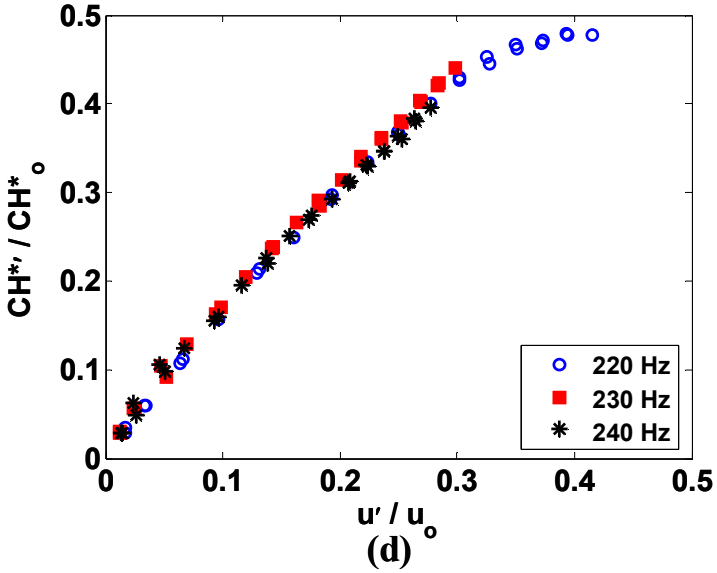

(d)

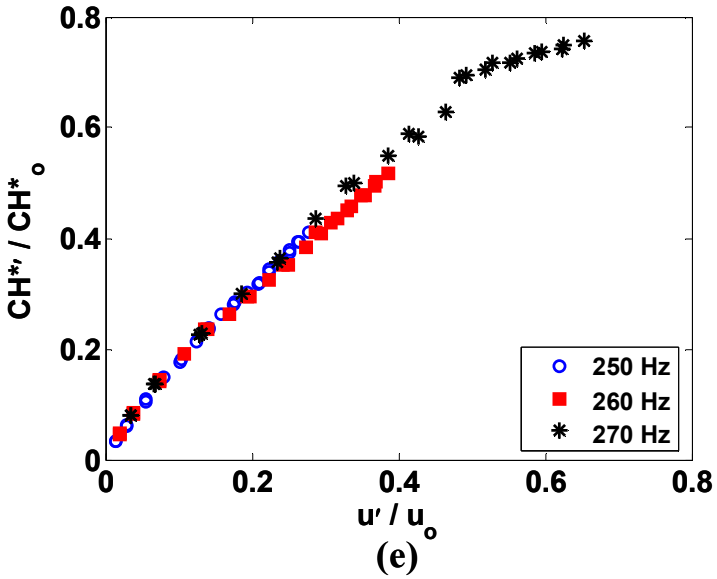

(e)

Figure 86 continued

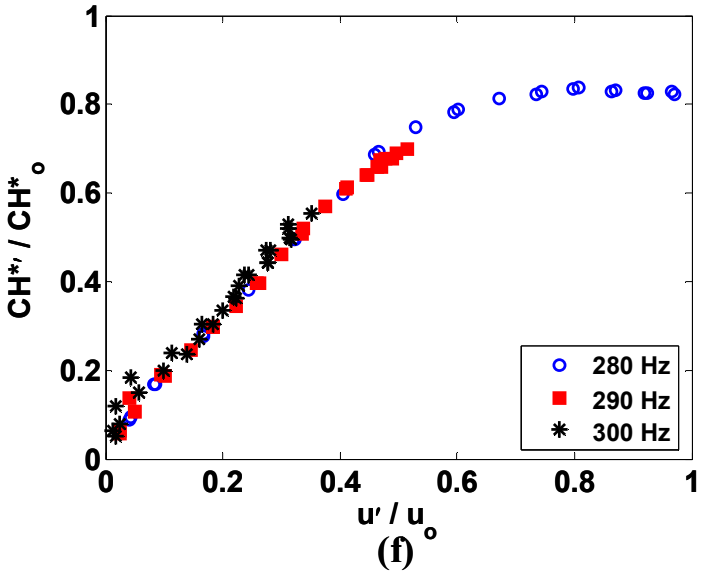

(f)

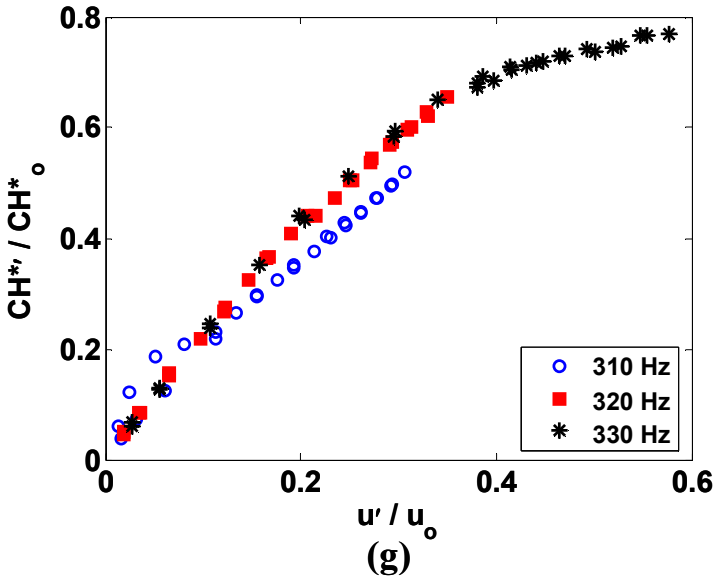

(g)

Figure 86 continued

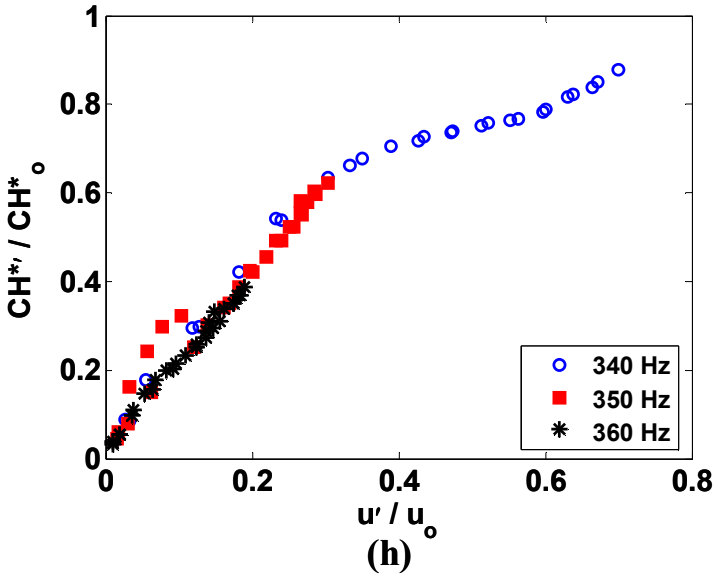

(h)

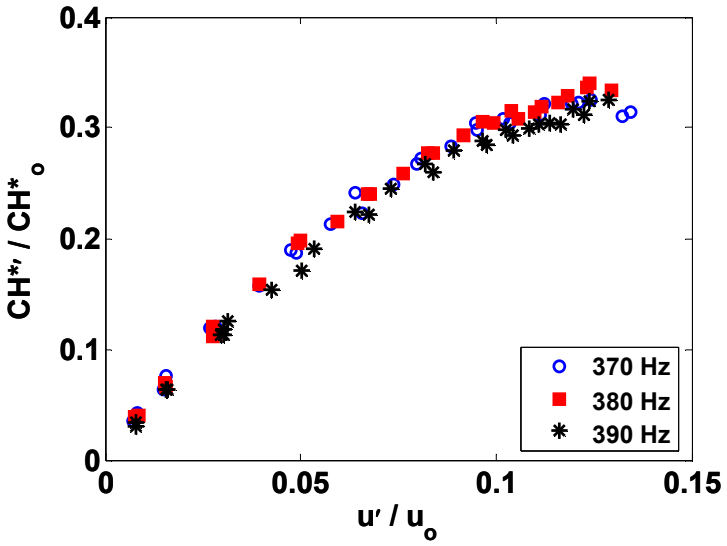

(i)

Figure 86 continued

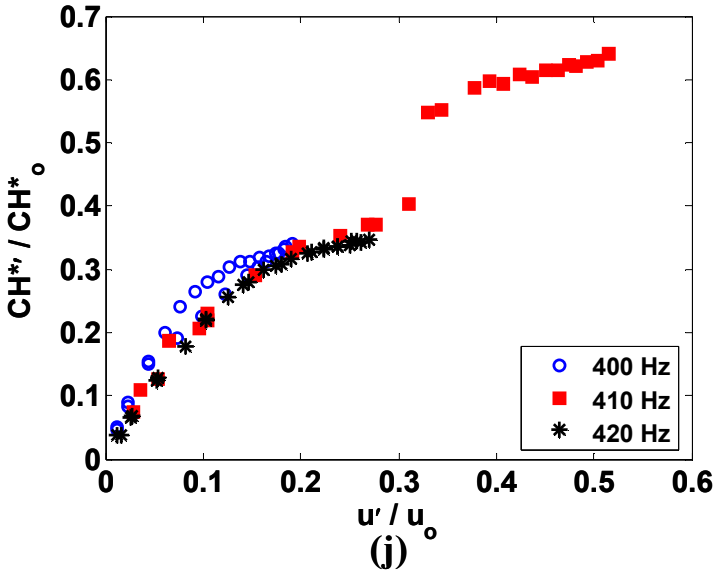

Figure 86 continued

The corresponding *u'-CH*'* phase angles for this frequency range are shown below in Figure 87.

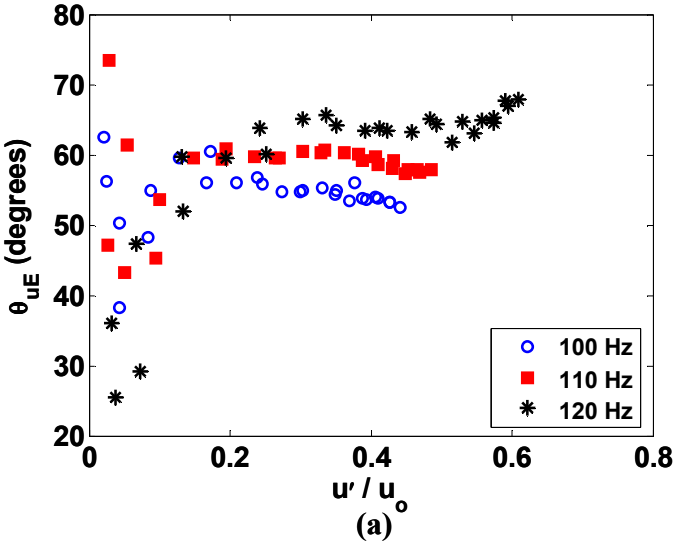

Figure 87(a-j). Dependence of *u'-CH*'* phase angle on amplitude of velocity fluctuations for varying driving frequency (f_{drive} = 100 – 420 Hz, Re_D = 21000, ϕ = 0.80). Uncertainty in phase angle < 5°.

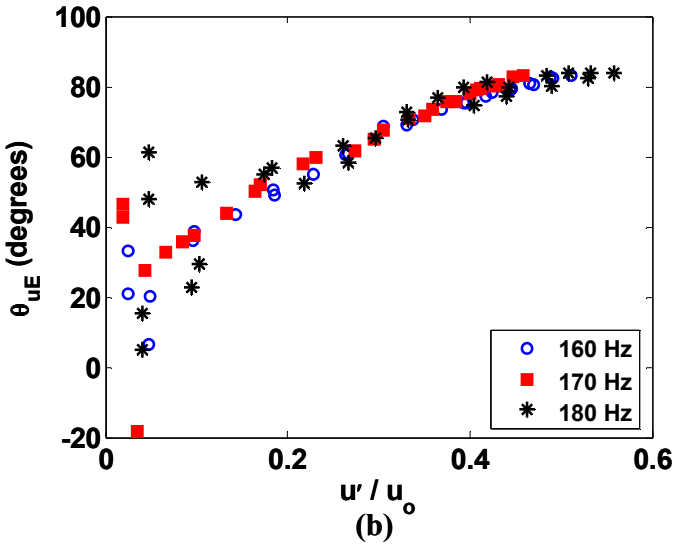

(b)

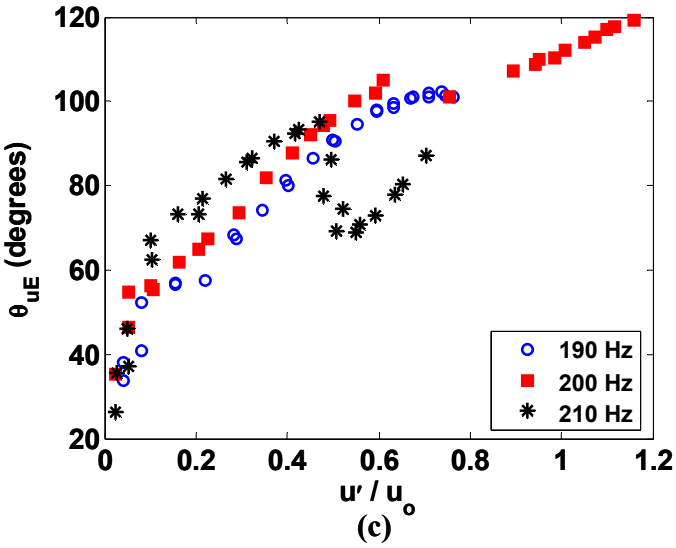

(c)

Figure 87 continued

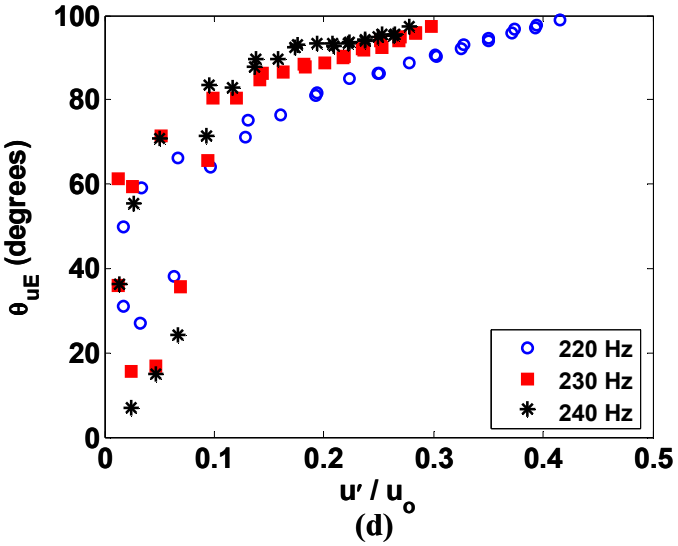

(d)

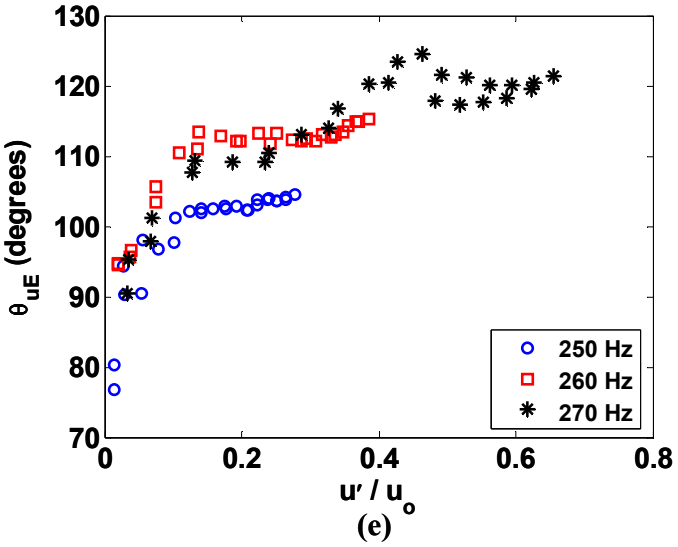

(e)

Figure 87 continued

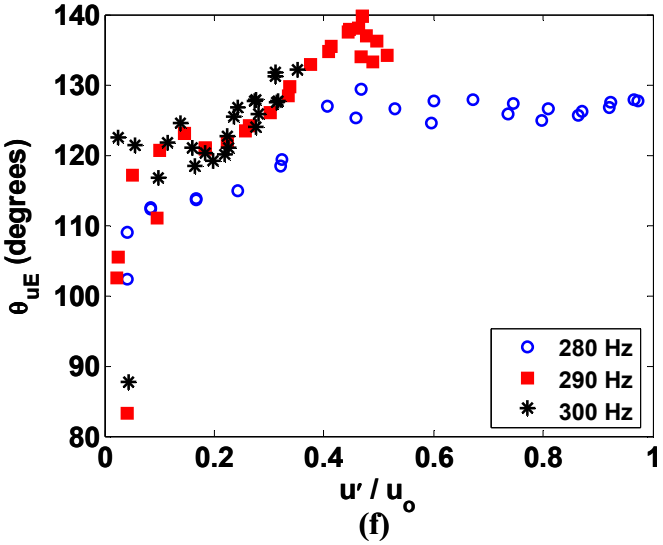

(f)

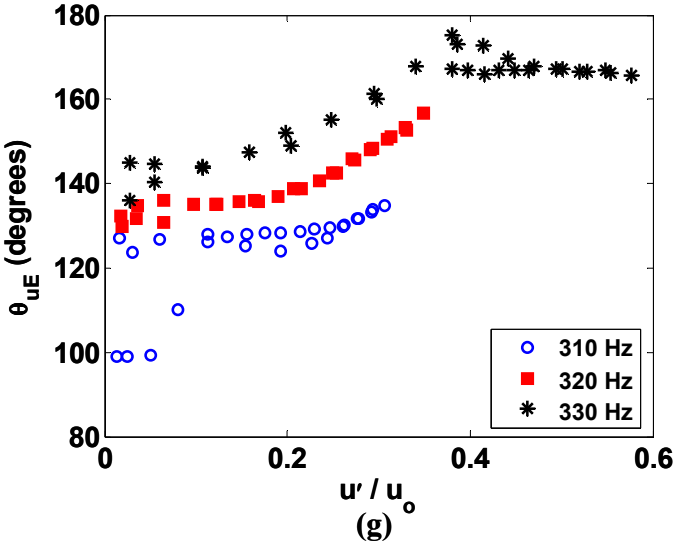

(g)

Figure 87 continued

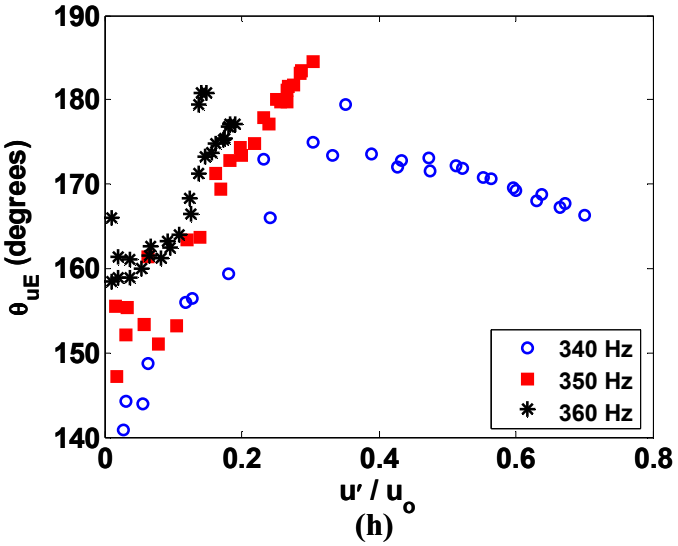

(h)

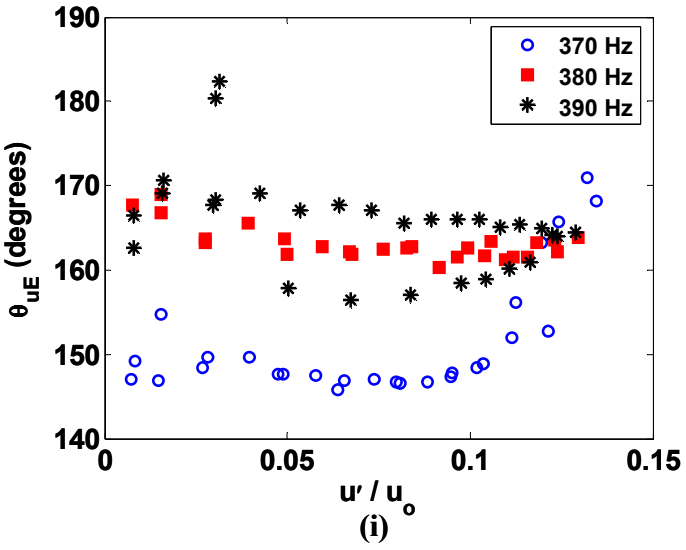

(i)

Figure 87 continued

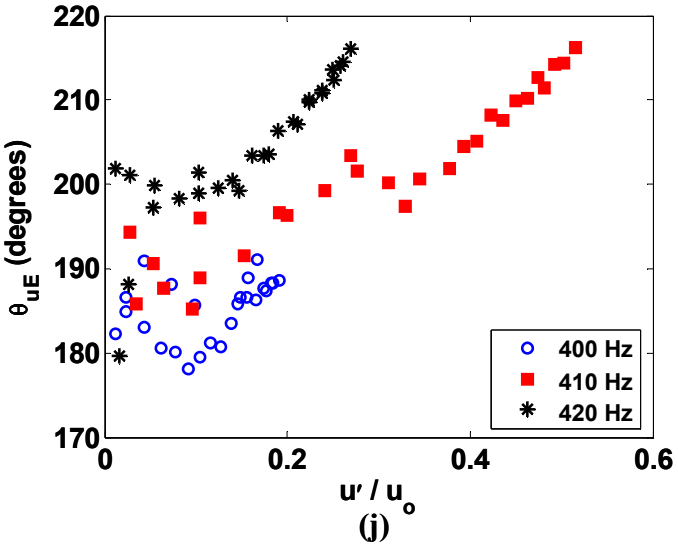

Figure 87 continued

C.2.2 Re_D = 30000

This section presents additional transfer function and phase angle results for Re_D = 30000. Flame transfer functions in the frequency range of 100 – 420 Hz are presented in Figure 88. In addition, the corresponding *u'-CH** phase angle are presented for the entire frequency range in Figure 89.

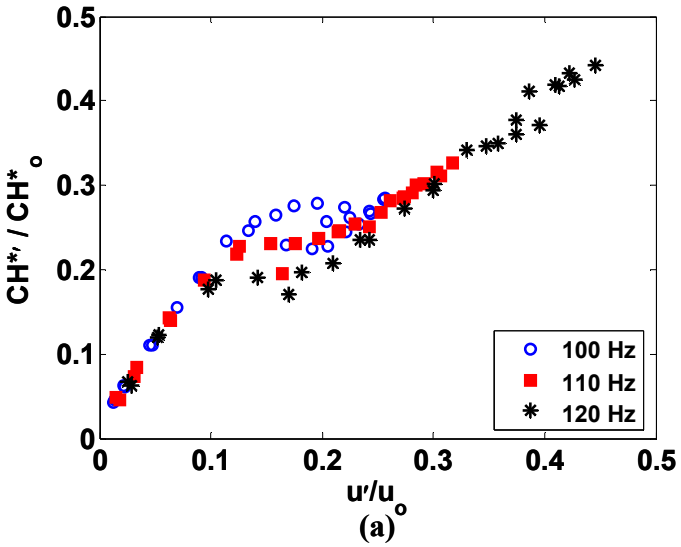

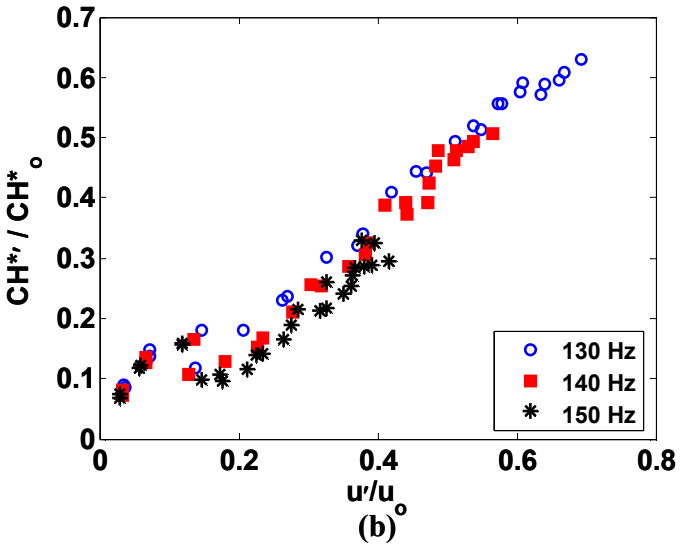

Figure 88(a-j). Dependence of CH* chemiluminescence oscillation amplitude on amplitude of velocity fluctuations for varying driving frequency (f_{drive} = 100 – 420 Hz, Re_D = 30000, ϕ = 0.80).

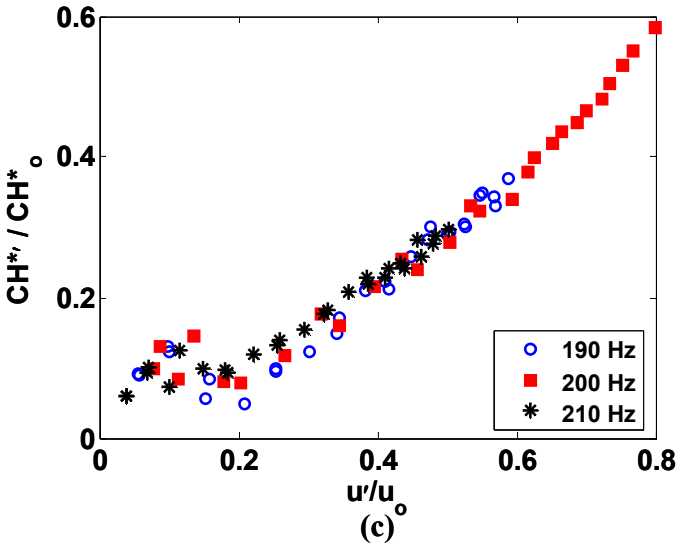

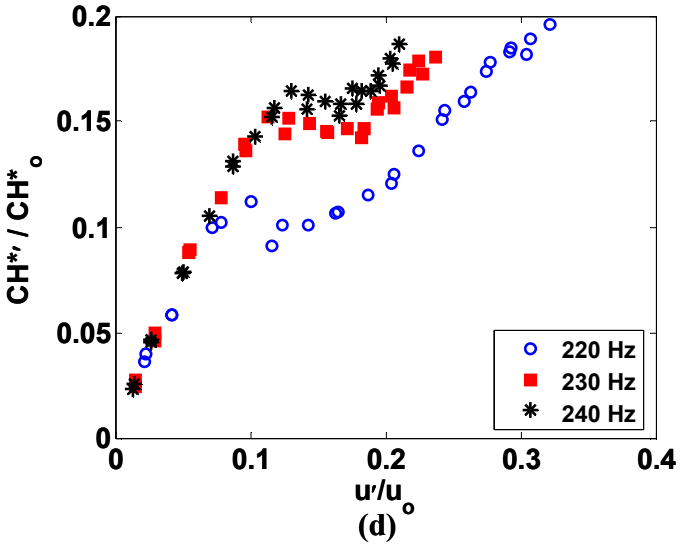

Figure 88 continued

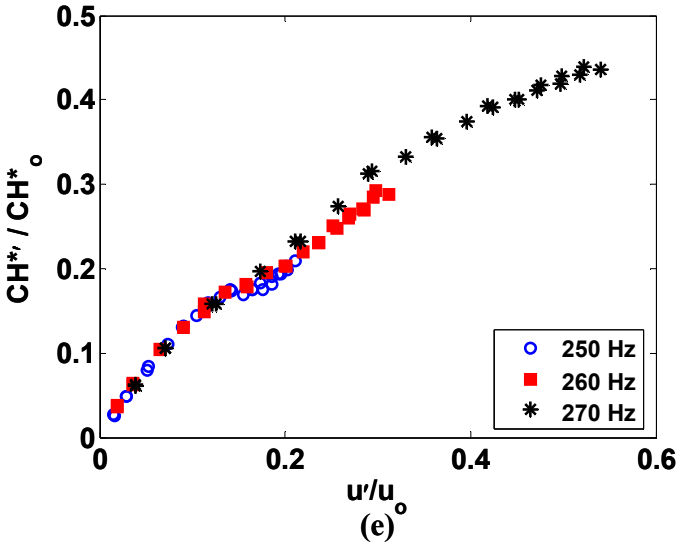

(e)

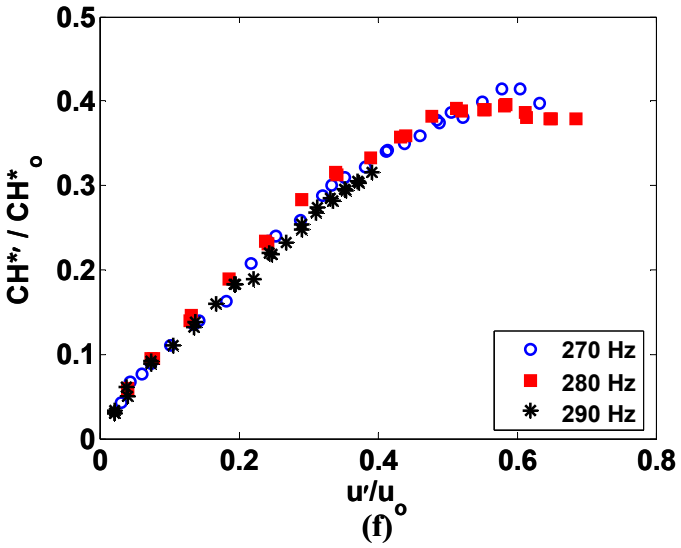

(f)

Figure 88 continued

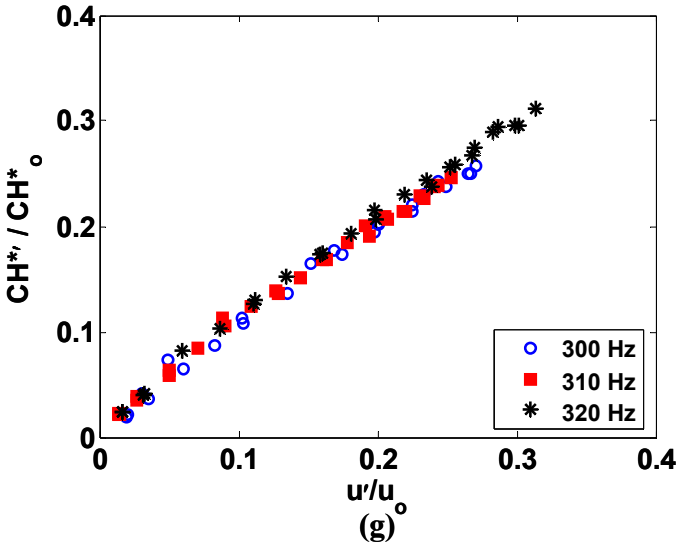

(g)

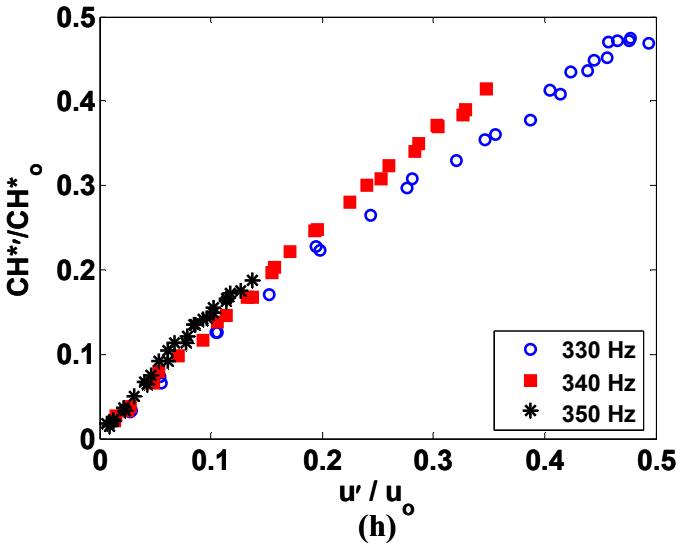

(h)

Figure 88 continued

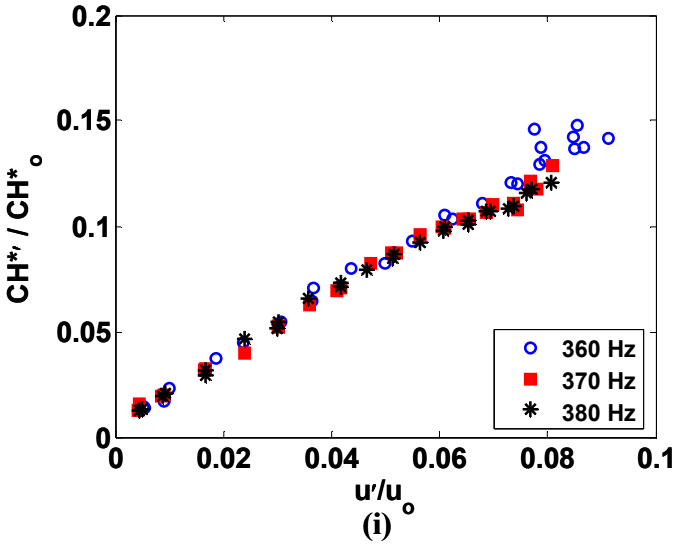

(i)

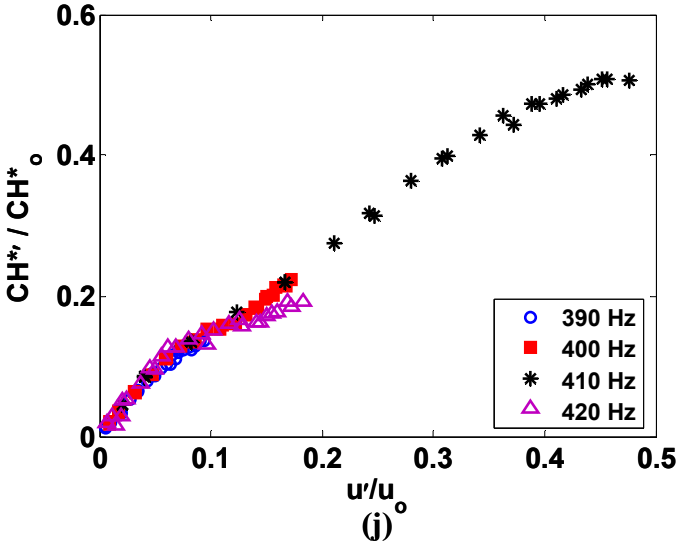

(j)

Figure 88 continued

The *u'-CH*'* phase angles for the entire frequency range at this Reynolds number are presented below in Figure 89.

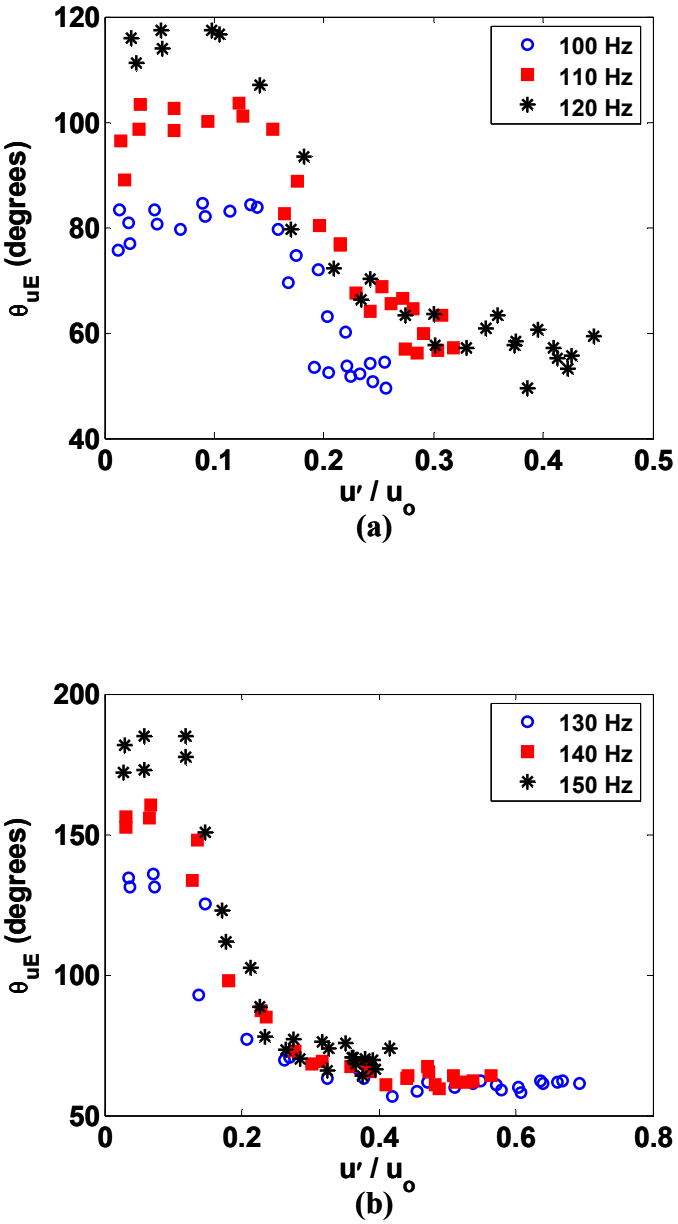

Figure 89(a-k). Dependence of *u'-CH*'* phase angle on amplitude of velocity fluctuations for varying driving frequency (f_{drive} = 100 – 420 Hz, Re_D = 30000, ϕ = 0.80). Uncertainty in phase angle < 5°.

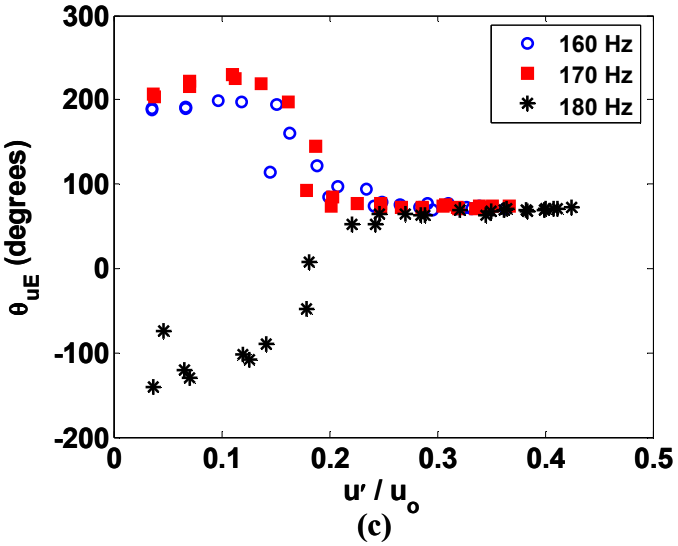

(c)

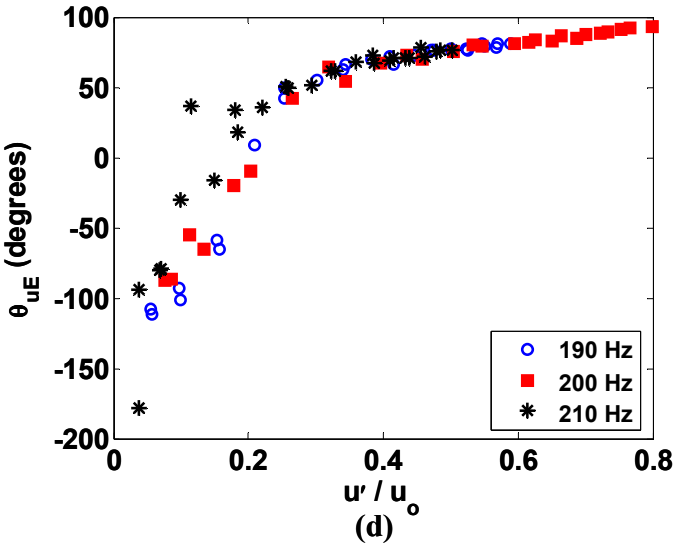

(d)

Figure 89 continued

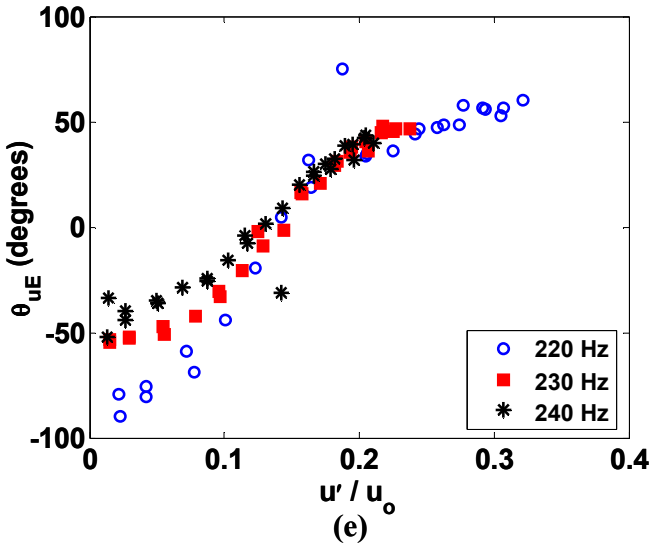

(e)

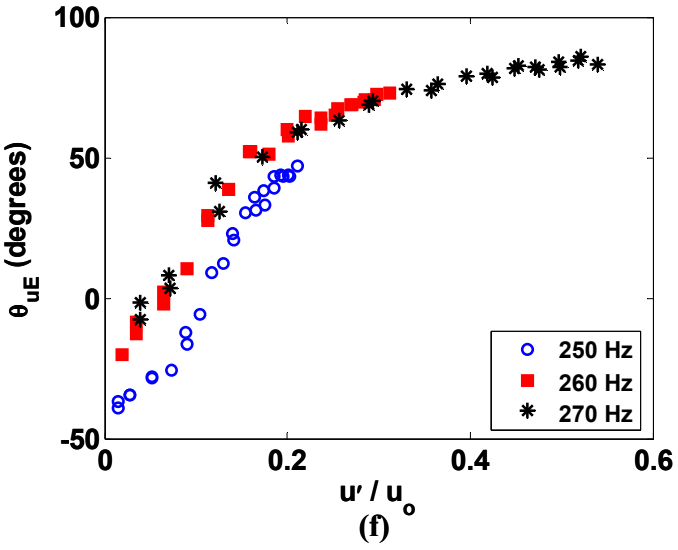

(f)

Figure 89 continued

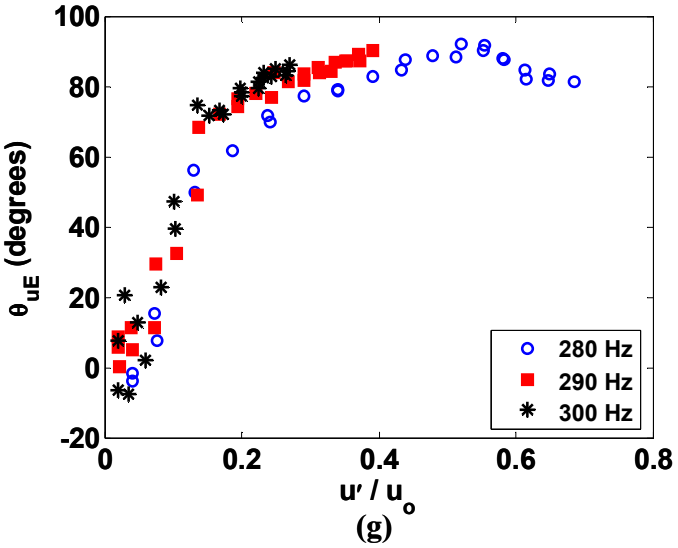

(g)

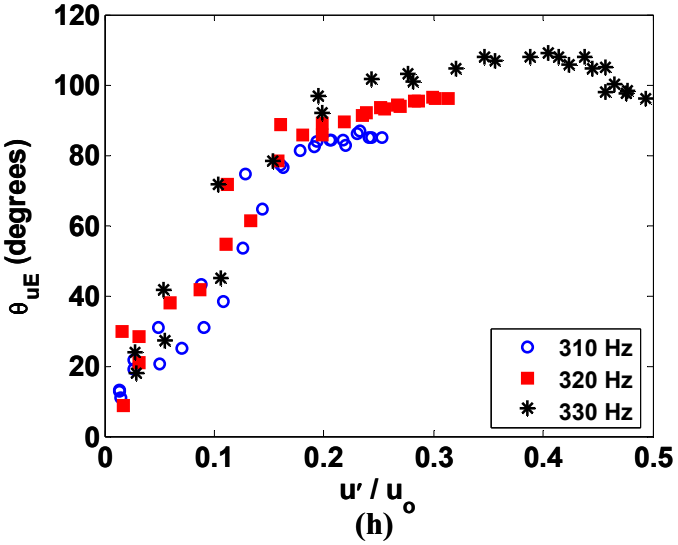

(h)

Figure 89 continued

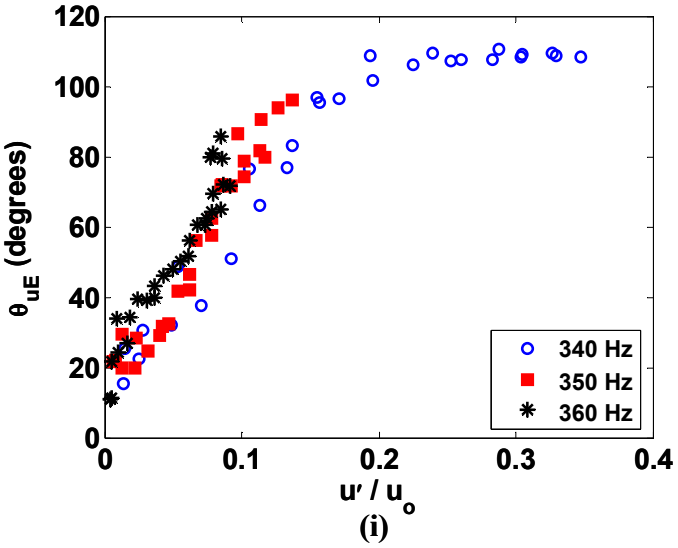

(i)

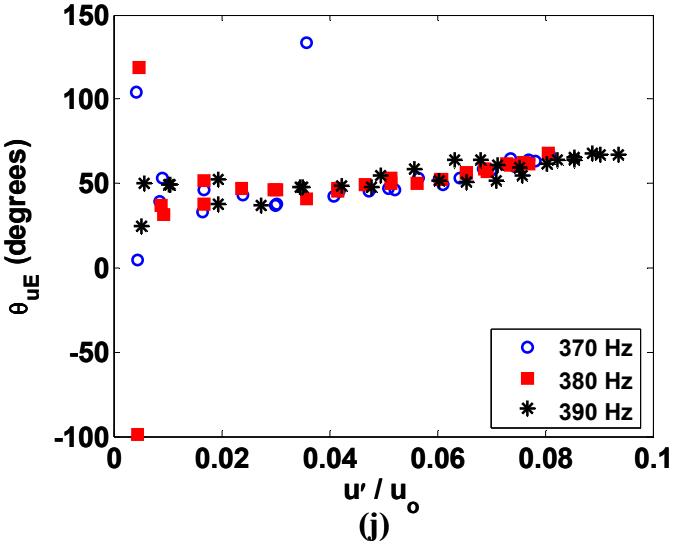

(j)

Figure 89 continued

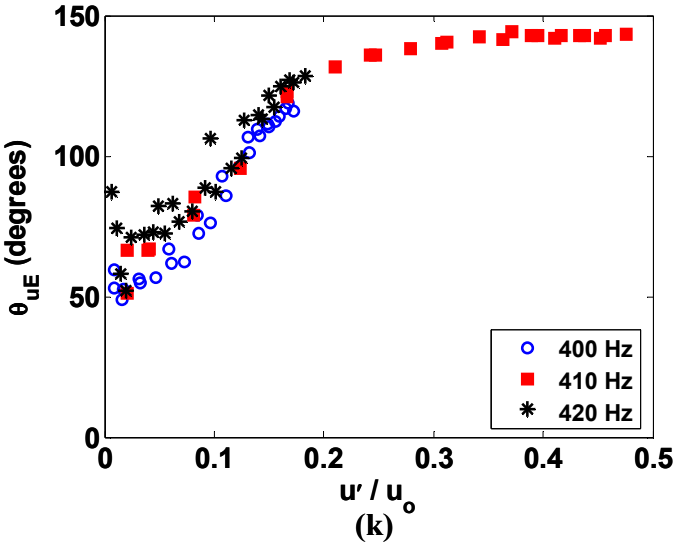

Figure 89 continued

C.2.3 Re_D = 41000

This section presents additional transfer function and phase angle results for the largest Reynolds number investigated in this thesis. Flame transfer functions for f_{drive} = 190 – 320 Hz were previously presented in Chapter 5. The rest of the flame transfer functions in the frequency range of 100 – 420 Hz are presented in Figure 90. In addition, the corresponding *u'-CH** phase angle are presented for the entire frequency range in Figure 91.

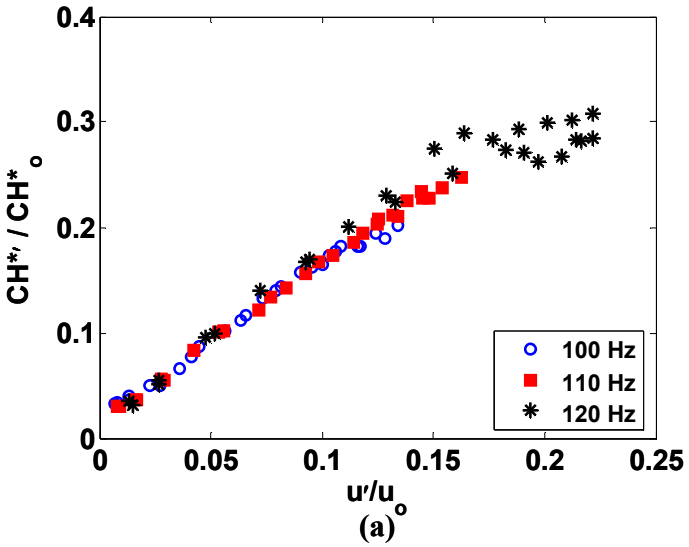

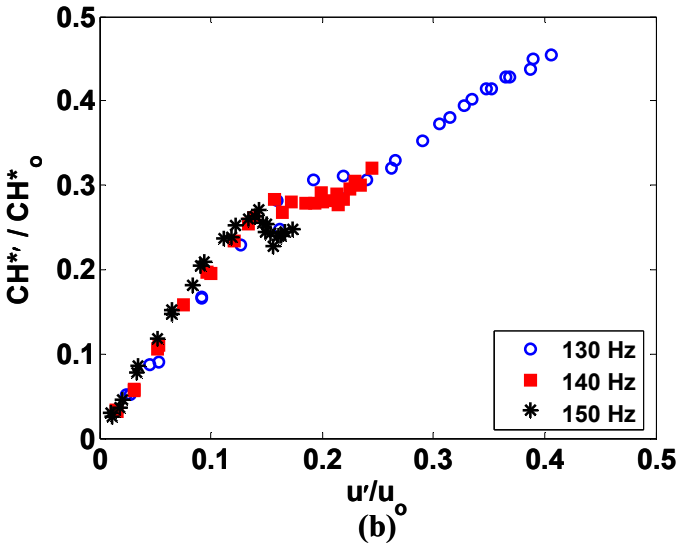

Figure 90(a-d). Dependence of CH* chemiluminescence oscillation amplitude on amplitude of velocity fluctuations for varying driving frequency (f_{drive} = 100-160, 360-420 Hz, Re_D = 43000, ϕ = 0.80).

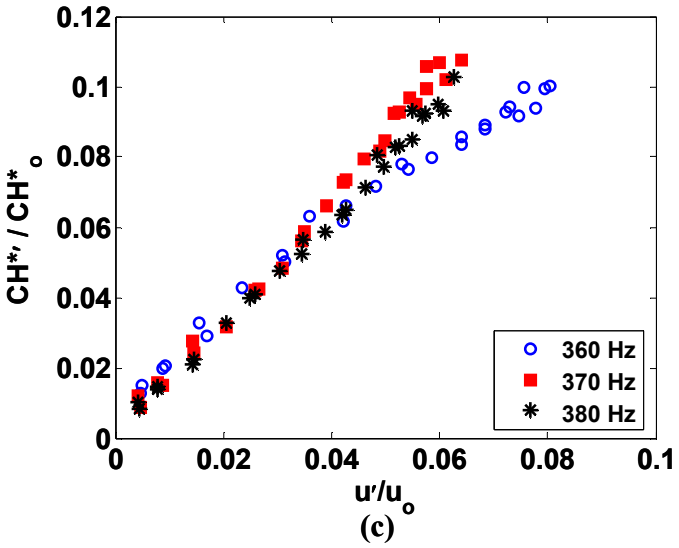

(c)

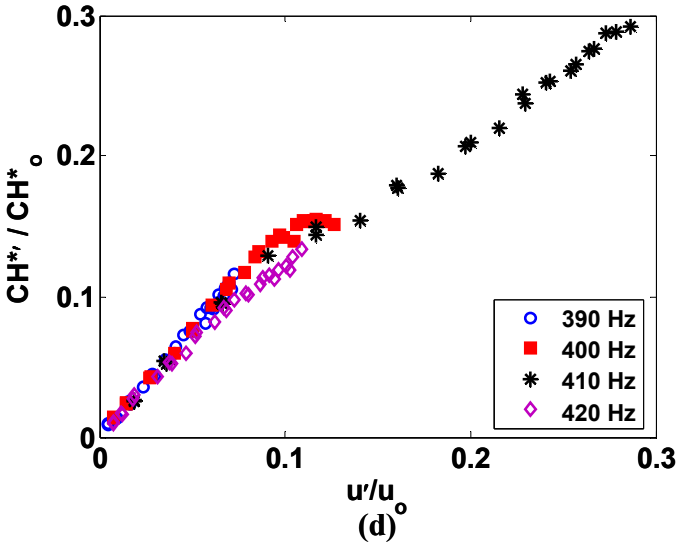

(d)

Figure 90 continued

The *u'-CH*'* phase angles over the entire frequency range at this Reynolds number are presented below in Figure 91.

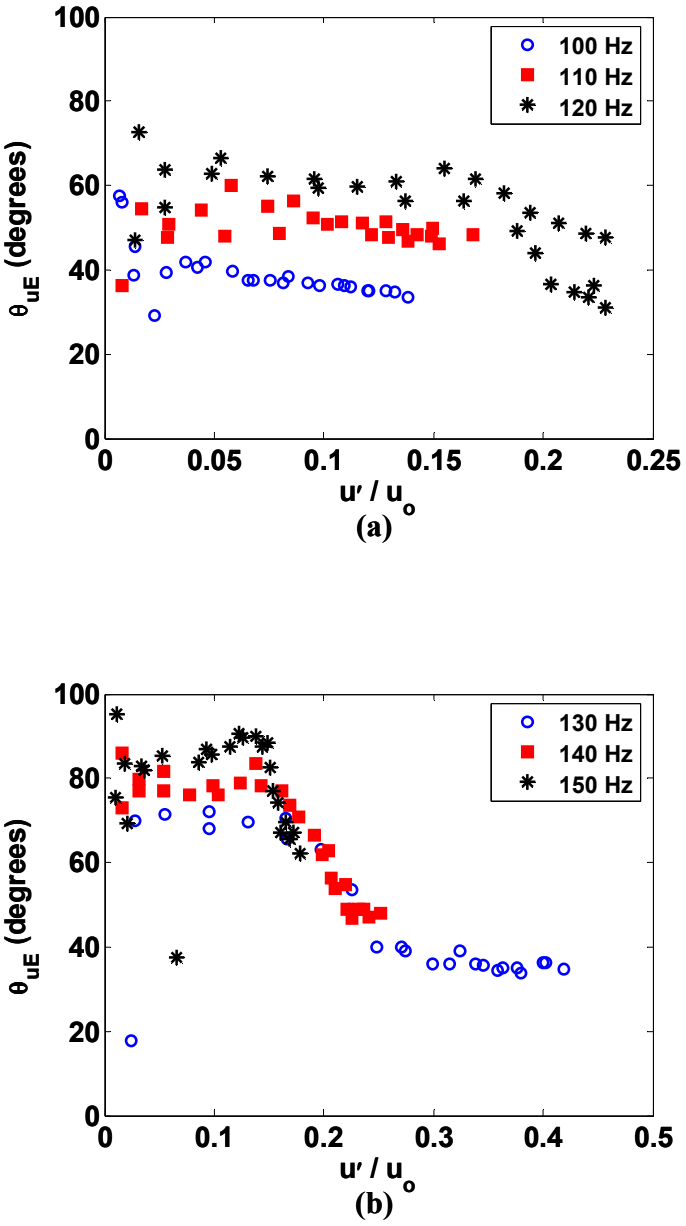

Figure 91(a-k). Dependence of *u'-CH*'* phase angle on amplitude of velocity fluctuations for varying driving frequency (f_{drive} = 100 – 420 Hz, Re_D = 43000, ϕ = 0.80). Uncertainty in phase angle < 5°.

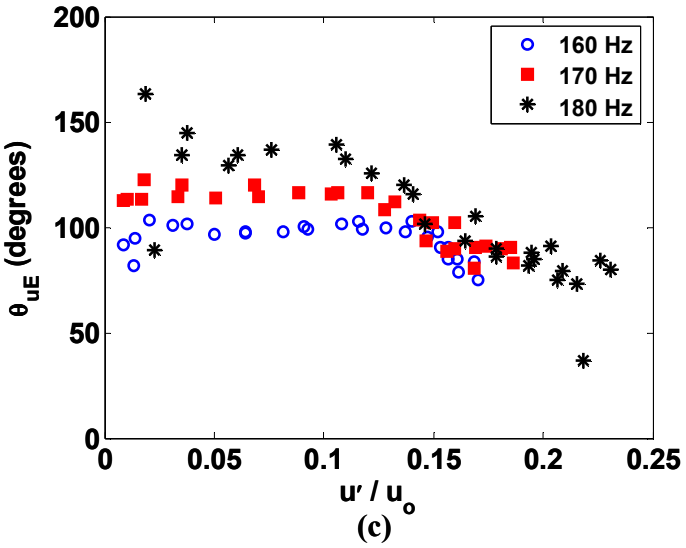

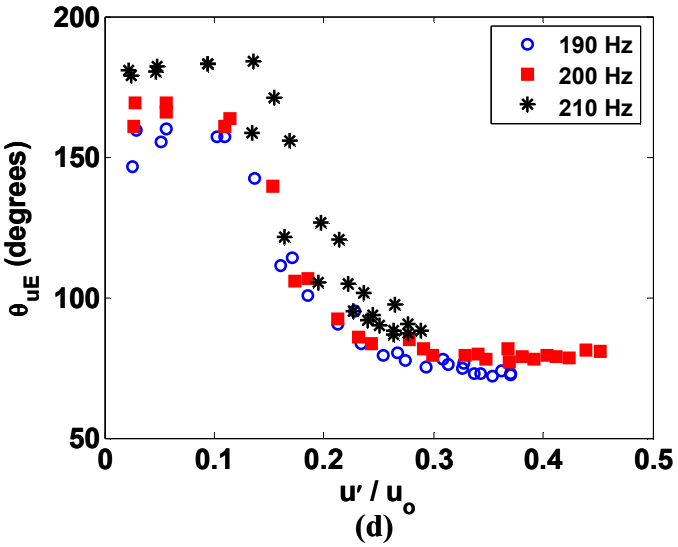

Figure 91 continued

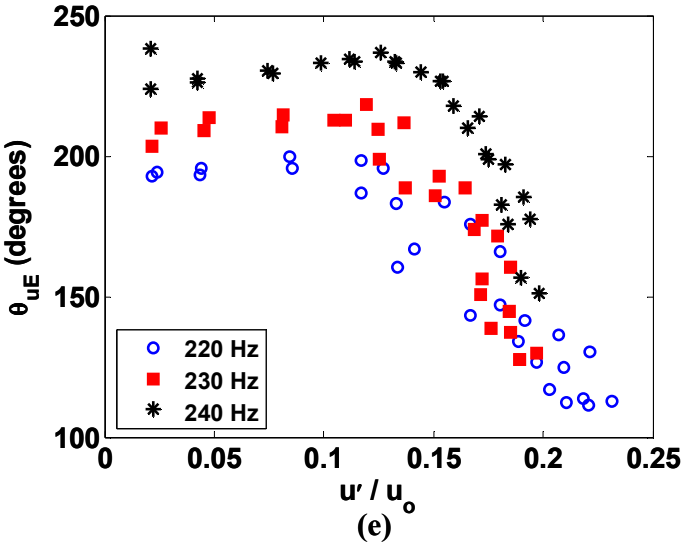

(e)

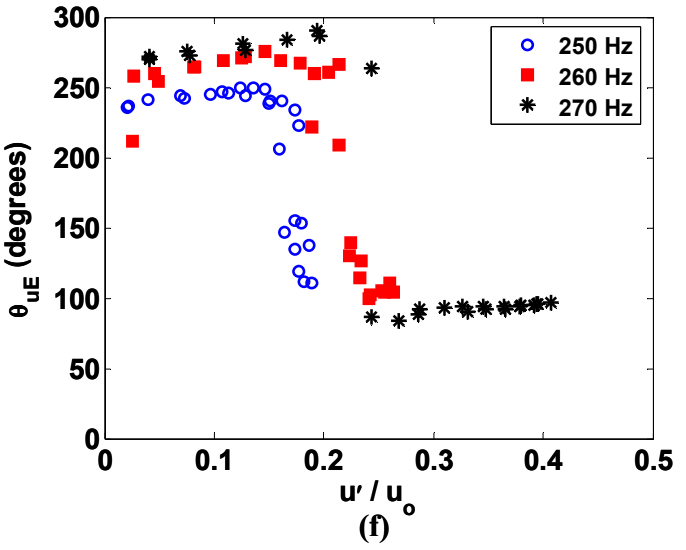

(f)

Figure 91 continued

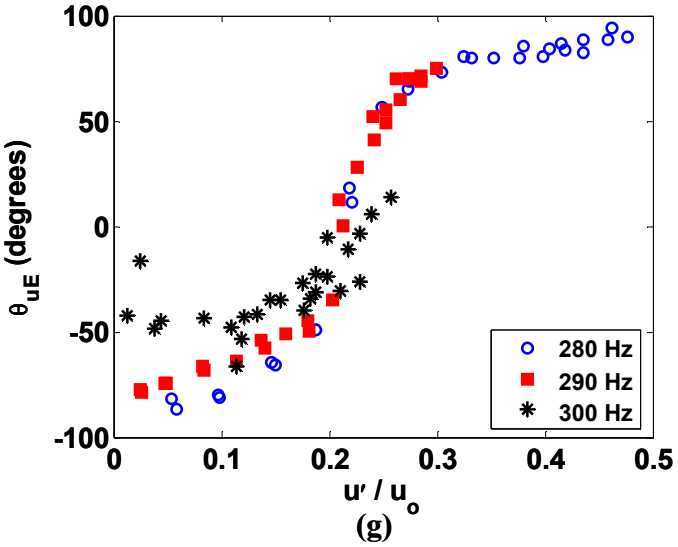

(g)

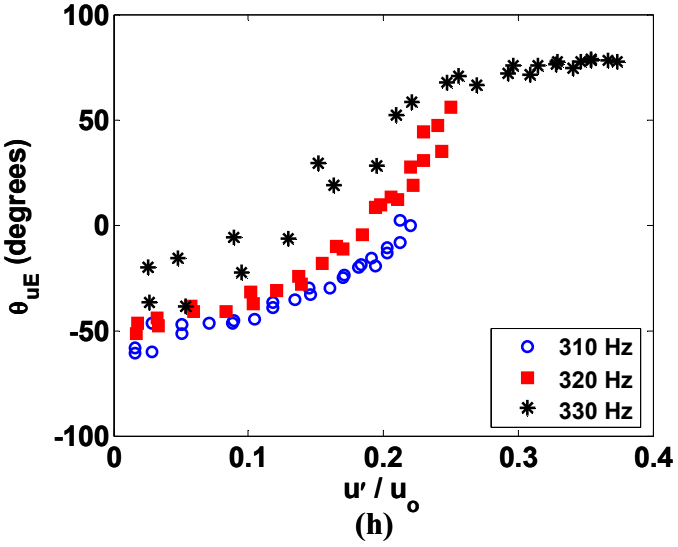

(h)

Figure 91 continued

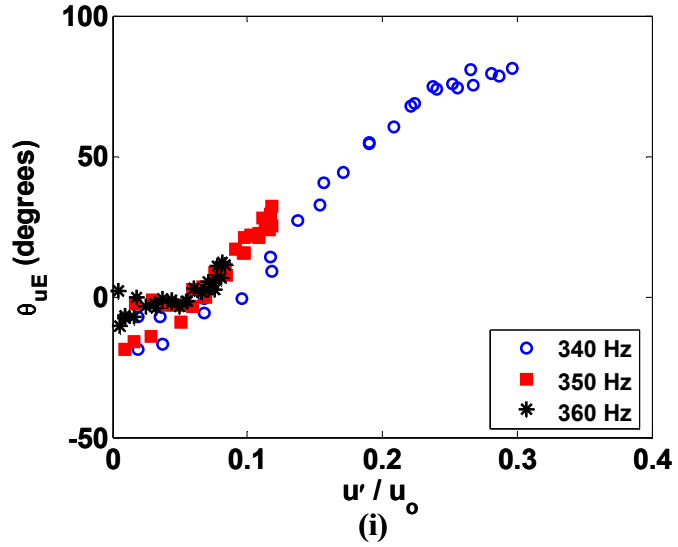

(i)

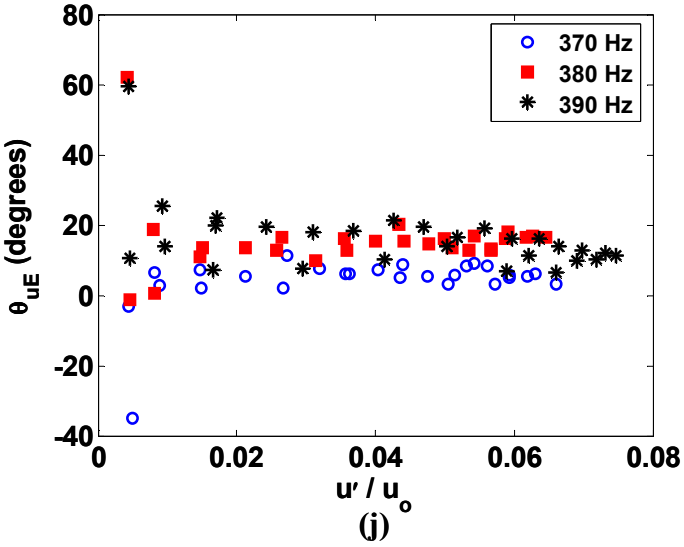

(j)

Figure 91 continued

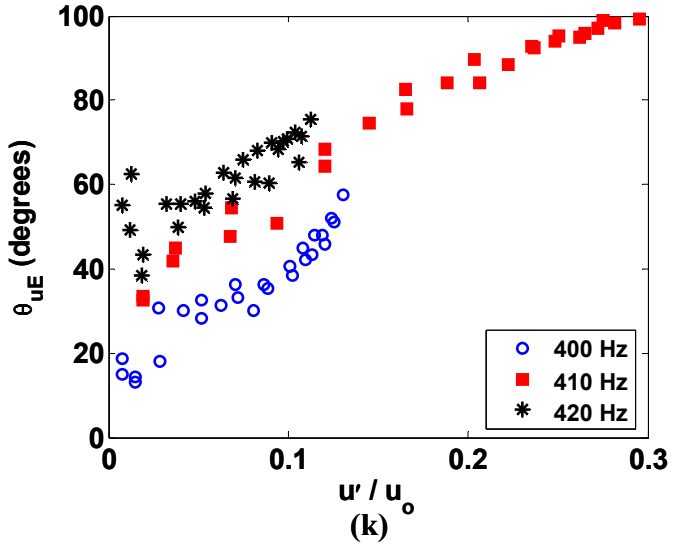

Figure 91 continued

APPENDIX D

AVERAGED OH PLIF IMAGES

This appendix presents averaged flame edges determined from the OH PLIF images for the remainder of the velocity oscillation amplitudes investigated in Chapter 5. The Chapter 5 results illustrated the sequence of flame edges over one acoustic cycle for the lowest and highest amplitude forcing for f_{drive} = 130 and 410 Hz. The flame response at four other driving amplitudes was also obtained for each frequency.

Figure 92(a-d) shows ensemble averaged flame edges for f_{drive} = 130 Hz at velocity oscillation amplitudes, u'/u_o = 0.45, 0.6, 0.75, 0.83. Recall from Figure 46 that saturation of the transfer function occurs around $u'/u_o \sim$ 0.75-0.8. Thus, Figure 92(c-d) shows flame edges at acoustic forcing amplitudes near or beyond the saturation point of the transfer function. Vortex rollup is seen at 90 degrees in Figure 92(c-d), but not for velocity amplitudes where the transfer function remains linear; i.e. Figure 92(a-b).

Similarly, Figure 93(a-d) illustrates ensemble averaged flame edges for f_{drive}= 410 Hz at velocity oscillation amplitudes, u'/u_o = 0.27, 0.35, 0.45, 0.52. Again, recall from Figure 47 that saturation of the transfer function occurs around $u'/u_o \sim$ 0.35. Therefore, Figure 93(b-d) shows flame edge sequences at acoustic forcing amplitude near or beyond the transfer function saturation point. Unsteady flame liftoff is seen throughout the acoustic cycle in Figure 93(b-d), but not for velocity amplitude where the transfer function remains linear; i.e., Figure 93(a).

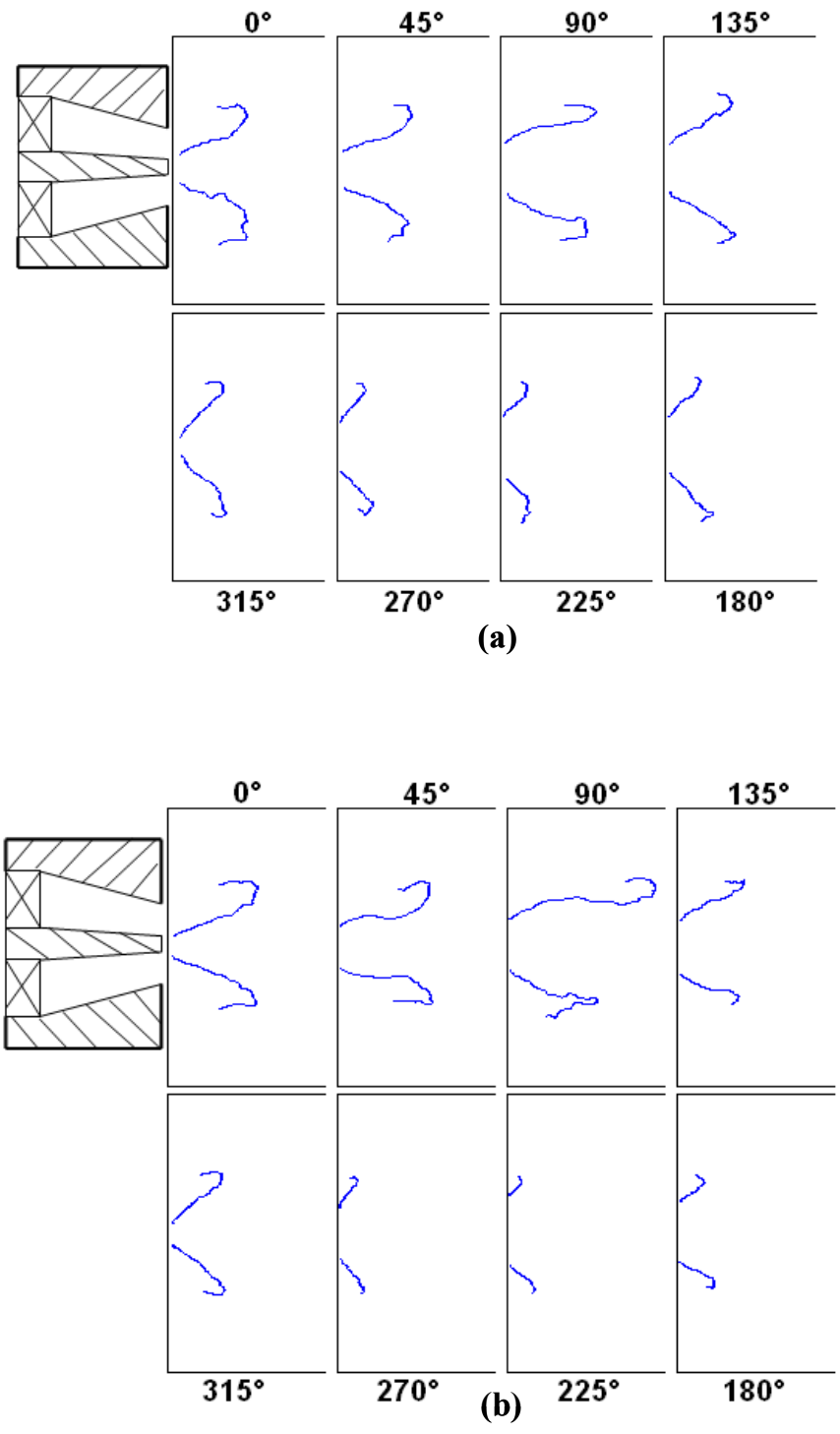

Figure 92. Phase-averaged flame edges showing evolution of flame response over 1 cycle of acoustic forcing for (a-b) low (linear, u'/u_o = 0.45, 0.6) and (c-d) high (nonlinear, u'/u_o = 0.75, 0.83) velocity oscillation amplitudes (f_{drive} = 130 Hz).

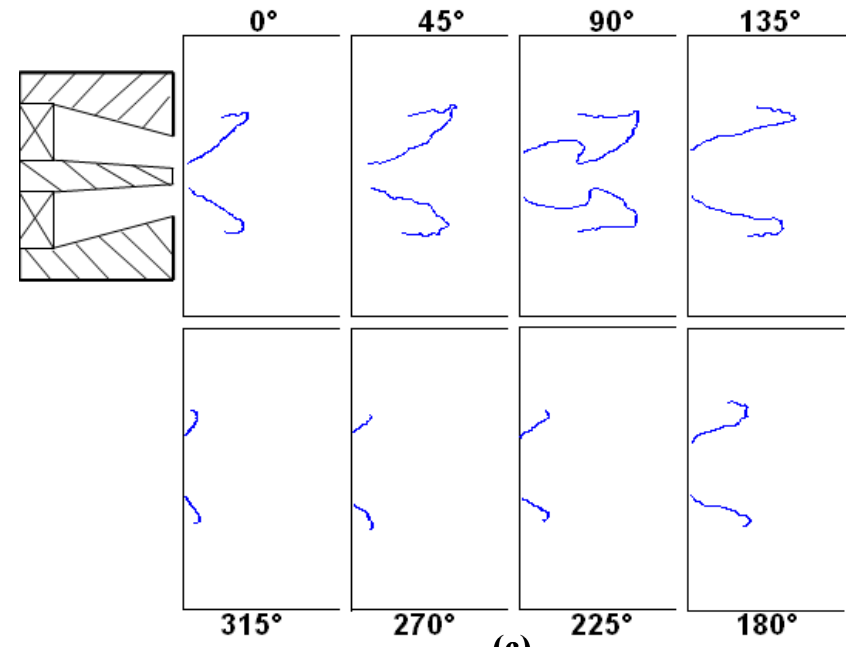

(c)

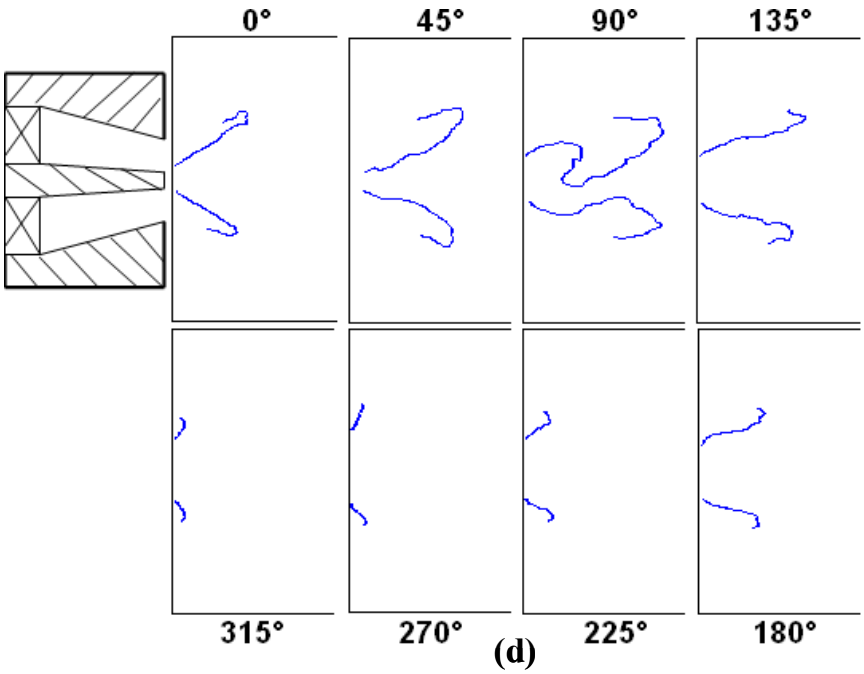

(d)

Figure 92 continued

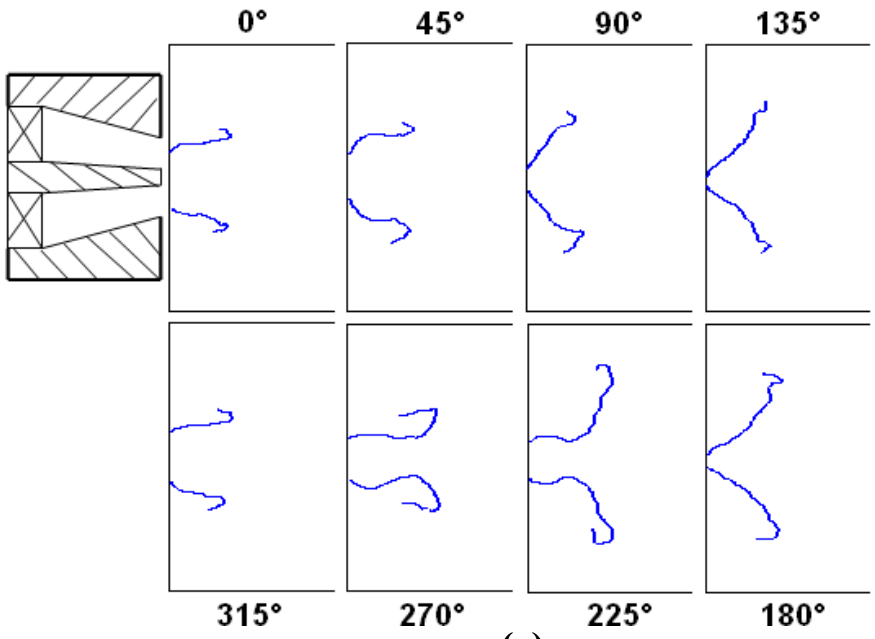

(a)

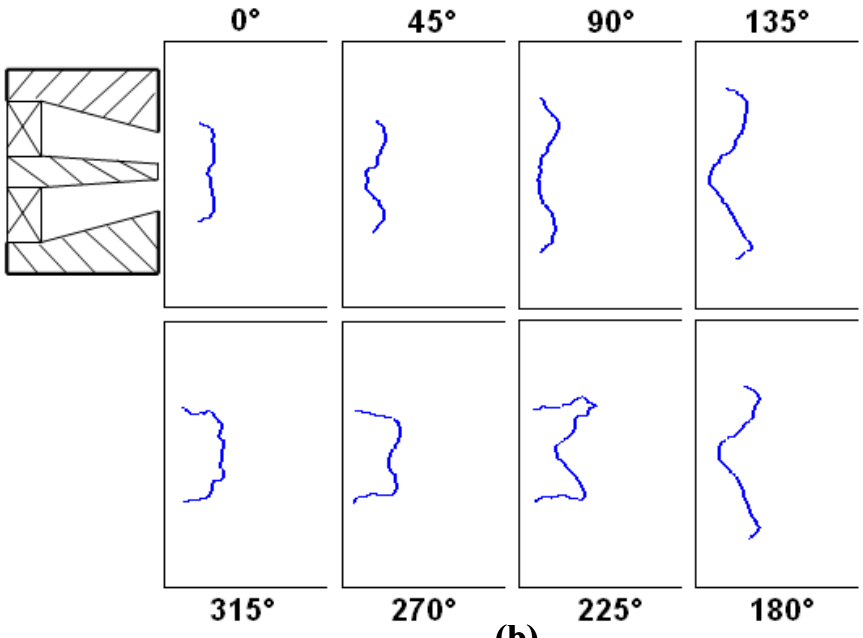

(b)

Figure 93. Phase-averaged flame edges showing evolution of flame response over 1 cycle of acoustic forcing for (a) low (linear, u'/u_o = 0.27) and (b-d) high (nonlinear, u'/u_o = 0.35, 0.45, 0.52) velocity oscillation amplitudes (f_{drive} = 410 Hz).

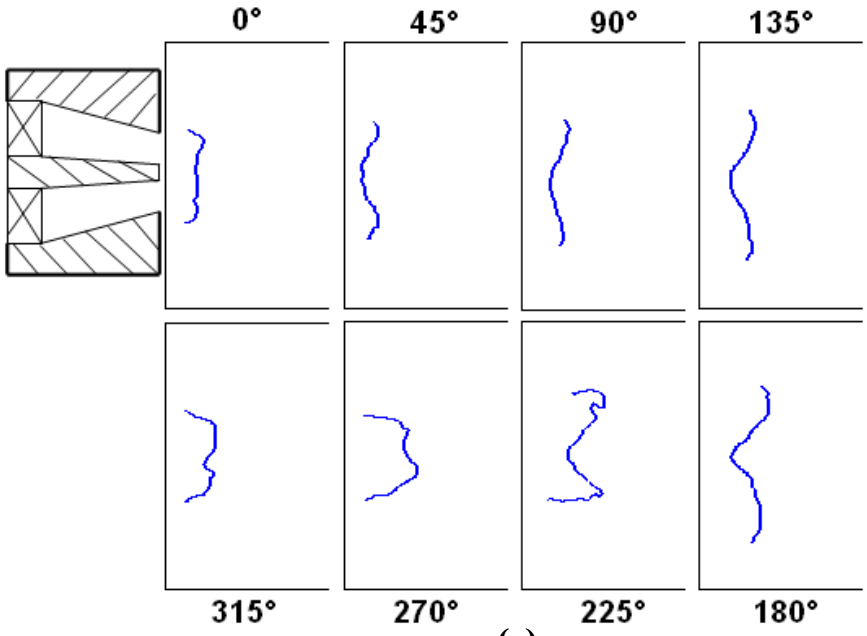

(c)

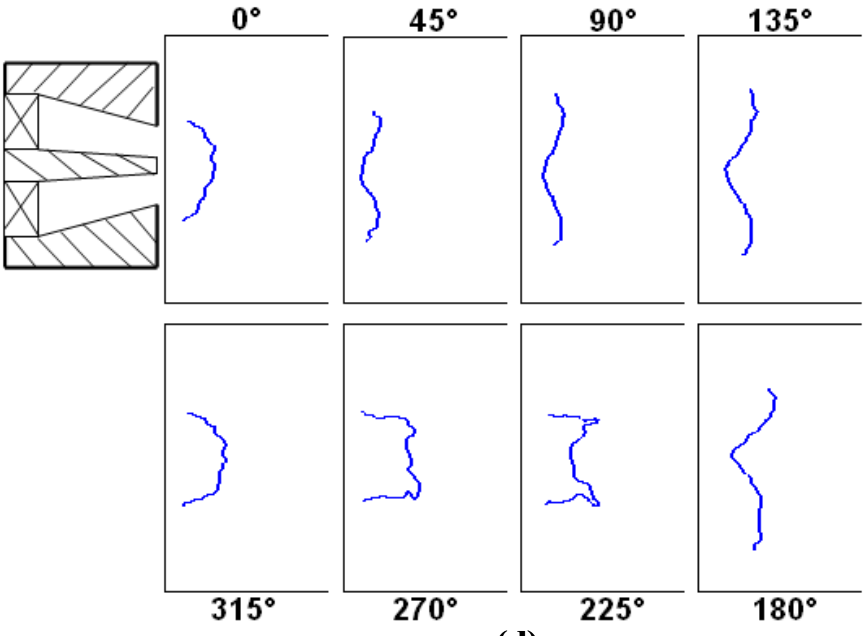

(d)

Figure 93 continued

REFERENCES

[1] Correa, S.M., "A Review of NO_X Formation under Gas-Turbine Combustion Conditions," *Combustion Science and Technology,* Vol. 87, pp.329-362, 1993.

[2] Turns, S. *An Introduction to Combustion*: *Concepts and Applications*, 2nd Edition, McGraw Hill, 2000.

[3] Cohen, J., Anderson, T., Experimental Investigation of Instabilities in a Lean, Premixed Step Combustor, *AIAA Paper #96-0819,* 1996.

[4] Straub, D.L., Richards, G.A., Effect of Fuel Nozzle Configuration on Premix Combustion Dynamic, *ASME Paper #98-GT-492*, 1998.

[5] Paschereit, C.O., Gutmark, E., Weisenstein, W., Control of Thermo-Acoustic Instabilities and Emissions in an Industrial Type Gas Turbine Combustor, *Proc. Comb. Inst.,* Vol. 27, 1998.

[6] Hsiao, G.C., Pandalai, R.P., Hura, H.S., Mongia, H.C., Combustion Dynamic Modeling for Gas Turbine Engines, *AIAA paper #98-3380,* 1998.

[7] Lieuwen, T., PhD Thesis, Investigation of Combustion Instability Mechanisms in Premixed Gas Turbines, Georgia Institute of Technology, 1999.

[8] Rayleigh, J.S.W., *The Theory of Sound*, Vol. 2, New York, 1945.

[9] Crocco, L., Cheng, S., *Theory of Combustion Instability in Liquid Propellant Rocket Motors*, Butterworths Scientific Publications, London, 1956.

[10] Zinn, B.T., Powell, E.A., Nonlinear Combustion Instability in Liquid-Propellant Rocket Engines, *Proc. Comb Inst.*, Vol. 13, pp. 491-503, 1970.

[11] Schadow, K. C., Gutmark, E., Combustion Instabilities Related to Vortex Shedding in Dump Combustors and Their Passive Control, *Prog. Energy Combust. Sci*., Vol. 18, pp. 117-132, 1992.

[12] Langhorne, P.J., Reheat Buzz: An Acoustically Coupled Combustion Instability. Part 1. Experiment*, J. Fluid Mech*., Vol. 193, pp. 417-443, 1988.

[13] Bloxsidge, G., Dowling, A., Langhorne, P., Reheat Buzz: An Acoustically Coupled Combustion Instability. Part 2. Theory*, J. Fluid Mech*. Vol. (193), pp. 445-473, 1988.

[14] Munjal, M., *Acoustics of Ducts and Mufflers*, John Wiley & Sons: New York, 1987.

[15] Fleifil, M. Annaswamy, A.M., Ghoniem, Z.A., Ghoniem, A.F., Response of a Laminar Premixed Flame to Flow Oscillations: A Kinematic Model and Thermoacoustic Instability Results, *Comb. and Flame*, Vol. 106, pp.487-510, 1996.

[16] Ducruix, S., Durox, D., Candel, S., Theoretical and Experimental Determination of the Transfer Function of a Laminar Premixed Flame, *Proc. Comb. Inst.*, Vol. 28, pp. 765 – 773, 2000.

[17] Kruger, U., Huren, J., Hoffman, S., Krebs, W., Bohn, D., Prediction of Thermoacoustic Instabilities with Focus on the Dynamic Flame Behavior for the 3A-Series Turbine of Siemens KWU, *ASME paper #99-GT-111,* 1999.

[18] Walz, G., Krebs, W., Hoffman, S., Judith, H., Detailed Analysis of the Acoustic Mode Shapes of an Annular Combustion Chamber, *ASME paper # 99-GT-113,* 1999.

[19] Schuermans, B.H., Polifke, W., Paschereit, C.O., Modeling Transfer Matrices of Premixed Flames and Comparison with Experimental Results, *ASME paper # 99-GT-132,* 1999.

[20] McManus, K., Han, F., Dunstan, W., Barbu, C., Shah, M., Modeling and Control of Combustion Dynamics in Industrial Gas Turbines, *ASME paper #GT2004-53872*, 2004.

[21] Culick, F.E.C., Burnley, V., Swenson, G., Pulsed Instabilities in Solid-Propellant Rockets, *J. Prop. Power*, Vol. 11(4), p.657 – 665, 1995.

[22] Lieuwen, T., Experimental Investigation of Limit Cycle Oscillations in an Unstable Gas Turbine Combustor, *J. Prop Power*, Vol. 18(1), pp. 61 – 67, 2002.

[23] Dowling, A.P., Nonlinear Self-Excited Oscillations of a Ducted Flame, *J. Fluid Mech.*, Vol. 346, pp 271-290, 1997.

[24] Peracchio, A.A., Proscia, W.M., Nonlinear Heat Release/Acoustic Model for Thermo-Acoustic Instability in Lean Premixed Combustors, *Journal of Engineering for Gas Turbines and Power*, Vol. 121, pp. 415 – 421, 1999.

[25] Poinsot, T., Veynante, D., Bourienne, F., Candel, S., Esposito, E., Surget, J., Initiation and Suppression of Combustion Instabilities by Active Control, *Proc. Comb. Inst.,* Vol. 22, pp. 1363 – 1370, 1988.

[26] Stow, S.R., Dowling, A.P., Low-Order Modeling of Thermoacoustic Limit Cycles, *ASME paper #GT2004-54245*, 2004.

[27] Dowling, A.P., "A Kinematic Model of a Ducted Flame", *J. Fluid Mech*., Vol. 394, pp. 51-72, 1999.

[28] McIntosh, A. C., *Phil. Trans. R. Soc. Lond. A*. Vol. 357, pp. 3523-3538, 1999.

[29] Belucci, V., Schuermans, B., Nowak, D., Flohr, P., Paschereit, C.O., "Thermoacoustic Modeling of a Gas Turbine Combustor Equipped With Acoustic Dampers", *J. Turbomachinery*, Vol. 127, 2005, pp.372-379.

[30] Baillot, F., Durox, D., Prud'homme, R., "Experimental and Theoretical Study of a Premixed Vibrating Flame", *Comb. and Flame*, Vol. 88, pp.149-168, 1992

[31] Lieuwen, T., "Nonlinear Response of Premixed Flames to Harmonic Velocity Disturbances", *Proc. Comb. Inst.* Vol. 30, pp. 1725 – 1732, 2005.

[32] Santosh, H., Lieuwen, T., "Response of Turbulent Premixed Flames to Harmonic Acoustic Forcing", *submitted to 31st Combustion Symposium*, 2006.

[33] Lieuwen, T., Neumeier, Y., Nonlinear Pressure-Heat Release Transfer Function Measurements in a Premixed Combustor, *Proc. Comb. Inst.*, Vol. 29, pp. 99-105, 2002.

[34] Lee, J., Santavicca, D., Experimental Diagnostics for the Study of Combustion Instabilities in Lean, Premixed Combustors, *J. Prop. Power*, Vol. 19(5), pp. 735-750, 2003.

[35] Balachandran, R., Ayoola, B.O., Kaminski, C.F., Dowling, A.P., Mastorakos, E., Experimental Investigation of the Nonlinear Response of Turbulent Premixed Flames to Imposed Inlet Velocity Oscillations, *Comb. and Flame*, Vol. 143(1-2), pp. 37-55, 2005.

[36] Kulsheimer, C., Buchner, H. Combustion Dynamics Of Turbulent, Swirling Flows, *Comb. And Flame*, Vol. 131, pp.70-84, 2002.

[37] Hosseini, S.M.R., Lawn, C.J., "Non-linearities in the Thermo-Acoustic Response of a Premixer, Swirl Burner", *Proc. 12th International Congress on Sound and Vibration*, Lisbon, 2005.

[38] Bourehla, A., Baillot, F., "Appearance and Stability of a Laminar Conical Premixed Flame Subjected to an Acoustic Perturbation", *Comb. and Flame*, Vol. 114, pp. 303-318, 1998

[39] Durox, D., Baillot, F., Searby, G., Boyer, L., "On the Shape of Flames Under Strong Acoustic Forcing: A Mean Flow Controlled by an Oscillating Flow", *J. Fluid Mech.*, Vol. 350, pp. 295-310, 1997.

[40] Baillot, F., Bourhela, B., Durox, D., The Characteristic Method and Cusped Flame Fronts*, Comb. Sci. Tech.*, Vol. 112, pp. 327-350, 1996.

[41] Durox, D., Schuller, T., Candel, S., *Proc. Comb. Inst.*, Vol. 29, pp.69-75, 2002

[42] Lee, S.-Y., Seo, S., Broad, J.C., Pal, P., Santoro, R.J., *Proc. Comb. Inst.* Vol. 28, pp.775-782, 2000.

[43] Santhanam, V., Knopf, F.C., Acharya, S., Gutmark, E., *J. Prop. Power*, Vol. 18, pp.855-865, 2002.

[44] Durox, D., Schuller, T., Candel, S. "Combustion Dynamics of Inverted, Conical Flames", *Proc. Comb. Inst.*, Vol. 30, pp.1717-1724, 2005.

[45] Huang, Y., Yang, V., Large-Eddy Simulation of Combustion Dynamics of Lean, Premixed Swirl-Stabilized Combustor, *J. Prop. Power*, Vol. 19(5), pp.782-794, 2003.

[46] Boden, H., Abom, M., Influence of Errors on the Two Microphone Method for Measuring Acoustic Properties in Ducts, *J. Acoust. Soc. Amer.,* Vol. 79(2), pp.541-549, 1986.

[47] Waser, M.P., Crocker, M.J., "Introduction to the Two-Microphone Cross-Spectral Method of Determining Sound Intensity", *Noise Control Engineering Journal*, Vol. 22(3), pp. 76-85, 1984.

[48] Gaydon, A.G. and Wolfhard, H.G., *Flames: Their Structure, Radiation, and Temperature,* Chapman and Hall, 1978.

[49] Keller, J.O. and Saito, K., "Measurements of the Combusting Flow in a Pulse Combustor", *Combustion Science and Technology*, Vol. 53, pp. 137-163, 1987.

[50] Lawn, C.J., "Distributions of Instantaneous Heat Release by the Cross-Correlation of Chemiluminescent Emissions," *Combustion and Flame*, Vol. 132, pp. 227-240, 2000.

[51] Roby, R.J., Hamer, A.J., Johnsson, E.L., Tilstra, S.A., and Burt, T.J., "Improved Method for Flame Detection in Combustion Turbines", *Transactions of the ASME*, Vol. 117, pp. 332 –340, 1995.

[52] Mehta, G.K., Ramachandra, M.K., and Strahle, W.C., "Correlations between Light Emission, Acoustic Emission and Ion Density in Premixed Turbulent Flames", *Proc. Comb. Inst.*, Vol. 18, pp 1051-1059, 1981.

[53] Khanna,V.K., Vandsburger, U., Saunders W. R., Baumann, W. T., "Dynamic Analysis of Swirl Stabilized Turbulent Gaseous Flames", *ASME paper #GT-2002-30061*

[54] Higgins, B., McQuay, M. Q., Lacas, F., Rolon, J. C., Darabiha, N., and Candel, S., "Systematic measurements of OH chemiluminescence for fuel-lean, high-pressure, premixed, laminar flames", *Fuel,* Vol. 80, pp 67-74, 2001.

[55] Roby, R. J., Reaney, J .E., and Johnsson, E. L., "Detection of Temperature and Equivalence Ratio in Turbulent Premixed Flames Using Chemiluminescence," *Proceedings of the 1998 Int. Joint Power Generation Conference,* Vol. 1, pp. 593-602, 1998,.

[56] Morrell, R., Seitzman, J., Wilensky, M., Lee, J., Lubarsky, E., and Zinn, B., "Interpretation Of Optical Flame Emissions For Sensors In Liquid-Fueled Combustors," *AIAA paper 2001-0787*, 2001

[57] Neumeier, Y., Nabi, A., Zinn, B.T., Investigation of Open Loop Performance of an Active Control System Utilizing a Fuel Injector Actuator, *AIAA Paper# 96-2757*, 1996.

[58] Broda, J.C., Seo, S., Santoro, S.J., Shirhattikar, G., Yang, V., An Experimental Investigation of Combustion Dynamics of a Lean, Premixed Swirl Injector, *Proc. Comb. Inst.*, Vol. 27, pp. 1849 – 1856, 1998.

[59] Bendat, J., Piersol, A., *Random Data: Analysis and Measurement Procedures*, John Wiley and Sons: New York, 1986.

[60] Schuller, T., Durox, D., Candel, S., A Unified Model for the Prediction of Laminar Flame Transfer Functions: Comparisons Between Conical and V-Flame Dynamics, *Comb and Flame*, Vol. 134, pp.21-34, 2003.

[61] Lieuwen, T., Torres, H., Johnson, C., Daniel, B.R., Zinn, B.T., A Mechanism For Combustion Instabilities In Premixed Gas Turbine Combustors, *Journal Of Engineering For Gas Turbines And* Power, Vol. 123(1), pp. 182-190, 2001,.

[62] Coats, C., Coherent Structures in Combustion, *Prog. Energy Comb. Sci.,* Vol. 22, pp.427-509, 1996.

[63] Baillot, F. Durox, D., Searby, G., Boyer, L., Parametric Response of a Conical Flame to Acoustic Waves, *Comb. Sci. Tech.*, Vol. 42, pp.91-109, 1999.

[64] Durox, D., Ducruix, D., Baillot, F., Strong Acoustic Forcing on Conical Premixed Flames, *Proc. Comb. Inst.*, Vol. 27**,** pp.993-889, 1998.

[65] Clavin, P., Pelce, P., He, L., One-Dimensional Vibratory Instability of Planar Flames Propagating in Tubes, *J. Fluid Mech.*, Vol. 216, pp. 299-322, 1990.

[66] Searby, G., Rochwerger, D., A Parametric Acoustic Instability in Premixed Flames, *J. Fluid Mech.*, Vol. 231, pp. 529-543, 1991.

[67] Vaezi, V., Aldredge, R.C., Laminar Flame Instabilities in a Taylor-Couette Combustor, *Comb. and Flame,* Vol. 121, pp. 356-366, 2000.

[68] Vaezi, V., Aldredge, R.C., Influences of Acoustic Instabilities on Turbulent-Flame Propagation, *Experimental Thermal and Fluid Science*, Vol. 20, pp.162-169, 2000.

[69] Markstein, G., "Flames as Amplifiers of Fluid Mechanical Disturbances", *Proceedings of the Sixth National Congress on Applied Mechanics*, pp. 11-33, 1970.

[70] Egolfopoulos, F.N., Zhu, D.L., Law, C.K., Experimental and Numerical Determination of Laminar Flame Speeds: Mixtures of C2 Hydrocarbons with Oxygen and Nitrogen, *Proc. Comb. Inst.*, Vol. 23, pp. 471 – 478, 1990.

[71] Wee, D., Yi, T., Annaswamy, A., Ghoniem, A.F., Self-sustained Oscillations and Vortex Shedding in Backward-facing Step Flows: Simulation and Linear Instability Analysis, *Phys. Fluids*, Vol. 16, pp.3361-3373, 2004.

[72] Huang, Y., Wang, S., Yang, V., in: T. Lieuwen, V. Yang (Eds.), *Combustion Instabilities in Gas Turbines: Operational Experience, Fundamental Mechanisms, and Modeling*, American Institute of Aeronautics and Astronautics, Reston, VA, 2005, p.213.

[73] Culick, F.E.C., Non-Linear Growth and Limiting Amplitude of Acoustic Oscillations in Combustion Chambers, *Comb. Sci. Tech.*, Vol. 3(1), pp. 1 – 16, 1971.

[74] Nayfeh, A.H., Mook, D.T., *Nonlinear Oscillations*, John Wiley and Sons: New York, 1995.

[75] Ji, J.C., Local Bifurcation of a Forced Single Degree of Freedom Nonlinear System: Saddle-Node Bifurcation, *Nonlinear Dynamics*, Vol. 26, pp. 369 – 382, 2001.

[76] Beckwith, T.G., Marangoni, R.D., Lienhard V., J.H., *Mechanical Measurements*, Addison-Wesley: New York, 1993.

[77] Pierce, A.D., *Acoustics: An Introduction to its Physical Principles and Applications*, Acoustical Society of America: New York, 1991.